

## INFORMATION TO USERS

This manuscript has been reproduced from the microfilm master. UMI films the text directly from the original or copy submitted. Thus, some thesis and dissertation copies are in typewriter face, while others may be from any type of computer printer.

**The quality of this reproduction is dependent upon the quality of the copy submitted.** Broken or indistinct print, colored or poor quality illustrations and photographs, print bleedthrough, substandard margins, and improper alignment can adversely affect reproduction.

In the unlikely event that the author did not send UMI a complete manuscript and there are missing pages, these will be noted. Also, if unauthorized copyright material had to be removed, a note will indicate the deletion.


Oversize materials (e.g., maps, drawings, charts) are reproduced by sectioning the original, beginning at the upper left-hand corner and continuing from left to right in equal sections with small overlaps. Each original is also photographed in one exposure and is included in reduced form at the back of the book.

Photographs included in the original manuscript have been reproduced xerographically in this copy. Higher quality 6" x 9" black and white photographic prints are available for any photographs or illustrations appearing in this copy for an additional charge. Contact UMI directly to order.

# UMI

A Bell & Howell Information Company  
300 North Zeeb Road, Ann Arbor MI 48106-1346 USA  
313/761-4700 800/521-0600





# **THE ROLE OF TEXTURE AND MORPHOLOGY IN OPTIMIZING THE CORROSION RESISTANCE OF ZINC-BASED ELECTROGALVANIZED COATINGS**

by

**Hyoungsoo Park**

A thesis submitted to the Faculty of Graduate Studies and Research  
in partial fulfillment of the requirements for the degree of  
Doctor of Philosophy

Department of Mining and Metallurgical Engineering  
McGill University, Montreal, Canada  
February 1997

© **Hyoungsoo Park, 1997**





National Library  
of Canada

Acquisitions and  
Bibliographic Services

395 Wellington Street  
Ottawa ON K1A 0N4  
Canada

Bibliothèque nationale  
du Canada

Acquisitions et  
services bibliographiques

395, rue Wellington  
Ottawa ON K1A 0N4  
Canada

*Your file    Votre référence*

*Our file    Notre référence*

The author has granted a non-exclusive licence allowing the National Library of Canada to reproduce, loan, distribute or sell copies of this thesis in microform, paper or electronic formats.

The author retains ownership of the copyright in this thesis. Neither the thesis nor substantial extracts from it may be printed or otherwise reproduced without the author's permission.

L'auteur a accordé une licence non exclusive permettant à la Bibliothèque nationale du Canada de reproduire, prêter, distribuer ou vendre des copies de cette thèse sous la forme de microfiche/film, de reproduction sur papier ou sur format électronique.

L'auteur conserve la propriété du droit d'auteur qui protège cette thèse. Ni la thèse ni des extraits substantiels de celle-ci ne doivent être imprimés ou autrement reproduits sans son autorisation.

0-612-30355-1

## ABSTRACT

Zinc-based electrogalvanized coatings have attracted increasing interest from the automobile industry and steelmakers because of their excellent corrosion resistance and good mechanical properties. The coating properties are closely related to the microstructure of deposit. Among them, texture is a key factor which influences the coating properties. This study demonstrates the microstructure and corrosion behaviors of the electrodeposited zinc, zinc-iron, and zinc-nickel coatings on steel sheet deposited at different current density, pH and coating thicknesses. The evolution of the coating microstructure - texture, surface morphology, interplanar spacings, microstress, alloy content, and phase composition - is investigated in various deposition conditions. This work also demonstrates the influence of the coating microstructure upon corrosion behavior. In addition, the early stage of deposition behavior is observed in order to demonstrate the growth mechanism of deposits.

The surface morphology and texture of coatings are investigated using AFM (Atomic Force Microscope), SEM and x-ray diffractometers. Corrosion behaviors are analyzed by the Tafel extrapolation method from the potentiodynamic polarization curves as well as by the electrochemical noise tests.

It is found that the zinc based coatings show a significant variation in texture with the change of deposition parameters. The present work suggests that the transformation of texture is closely related to the evolution of coating morphology and the change of alloy content in the deposit as well as phase composition. This work also demonstrates that there is a correlation between morphology and the texture of coatings. The morphology of hexagonal platelets represents the basal {0001} fiber texture. The morphology of hexagonal ridges represents the pyramidal non-fiber texture and the morphology of triangular-based

pyramids represents the pyramidal  $\{10\bar{1}X\}$  fiber texture. From the corrosion test, it is found that the texture of coatings strongly influences corrosion resistance. The coatings with strong  $\{0001\}$  texture have better corrosion resistance than the coatings with weak  $\{0001\}$  texture or a  $\{10\bar{1}X\}$  fiber texture component. The influence of alloy content and phase composition upon corrosion behavior is also discussed. Consequently, it is proposed how to optimize the deposition process to obtain the desirable texture, morphology and alloy content of the deposit for better corrosion resistance.

## RÉSUMÉ

La galvanisation par revêtement au zinc est devenue un domaine d'intérêt pour l'industrie automobile et sidérurgique; un tel revêtement assure une bonne résistance à la corrosion et des propriétés mécaniques accrues. Les propriétés du revêtement, en particulier leurs textures, sont particulièrement dépendantes de la microstructure du dépôt. La présente étude s'intéresse aux effets du courant, pH et épaisseur du dépôt, sur les microstructures et les propriétés de corrosion des revêtement de zinc, zinc-fer et zinc-nickel. L'évolution de la texture, de la morphologie de surface, de la distance interplanare, des micro-contraintes, de la composition de l'alliage et de la composition des phases sont étudiées sous différentes conditions de dépôt. Ce travail montre que la texture a une forte influence sur le comportement sous corrosion. Il a été également trouvé que le revêtement se développe suivant une loi de croissance de dépôt.

La morphologie et la texture sont étudiées grâce au microscope à résonance atomique, un microscope électronique à balayage et un diffractomètre à rayon X. Le comportement en corrosion a été analysé par la méthode d'extrapolation de Tafel, utilisant les courbes de polarisation par potentiométrie dynamique et le test de bruit électrochimique.

Il a été trouvé que le revêtement à base de zinc varie de manière importante avec un changement de texture. Le présent travail suggère que la transformation de texture est reliée à l'évolution de la morphologie du revêtement, aux changements d'éléments d'alliages, et à la composition de la phase développée. Ce travail démontre aussi qu'il y a une corrélation entre la morphologie et la texture des revêtements. Une morphologie de type plaquettes hexagonales représente une texture à base  $\{0001\}$  alors qu'une morphologie pyramidale à base triangulaire forme une fibre  $\{10\bar{1}X\}$ , et une morphologie d'arête hexagonale donne une texture

pyramidale sans fibre. Les tests de corrosion montrent que la texture du revêtement influence fortement la résistance à la corrosion. Une forte texture  $\{0001\}$  induit une meilleure résistance à la corrosion qu'une faible texture  $\{0001\}$  ou une texture de fibre de type  $\{10\bar{1}X\}$ . L'influence des éléments d'alliage et des phases présentes est aussi considérée. En conséquence, il est possible d'optimiser le procédé de déposition pour obtenir une meilleure résistance à la corrosion.



## ACKNOWLEDGMENT

The author wishes to express his sincere gratitude to the supervisor of this thesis, Professor Jerzy A. Szpunar, for the extensive academic guidance, assistance and constant encouragement over the past four years. Professor Szpunar has helped extend the author's expertise from conventional Metallurgy to Advanced Material Science.

The author deeply appreciates the support and encouragement of Professor G. P. Demopoulos and his staff members in carrying out the experimental work on corrosion tests which are essential parts of this research.

The author is also grateful to Dr. F. Czerwinski and Mr. P. Blandford for their invaluable discussions, and in particular involving Texture Analysis of Electrodeposited Coatings. The author would also like to thank his fellow researchers Mr. Kitae Lee, Mr. B. Morris, Mr. Jaeyoung Cho, Dr. A. Jiliaev, Mr. M. Glavicic, Mr. H. Lee, Mr. R. Narayanan, Dr. V. Gertsman, Mr. M. Nilsson for their friendship and timely help. Particular thanks are due to Mr. S. Poplawski who provided professional services and sincere assistance in the experimental work of this research.

Finally, the author wishes to express his acknowledgment to the Natural Sciences and Engineering Research Council of Canada for their financial support.

# TABLE OF CONTENTS

<b>ABSTRACT .....</b>	<b>ii</b>
<b>RÉSUMÉ .....</b>	<b>iv</b>
<b>ACKNOWLEDGMENT .....</b>	<b>vi</b>
<b>TABLE OF CONTENTS .....</b>	<b>vii</b>
<b>LIST OF FIGURES .....</b>	<b>xi</b>
<b>LIST OF TABLES .....</b>	<b>xviii</b>
 <b>CHAPTER 1. INTRODUCTION .....</b>	 <b>1</b>
 <b>CHAPTER 2. LITERATURE REVIEW.....</b>	 <b>6</b>
2.1. The Application of Zn-based Galvanized Steel in the Automotive Industry .....	6
2.2. Galvanizing Process for Sheet Steel.....	9
2.3. Microstructure of Zn-based Electrodeposited Coatings.....	12
2.4. Fundamental Aspects of Electrodeposition.....	17
2.5. Alloy Codeposition behaviors: Anomalous Codeposition.....	23
2.6. Nucleation Process.....	26
2.7. Evolution of Texture during Electrodeposition.....	28
2.8. Epitaxy and Coating Morphology of Electrodeposit.....	32
2.9. Microstructure and Corrosion Properties of Zn-based Coatings.....	35
 <b>CHAPTER 3. EXPERIMENTAL PROCEDURES.....</b>	 <b>39</b>
3.1. Sample Preparation .....	39
3.2. Description of Electrodeposition Procedures.....	39
3.3. Microstructure Characterization Techniques.....	42
3.3.1. Atomic Force microscopy (AFM).....	42
3.3.2. X-ray Diffractometry.....	44
3.3.3. Texture Measurement.....	44

3.4. Electrochemical Corrosion Tests.....	46
3.4.1. Tafel Extrapolation Method .....	47
3.4.2. Electrochemical Noise Measurement (ENM) .....	49

## **CHAPTER 4. SURFACE MORPHOLOGY AND TEXTURE OF ZINC COATINGS..... 51**

4.1. Effects of Deposition Parameters on the Characteristics of Surface Morphology.....	51
4.1.1. Morphology Variation with Changing Current Density.....	51
4.1.2. Morphology Variation with Changing pH Value of the Electrolyte.....	56
4.1.3. Morphology Variation with Changing Coating Thickness.....	60
4.1.4. Summary.....	63
4.2. Evolution of Texture at Different Deposition Parameters.....	64
4.2.1. Influence of Current Density.....	64
4.2.2. Influence of pH.....	70
4.2.3. Influence of Coating Thickness.....	73
4.2.4. Summary.....	76

## **CHAPTER 5. CHARACTERISTICS OF ZINC ALLOY COATINGS..... 78**

5.1. Surface Morphology at the Early Stage of Deposition.....	78
5.2. Surface Morphology of Zinc Alloy Coatings.....	83
5.2.1. Influence of Current Density (Zinc-Iron Coatings).....	84
5.2.2. Influence of Coating Thickness (Zinc-Iron Coatings).....	89
5.2.3. Influence of Current Density (Zinc-Nickel Coatings).....	92
5.2.4. Summary.....	97
5.3. Interplanar Spacings and Microstress of Coatings.....	98
5.3.1. Change of Interplanar Spacings of Zinc-Iron Coatings with Current Density.....	98

5.3.2. Change of Phase Composition of Zinc-Nickel Coatings with Current Density.....	102
5.3.3. Microstress of Zinc-Iron Coatings.....	105
5.3.4. Summary.....	108
5.4. Evolution of Texture with Changing Current Density.....	108
5.4.1. Texture of Zinc-Iron Coatings.....	108
5.4.2. Texture of Zinc-Nickel Coatings.....	112
5.4.3. Summary.....	117

## **CHAPTER 6. CORROSION PROPERTIES OF**

<b>ZINC AND ZINC ALLOY COATINGS.....</b>	<b>118</b>
6.1. Corrosion Behavior of Zinc Coatings.....	118
6.1.1. Influence of Texture and Morphology upon Corrosion Resistance.....	118
6.1.2. Optimum Current Density for the Best Corrosion Resistance.....	122
6.1.3. Summary.....	123
6.2. Corrosion Properties of Zinc Alloy coatings.....	124
6.2.1. Corrosion Behavior of Zinc-Iron Coatings.....	125
6.2.2. Corrosion Behavior of Zinc-Nickel Coatings.....	130
6.2.3. Optimum Deposition Conditions for the Best Corrosion Resistance of Zinc Alloy Coatings.....	139
6.2.4. Summary.....	141

## **CHAPTER 7. MICROSTRUCTURAL CHARACTERIZATION**

<b>OF ZINC ALLOY COATINGS.....</b>	<b>143</b>
7.1. Change of Morphology and Alloy Composition with Coating Thickness	143
7.2. The Oversaturated $\eta$ Phase of Zinc-Iron Coatings.....	145
7.3. Anomalous Codeposition of Zinc Alloy Coatings.....	147
7.4. Phase Composition and Morphology of Zinc-Nickel Coatings.....	147

<b>CHAPTER 8. SUMMARY AND CONCLUSIONS.....</b>	<b>149</b>
8.1. Summary and Conclusions.....	149
8.2. The Contribution to Original Knowledge.....	152
8.3. Suggestions for Further Work.....	154
<b>REFERENCES.....</b>	<b>156</b>

## LIST OF FIGURES

Figure 1.1. Three primary texture components in zinc electrodeposited coatings: (a) basal texture, (b) pyramidal texture and (c) prismatic texture [Pak 1991].....	3
Figure 2.1. Use of zinc-coated steels in a car by one U.S. automaker [Metals Handbook 1990].....	7
Figure 2.2. Typical usage of zinc-coated steel components for body, chassis, and power train applications in a car manufactured by a U.S. automaker [Metals Handbook 1990].....	8
Figure 2.3. A schematic diagram of an electrogalvanizing line [Bush 1989].....	10
Figure 2.4. Three types of plating cells for the electrogalvanizing process: (a) the horizontal cell, (b) the vertical cell and (c) the radial cell [Bush 1989].....	11
Figure 2.5. Equilibrium phase diagrams of zinc-iron and zinc-nickel binary systems [Kubaschewski 1991].....	15
Figure 2.6. Differences in phase compositions between (a) the equilibrium [Kubaschewski 1991] and (b) electrodeposited non-equilibrium states in the zinc-iron system [Adaniya et al. 1985].....	16
Figure 2.7. Schematic representation of the mechanism of cathodic metal deposition [Li 1995].....	18
Figure 2.8. Current density-cathode potential relationship [Parthasaradhy 1989]...	22
Figure 2.9. Effect of current density on the zinc content of zinc-iron electrodeposited alloys: (a) low current density and (b) high current density range [Brenner 1963].....	25
Figure 2.10. Steps and kinks are preferred sites for ad-atoms to get incorporated into the metal lattice [Li 1995].....	27
Figure 2.11. Schematic drawing of a single cubic lattice showing different possible sites of incorporation of an atom in the lattice [Winand 1990].....	27
Figure 2.12. Schematic illustration of the formation of the grain boundary in the deposition process. The boundary bends to reach the equilibrium state [Li 1995].....	31
Figure 2.13. Atomic arrangements of both phases on the $\{0001\}_{\eta\text{-Zn}} // \{110\}_{\alpha\text{-Fe}}$ interface [Ohmori et. al. 1993].....	34

Figure 2.14. Relationship between the alloy composition and corrosion rate of zinc alloy electrodeposited coatings: (a) Zn-Ni coatings and (b) Zn-Mn coatings [Vlad 1990].....	37
Figure 3.1. Schematic illustration of the electrodeposition set.....	40
Figure 3.2. Schematic of the sensing system of an atomic force microscope [Digital Instruments 1993].....	43
Figure 3.3. Schematic illustration of x-ray diffraction method (Schulz reflection method) [Cullity 1978].....	45
Figure 3.4. Experimentally measured Tafel plot [EG&G 1982].....	46
Figure 3.5. Schematic diagrams of (a) the corrosion cell and (b) the electrode arrangement [EG&G 1986].....	48
Figure 3.6. Schematic illustration of the arrangement for electrochemical noise measurement.....	50
Figure 4.1. The SEM images exhibit morphological evolution of zinc electrodeposited coatings at different current density: (a) 30, (b) 100, (c) 300, (d) 400 mA/cm <sup>2</sup> .....	52
Figure 4.2. The AFM morphology and section profile analysis of hexagonal ridges in the zinc electrodeposited coatings; The ridges are aligned to the rolling direction and tilted about 35 degrees against the substrate surface.....	54
Figure 4.3. The SEM morphology of zinc electrodeposited coatings at different pH of electrolyte: (a) large portions of flat area and hexagonal ridges are observed at pH 1, (b) the flat area disappears, whereas the ridges are well aligned to the rolling direction at pH 5 (x2000), (c) detailed image of ridges at pH 5 (x7000).....	57
Figure 4.4. The AFM morphology of the flat area in the zinc electrodeposited coatings; The massive flat area is covered with numbers of tiny particles.....	58
Figure 4.5. Correlation between hydrogen adsorption and surface energy of iron; The deposits' surface energy decreases as the amount of adsorbed hydrogen increases [Petch 1956].....	59

- Figure 4.6. The SEM images exhibit a morphological evolution of zinc electrodeposited coatings at different coating thickness: (a) 600 nm, (b) 6  $\mu\text{m}$ , (c) 10  $\mu\text{m}$ , (d) 30  $\mu\text{m}$ , and (e) 100  $\mu\text{m}$ . .....61
- Figure 4.7. The pole figures of zinc electrodeposited coatings deposited at different current density: (a) 30, (b) 300, (c) 400, (d) 500  $\text{mA}/\text{cm}^2$ ; The basal component completely disappears while the non-fiber pyramidal component evolves to fiber at high current density.....65
- Figure 4.8. The pole figures and ODF of steel substrate exhibit typical annealing texture of steel sheet; The poles of  $\{110\}$  plane are tilted about 35 degrees from the center of  $\{110\}$  pole figure.....68
- Figure 4.9. The pole figures of zinc electrodeposited coatings deposited at different pH value of electrolyte: (a) pH 1, (b) pH 2, (c) pH 3.8, (d) pH 5; The extremely strong basal texture becomes weak, while the pyramidal component becomes predominant as the pH value increases.....71
- Figure 4.10. The pole figures of zinc electrodeposited coatings deposited at different coating thicknesses: (a) 600 nm, (b) 6  $\mu\text{m}$ , (c) 30  $\mu\text{m}$ , (d) 100  $\mu\text{m}$ ; Both of the texture components become weak and dispersed as the coating thickness increases.....74
- Figure 5.1. The AFM morphology and section profile analysis show the evolution of deposit with coating time: (a) the initial morphology of deposits in the form of “fish scale-like” platelets slightly tilted from substrate surface (coating time-30 sec), (b) the section analysis exhibits that the platelets are tilted about 1~3 degrees (arrow marked) from substrate surface, (c) the growing surface is covered by a number of particles (c.t.-90 sec), (d) detailed morphology of particles in (c), (e) formation of pyramidal grains (c.t.-300 sec), and (f) well developed morphology of pyramidal grains (c.t.-1800 sec).....79
- Figure 5.2. The SEM images show (a) the particle formation, (b) the pyramidal grains in the evolution of coating morphology.....82
- Figure 5.3. Schematic illustration of the terraced growth; The platelets of the terraces are slightly tilted with respect to the substrate surface by angle  $\alpha$ . The morphology is characterized by periodic tread and riser surfaces.....82



- Figure 5.4. The SEM images exhibit morphological evolution of zinc-iron electrodeposited coatings at different current density: (a) 50, (b) 100, (c) 200, (d) 300 mA/cm<sup>2</sup>; The morphology of coatings continuously changes from hexagonal platelets and ridges to triangular-based pyramids with current density increase.....85
- Figure 5.5. The AFM morphology and section profile analysis of triangular pyramidal morphology of zinc-iron electrodeposited coatings; The pyramid represents part of a hexagonal columnar crystal tilted from the substrate surface. Thus, one wall represents {0001} plane while the other two walls represent {10 $\bar{1}$ 0} planes. The section analysis exhibits the angle between each {10 $\bar{1}$ 0} plane is about 120 deg. which corresponds to the hexagonal geometry. ....87
- Figure 5.6. The change of iron content in the zinc-iron electrodeposited coatings at various current densities.....88
- Figure 5.7. The SEM images exhibit morphological evolution of zinc-iron electrodeposited coatings at different coating thicknesses (current density at 300mA/cm<sup>2</sup>): (a) 5 $\mu$ m, (b) 10  $\mu$ m, (c) 30  $\mu$ m, (d) 100 $\mu$ m. ...90
- Figure 5.8. The SEM image of zinc-iron electrodeposited coating with a coating thickness of 100  $\mu$ m, deposited at 500mA/cm<sup>2</sup>.....91
- Figure 5.9. Correlation between coating thickness and percent of iron in the zinc-iron electrodeposited coatings.....91
- Figure 5.10. The SEM images exhibit morphological evolution of zinc-nickel electrodeposited coatings at different current density: (a) 50, (b) 200, (c) 500, (d) 1200 mA/cm<sup>2</sup>.....93
- Figure 5.11. The AFM morphology of zinc-nickel electrodeposited coatings at different deposition current density: (a) pyramidal grains at 200 mA/cm<sup>2</sup>, (b) mixed morphology of triangular pyramids and tiny particles at 50 mA/cm<sup>2</sup>.....95
- Figure 5.12. Correlation between current density and percent of nickel in the zinc-nickel electrodeposited coatings.....96
- Figure 5.13. X-ray diffractometry of zinc-iron electrodeposited coatings at various current density: (a) zinc random powder (b) 50 , (c) 100, (d) 200, (e) 300, (f) 400, (g) 500 mA/cm<sup>2</sup>; Each of the peaks shift either to higher or lower 2 $\theta$  angles as the current density changes.....99

Figure 5.14. Correlation between deposition current density and interplanar spacings of zinc-iron electrodeposited coatings.....	101
Figure 5.15. Correlation between deposition current density and c/a ratio of zinc-iron electrodeposited coatings.....	102
Figure 5.16. X-ray diffractometry of zinc-nickel electrodeposited coatings at various current density: (a) 50, (b) 100, (c) 200, (d) 300, (e) 500, (f) 900, (g) 1200 mA/cm <sup>2</sup> , and (h) standard peak position of $\gamma$ phase of zinc-nickel.....	104
Figure 5.17. Change of FWHM of zinc-iron electrodeposited coatings with current density.....	106
Figure 5.18. Change of FWHM of zinc-iron electrodeposited coatings with coating thickness.....	106
Figure 5.19. Difference of FWHM between hot-dip zinc-iron galvanized coating and electrodeposited zinc-iron coatings obtained at various current densities.....	107
Figure 5.20. The pole figures of zinc-iron electrodeposited coatings deposited at different current density: (a) 50, (b) 100, (c) 200, (d) 300, (e) 400, (f) 500 mA/cm <sup>2</sup> ; The basal component completely disappears at 200 mA/cm <sup>2</sup> while the non-fiber pyramidal component gradually evolves to fiber at higher current density.....	109
Figure 5.21. The pole figures of zinc-nickel electrodeposited coatings deposited at different current density: (a) 50, (b) 200, (c) 700, (d) 900, (e) 1200 mA/cm <sup>2</sup> .....	113
Figure 5.22. Correlation between the intensity of texture and nickel percentage in the zinc-nickel coatings.....	115
Figure 6.1. Correlation between intensity of {0001} texture and corrosion current of zinc electrodeposited coatings.....	119
Figure 6.2. Schematic illustration of three different types of coating surface: (a) basal, (b) pyramidal non-fiber, (c) pyramidal fiber textured coating morphology. ....	121
Figure 6.3. Correlation between deposition current density and corrosion current as well as intensity of {0001} texture of the zinc electrodeposited coatings.....	122

Figure 6.4. Polarization curves of zinc-iron electrodeposited coatings exhibit different corrosion behavior of the coatings deposited at low (A) and high (B) current density.....	126
Figure 6.5. Correlation between intensity of {0001} texture and corrosion current of zinc-iron electrodeposited coatings.....	127
Figure 6.6. Correlation between iron content in the deposit and corrosion current of zinc-iron electrodeposited coatings.....	127
Figure 6.7. Correlation between iron content in the deposit and corrosion potential of zinc-iron electrodeposited coatings.....	129
Figure 6.8. Electrochemical noise resistance measurement exhibits different corrosion behavior of zinc-iron electrodeposited coatings deposited at different current density; The coating of 50 mA/cm <sup>2</sup> shows large fluctuation of noise resistance possibly induced by the repeated reaction of passivation and localized corrosion attack, while the other coating of 500 mA/cm <sup>2</sup> shows a relatively small variation interpretable as an overall corrosion attack.....	129
Figure 6.9. Correlation between nickel content in the deposit and corrosion current of zinc-nickel electrodeposited coatings.....	131
Figure 6.10. Correlation between intensity of texture and corrosion current of zinc-nickel electrodeposited coatings.....	132
Figure 6.11. Correlation between nickel content in the deposit and corrosion potential of zinc-nickel electrodeposited coatings.....	133
Figure 6.12. Polarization curves of zinc-nickel electrodeposited coatings exhibit different corrosion behavior from the coatings of polished surface and as-deposited. ....	135
Figure 6.13. Change of corrosion current as a function of time for the zinc-nickel electrodeposited coatings of different surface morphology.....	135
Figure 6.14. Change of corrosion potential as a function of time for the zinc-nickel electrodeposited coatings of different surface morphology.....	137
Figure 6.15. X-ray diffractometry exhibits that after the corrosion test, the polished coating has weaker Fe substrate peaks compared to those of the as-deposited coating: (a) as-deposited coating and (b) polished coating. ....	138

Figure 6.16. Correlation between deposition current density and corrosion  
current of zinc-iron electrodeposited coatings.....140

Figure 6.17. Correlation between deposition current density and corrosion  
current of zinc-nickel electrodeposited coatings.....140

## LIST OF TABLES

Table 2.1. Use of zinc-coated steel for a typical model of U.S. car [Metals Handbook 1990].....	8
Table 2.2. Crystal structure, lattice parameter and the chemical formula of Zn-Fe and Zn-Ni intermetallic phases [Mackowiak and Short 1979].....	15
Table 2.3. Standard electrode potentials of systems important in plating technology [Parthasaradhy 1989].....	20

# ***CHAPTER ONE***

## **INTRODUCTION**

Over the last few decades, the automotive industry has paid much attention to automobile corrosion which has become a serious concern due to the increasing usage of snow melting salt in Canada, the United States and northern Europe [Inagaki et. al. 1991, Lindsay 1989, Kondo 1994]. In the late 1970's, a Canadian code was adopted to improve the corrosion resistance of automobiles. During the 1980's, the automotive industry started to set new standards for body panels with galvanized steel sheets. The painted sheet metal of a car body should have 5-years resistance to "cosmetic" deterioration and 10-years resistance to perforation. To meet the market demands from the automobile industry, the steel makers have developed several coating products. A number of galvanized coatings are applied to steel sheets for enhanced corrosion resistance. Although various types of zinc-based coatings significantly improved corrosion resistance when compared with bare steel sheets, they also created new problems in the manufacturing process, particularly when brittle intermetallic compounds were involved. For instance, the coatings could be damaged by galling, powdering, flaking and cracking during forming operations. Consequently, the study of coated steels is concentrated on corrosion performance and the formability of autobody panels. The electrogalvanized coatings are known to have a better coating uniformity, more consistent weldability and better formability than the hot-dip galvanizing products [Pak and Meshii 1990, Lin 1992]. Electrogalvanized zinc, zinc-iron and zinc-nickel coatings are the major products for the automobile body due to their excellent corrosion resistance and good mechanical properties [Chen and Snyder 1990, Lin 1992, Alfantazi, El-Sherik and Erb 1994].

It is well known that material properties are closely related to their microstructural characteristics. The microstructure of coatings have often been described by referring to the microscopic appearance of the as-deposited surface morphology since the metallographic preparation of thin coatings of zinc on steel substrate is difficult [Lindsay et. al. 1989, Lin 1992]. By controlling the deposition parameters, the microstructure of coatings can be significantly changed. Much research has been carried out in this field. For instance, the study of surface morphology by Lindsay et. al. indicates that the primary characteristics of electrodeposited zinc coatings is the predominance of hexagonal crystal platelets of about 5 to 10  $\mu\text{m}$  in diameter, whose basal plane faces are tilted with respect to the substrate surface. The microstructure of coatings evolves as a function of current density, pH, temperature of the bath, and coating thickness. High current density causes a high nucleation rate and subsequently, leads to fine grain size with weak crystallographic anisotropy. Change of the pH value of the electrolyte can affect the coating microstructure.

Texture of the coatings tends to be related to the surface morphology of coatings. Optimizing the texture and morphology can be a key factor for enhancing corrosion resistance of coatings as well as other properties. In general, the textures can be divided into three types based on the predominant crystallographic plane parallel to the plane of the zinc coating surface: (1) basal texture, in which the majority of the  $\{0001\}$  basal planes of the zinc crystals are parallel to the substrate surface, (2) pyramidal texture, in which basal planes are tilted at a certain angle to the substrate surface, thereby  $\{10\bar{1}X\}$  or  $\{11\bar{2}X\}$  planes are parallel to the surface, (3) prismatic texture, in which basal planes are perpendicular to the surface, so that the prismatic plane  $\{10\bar{1}0\}$  or  $\{11\bar{2}0\}$  are parallel to the surface [Pak 1991]. Fig. 1.1 illustrates examples of primary texture components in zinc coatings.

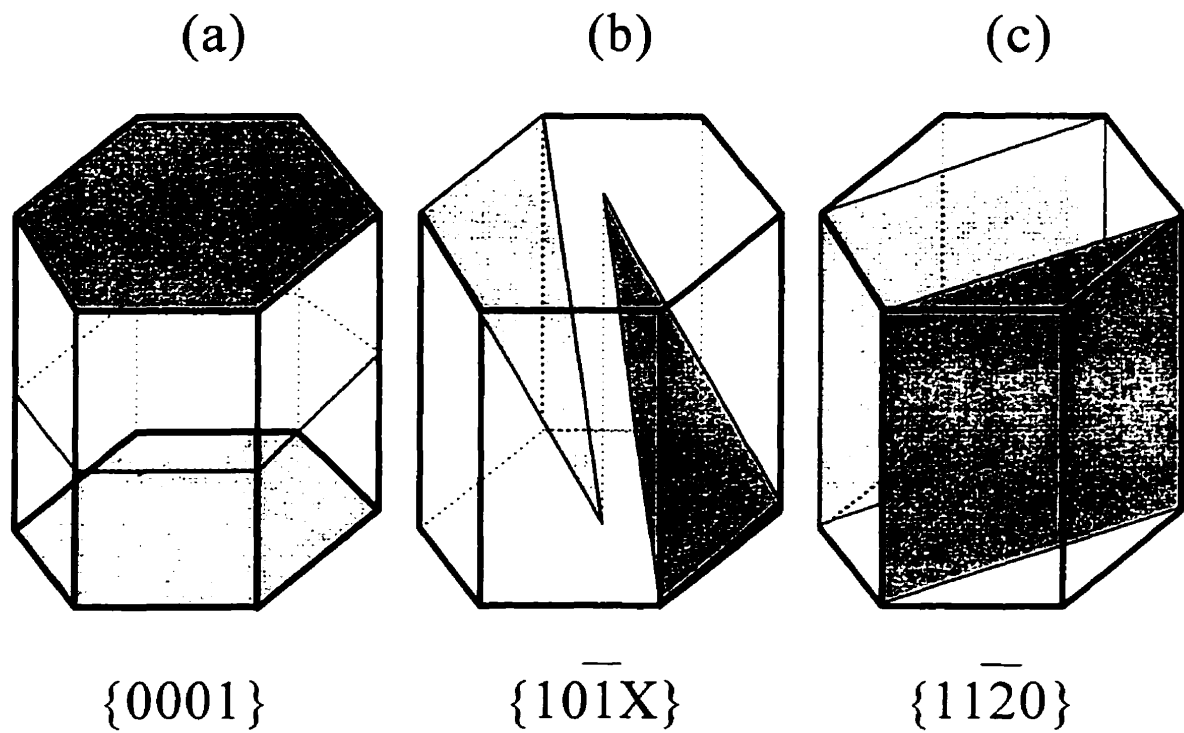


**Figure 1.1. Three primary texture components in zinc electrodeposited coatings: (a) basal texture, (b) pyramidal texture and (c) prismatic texture [Pak 1991].**

Preferred crystallographic orientations can be deliberately produced in electrodeposited coatings. A strong basal zinc  $\{0001\}$  texture is predominant at low pH values of sulfate baths, whereas the pyramidal  $\{10\bar{1}X\}$  texture becomes predominant at higher pH value. At a low current density and thin coating thickness, the texture of coatings tends to follow the crystallographic orientation of the substrate surface. The evidence of a strong influence of the substrate has been found in zinc electrodeposited coatings [Itoh et. al. 1974, Ohmori et. al. 1993].



The electrodeposited zinc-based alloy coatings have more advantages than conventional pure zinc coatings. Among them, the electrodeposited zinc-iron and zinc-nickel coatings are widely accepted for automobile body panel material. It has been known that two or more metals can be co-deposited on a steel substrate under proper conditions. Since alloy electrodeposition is more complicated than the deposition of pure metal, two conditions are critical for the alloy deposition : (1) at least one of the metals must be capable of being deposited independently, and (2) their deposition potentials must have similar values. The second condition is essential in order to avoid preferential deposition of a more noble metal which has a greater deposition driving force [Brenner 1963, Lowenheim 1978]. The electrodeposition of zinc-iron and zinc-nickel coatings provide various textural and morphological characteristics based on different alloy composition of the deposits. Alloy composition of the coatings is not only governed by the bath composition but also by the applied current density, because the current density is responsible for the anomalous codeposition behavior. Moreover, crystallographic structure and phase composition of the coatings are directly influenced by the anomalous codeposition behavior. It is necessary, therefore, to demonstrate how the texture and morphology of coatings evolve at various deposition conditions in conjunction with compositional change during the alloy codeposition.

The zinc and zinc alloy coatings protect steel substrates by either the sacrificial corrosion against galvanic attack or the mechanical blocking of the corrosion site by zinc oxide. Thus, it is necessary to retard the corrosion rate of coated steels by enhancing the corrosion resistance of the coatings themselves. The corrosion behavior of coatings is closely related to their microstructure. Recently, extensive research has been conducted to investigate the microstructure and corrosion behavior. However, not much systematic work has been done to correlate the microstructure, the deposition parameters and the corrosion behavior of coatings.

The overall objective of this research is to achieve a better understanding of the microstructure and the corrosion behavior of zinc-based electrodeposited coatings. Specifically, this program is designed to:

1. Demonstrate the correlation between the microstructure of coating - texture, morphology and chemical composition - and the deposition parameters - current density, pH, coating thickness.
2. Demonstrate the correlation between texture, morphology, alloy composition and corrosion resistance of coatings.
3. Determine the most desirable coating microstructure by optimizing the electrodeposition parameters for the best corrosion resistance.

## **CHAPTER TWO**

### **LITERATURE REVIEW**

#### **2.1. THE APPLICATION OF Zn-BASED GALVANIZED STEEL IN THE AUTOMOTIVE INDUSTRY**

Zinc-based galvanized steel has attracted considerable attention from the automobile industry for its excellent corrosion resistance. The applications of zinc-based galvanized steels range widely from structural steelworks for buildings and bridges, to various types of house appliances and industrial machine parts [Porter 1991]. The excellent corrosion performance of the galvanized sheets, either as pure zinc or zinc alloy, has created an enormous demand from the automobile industry which, in turn, has become one of the most dynamic markets for the coated steel sheets.

For decades, the production of zinc-based galvanized steels has dramatically increased. In the United States, more than 10 million tons of steel is produced annually by galvanized coating. A large amount of this total is used by the automotive industry for both unexposed and exposed panels - from frames and floor pans to doors, fenders and hoods (Fig. 2.1). Typically, 75% of the body, chassis, and power train components of an American automobile consist of galvanized precoated steel (Fig. 2.2). Table 2.1 indicates that a typical American car utilizes nearly 160 kg of zinc coated steel components. In Japan, the demand for the precoated sheet steels began increasing in the mid 70's and has shown a remarkable growth in the late 80's and 90's and a continuous increase is expected [Kondo 1994]. In the future, the automotive industry will remain the greatest demand market for the coated sheet steels. Moreover, increasing consumer demands for more durable vehicles has encouraged automakers to develop anticorrosion guarantees of 5 years against cosmetic rust and 10 years against

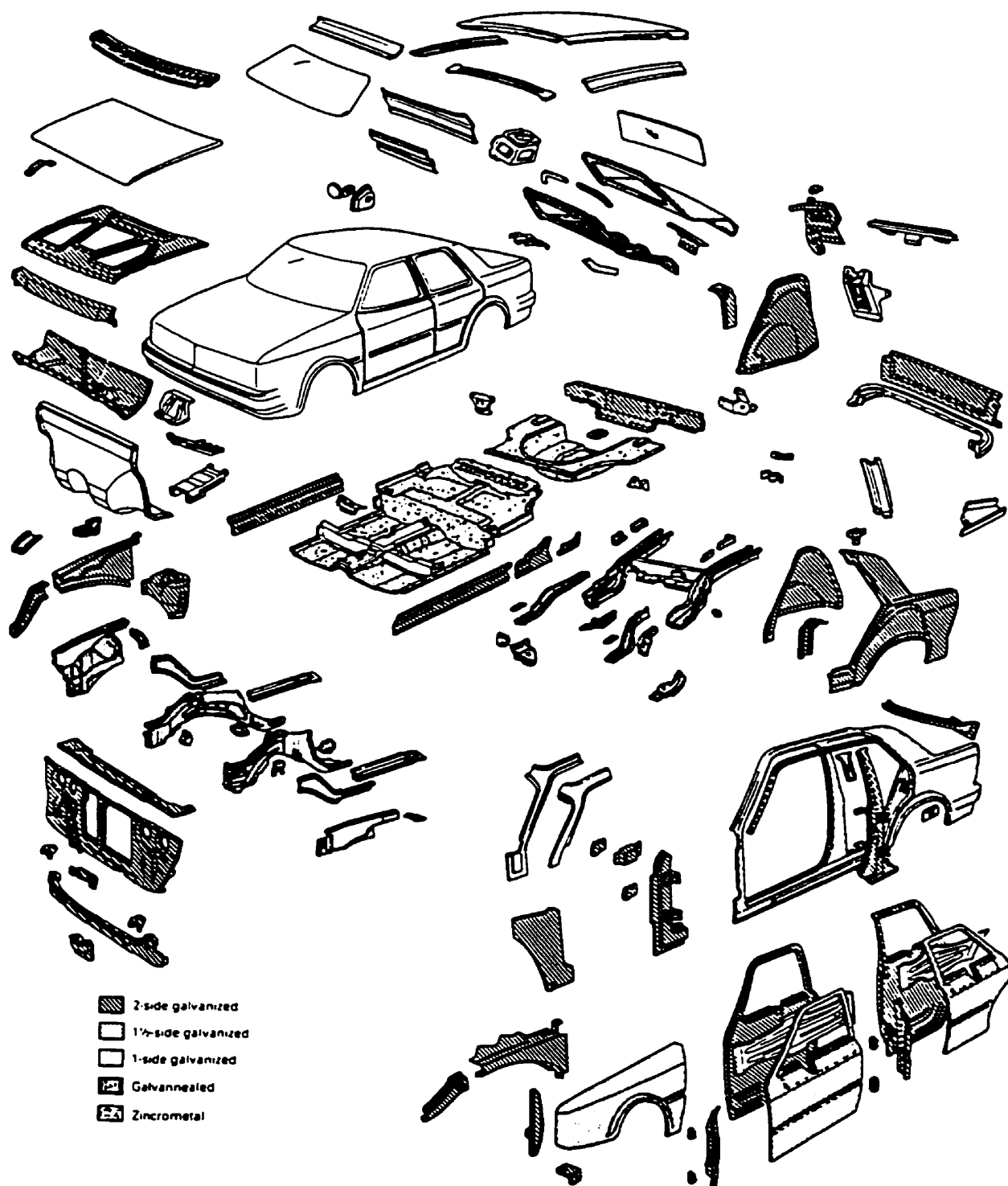
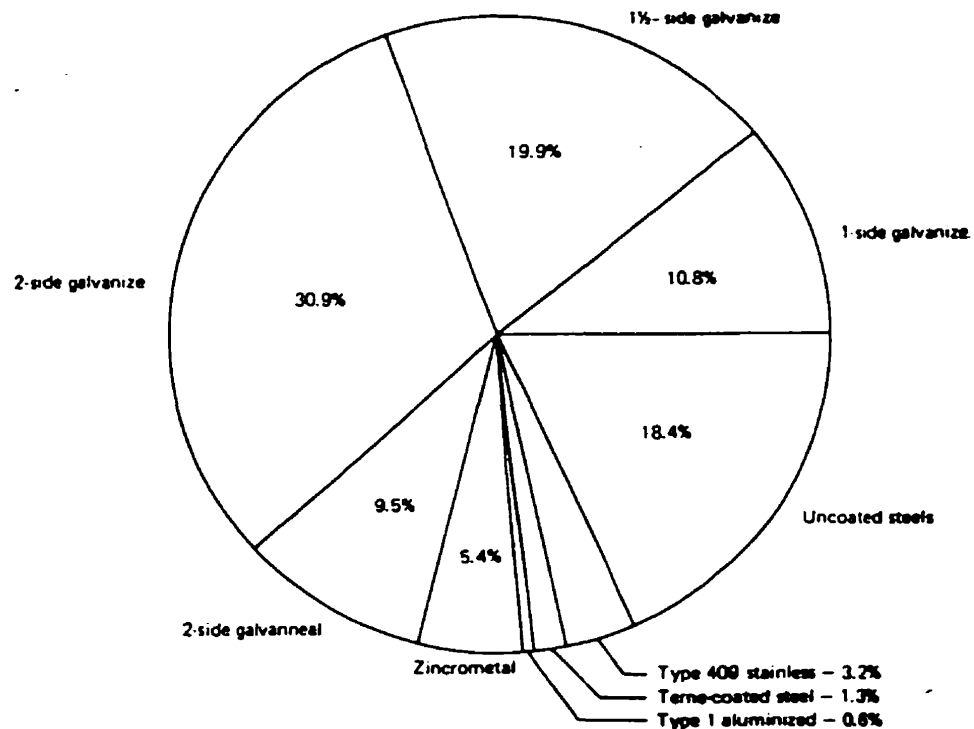


Figure 2.1. Use of zinc-coated steels in a car by one U.S. automaker [Metals Handbook 1990].

perforation. To fulfill these requirements, research should focus on the improvement of corrosion resistance either by optimizing the microstructure of existing coatings or by developing new alloy coatings.



**Figure 2.2. Typical usage of zinc-coated steel components for body, chassis, and power train applications in a car manufactured by a U.S. automaker [Metals Handbook 1990].**

Type	Amount of steel (kg)	Amount of zinc (kg)
One-side galvanized	33.5	0.55
Two-side galvanized	93	3.05
Zincrometal	29.5	0.19
Net total	156	3.8

**Table 2.1. Use of zinc-coated steel for a typical model of U.S. car [Metals Handbook 1990].**

## 2.2. GALVANIZING PROCESS FOR SHEET STEEL

Zinc-based galvanized steel sheet is mainly produced by two processes: (1) hot dip galvanizing, and (2) electrogalvanizing. Hot dip galvanizing is the process where the steel sheets, after proper surface pre-treatment, are dipped into a molten zinc bath. The most important factors of hot dip galvanizing, which closely control the coating properties, are the dipping time and the bath temperature. Electrogalvanizing is the process, in which pure zinc or zinc alloy is electrochemically deposited on the surface of steel sheets. In the electrogalvanizing process, the coating properties are controlled mainly by the current density, plating time, pH, temperature and chemical composition of the electrolyte. In general, there are significant differences in coating properties between the electrodeposited coatings and the hot-dip galvanized coatings. The electrodeposited zinc-based coatings are considered to have better coating uniformity, more consistent weldability and better formability than hot-dip galvanized coatings [Lin 1992]. This review focuses on some details of the electrogalvanizing process because this research work has been mainly carried out with electrodeposited zinc and zinc alloy coatings.

The electrogalvanizing process does not include any annealing process, whereas the hot dip galvanizing process has optional annealing steps for producing intermetallic coating layers by a diffusion reaction between the coating and the steel substrate. For alloy codeposition, electrodeposition is performed in the plating bath which contains the alloying elements. A schematic diagram of a typical continuous strip electrogalvanizing line is given in Fig. 2.3. A pre-treatment is important for the best adhesion of plated layer to the substrate. In the continuous processing lines, the steel sheets are cleaned in a hot alkaline solution to remove oil and grease from the surface of the sheets and subsequently, pickled lightly in an acid (usually hydrochloric or sulfuric acid) to remove oxides. After pre-treatment, the steel sheets pass through electrolytic cells in which the current flows from the anode to the cathode (steel sheet) through the electrolyte.

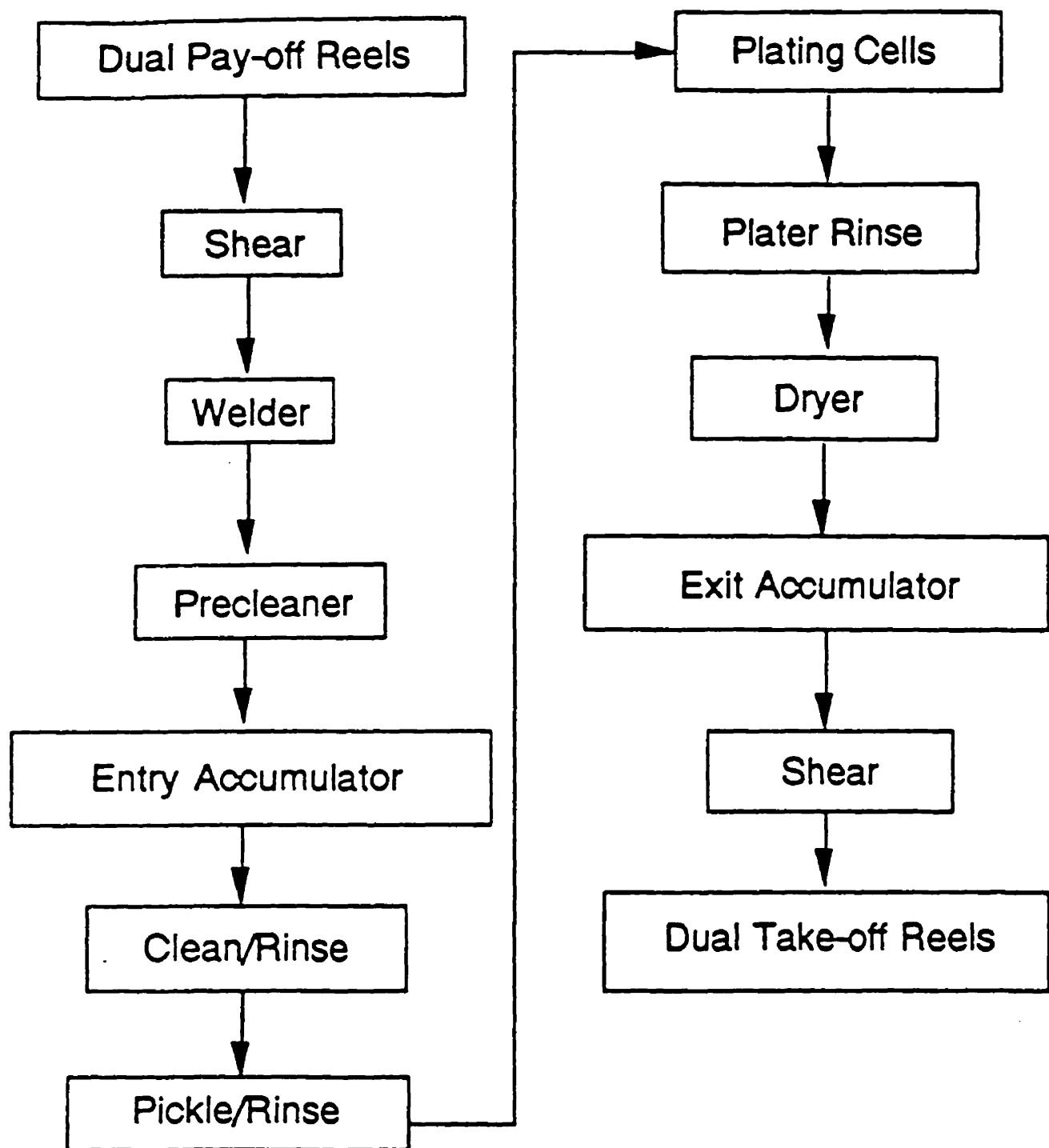


Figure 2.3. A schematic diagram of an electrogalvanizing line [Bush 1989].

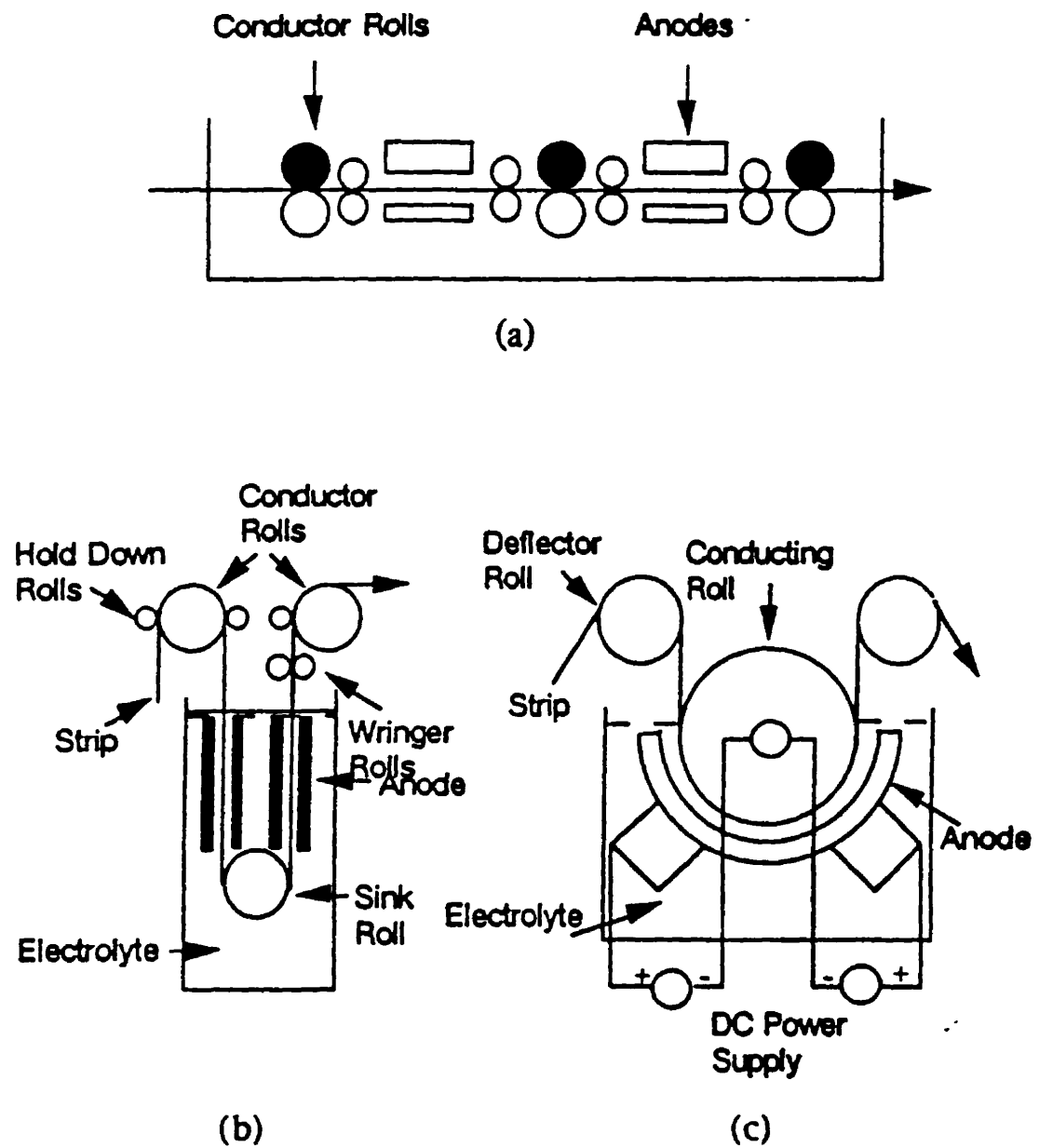


Figure 2.4. Three types of plating cells for the electrogalvanizing process: (a) the horizontal cell, (b) the vertical cell and (c) the radial cell [Bush 1989].



The electrolytic cells are either horizontal, vertical or radial according to the relative orientation of the cathodes and the anodes (Fig. 2.4) [Bush 1989]. The anodes can be either soluble zinc or platinized titanium. Zinc plating baths are of three main types: alkaline cyanide, alkaline noncyanide and acid [Lowenheim 1978]. Each of these can be further subdivided: the cyanide into conventional and low cyanide, and the acid into sulfate and chloride. The conventional cyanide bath has been preferred for general zinc plating since it has good throwing power, and a wide operation range. However, the high content of cyanide in effluents could not meet the stringent environmental standards. Therefore, acid zinc plating has been developed to overcome the problems of a cyanide bath. The most widely used acid bath is based on zinc sulfate. The acid bath has become widely adopted because of its high plating speed and low operating costs. The relatively poor throwing power, and less bright deposit surface are not considered serious drawbacks.

### 2.3. MICROSTRUCTURE OF Zn-BASED ELECTRODEPOSITED COATINGS

It is well known that the microstructure of zinc-based electrodeposited coatings is significantly influenced by the deposition parameters as well as by the substrate microstructure [Jiricny et. al. 1987, Lindsay et. al. 1989, Lin 1992, Ohmori et. al. 1993, Kondo 1994, Li 1997]. The main parameters that affect the microstructure of coatings are current density, pH, and temperature of the bath [Lawless 1967, Wright 1975]. For example, the applied current density can significantly influence the morphology of deposits. Ohtsubo et. al. [1994] studied the morphological evolution of zinc electrodeposit with current density change. They found that the surface morphology evolves from the layered thin hexagonal platelets, the blocky crystals comprising the stacked thin platelets to the hexagonal faced columnar crystals with increasing the applied current density. Yim et. al. [1995] reported that with increasing current density, the surface morphology changed from flat facets of crystal platelets toward an inclined aggregation of the platelets with their facets edge on.

Although the correlation between deposition parameters, surface morphology and texture of zinc coatings is not well understood at the present time, studies have been carried out to characterize the morphology of zinc coatings [Marder 1990, Lindsay et. al. 1989, Shaffer et. al. 1990]. The surface morphology of electrodeposited zinc coatings is usually characterized by sets of parallel hexagonal ridges which represent the edge of zinc basal planes tilted with respect to the substrate surface. Most of the ridges are aligned towards the rolling direction of the steel substrate in the case of the coating deposited at low applied current density. This was attributed to the strong influence of substrate microstructure. Lindsay et. al. [1989] reported that the primary characteristic of zinc coatings is the predominance of hexagonal crystal platelets of about 5 to 10  $\mu\text{m}$  in size. The hexagonal platelets, which represent the faces of zinc basal plane, are tilted with respect to the substrate surface. Lindsay et. al. also proposed that surface morphology of the zinc coating is a major factor of coating performance and is determined by deposit grain size and crystallographic orientation. Another observation made by Lin indicates the morphological change of zinc coatings with different coating thickness. Lin described the change of surface morphology as a transformation from a thin, plate-like feature to a bulky hexagonal feature with increasing coating thickness.

Rangarajan et. al. [1990] suggested a relationship between the coating morphology and texture. In their work, the electrodeposited zinc coatings which have parallel ridges, exhibit a dominant  $\text{Zn } \{10\bar{1}3\}$  peak, whereas the hot dip zinc coatings consisting of polygonal plates with no ridges exhibit a strong intensity of  $\text{Zn } \{0001\}$  peaks from an X-ray diffraction pattern. None of the above works clearly demonstrated how the morphology and texture of a coating evolves at specific deposition condition. Besides, the description of preferred orientation by comparing the X-ray peak intensity can not fully justify the nature of coating texture.

Zinc alloy coatings have been widely used by the automotive industry because of some advantages which zinc coatings cannot provide. Chen et. al.

[1990] reported that by alloying zinc with another elements, a thinner, less anodic coating is formed which can provide similar corrosion resistance to pure zinc coatings. The other advantages of zinc alloy coatings are improved formability and weldability: since the zinc coating, being relatively soft, tends to gall in the dies during the forming operations. It also causes difficulties in welding due to its low melting point and tendency to alloy with the welding tips. It has been reported that zinc-iron and zinc-nickel alloy coatings not only provide excellent corrosion resistance but also exhibit improved mechanical properties compared to zinc coatings.

The microstructure of zinc alloy coatings is closely related to the alloy content and phase composition of the deposit. The phase composition of electrodeposited zinc alloy coatings is found to be different from that of thermally prepared zinc alloy coatings [Lin 1992]. This is attributed to the formation of a metastable or non-equilibrium phase upon electrodeposition. Fig. 2.5 illustrates the equilibrium phase diagrams of zinc-iron and zinc-nickel binary systems. The phases found in the current diagram are outlined in Table 2.2 [Mackowiak and Short 1979, Villars and Calvert 1986, Villars and Calvert 1991]. The differences in phase compositions between the equilibrium and the electrodeposited non-equilibrium states are shown in Fig. 2.6 [Kubaschewski 1991, Adaniya et. al. 1985]. The phase composition of zinc alloy electrodeposited coatings has been reported by other workers. Shima et. al. [1986] found that the zinc-iron electrodeposits containing iron in the range of 0.9 ~ 17 % had an hcp structure of the iron oversaturated  $\eta$  phase, and the deposits had a bcc structure of  $\Gamma$  phase in the range of 18.5 ~ 40 % iron. The deposits containing more than 50 % iron had a bcc structure corresponding to the zinc oversaturated  $\alpha$  phase. The metastable  $\eta$  phase is also found in zinc electrodeposited coatings after a relatively short annealing treatment [Gu et. al. 1989]. Gu et. al. reported the formation of the iron oversaturated  $\eta$  phase by annealing the specimen at 200 °C for 10 minutes. This metastable  $\eta$  phase was then transformed to the stable phase as a higher annealing temperature was applied. This phase transformation was attributed to the effect of

applied high temperature which enables the state to overcome the free energy hump between the metastable and the stable condition.

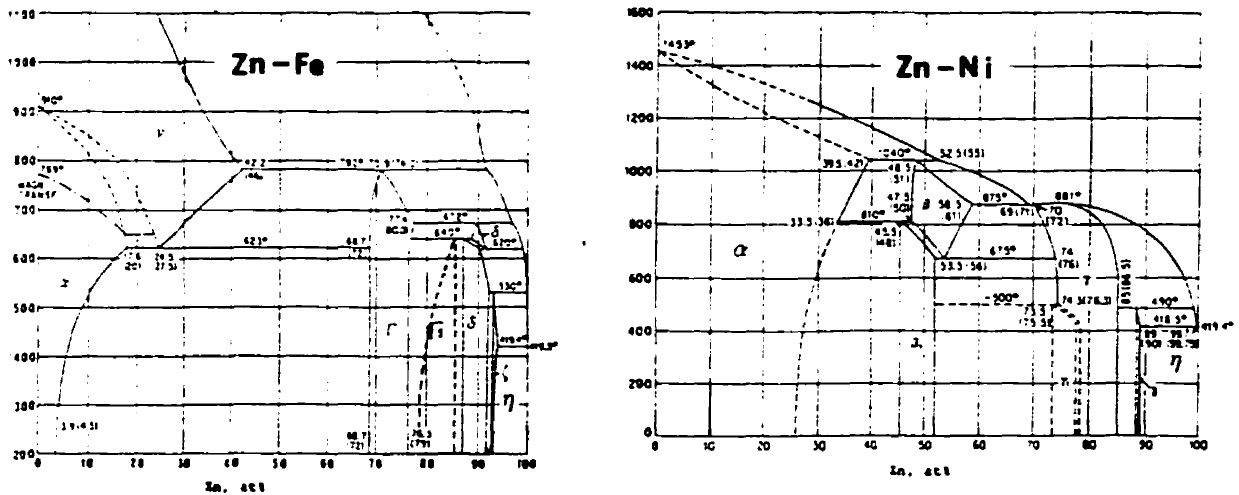


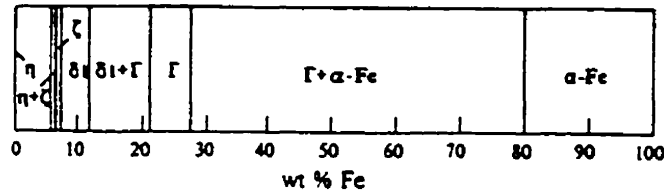
**Figure 2.5. Equilibrium phase diagrams of zinc-iron and zinc-nickel binary systems [Kubaschewski 1991].**

Phases (Zn-Fe)	Chemical formula	Crystal structure	Lattice parameter (Å)
η	Zn	hcp	a=2.67, c=4.95
ξ	Zn <sub>13</sub> Fe	monoclinic	a=13.4, b=7.5, c=5.1, β=128°
δ <sub>1</sub>	Zn <sub>10</sub> Fe	hcp	a=12.8, c=57.6
Γ <sub>1</sub>	Zn <sub>21</sub> Fe <sub>5</sub>	fcc	a=17.96
Γ	Zn <sub>10</sub> Fe <sub>3</sub>	bcc	a=8.97
α-Fe	Fe	bcc	a=2.87

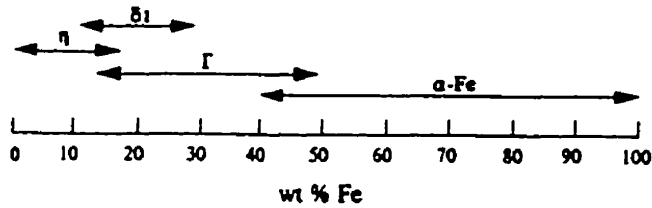
  

Phases (Zn-Ni)			
δ	Zn <sub>22</sub> Ni <sub>3</sub>	tetragonal	a=8.922, c=9.254
γ	Zn <sub>21</sub> Ni <sub>5</sub>	bcc	a=8.920
α-Ni	Ni	fcc	a=3.52

**Table 2.2. Crystal structure, lattice parameter and the chemical formula of Zn-Fe and Zn-Ni intermetallic phases [Mackowiak and Short 1979].**



(a)



(b)

**Figure 2.6. Differences in phase compositions between (a) the equilibrium [Kubaschewski 1991] and (b) electrodeposited non-equilibrium states in the zinc-iron system [Adaniya et al. 1985].**

Kondo et. al. [1988] used an electron diffraction technique to determine the phase structure of the zinc-iron coatings from a sulfate bath. The phases were identified as  $\eta$  phase (0 ~ 14 % Fe),  $\Gamma$  phase (11 ~ 48 %),  $\Gamma_1$  phase (19 ~ 34 %) and  $\alpha$  phase (34 ~ 100 %). The surface morphology of zinc alloy coatings was also found to be correlated with the alloying element in the deposits. Changes in morphology was reported by Kondo et. al. based on both the structure of the crystals and the zinc-iron ratio in the electrodeposits. It was observed that the hexagonal thin platelets of the  $\eta$  phase formed in the iron content range below 14 %. In the  $\eta$  /  $\Gamma$  two phase regions, the hexagonal platelets increase in thickness and become pyramidal in shape from SEM observations. The fine  $\Gamma$  particles observed by TEM are dispersed between these coarse  $\eta$  particles. A further increase in iron content reduces the coarse  $\eta$  particle formation and produces more  $\Gamma$  phase.

## 2.4. FUNDAMENTAL ASPECTS OF ELECTRODEPOSITION

The electrodeposition technology has been developed to produce metallic coatings on substrates for the improvement of (1) appearance of the substrate surface, (2) protection of the substrate, (3) special surface properties and (4) engineering or mechanical properties [Lowenheim 1978, Gawne and Gudyanga 1984]. Electrodeposition is an ideal means of providing a thin coating surface which has superior properties to the substrate. It is, therefore, possible to achieve good resistance against corrosion and wear by applying suitable electrodeposited coatings on the less expensive substrate metals [Li 1997]. The common copper/nickel/chromium deposit, for instance, applied to automotive hardware and numerous other items not only imparts a pleasing appearance but also protects the substrate from corrosion. However, when it comes to corrosion prevention as a principal aim of the coating, zinc and zinc alloy coatings are the most economical and most effective for the steel substrate. The electrodeposition technology has also been developed to improve the wear resistance for engineering applications. Chromium coating, for example, is deposited on gun barrels, rolls for paper-mill machinery as well as Diesel engine cylinders, and other parts which require high hardness and resistance to wear [Wranglen 1985, Lowenheim 1978].

Electrodeposition is the process where a mass transfer is accompanied by a charge transfer [Bockris and Razumney 1967, Raub et. al. 1967, Crow 1974, Parthasaradhy 1989, Winand 1990, Walsh et. al. 1991]. Mass transfer is the movement of metal atoms which are ionized and hydrated at the anode, and move to the cathode under the imposed external electrical field. The electrical field is applied to the electrodes to provide a driving force for the mass transfer. Convection can be another factor for the mass transfer since it also governs the migration of ions through the electrolyte. As the electrodeposition proceeds, the metal ions can be depleted near the cathode. As a consequence, the density of the solution at the face of the cathodes becomes lower than the density of the bulk

solution. To avoid this inhomogeneity of the density of the solution, convection of the electrolyte is required either by natural or artificial method. For instance, heating or cooling coils are used to create temperature gradients for aid in convective mass transport. In continuous plating, the cathode is moved through the solution at a relatively high speed to enhance the convection effect.

Once metal ions reach the vicinity of the cathode surface, the effect of convection becomes negligible, and diffusion becomes an important factor for ionic migration. Since diffusion is the movement of substances as a result of a concentration gradient, the depletion of metal ions near the cathode causes a movement of ions from the bulk of the solution toward the cathode. The metal ion approaches the surface of the cathode, is then discharged and becomes a so called ad-atom. Consequently, this ad-atom diffuses through the surface and is incorporated into the site where the local free energy due to the accommodation of an ad-atom can be minimized. Fig. 2.7 illustrates the cathodic metal deposition.

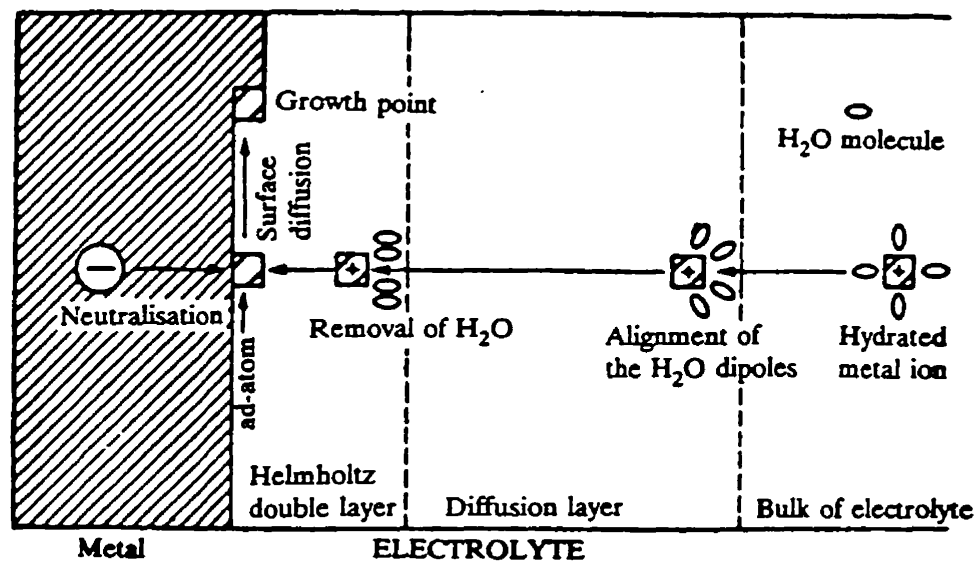


Figure 2.7. Schematic representation of the mechanism of cathodic metal deposition [Li 1995].

The driving force for electrodeposition is the overpotential which represents a difference between the cathode potential and its equilibrium potential. The equilibrium potential is defined as the potential at which the net deposition current equals zero. When a metal is dipped into a solution of its own ions, two reactions occur. There is a tendency for the metal to dissolve in the solution, leaving an electron behind on the surface of the anode. Thus, the reaction  $M \rightarrow M^{z+} + ze$  takes place at a definite rate. At the same time, there is a tendency for the metal ions in the solution to deposit as atoms on the metal surface; i.e.  $M^{z+} + ze \rightarrow M$  takes place at a specific rate. Initially, one of these reactions may occur faster than the other, but this in turn, increases the rate of the reverse reaction. Eventually, an equilibrium will be established when metal atoms are dissolved in a solution at the same rate as ions in the solution are deposited to the metal surface. This process is completed long before any detectable concentration changes take place. The established equilibrium results in a potential at the specimen's solution interface. This potential is called the equilibrium potential. The equilibrium potential for the simple cathodic reaction can be calculated by using the Nernst equation:

$$E_{eq} = E_o + (RT/zF) \ln C$$

where  $E_o$  is a constant for the metal and is called the standard potential,  $R$  is the gas constant,  $T$  is the absolute temperature of the solution,  $z$  is the charge of the ion.  $F$  is Faraday's constant and  $C$  is the concentration of the ions in gram ion per liter. At room temperature,  $RT/F = 0.059$ . Hence, the equation at 25 °C is given by :

$$E = E_o + (0.059 / z) \ln C$$

Table 2.3 exhibits the standard potentials of metals. For electrodeposition, the applied cathode potential should be more negative than the equilibrium potential. This extra potential required to deposit metal is called overpotential. The total



System	Potential (V)	System	Potential (V)
$\text{Au}^+/\text{Au}$	+1.7	$\text{Fe}^{3+}/\text{Fe}$	-0.036
$\text{Au}^{3+}/\text{Au}$	+1.42	$\text{Pb}^{2+}/\text{Pb}$	-0.126
$2\text{H}/\text{O}_2$	+1.23	$\text{Sn}^{2+}/\text{Sn}$	-0.140
$\text{Pt}^{2+}/\text{Pt}$	+1.2	$\text{Ni}^{2+}/\text{Ni}$	-0.23
$\text{Pd}^{2+}/\text{Pd}$	+0.83	$\text{In}^+/\text{In}$	-0.25
$\text{Pb}^{4+}/\text{Pb}$	+0.80	$\text{Co}^{2+}/\text{Co}$	-0.27
$\text{Ag}^+/\text{Ag}$	+0.799	$\text{In}^{3+}/\text{In}$	-0.34
$\text{Rh}^{3+}/\text{Rh}$	+0.6	$\text{Cd}^{2+}/\text{Cd}$	-0.402
$\text{Cu}^+/\text{Cu}$	+0.52	$\text{Fe}^{2+}/\text{Fe}$	-0.44
$\text{Cu}^{2+}/\text{Cu}$	+0.34	$\text{Cr}^{3+}/\text{Cr}$	-0.71
$\text{Sn}^{4+}/\text{Sn}$	+0.005	$\text{Zn}^{2+}/\text{Zn}$	-0.763
$2\text{H}^+/\text{H}_2$	0.00	$\text{Al}^{3+}/\text{Al}$	-1.66
		$\text{Ti}^{2+}/\text{Ti}$	-1.75

**Table 2.3. Standard electrode potentials of systems important in plating technology [Parthasaradhy 1989].**

overpotential observed at an electrode is made up of three factors: concentration overpotential, ohmic overpotential and activation overpotential. Concentration overpotential is caused by a shift in potential due to concentration changes of metal ions arising from a slow diffusion rate at the interface of electrolyte and the cathode surface. Concentration polarization may take place at a cathode in another form if the deposition of metal is accompanied by hydrogen evolution. The discharge of hydrogen ion results in a decrease of their concentration in the vicinity of the cathode which in turn, leads to an increase in the concentration of hydroxyl ion. Subsequently, the metal hydroxide or its basic salts may be precipitated, thereby reducing the metal ion concentration in the cathode surroundings. Ohmic potential is caused by the resistance increasing effects of oxide layers, gases, greases or poorly conducting liquid layers which result in a potential change.

Activation overpotential is caused by the difference in rate of reaction during deposition step. Since the slowest step governs the overall reaction rate, the slowness of the step is equivalent to a resistance offered to the progress of the plating process. This is reflected in the observed overpotential. The contribution of this factor related to the electrode reaction is called activation overpotential. It depends on the nature of the cathodic current density, temperature and concentration of the electrolyte.

During the electrodeposition process, the growth rate of a coating is mainly controlled by the current density. The amount of deposit produced by electrodeposition can be described by Faraday's law:

$$W = (It / 96500) \times (A / z)$$

where  $W$  is the quantity of metal deposited,  $I$  is the current passed in amperes,  $t$  is the time of deposition in seconds,  $A$  is the atomic weight and  $z$  is the valency of the metal. The higher the current density, the more metal can be deposited. Among the various parameters which influence the deposition process, the current density is the main controlling factor for the electrodeposition. As the current density increases, the discharging rate of a metal ion increases up to the level where the diffusion rate of the metal ion to the cathode surface reaches its maximum. When the current density is increased further, hydrogen ions are discharged together with the metal ions, thereby resulting in a rise of the cathode potential. Therefore, the current efficiency for metal deposition is less than 100 % since a portion of the current is consumed for hydrogen evolution. The critical current density value at which the current efficiency for metal deposition remains 100 % is called the limiting current density. Fig. 2.8 represents the limiting current density [Parthasaradhy 1989]. Since hydrogen discharge along with metal deposition is not desirable, the limiting current density should be kept as high as possible. The limiting current density can be increased by (1) increasing the

solution concentration, (2) agitating or stirring the solution and (3) raising the bath temperature.

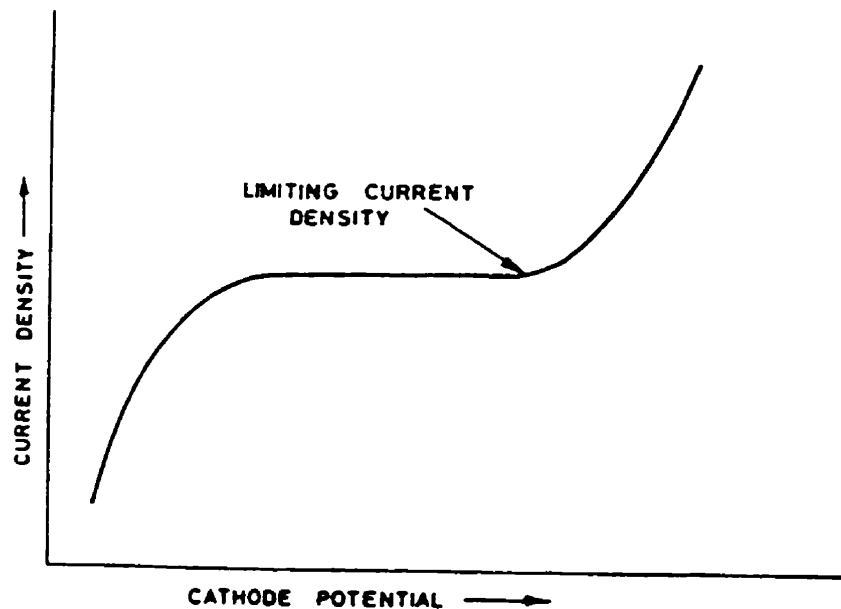


Figure 2.8. Current density-cathode potential relationship [Parthasaradhy 1989].

The pH of the electrolyte is another important parameter in order to operate the bath with optimum efficiency and to maintain the desirable properties of deposits. Carrying out the electrodeposition outside the recommended pH range often results in pitted, cracked or porous deposit structures. Moreover, too low a pH may lead to excessive hydrogen codeposition and consequently, not only decrease metal deposition efficiency but also alter the structure of deposits. The accumulation of hydroxyl ions in the vicinity of the cathode due to the deficiency of hydrogen ions and consequent precipitation of basic salts can lead to detrimental effects on the deposit properties. The hydrogen codeposition during the metal deposition can take place when the hydrogen discharge potential is attained. The deposition potential  $E_H$  for hydrogen evolution at atmospheric pressure and normal temperature is given by the equation:

$$E_H = -0.059 \text{ pH} - \eta_H$$

where the  $\text{pH}$  represents the pH value of the electrolyte and  $\eta_H$  is the hydrogen overpotential. The value of hydrogen overpotential varies with the type of metal used for the cathode. The hydrogen overpotential gives a significant advantage to the practical plating process because the hydrogen overpotential decreases the hydrogen deposition potential, thereby the metal ions are deposited prior to the hydrogen ions. If the current density is increased, the hydrogen overpotential is increased, thus the hydrogen discharge is further retarded and the deposition efficiency can be improved. Once the cathode potential reaches the value of the discharge potential for hydrogen evolution, hydrogen ions will be discharged during electrodeposition. Hydrogen evolution can affect electrodeposition processes and influence the properties of the deposit. While the majority of the discharged hydrogen ions evolve as hydrogen gas on the cathode surface, some hydrogen atoms may codeposit with the metal during cathodic metal deposition. This hydrogen codeposition is also responsible for the hydrogen embrittlement of electrodeposits [Li 1997]. Once the hydrogen evolution occurs, the efficiency of metal deposition decreases because part of the applied current is consumed for hydrogen evolution. The hydrogen evolution is closely related to the cathode potential and the hydrogen discharge potential ( $E_H$ ) which is a function of pH, temperature and hydrogen overpotential.

## 2.5. ALLOY CODEPOSITION BEHAVIORS: ANOMALOUS CODEPOSITION

In the case of alloy codeposition, the alloy content in the deposit changes upon various deposition parameters. Usually, a more noble metal deposits preferably to a less noble metal. As a result, the alloy proportion of the more noble metal is higher in the deposit than in the bath. Under certain deposition conditions, the less noble metal deposits preferably to the more noble metal [Brenner 1963]. The most important characteristic of anomalous codeposition behavior is an

unusual variation of alloy composition with the change of the applied current density. Zinc-iron electrodeposited coatings, for instance, exhibit a continuous increase in zinc content (less noble metal) as the applied current density increases (Fig. 2.9a). However, this aspect of codeposition is confined to a relatively low current density range. Fig. 2.9b exhibits that the zinc content decreases with increasing the applied current density at high current density range. Brenner explained how the current density influences the alloy deposition behavior. There are two view points closely related to the current density: (1) the cathode potential, and (2) the diffusion control. An increase of current density causes the cathode potential of the substrate to become more negative (less noble) and hence, promotes the deposition of the less noble metal on to the substrate.

The deposition rate of metal has an upper limit which is determined by the diffusion rate of metal ions through the diffusion layer near the cathode surface. At a given current density, the deposition rate of a more noble metal is much closer to its limiting value than that of a less noble metal. Additional increases of current density therefore, promote an increase in the deposition rate of the less noble metal. Nevertheless, the deposition rate of less noble metals is decreased again when the current density range is sufficiently high as is shown in Fig. 2.9b. Fig. 2.9b clearly illustrates that the percentage of zinc in the deposits continuously decreases as the current density increases. Since the zinc alloy electrodeposits are commercially produced at high current density range for high productivity, the understanding of anomalous codeposition at high current density range is important. This anomalous codeposition behavior was attributed by Brenner [1963] that the electrolyte near the cathode surface is depleted of zinc ions at high current density because the transfer of metal ion is under diffusion control.

Experimental results have been found regarding the anomalous codeposition of zinc-iron coatings [Irie et. al. 1990, Johnson et. al. 1984, Lin 1992]. Irie et. al. observed that the iron content increases rapidly with increasing current density during zinc-iron codeposition. Lin found that the iron content continuously

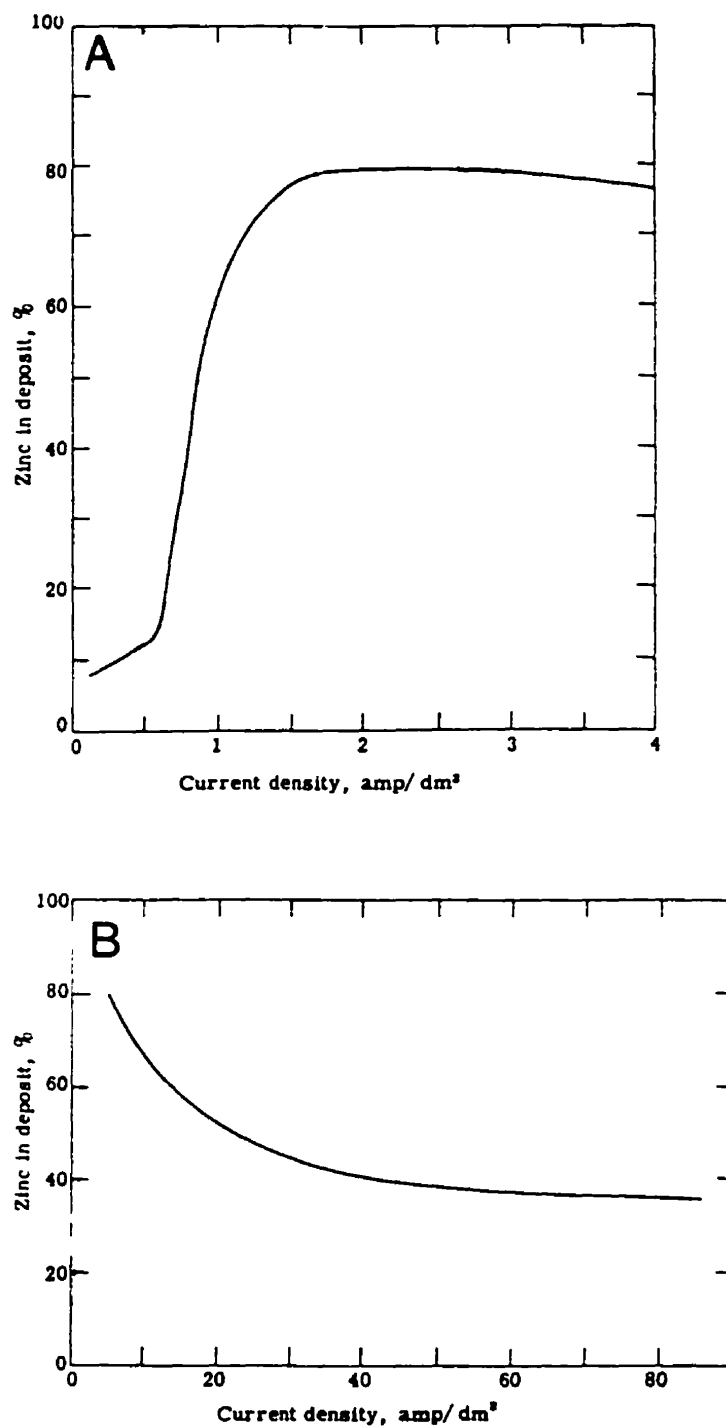


**Figure 2.9. Effect of current density on the zinc content of zinc-iron electrodeposited alloys: (a) low current density and (b) high current density range [Brenner 1963].**

increases from about 3 to 14 %, while the current density increases from 450 to 1080 mA/cm<sup>2</sup>. Lin also reported that the surface roughness of coatings decreases when the iron content is increased. The author attributed this to the different grain size of each coatings induced by different chemical composition. On the other hand, Johnson et. al. found that such an anomalous codeposition could be avoided by increasing the concentration of chloride ion in the bath. Geduld [1988] suggested the anomalous codeposition behavior is due to the influence of zinc hydroxide film during the codeposition process. According to Geduld, the zinc hydroxide film suppresses the deposition of iron and subsequently, the formation of this film causes a decrease of iron content in the deposit. Raising the current density, Geduld claimed, promotes the dissolution of the zinc hydroxide film and thus, increases the iron content in the deposit.

## 2.6. NUCLEATION PROCESS

As metal ions arrive on the cathode surface, the discharged ions eventually migrate into the most favorable sites of the metal lattice. The sites may be the steps or kinks where the free energy increase due to the accommodation of the metal atoms can be minimized. Fig. 2.10 represents the sequence of the incorporation of growth units at a kink and step site. These steps or kinks may result from two dimensional nucleation, screw dislocations or some other defects on the surface. The idea of two dimensional nucleation is suggested by Kossel and Stranski and has been largely accepted. Their model assumes that the crystal growth occurs in repeated monatomic layers after two dimensional nucleation [Bockris and Khan 1993, Winand 1990]. The model is based on the hypothesis that the probability of incorporation of an atom at the surface of a crystal is greater at the sites which have higher surface energy. Many experimental facts show the importance of this growth process in the electrodeposition of metals [Winand 1990]. Fig. 2.11 schematically illustrates a single cubic lattice showing different possible sites of incorporation of an atom in the lattice. It is evident that the most favorable incorporate site is the kink site A, which is at the same time

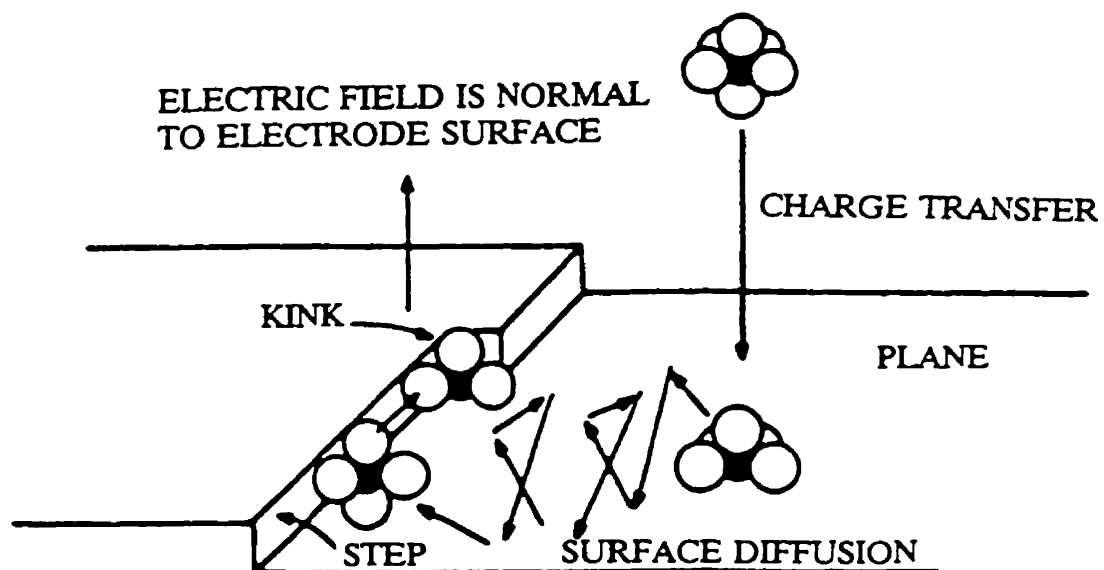


Figure 2.10. Steps and kinks are preferred sites for ad-atoms to get incorporated into the metal lattice [Li 1995].

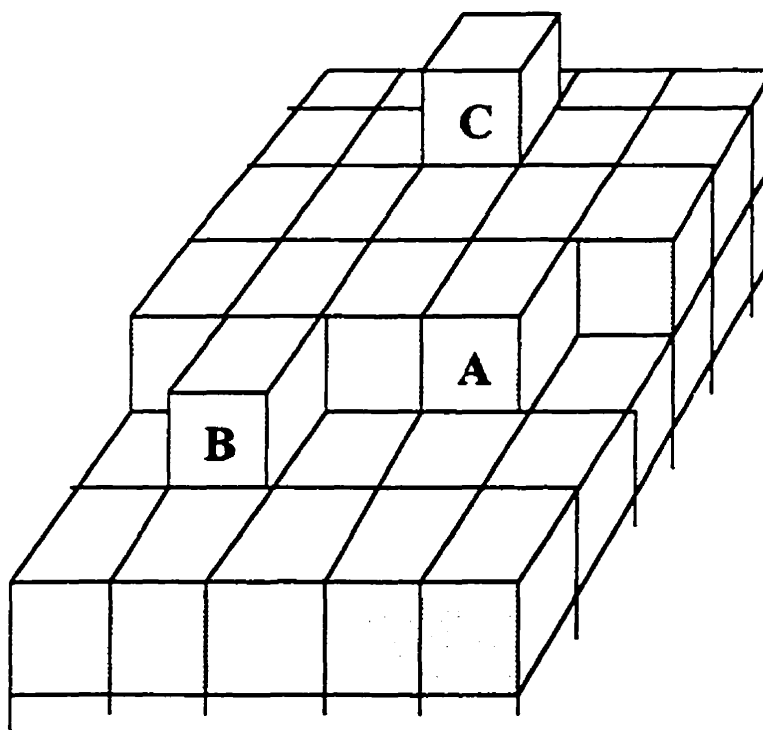


Figure 2.11. Schematic drawing of a single cubic lattice showing different possible sites of incorporation of an atom in the lattice [Winand 1990].



a repeatable step. Once the row is completed, the next possible site is B, creating a new one dimensional nucleus along the developing plane. The next favorable site is C where a new two dimensional nucleus starts to form. Therefore, the deposits grow through the competition between vertical growth, depending on two dimensional nucleation rate, and horizontal growth, depending on the rate of the repeatable step.

## 2.7. EVOLUTION OF TEXTURE DURING ELECTRODEPOSITION

The nature of orientation in electrodeposited metal is of considerable technical importance [Barrett and Massalski 1980]. The subject is complex, because growth of deposits is affected by various deposition conditions, e.g., the current density, temperature, hydrogen ion concentration in the bath and the orientation of substrate metal, etc. Research has been carried out to observe the texture evolution during the electrodeposition process [Lindsay et. al. 1989, Venkataraman et. al. 1989, Shaffer et. al. 1990, Pak 1991, and Lin 1992]. From the early study in 1924, Glocker and Kaupp first reported the existence of fiber textures in the electrodeposited metals. In hcp metals such as zinc deposits; they have  $\{11\bar{2}0\} + \{11\bar{2}2\}$ ,  $\{0001\}$ ,  $\{11\bar{2}4\}$ ,  $\{10\bar{1}1\}$ ,  $\{11\bar{2}2\}$  and  $\{11\bar{2}0\}$  fiber textures [Barrett and Massalski 1980]. The  $\{0001\}$ ,  $\{10\bar{1}0\}$  and  $\{10\bar{1}X\}$  textures are observed as major components. The domination of one component over another depends on the deposition parameters [Lindsay 1989, Venkataraman 1989, Shaffer 1990, Pak 1991, and Lin 1992]. For example, a strong  $\{10\bar{1}0\}$  texture was observed in zinc coatings which were electrodeposited in an alkaline cyanide bath [Teremura et. al. 1986], while the  $\{0001\}$  texture was found when an acid bath under low pH was used [Lindsay et. al. 1989]. Tomov [1994] found that the  $\{0001\}$  texture of zinc coating significantly decreases with an increase of coating thickness while the  $\{11\bar{2}0\}$  texture increases.

Typically, the electrodeposits of the fcc metals have  $\{110\}$  texture and the bcc metals have  $\{111\}$  texture. The change of texture was observed as well at various deposition conditions. For instance, it was reported that the texture of nickel deposit changes from  $\{110\}$ , through  $\{100\}$ , to  $\{210\}$  as the current density increases [Ye and Lee 1981, Amblard et. al. 1979]. The texture of copper electrodeposits varied with bath temperature [Handreg et. al. 1993]. Barrett and Massalski listed various texture components produced from different processing conditions. Silver deposit has  $\{111\}$ ,  $\{110\}$ ,  $\{211\}$  and  $\{111\}+\{100\}$  fiber textures; gold deposit has  $\{110\}$ ,  $\{111\}$  and  $\{111\}+\{100\}$  fiber textures; copper deposit has  $\{110\}$ ,  $\{100\}$ ,  $\{111\}$ ,  $\{110\}+\{100\}$ ,  $\{111\}+\{100\}$  fiber texture, etc.

Obviously, it is difficult to generalize, although a number of attempts have been made to explain the mechanism of texture formation during electrodeposition [Reddy 1963, Pangarov 1965, Baraboshkin et. al 1977/78, Amblard and Froment 1979, Ye and Lee 1981]. Reddy proposed two general groups of deposit growth; One is the lateral growth mode in which the deposits grow so that the dense packed crystallographic planes are parallel to the substrate surface. This type of coating growth is produced by high bath temperature and low current density. In the second type, the outward growth mode has the dense packed planes perpendicular to the surface of the cathode. This is produced by low bath temperature and a high current density.

A few theories on the development of coating texture have been proposed [Reddy 1963, Pangarov 1962, Li 1997]. Reddy suggested that the formation of texture was determined by the growth of the crystalline facets. He proposed that the adsorption of hydrogen atoms could modify the growth rate of these faces and subsequently, the texture of deposit would vary with the hydrogen codeposition. He also speculated that an increase in the temperature changed the texture of nickel coatings from  $\{210\}$  to  $\{100\}$ . Pangarov reported that the texture of electrodeposited metal depended upon the current density during the deposition of

metal ions and that the texture of nickel deposit should develop in the order of the  $\{111\}$ ,  $\{100\}$ , and  $\{111\}$ , and finally transformed to the random crystals with increasing the current density. He also suggested that the texture formation in the deposit is governed by different nucleation rates of two-dimensional nuclei. According to Pangarov, difference in nucleation rates is induced by different nucleation energies of crystallographic planes. Based on the differences in their nucleation energy, the grain with lower nucleation energy would evolve predominantly after the competition of nucleation. However, this theory is somewhat incompatible with experimental work. Because the differences of nucleation energy between each nuclei are quite minimal compared to the applied overpotential for practical electrodeposition, it should cause the formation of randomly oriented nuclei under normal operating overpotential.

Another theory which explains the texture formation during electrodeposition is the surface-energy anisotropy theory [Li 1997, 1995]. In this theory, the grain growth occurs selectively, caused by the difference in surface energy between grains. As a consequence, the texture evolves; i.e., the growth of deposit proceeds along the “path” where the systems free energy decreases. This selective grain growth induced by the anisotropy in surface free energy is largely responsible for the texture development since the initial texture components induced by different nucleation rate or by influences of substrate gradually diminish as the coating grows. Li simulated the mechanism of texture evolution by computer modeling based on the minimization of the system’s free energy. Li also described, in Fig. 2.12, the competition of two grains upon different surface energy during the deposition process. The triple junction of grain A, B and electrolyte tends to move to the direction where the system’s free energy is minimized. The grain A having lower surface free energy will grow preferentially after the competition in growth between grains. Li suggested that the equilibrium angle  $\Phi_0$  might never be reached during real electrodeposition since  $\Phi_0$  is only a theoretical equilibrium angle. The deposit tends to grow toward an equilibrium state following the minimum energy principle. The deposition rate is a key parameter

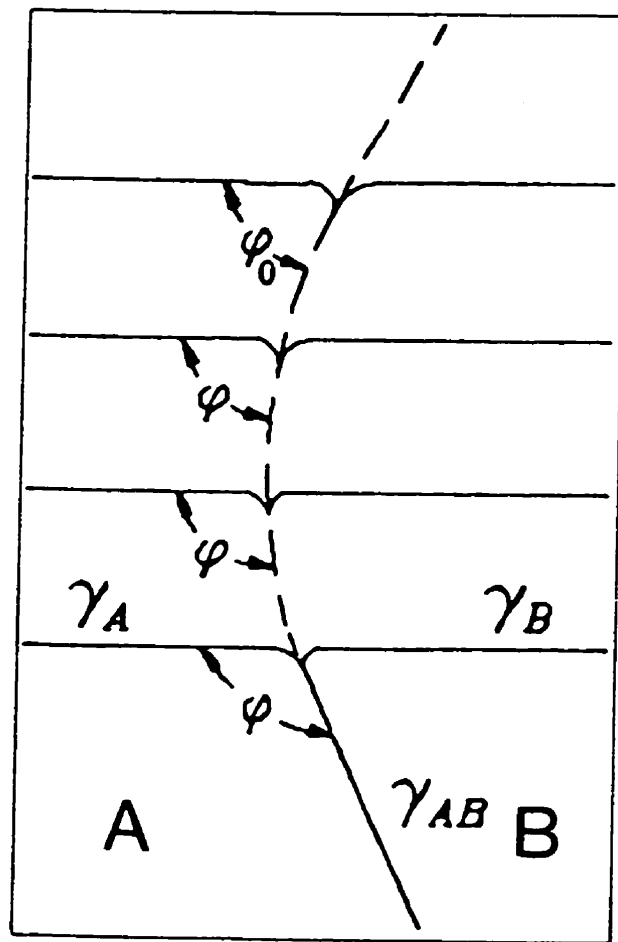


**Figure 2.12.** Schematic illustration of the formation of the grain boundary in the deposition process. The boundary bends to reach the equilibrium state [Li 1995].

controlling the state of the deposition process. At a high deposition rate, the deposition is far from equilibrium and the high nucleation rate may hinder the selective grain growth. As a result, the deposit has a fine grain size and is weakly textured or even randomly oriented [Winand 1990]. At a low current density, the nucleation rate is lower and ad-atoms may diffuse to favorable sites and be incorporated into the crystal lattice. Consequently, the deposit will be coarse-grained and more strongly textured.

## 2.8. EPITAXY AND COATING MORPHOLOGY OF ELECTRODEPOSIT

It is known that the zinc coating is electrodeposited under the influence of substrate steel microstructure [Kamei and Ohmori 1987, Marder 1990, Lin 1992, Ohtsubo et. al. 1994]. Deposition parameters often determine whether the epitaxial growth would occur or not. The applied current density and temperature of the bath are some of the most influencing parameters which determine the growth behavior of coatings. In case of high current density, for example, metal ions are forced to deposit randomly and the influence of substrate microstructure becomes weak. Conversely, elevated bath temperature and low current density permit the migration of ions to the sites where they can be incorporated into the existing structure, favor epitaxy.

It has been well established that most of the epitaxial layers show the morphology of ridges, pyramids or dendrites [Lawless 1967, Wright 1975, Suzuki 1973, Ahmed et. al. 1974]. The epitaxial growth of coatings from different substrate metals follows the general principles of epitaxy. It should be noted that the requirement of lattice matching is not very stringent for the epitaxial growth of electrodeposits [Ohmori et. al. 1993, Sheshadri and Setty 1974]. Successful growth of metal films with a lattice mismatch up to 37% has been reported by Ahmed [1974]. These epitaxial films also show spirals and hillocks, typical for the dislocation growth mechanism. Ahmed proposed that the growth of the layers takes place by the initiation and coalescence of island-like nuclei if the depositing metal is structurally dissimilar to the substrate metal. Sangwal et. al. [1991] deduced the evolution of coating morphology with current density: As the current density increases, the number of islands increases and the coalescence of islands leads to compact deposits. Above the limiting value of current density, the dendritic growth occurs. This dendritic growth results in the formation of sponge type, noncompact deposit, which is typical for polycrystalline deposition, at high current density. The dendrites emanate from tips of pyramidal hillocks and spirals.

An epitaxial relationship between the zinc electrodeposit and the steel substrate has been reported by a number of studies [Kamei and Ohmori 1987, Takechi et. al 1981]. Kamei and Ohmori found that the zinc electrodeposit nucleates in the form of hexagonal platelets which are parallel to the close-packed hexagonal plane. Other researchers claim that in the initial stage of deposition, the  $\eta$  phase zinc crystals nucleate on a steel substrate in the form of hexagonal platelets and have a specific orientation; i.e. epitaxial relationship with the ferrite grain [Marder 1990, Lin 1992]. Fig. 2.13 illustrates that the hcp of  $\eta$ -zinc coatings has a specific relationship of crystallographic orientation with the bcc steel substrate as follows [Ohmori et. al. 1993]:

$$\begin{aligned} \{0001\}_{\eta\text{-Zn}} // \{110\}_{\alpha\text{-Fe}} \\ \langle 1\bar{2}10 \rangle_{\eta\text{-Zn}} // \langle 1\bar{1}1 \rangle_{\alpha\text{-Fe}} \end{aligned}$$

The zinc coating will nucleate and grow on the substrate with the above crystallographic orientation relationship at low current density and thin coating thickness. According to Ohmori et. al., these  $\eta$  phase platelets are very thin in the direction of  $\langle 0001 \rangle$ . After the initial platelets form, the additional platelets are epitaxially nucleated on the previously formed  $\eta$  phase platelet surface in a side-by-side fashion. The platelets with the same orientation form a packet. The crystallographic orientation of a packet is closely related to the orientation of substrate grains because the boundary of packets in the coating corresponds to the grain boundary in the substrate.

In the polycrystalline steel substrates, Takechi et. al. found that the steel sheets with high Lankford  $r$ -values (i.e., containing a high concentration of  $\{111\}$  planes parallel to the sheet surface) have the  $\{10\bar{1}3\}$  pyramidal component as the main texture of the zinc coating in commercial electrogalvanized steel sheets. They also found that the decrease in  $r$ -values (i.e., lower concentration of  $\{111\}$  planes parallel to the sheet surface) leads to the texture change from the  $\{10\bar{1}3\}$  pyramidal to the  $\{0001\}$  basal fiber texture.

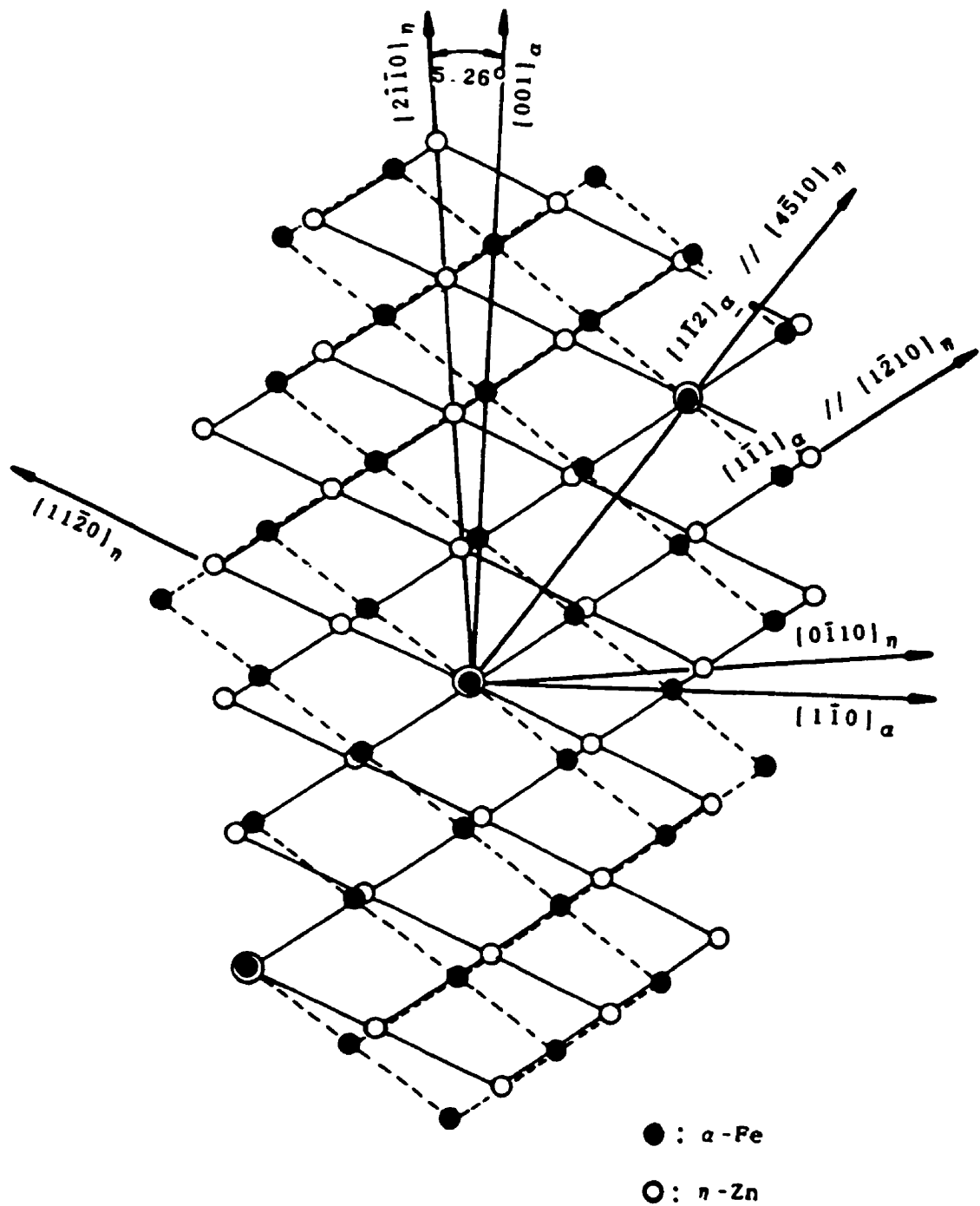


Figure 2.13. Atomic arrangements of both phases on the  $\{0001\}_{\eta\text{-Zn}} // \{110\}_{\alpha\text{-Fe}}$  interface [Ohmori et. al. 1993].

The occurrence of epitaxial growth is largely affected by the surface condition of the substrate, e.g., the increase in the thickness of the surface oxidized layer and the increase of the surface roughness decreases the possibility of epitaxial growth [Kamei and Ohmori 1987]. For good epitaxial growth of coatings, the applied current density should normally be kept small, but it varies from one material to another [Wright 1975].

## 2.9. MICROSTRUCTURE AND CORROSION PROPERTIES OF Zn-BASED COATINGS

A brief study of coating behavior upon various microstructures is reviewed in this section. The corrosion behavior of metallic coatings is closely dependent upon texture, morphology and chemical composition of the deposits [Takechi et. al. 1981, Alfantazi 1994, Vlad 1990, Girin and Panasenکو 1989]. When a metal is exposed to a corrosive environment, the corrosion rate of each grain varies because of the difference in free energy [Scully 1990, Bockris and Khan 1993]. According to Scully, the total energy involved in the breaking of the bonds and the subsequent dissolution of atoms is higher for the crystallographic planes which have a higher number of nearest neighbor atoms. Therefore, the close packed planes or the low-index planes are known to be more resistant to dissolution because of the higher binding energy of the surface atoms. Experimental evidence was found [Bockris and Khan 1993, Despic et. al. 1968, Damjanovic et. al. 1966]. Despic et. al. observed preferential dissolution of the high-index planes which emerged as a result of plastic deformation. They attributed the growth of stress-corrosion cracks to the emergence of high-index planes at the crack, and thereby concluded that different crystallographic orientations result in different corrosion resistance of grains. In addition to the various corrosion resistance due to the grain orientation, texture is also related to the grain boundary characteristics which eventually influences the intergranular corrosion behavior [Kim and Szpunar 1994].



Other observations have been made by several researchers to demonstrate the correlation between the texture and the corrosion behavior of coatings. Takechi et. al. [1981] reported that in hot-dip zinc coatings, the basal  $\{0001\}$  texture has a better corrosion resistance than the  $\{11\bar{2}2\}$  texture. A contrary view posed by Girin and Panasencko [1989] reported that the prismatic  $\{11\bar{2}0\}$  texture of zinc coatings had the best corrosion resistance. However, their results lack supportive experimental data of other textured coatings since a comparison was made only with the randomly oriented deposit.

Other hcp metals, such as  $\alpha$  cobalt exhibit a correlation of texture and corrosion resistance. Raichevski and Vitkova [1973] found from the result of a potentiodynamic polarization corrosion test that the  $\{0001\}$  texture exhibits the best corrosion resistance. The corrosion resistance of texture decreases with the order of  $\{0001\} > \{10\bar{1}1\} > \{11\bar{2}0\} > \{10\bar{1}0\}$ .

Corrosion behavior of coatings are also correlated to many other parameters. For instance, Fig. 2.14 shows a relationship between the chemical composition and corrosion rate of zinc alloy electrodeposited coatings [Vlad 1990]. From these curves, it is clear that the optimum corrosion protection can be achieved with the zinc alloys containing 10 to 16 % nickel in the case of zinc-nickel deposit, or about 50 % manganese in the case of zinc-manganese deposit. Similar results were obtained by Alfantazi's [1994] salt spraying corrosion test for zinc-nickel electrodeposited coatings. He found that the best corrosion resistance for pulse plated zinc-nickel coatings was obtained in the range of 14 to 20 % nickel. Out of this nickel percent range, coatings exhibited higher porosity and have dual phases. He speculated that the higher porosity and local corrosion cells between two different phases might be responsible for poorer corrosion resistance.

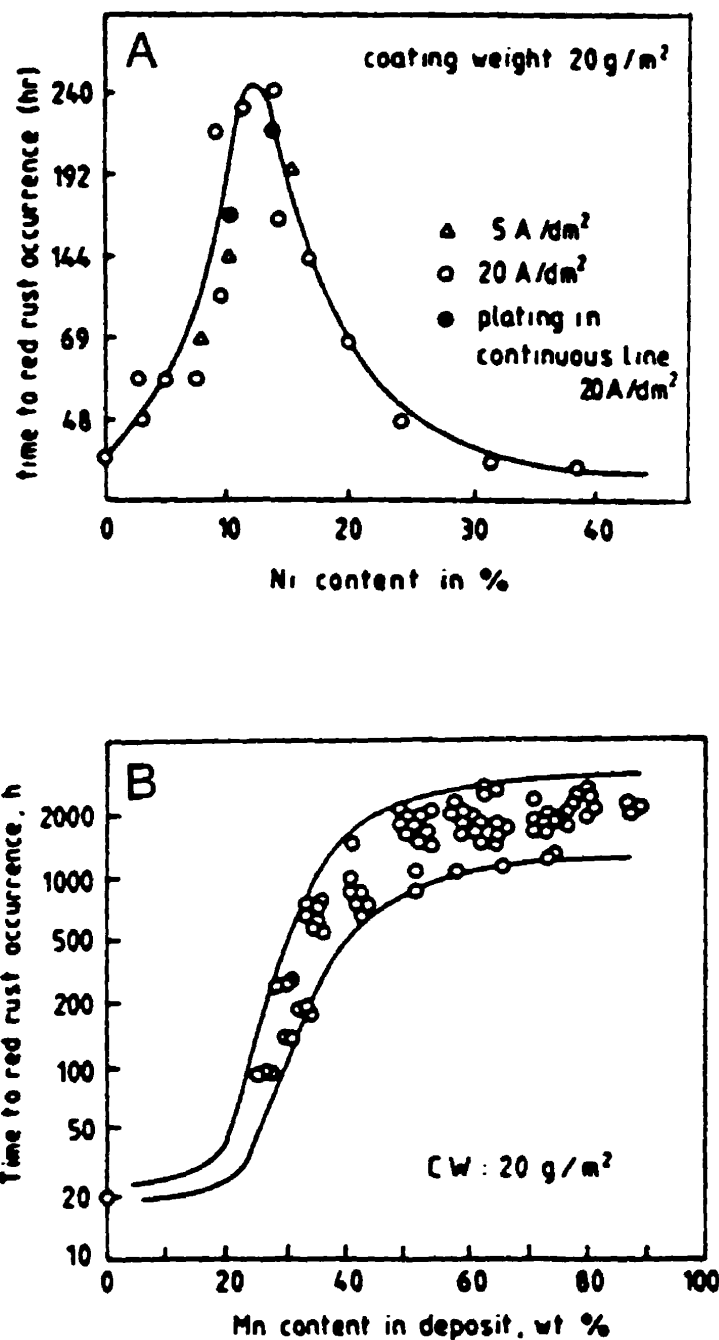


Figure 2.14. Relationship between the alloy composition and corrosion rate of zinc alloy electrodeposited coatings: (a) Zn-Ni coatings and (b) Zn-Mn coatings [Vlad 1990].

In addition to the influence of chemical composition, grain size of the deposit affects the corrosion resistance of the deposit as well. Tang et. al. [1995] focused his research on the influence of coating grain size on corrosion behavior. They found an improved corrosion resistance of the pulse plated nickel coating on steel substrate compared to the DC plated coatings. This was attributed to a finer grain size, which corresponds to lower porosity in the deposit. Moreover, reducing the grain size may be advantageous to the overall corrosion performance because the deposit with fine grains can avoid the detrimental corrosion reactions which preferably occur along the grain boundaries [Alfantazi 1994].

Texture of deposits influence other coating behaviors in addition to corrosion resistance. Takechi et. al. [1981] found a better paintability for a deposit that has a high intensity of the  $\{0001\}$  texture. They speculated that the superior paint adhesion was caused by the residual stress relief between the zinc coating and paint layer due to the generation of microcracks during deformation. Other studies have been made to demonstrate the influence of texture and mechanical properties of zinc electrodeposited coatings. Rangarajan et. al. [1989] observed that the electrodeposited zinc coatings with pyramidal texture exhibit plastic deformation upon applied uniaxial tensile stress. The basal textured coatings, on the contrary, exhibit no plastic deformation but showed microcrack formation. These experimental results were confirmed by other studies. Ye et. al. [1994] found that the electrodeposited zinc coatings with the basal planes parallel or perpendicular to the surface are less ductile than the coatings with the basal plane tilted to the surface. This was attributed to the fact that a slip on the basal plane is impossible when the load axis is parallel or perpendicular to the basal plane. Another experimental observation is consistent to the above result [Pak and Meshii 1990]. Pak and Meshii found no microcracking within the coating of  $\{10\bar{1}3\}$  pyramidal texture, whereas the coating of  $\{11\bar{2}0\}$  prismatic texture exhibited microcracks in the deposit during an axisymmetric forming test for the electrodeposited zinc coatings.

## **CHAPTER THREE**

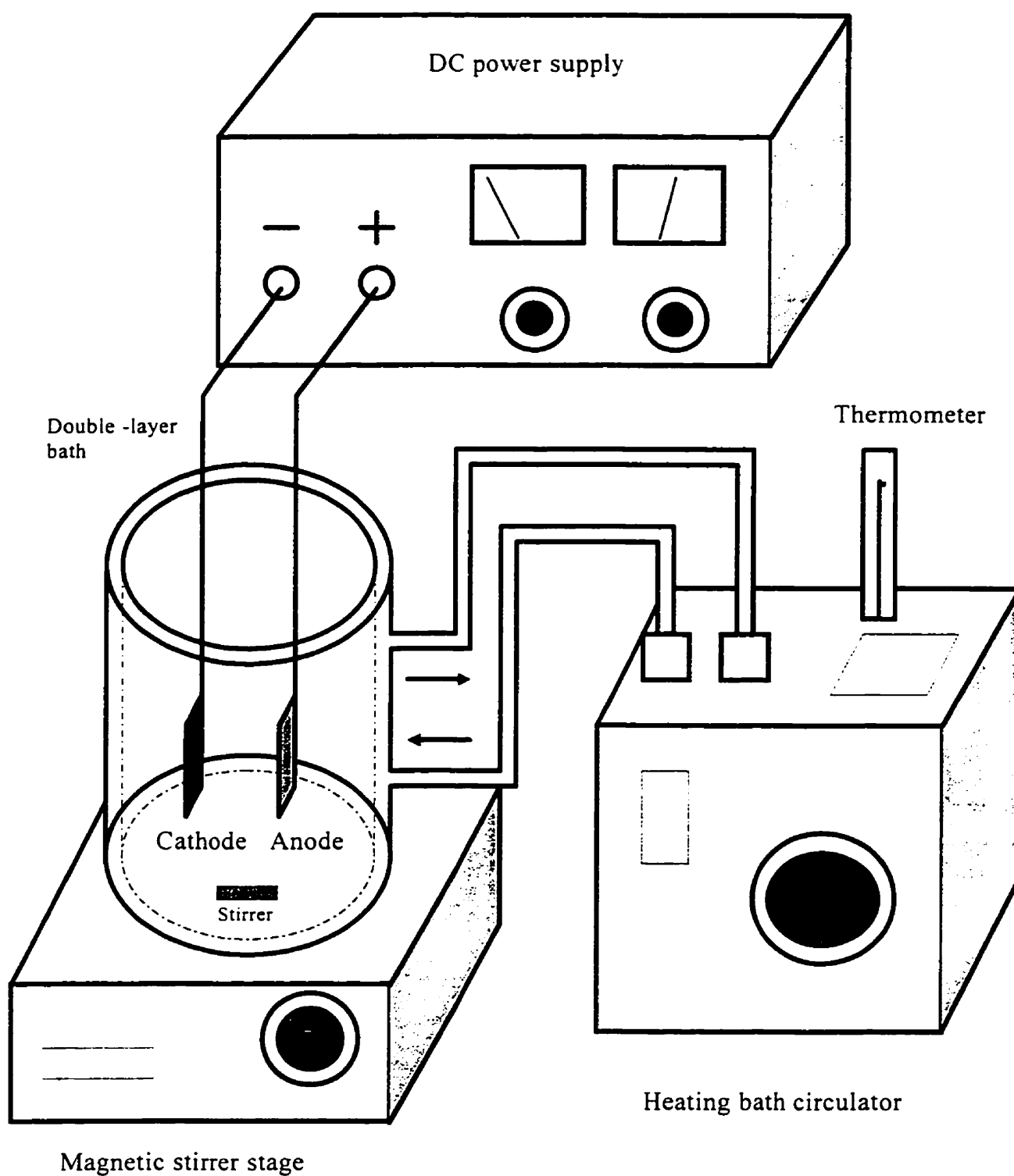
### **EXPERIMENTAL PROCEDURES**

#### **3.1. SAMPLE PREPARATION**

The specimens used for the substrate were prepared from a commercially cold rolled low carbon steel sheet with a thickness of 1 mm. The specimens were machined to a size of 12.5 mm in width and 25 mm in length. Each of the specimens was sealed in the iron foil sack and annealed at 880 °C for 3 hours (average grain size:  $\sim 50 \mu\text{m}$ ). They were then cooled in the furnace. The specimens used as substrates were mechanically ground down to 600  $\mu\text{m}$  using a SiC paper followed by polishing with diamond (1  $\mu\text{m}$ ) paste wheel. An electric cord was connected by spot welding to ensure the conduction of electric current. On top of that, the epoxy was applied to insulate the non-depositing area including the edge parts. Prior to the electrodeposition process, the substrate specimens were electrochemically polished in the solution of 95 % acetic acid and 5 % perchloric acid for about 2 to 3 minutes. This step is crucial since the electrochemical polishing provides the substrate with a stress-free and non oxide layered surface. Subsequently, the substrate was rinsed in distilled water and ethanol, and quickly dried.

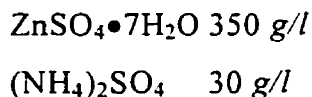
#### **3.2. DESCRIPTION OF ELECTRODEPOSITION PROCEDURES**

Fig. 3.1 illustrates the electrodeposition set used in this work. The apparatus includes a double-layered glass container with a capacity of 300 ml, a heating bath circulator, a magnetic stirrer and a DC power supply. The bath temperature can be controlled by circulating water from the heating bath circulator through the wall of the double-layered glass container. The magnetic stirrer was used to enhance the convection of the solution for efficient mass transfer. An electrolytic zinc plate was used as an anode which has the same size with the



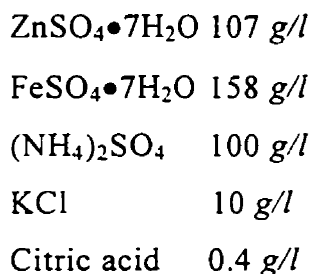
**Fig. 3. 1. Schematic illustration of the electrodeposition set.**

cathode. The distance between the cathode and the anode was about 27 mm. The electrodeposition was carried out in a bath of the following compositions from Geduld [1988]. In the case of pure zinc coating:



Different deposition parameters were applied to achieve various coating properties. In order to study the effect of current density on coating morphology and texture, the current density was varied within the range of 30 to 500 mA/cm<sup>2</sup>. The pH value was controlled in the range between 1 to 5 by adding sulfuric acid or sodium hydroxide. The deposition time was adjusted to produce coatings with a thickness ranging from 600 nm to 100  $\mu\text{m}$ . The bath temperature was kept constant at  $50 \pm 2$  °C.

For the zinc-iron coatings, the electrodeposition was performed in the bath of the following composition:



The ammonium sulfate in this formulation improves the quality of the deposit and widens the deposition range. The potassium chloride enhances the anode dissolution and the citric acid prevents the precipitation of ferric hydroxide by complexing ferric iron in the bath. The current density ranged from 50 to 500 mA/cm<sup>2</sup>. The deposition time was adjusted to produce coatings with a thickness ranging from 1 to 100  $\mu\text{m}$ . The pH value of electrolyte was kept about 3.5 ~ 4. The bath temperature was kept constant at  $50 \pm 2$  °C.

Finally, the zinc-nickel coatings were electrodeposited in the bath of composition as follows [Geduld 1988]:

$\text{ZnSO}_4 \cdot 7\text{H}_2\text{O}$  143 g/l

$\text{NiCl}_2 \cdot 6\text{H}_2\text{O}$  366 g/l

$(\text{NH}_4)_2\text{Cl}$  30 g/l

The deposition current density ranged from 50 to 1200 mA/cm<sup>2</sup>. The deposition time was adjusted to produce a coating with a thickness of about 15 μm. The pH value of bath was kept between 2.3. The bath temperature was kept constant at 50 ± 2 °C.

### 3.3. MICROSTRUCTURE CHARACTERIZATION TECHNIQUES

In order to perform meaningful microstructural analysis and interpretation of the results, it is necessary to understand the nature of characterization techniques. It is beyond the scope of this thesis to give a detailed description of the physical background for these techniques; but a brief introduction of the techniques used in this work should be useful and is given as follows.

#### 3.3.1. Atomic Force microscopy (AFM)

The AFM is a technique to analyze the surface morphology of material by measuring the interatomic forces between the probe and sample surface. A schematic of the sensing system of the AFM is illustrated in Fig. 3.2. A microfabricated silicon nitride cantilever with a sharp tip is lowered onto the specimen surface with a tip force of  $\approx 10^{-9}$  N. The surface is scanned using piezoelectric scanners. The beam from a laser diode is focused onto the back of the cantilever. The laser beam reflects off the back of the cantilever onto a segmented photodiode. The deflection of the cantilever is detected using a reflected laser beam. The amplified differential signal between the upper and lower photodiodes provides a sensitive measure of the

cantilever deflection. Any variation during scanning of the sample is corrected by retracting or extending the sample mount on a third piezoelectric scanner. A computer processes the data from the probe tip to form a three-dimensional image of the sample surface.

The experiments were performed using a Digital Instrument Nanoscope III contact-mode AFM fitted with a  $0.12 \text{ Nm}^{-1}$  cantilever. Samples were mounted on a piezoelectric scanner with a maximum lateral scan range of  $12.5 \text{ }\mu\text{m}$  and maximum vertical range of  $5 \text{ }\mu\text{m}$ . Data files of  $400 \times 400$  points were collected under conditions of constant force at scan rates of between 2 and 8 Hz.

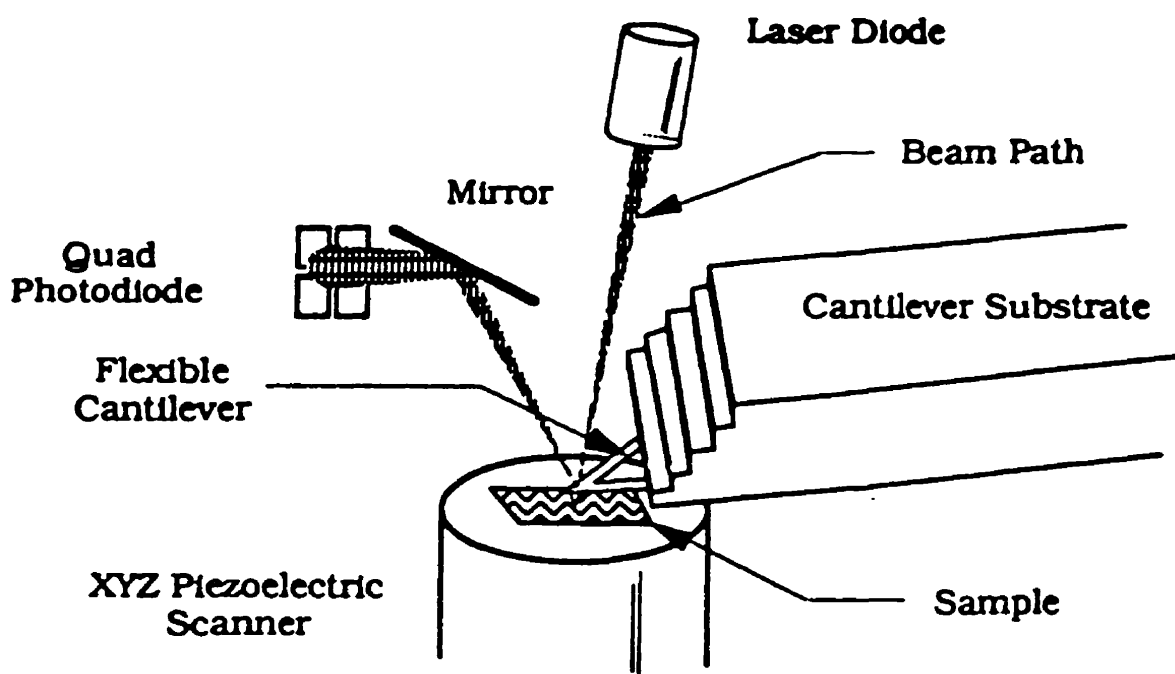


Figure 3.2. Schematic of the sensing system of an atomic force microscope [Digital Instruments 1993].



### 3.3.2. X-ray Diffractometry

X-ray diffraction techniques were used to study the crystallographic structure of investigated specimens. This technique enables one to determine the spacing  $d$  of various planes in a crystal using a known wavelength  $\lambda$  and measuring angle  $\theta$  [Cullity 1978]. X-ray diffraction also enables us to analyze the internal microstress by measuring the breadth of the diffraction peak [Cullity 1978].

In this work, a Rigaku X-ray spectrometer was operated using Cu-K $\alpha$  radiation at an accelerating voltage of 50 kV and current of 150 mA. The change of interplanar spacings and c/a ratio were calculated from the shifted angles of each diffraction peak. The FWHM (Full Width Half Maxima) of peaks were measured to estimate a change of the internal stress of the specimens.

### 3.3.3. Texture measurement

Texture is usually described by means of pole figures [Hatherley 1979, Cullity 1978, Barrett and Massalski 1980]. A pole figure is a stereographic projection of the orientation of a selected set of crystal planes onto the surface of the specimen. The crystallographic planes in the crystal are represented by polar coordinates of plane normals. The texture of a material can also be represented by the crystal Orientation Distribution Function (ODF). The ODF is a quantitative description of the spatial distribution of individual crystals within the specimens reference frame. This function describes by volume fraction, the orientation of the grains within the specimen. Formally, the ODF is defined as follows:

$$f(\varphi_1, \phi, \varphi_2) = 8\pi^2 \cdot \frac{dV}{\sin \phi \cdot d\varphi_1 \cdot d\phi \cdot d\varphi_2}$$

where  $(\varphi_1, \phi, \varphi_2)$  are the Euler angles,  $\sin \phi \cdot d\varphi_1 \cdot d\phi \cdot d\varphi_2$  is the element of the orientation space and  $dV$  is volume fraction of the grains. Mathematical methods have been developed which allow the ODF to be calculated from several experimental pole figures [Bunge 1982].

The pole figures are determined using the established principle of X-ray diffractometry. This technique uses a monochromatic beam of X-ray radiation to measure diffraction from crystallographic planes. The detector is positioned to register one type of Bragg reflection, and the specimen rotates through a wide range of angles so that differently oriented planes in the specimen are brought into coincidence with the scattering vector. The diffracted intensity is proportional to the number of  $\{hkl\}$  planes having specified orientation. In other words, the measured intensity at a given time is directly proportional to the pole density in the pole figure at the position under investigation. Fig. 3.3 is a schematic illustration of the X-ray diffraction method.

In this work, the texture of specimens were measured using a Siemens X-ray diffractometer. The diffractometer was operated using Cu-K $\alpha$  radiation at an accelerating voltage of 40 kV and current of 40 mA. Pole figures were measured using the reflection technique up to 80 deg maximum tilt of the specimen in 5 deg polar and angular intervals.

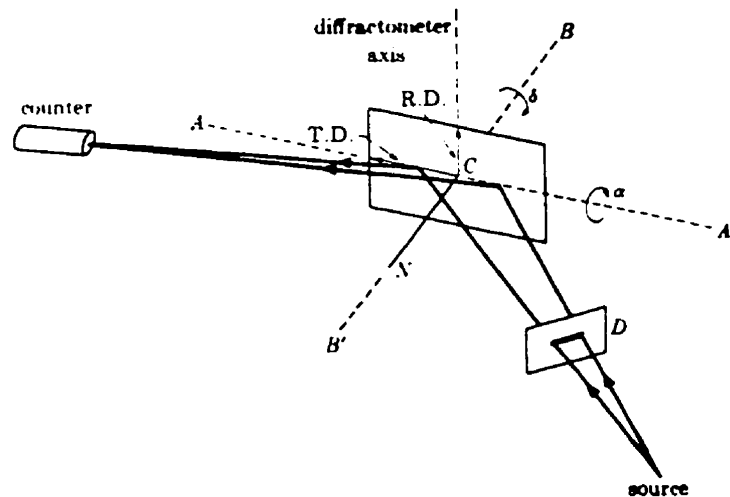


**Figure 3.3. Schematic illustration of x-ray diffraction method (Schulz reflection method) [Cullity 1978].**

## 3.4. ELECTROCHEMICAL CORROSION TESTS

Electrochemical techniques of corrosion measurement have been widely used due primarily to the rapidity and the accuracy in data acquisition. In this thesis, the corrosion behavior of specimens were determined using the Tafel plot analysis from the polarization curves as well as the electrochemical noise measurement (ENM). A brief introduction of the techniques is given as follows.

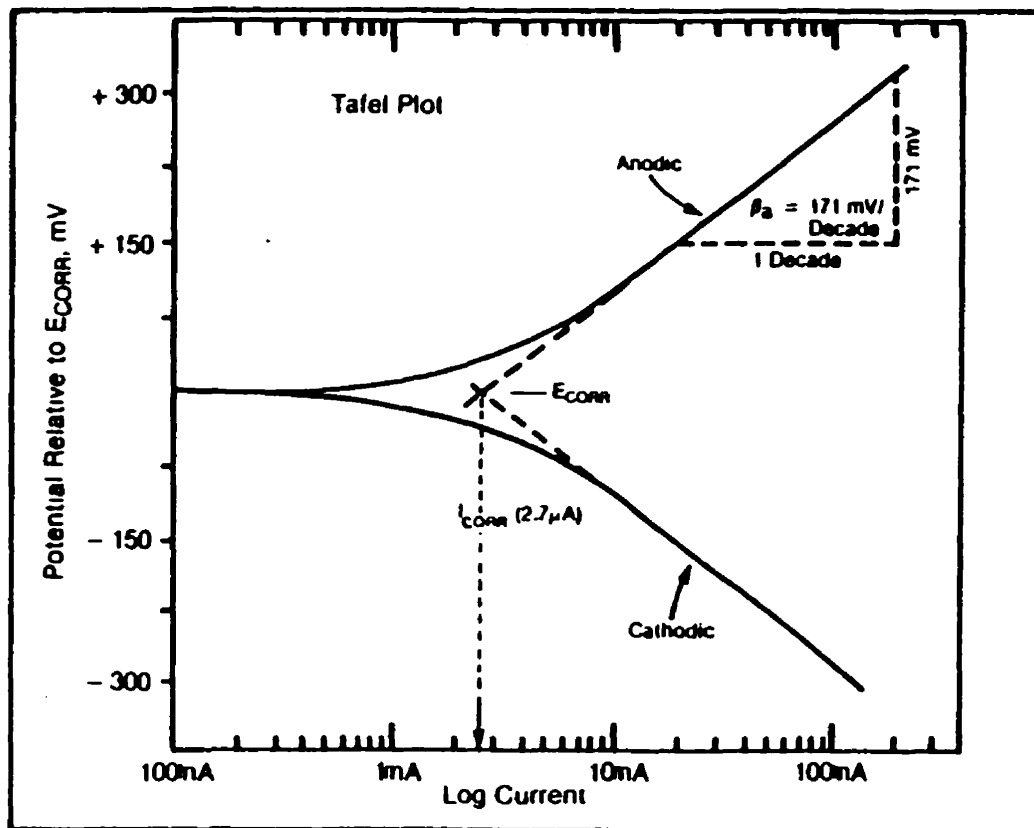


Figure 3.4. Experimentally measured Tafel plot [EG&G 1982].

### 3.4.1. Tafel Extrapolation Method

The Tafel method is a technique to determine the corrosion rate of a specimen by analyzing the cathodic or anodic polarization curves. The accuracy of the Tafel method is equal to or greater than conventional weight-loss methods under ideal conditions [Fontana and Greene 1978]. A Tafel plot is performed on a metal specimen by polarizing the specimen to about 300 mV anodically and cathodically from the corrosion potential,  $E_{\text{corr}}$ , as shown in Fig. 3.4. The potential is scanned with a scan rate of 0.1 ~ 1 mV/sec. The resulting current is plotted on a logarithmic scale. The corrosion current,  $I_{\text{corr}}$ , is directly related to the corrosion rate and obtained from a Tafel plot by extrapolating the linear portion of the curve to  $E_{\text{corr}}$ .

In this work, corrosion tests were conducted in deaerated 5 % NaCl solution at room temperature using an EG&G Princeton Applied Research Model 273 potentiostat, a standard corrosion cell kit containing the working electrode, two graphite counter electrodes and a saturated calomel reference electrode (SCE) as described by ASTM standard G3-89. Schematic diagrams of the corrosion cell and the electrode arrangement are illustrated in Fig. 3.5. The corrosion test monitors both the galvanic current between the anode (the working electrode) and the cathode (the counter electrode) and the potential between the anode and the reference electrode. The volume of electrolyte for each test was 500 ml and the solution was stirred and purged with nitrogen gas 10 minutes prior to and during the corrosion test in order to remove oxygen from the electrolyte. Potentiodynamic scanning was conducted by stepping the potential at a scan rate of 1 mV/sec from -250 mV (SCE) to +250 mV (SCE). From the automatic data acquisition system, the polarization curves were plotted and the corrosion current and potential were calculated by the Tafel extrapolation method.

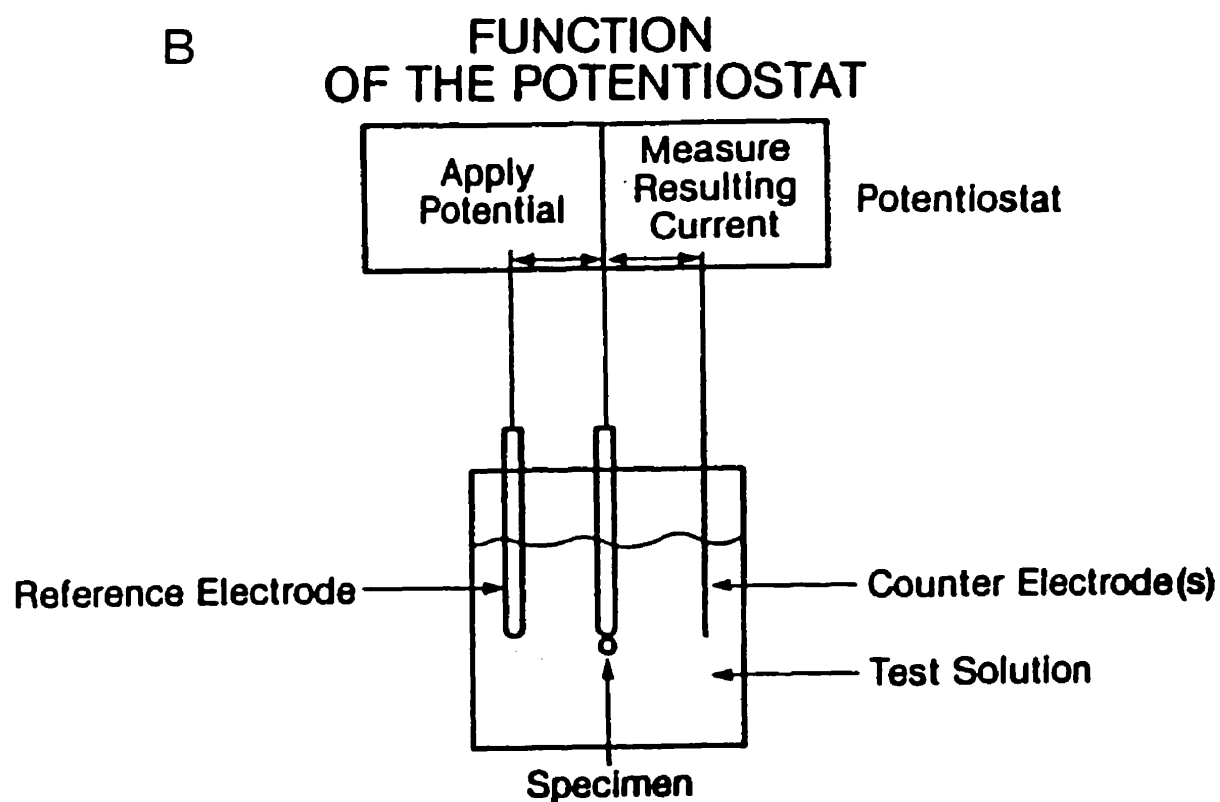
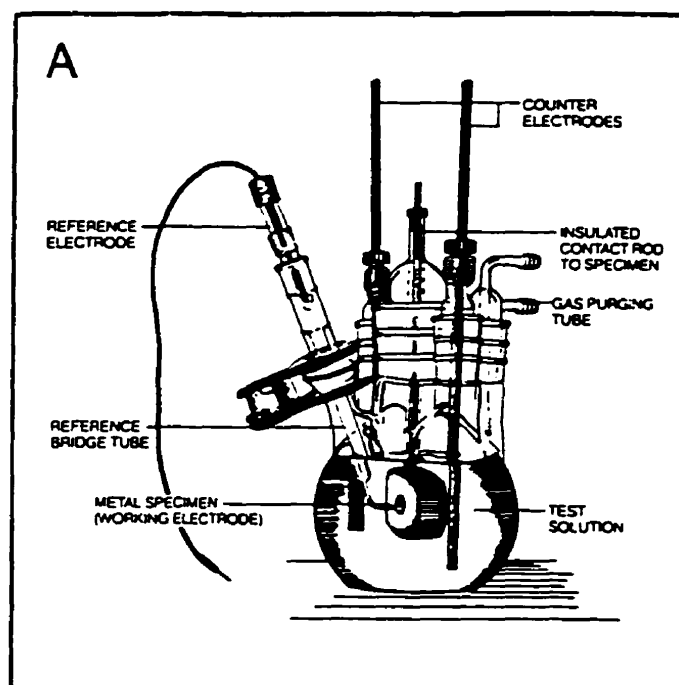
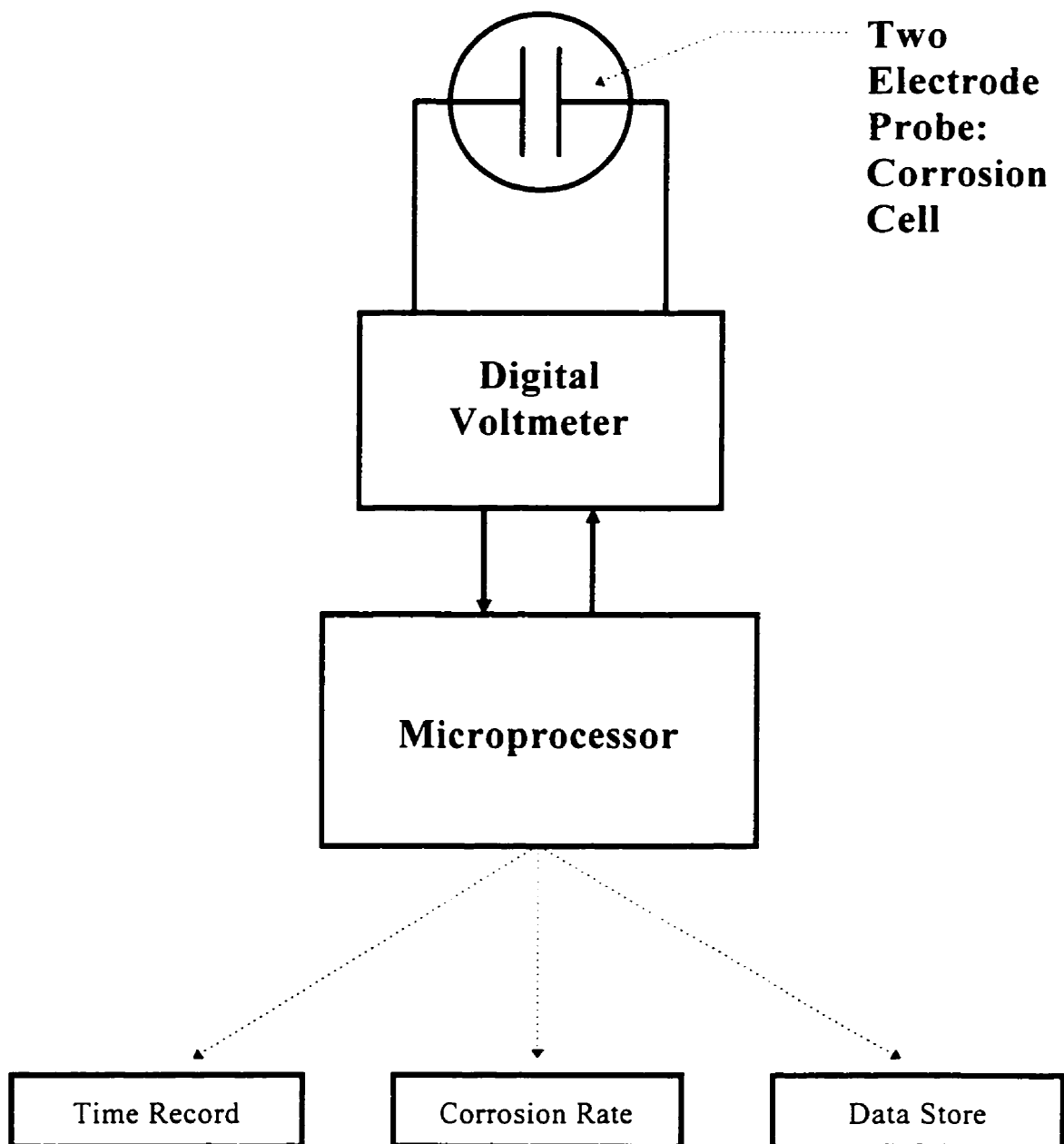


Figure 3.5. Schematic diagrams of (a) the corrosion cell and (b) the electrode arrangement [EG&G 1986].

### 3.4.2. Electrochemical Noise Measurement (ENM)

ENM is a technique used to provide the electrochemical noise data to assess the corrosion rate and to identify the presence of a general or localized corrosion process. Electrochemical noise is observed as spontaneous fluctuations of current or potential during the corrosion process [Dawson et. al. 1982]. The source of the noise is related to the continuous corrosion process which occurs during passive film breakdown and metal dissolution. As a practical method of corrosion monitoring, ENM analyzes the small amplitude and low frequency change of corrosion currents and corrosion potentials. The ENM technique uses a three electrode configuration comprised of two identical working electrodes and a reference electrode. The standard reference electrode, e.g. saturated calomel is commonly used as a reference electrode. During electrochemical potential and current noise measurements, the cell is not subjected to any external voltage or current perturbation, i.e. only the naturally occurring potentials and currents in the corrosion cell are measured. Fig. 3.6 schematically illustrates the arrangement for the ENM. An electrochemical signal from the two electrode probes is measured by a digital multimeter and the time record obtained is stored via the microprocessor which is also used to analyze and interpret the data.

In this work, ENM was conducted at the Ontario Hydro Technology Center using a Digital Electrochemical Noise Integrated System (DENIS) made by CAPCIS MARCH Ltd.



**Figure 3.6. Schematic illustration of the arrangement for electrochemical noise measurement**

## **CHAPTER FOUR**

# **SURFACE MORPHOLOGY AND TEXTURE OF ZINC COATINGS**

### **4.1. EFFECTS OF DEPOSITION PARAMETERS ON THE CHARACTERISTICS OF SURFACE MORPHOLOGY**

As previously mentioned in chapter 2, the morphology of coatings can be influenced significantly by different deposition parameters. A number of attempts have been made to investigate the characteristics of coating morphology. However, so far it is not clear how the deposition conditions influence the coating morphology. The present work is mainly focused on characterizing the zinc coating morphology at different current density, pH of electrolyte, and thickness of deposits. The change of coating morphology will be discussed later in conjunction with the evolution of coating texture.

#### **4.1.1. MORPHOLOGY VARIATION WITH CHANGING CURRENT DENSITY**

The zinc coatings were electrodeposited at different current densities ranging from 30 to 500 mA/cm<sup>2</sup> and a pH of the electrolyte of about 3.8. The electrodeposition time was adjusted to produce coatings with a thickness of 6 µm. The morphology of coatings completely changes with the applied current density change, as is shown in Fig. 4.1. The coatings deposited at the current density range of 30 to 300 mA/cm<sup>2</sup> exhibit the morphology of hexagonal platelets and ridges. The hexagonal platelets are parallel to the substrate surface. The ridges represent parts of the hexagonal platelets which are tilted with respect to the substrate



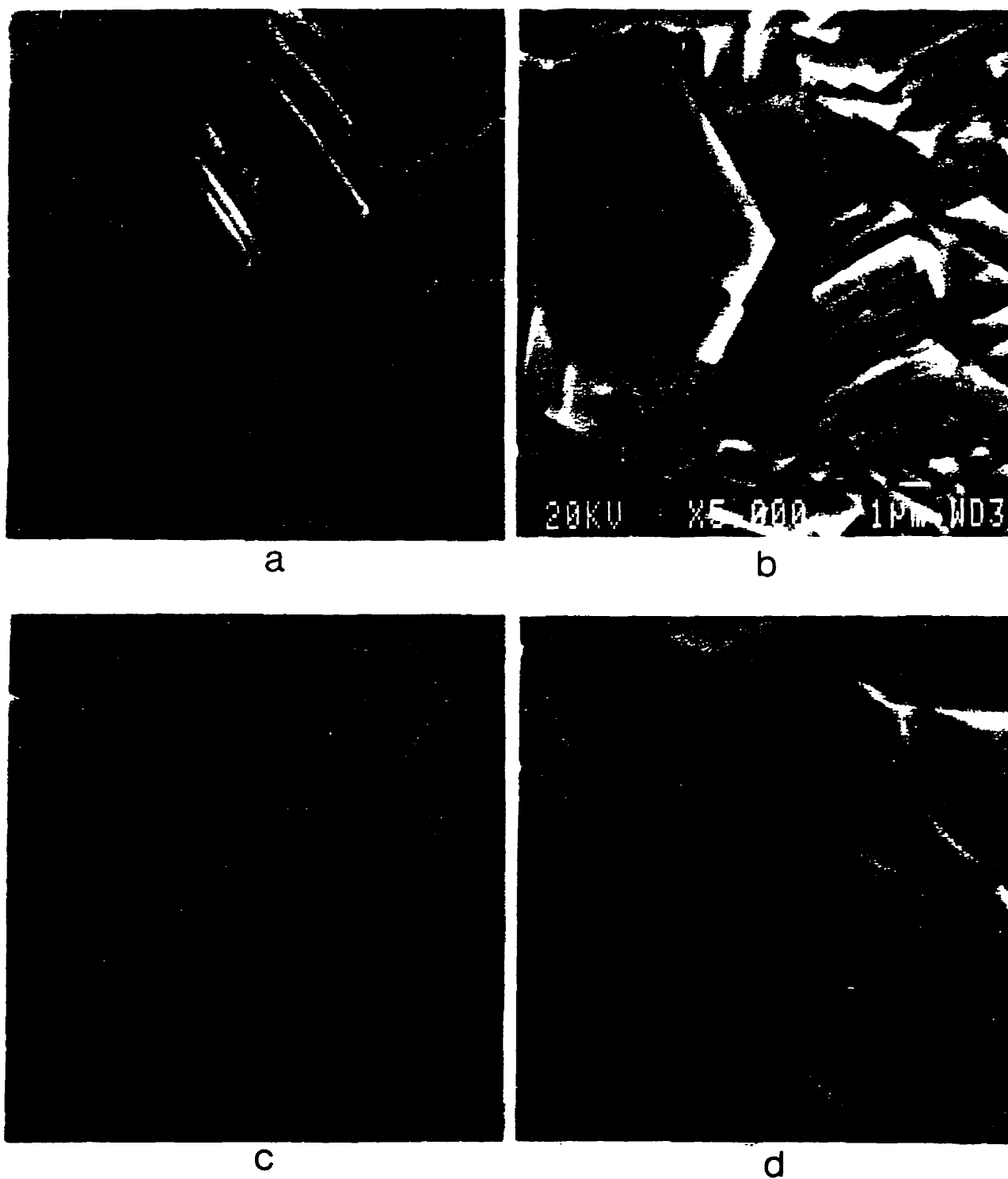
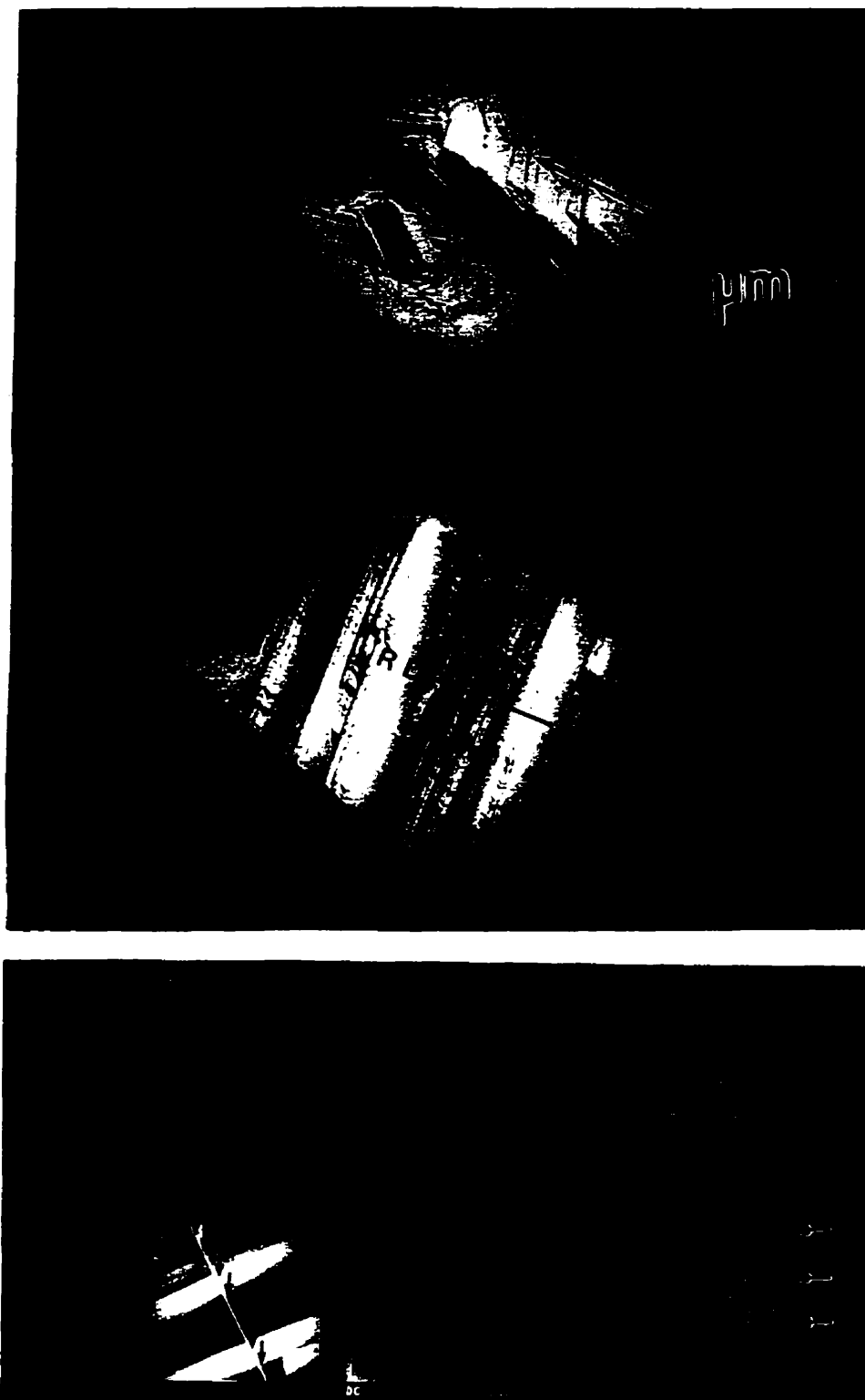


Figure 4.1. The SEM images exhibit morphological evolution of zinc electrodeposited coatings at different current density: (a) 30, (b) 100, (c) 300, (d) 400 mA/cm<sup>2</sup>.

surface. These hexagonal ridges are thin and are in the direction of  $[0001]$ . The sides of the ridges are about 4 to 6  $\mu\text{m}$  in size. It is a characteristic that the hexagonal ridges are aligned in specific directions rather than randomly oriented. As the current density increases to the range of 400 to 500  $\text{mA}/\text{cm}^2$ , the coating exhibits the morphology of pyramidal grains. The average size of grains on the planar surface is about 4 to 6  $\mu\text{m}$ . Although the pyramidal morphology has been frequently found in zinc-iron and zinc-nickel coatings, it was not reported in zinc electrodeposited coatings. Thus, it would be useful to characterize the pyramidal grains in the zinc coating system.

In order to discuss the morphological change of zinc coatings, it is necessary to take into account the two factors responsible for the evolution of coating morphology: (1) the influence of substrate microstructure; (2) the deposition parameters which cause the selective grain growth introduced in section 2.7. The morphology of hexagonal platelets and ridges obtained at current densities ranging from 30 to 300  $\text{mA}/\text{cm}^2$  can be attributed to the effect of the substrate orientation as well as to the influence of the current density which causes the selective grain growth. Let us first consider the effect of substrate orientation. It has been known that the zinc crystals nucleate on the steel substrate as small hexagonal platelets with a specific orientation relationship to the ferrite grains:  $\{0001\}_{\text{Zn}} // \{110\}_{\text{Fe}}$  and  $\langle 1\bar{2}10 \rangle_{\text{Zn}} // \langle 1\bar{1}1 \rangle_{\text{Fe}}$ . In this case, it should be noted that many hexagonal ridges are not only tilted by a certain angle from the substrate surface but also aligned parallel to the rolling direction of the steel substrate. The morphology of hexagonal ridges, therefore, indicates the evidence of epitaxial coating growth. This is true because the steel substrate has the  $\{110\}$  planes also tilted about 35 degrees from the substrate surface and aligned towards the rolling direction (refer to section 4.2.1). Moreover, the results of AFM morphology and section profile analysis shown in Fig. 4.2 support the idea of epitaxial growth of coatings. Fig. 4.2 shows that the hexagonal ridges are aligned parallel to the rolling direction and tilted about 35 degrees from the substrate surface. The existence of epitaxy will be



**Figure 4.2.** The AFM morphology and section profile analysis of hexagonal ridges in the zinc electrodeposited coatings; The ridges are aligned to the rolling direction and tilted about 35 degrees against the substrate surface.

later confirmed by the texture measurement which is discussed in section 4.2.

The above discussion suggested that the morphology of aligned ridges is formed due to the strong influence of the substrate orientation. The morphology of hexagonal platelets, on the other hand, implies the evolution of coating morphology upon the selective grain growth which is closely related to the deposition current density. The current density provides the electrical charge to transfer the metal ions to the cathode surface, and thus is one of the primary factors which strongly influences the coating characteristics. In our system, the hexagonal platelets are transformed to the randomly oriented pyramidal grains at the higher current density range (400 to 500 mA/cm<sup>2</sup>). Thus, it is evident that the change of applied current density is directly responsible for the evolution of coating morphology. This indicates that the morphology of hexagonal platelets is attributed to the lateral growth mode which is the predominant growth mechanism at low current densities. Whereas, the pyramidal morphology at high current density is caused by the outward growth mode.

The morphology of pyramidal grains can be attributed to the fact that high current density promotes non-epitaxial growth and high nucleation rate. Moreover, high current density causes an expansion of a zinc ion deficient layer near the cathode surface which is under diffusion control. The deficiency of zinc ions would promote the outward growth mode because the growing tip would have high zinc ion concentration.

From the previous discussion, a correlation is found between surface morphology of zinc coatings and current density. At low current densities, zinc coatings exhibit the morphology of hexagonal platelets and ridges. At high current densities, the coatings have the morphology of randomly oriented pyramidal grains.

## 4.1.2. MORPHOLOGY VARIATION WITH CHANGING pH VALUE OF THE ELECTROLYTE

The pure zinc coatings were electrodeposited at different pH values of the electrolyte varying from 1 to 5. The current density was kept constant at 300 mA/cm<sup>2</sup> and the deposition time was adjusted to produce a coating thickness of 6 μm. Fig. 4.3 shows the morphology of coatings deposited at different electrolyte pH. At the lowest pH value of 1, the coating shows the morphology of a large flat area and hexagonal ridges. The flat area represents the {0001} crystals parallel to the substrate surface, and the hexagonal ridges represent the {0001} crystals tilted from the substrate surface. The surface of the flat area is so fine and flat that it is impossible to distinguish the grain boundaries from the SEM observation. However, the AFM analysis shows details of the surface morphology on the flat area in Fig. 4.4. The AFM picture clearly shows the massive flat area covered with numbers of tiny subgrains with a size of about 50 nm.

As the pH of the electrolyte increases, the morphology of hexagonal ridges becomes predominant while the morphology of flat area completely disappears. Fig. 4.3b, c exhibits the morphology of coatings deposited at a pH of 5. The hexagonal ridges are well-aligned towards the rolling direction of the substrate. The steps between each ridges are 0.5 to 1 μm in width.

Under typical commercial operating conditions, zinc coatings are electrodeposited within the pH range of 3.0 to 4.5 [Geduld 1988]. In the present work, however, the pH value is extended to the extreme low range in order to observe the influence of hydrogen concentration in the electrolyte on the deposition behavior. The morphology of coatings obtained at pH = 1 shows a large portion of flat area. As the hydrogen concentration decreases, the morphology of hexagonal ridges becomes predominant whereas the flat area disappears. The change of morphology at different pH values is indication of the influence of hydrogen concentration on coating growth. At higher concentrations of hydrogen in the

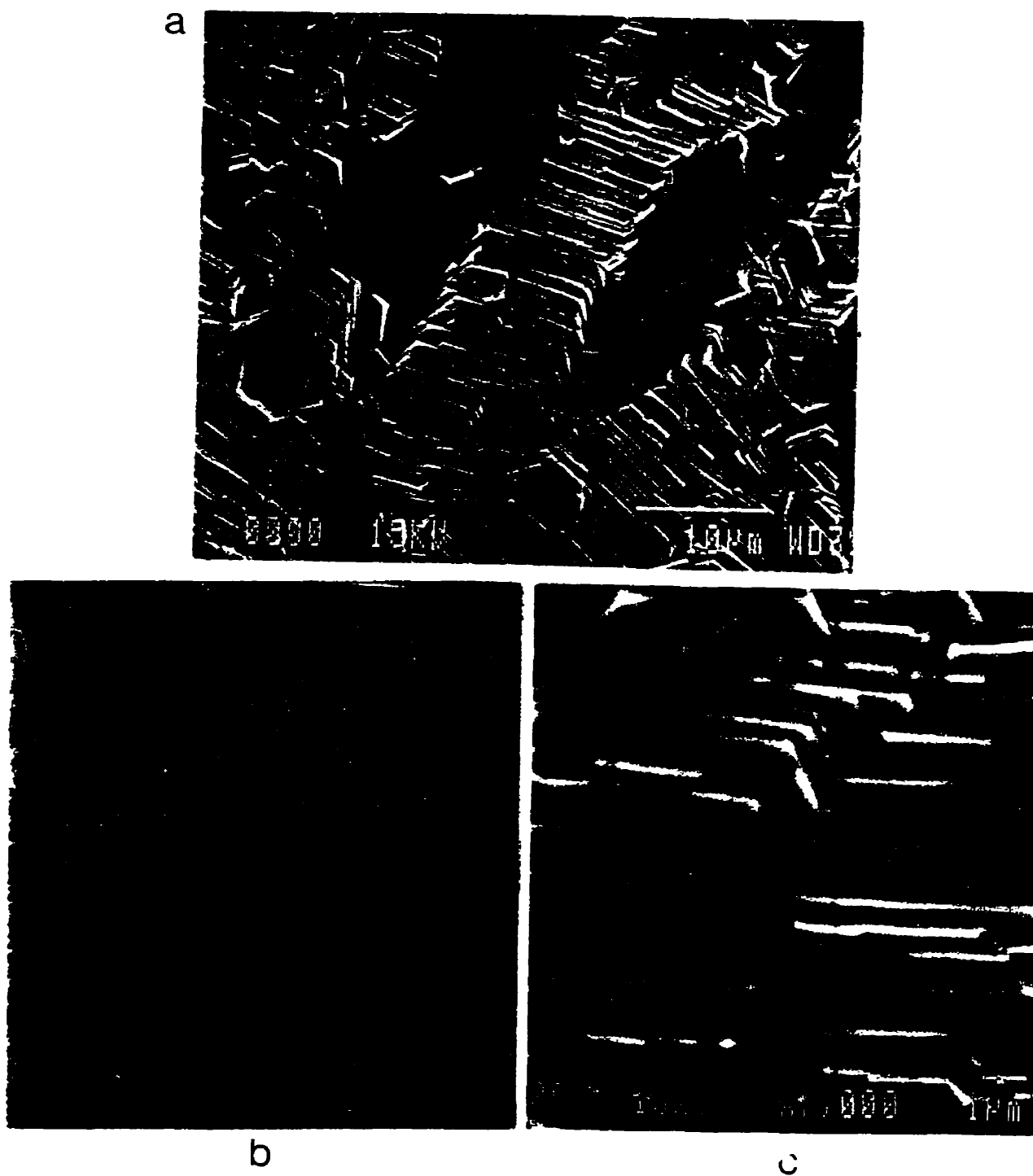


**Figure 4.3.** The SEM morphology of zinc electrodeposited coatings at different pH of electrolyte: (a) large portions of flat area and hexagonal ridges are observed at pH 1, (b) the flat area disappears, whereas the ridges are well aligned to the rolling direction at pH 5 (x2000), (c) detailed image of ridges at pH 5 (x7000).

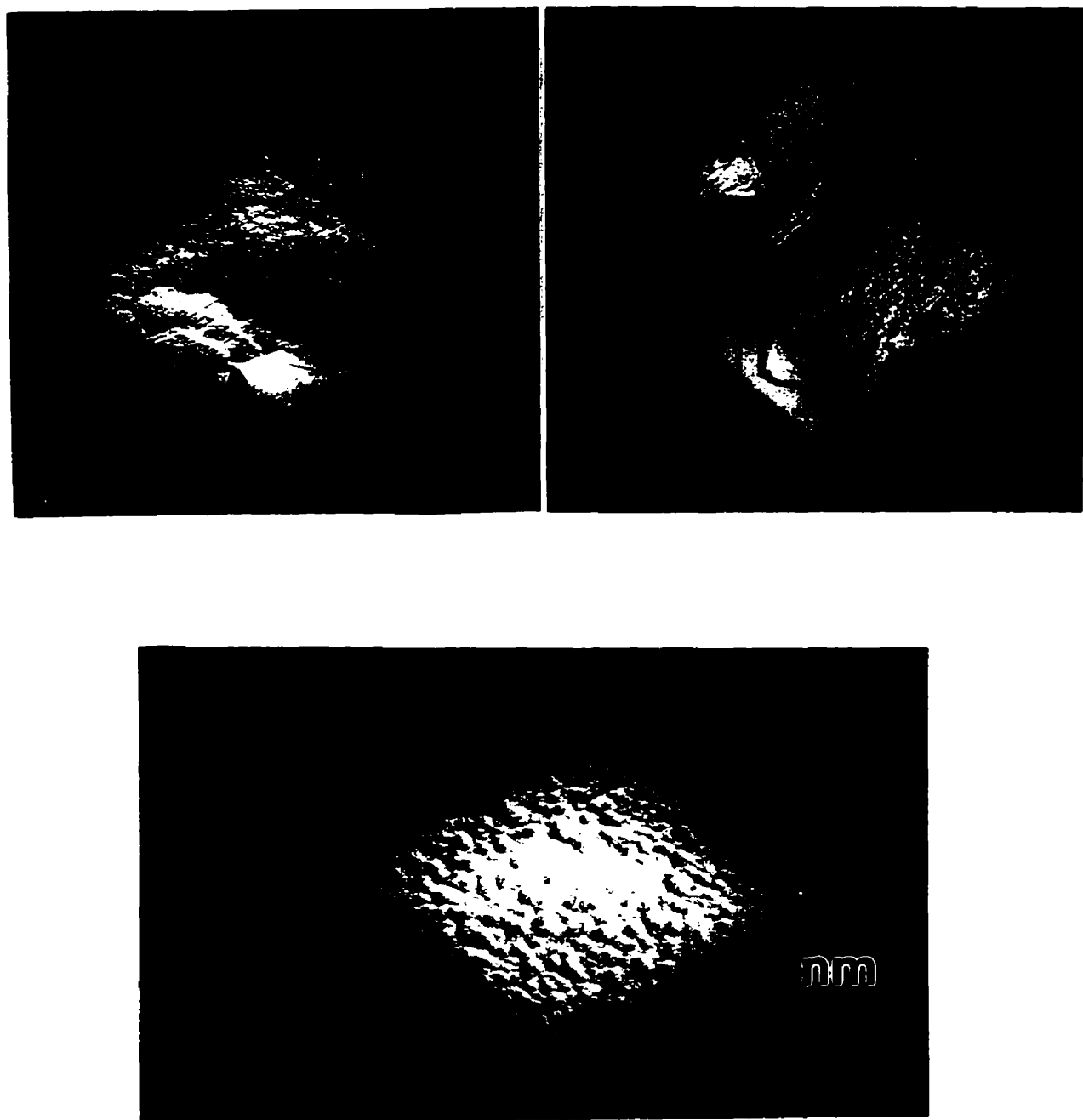


**Figure 4.4.** The AFM morphology of the flat area in the zinc electrodeposited coatings; The massive flat area is covered with numbers of tiny particles.

electrolyte, the codeposition of hydrogen ion with zinc ion occurs more frequently than in the electrolyte of lower hydrogen concentration. The hydrogen codeposition significantly influences the surface energy of deposit. Petch [1956] demonstrated in Fig. 4.5 that the deposit's surface energy decreases as the amount of adsorbed hydrogen increases. The degree of surface energy decrease is different for each of the  $\{hkl\}$  planes because of the difference in hydrogen adsorption capability [Li and Szpunar 1997, Reddy 1963]. The hydrogen codeposition takes place preferentially at the site where the surface energy can be minimized. Therefore, the crystallographic planes which can accommodate more hydrogen atoms with minimum free energy increase would grow preferentially during the deposition process. It appears that the flat area which represents the basal planes parallel to the substrate surface can accommodate more hydrogen atoms than other planes as evidenced by the morphology of the flat area being predominant at higher hydrogen concentration.

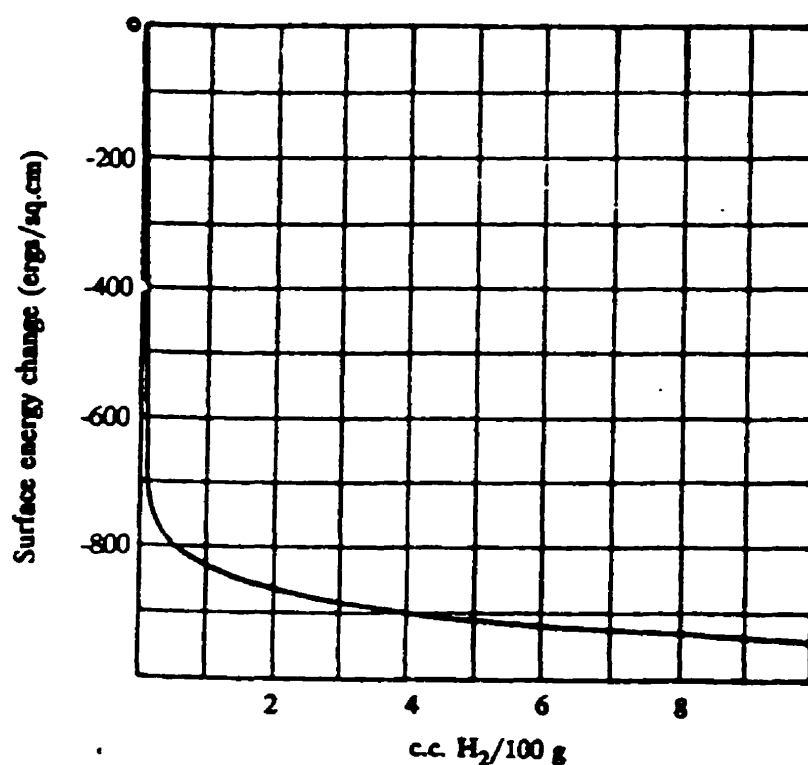


Figure 4.5. Correlation between hydrogen adsorption and surface energy of iron; The deposits' surface energy decreases as the amount of adsorbed hydrogen increases [Petch 1956].



From the previous discussion, a correlation is found between the surface morphology of zinc coatings and the pH of electrolyte. At low pH values, zinc coatings exhibit the morphology of flat areas and well-aligned hexagonal ridges. At high pH values, the flat area disappears while the coatings have the morphology of well-aligned hexagonal ridges.

#### 4.1.3. MORPHOLOGY VARIATION WITH CHANGING COATING THICKNESS

The pure zinc coatings were electrodeposited at different deposition times to produce coating thicknesses of 600 nm, 6  $\mu\text{m}$ , 10, 30, and 100  $\mu\text{m}$ . The current density was kept constant at 30  $\text{mA}/\text{cm}^2$  and the pH of electrolyte was 3.8. The morphology of zinc coatings at different thicknesses are shown in Fig. 4.6. The coating morphology varies significantly as the coating thickness increases. The coating of 600 nm shows the morphology of sub-micron sized particles (Fig. 4.6a). As the thickness increases to 6  $\mu\text{m}$ , the tiny particles disappear and the thin well-aligned hexagonal ridges form (Fig. 4.6b). Further increase in thickness to 10  $\mu\text{m}$  results in the morphology of thick platelets (Fig. 4.6c). It is a characteristic that the platelets are randomly oriented. At the thickness of 30  $\mu\text{m}$ , the coating morphology exhibits “cauliflower-like” structures in which randomly oriented hexagonal ridges conglomerate together (Fig. 4.6d). Eventually, the morphology of columnar crystals evolve with a coating thickness of 100  $\mu\text{m}$  (Fig. 4.6e). These columnar crystals have flat hexagonal faces, which represent the {0001} basal planes. The growing direction of columnar crystals are mostly perpendicular to the substrate surface, while the branches protrude toward random orientations.

It should be noted that the morphology of hexagonal platelets transforms from well-aligned ridges, to randomly oriented packets of thicker platelets and to a “cauliflower-like” structure as the coating thickness increases from 6 to 10 to 30  $\mu\text{m}$  (Fig. 4.6b, c, d). This finding suggests that the influence of substrate

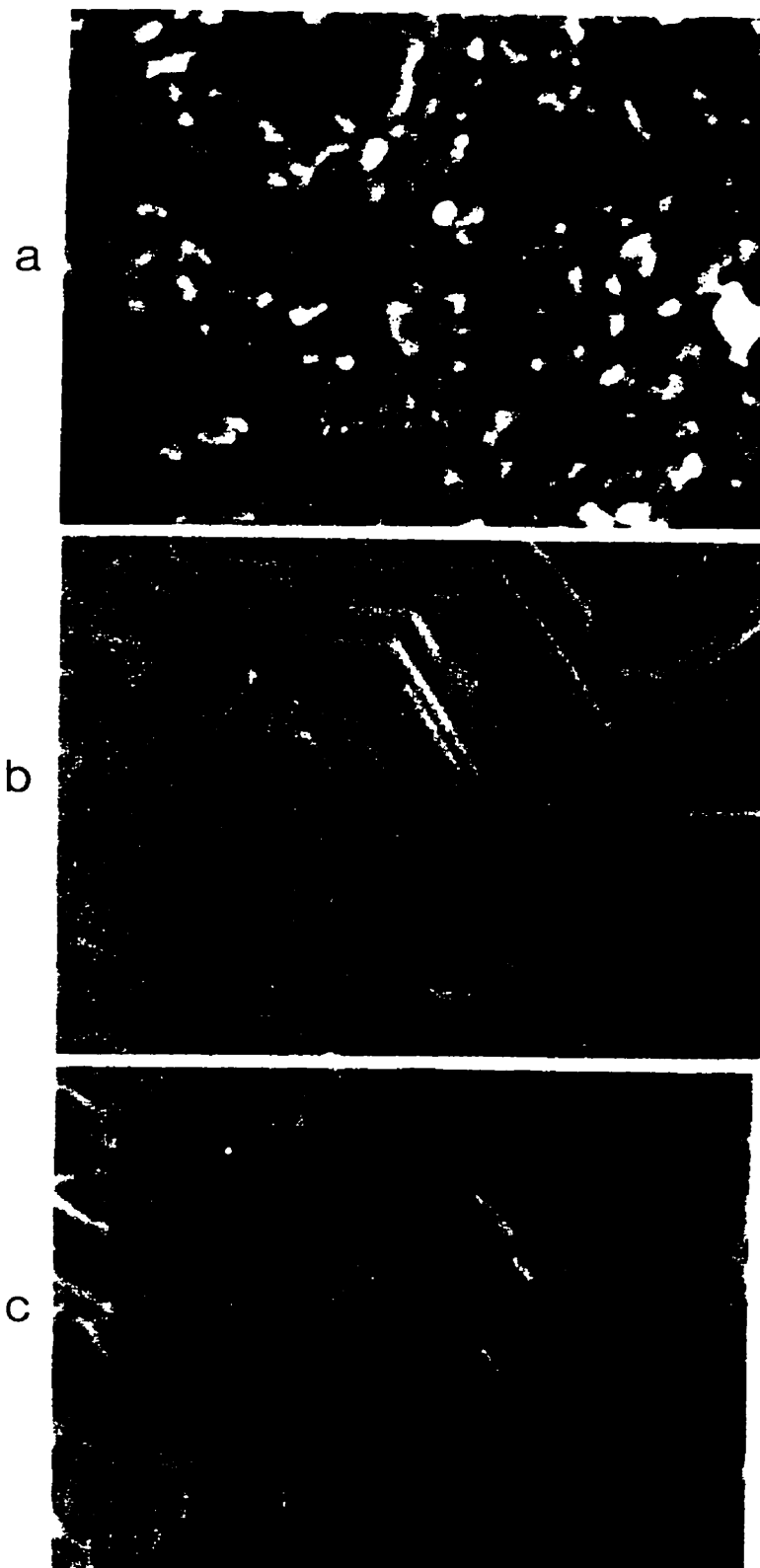
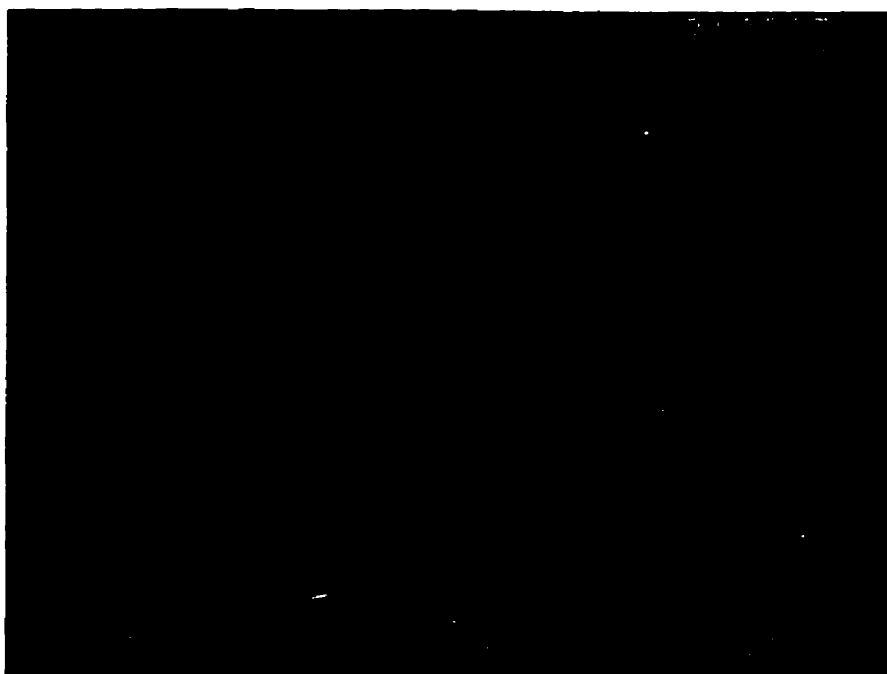


Figure 4.6. The SEM images exhibit a morphological evolution of zinc electrodeposited coatings at different coating thickness: (a) 600 nm, (b) 6  $\mu\text{m}$ , (c) 10  $\mu\text{m}$ , (d) 30  $\mu\text{m}$ , and (e) 100  $\mu\text{m}$ .

d



e

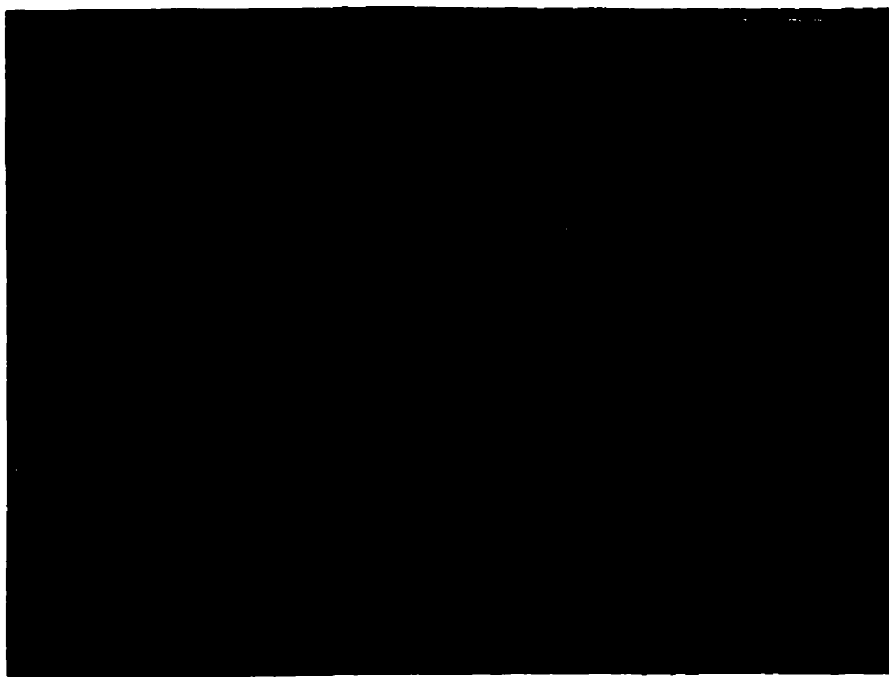


Figure 4.6. Continued

orientation becomes weak as the coating thickness increases. The “cauliflower-like” structure represents the randomly oriented hexagonal ridges evolved without the substrate influence.

As coating thickness increases, the coating surface becomes rough. Subsequently, the actual surface area of coating increases. For this reason, the actual current density applied to the coating surface decreases. The decrease of actual current density, which is in favor of depositing the basal plane parallel to the cathode surface, results in the formation of columnar crystals of hexagonal faces (Fig. 4.6e).

#### 4.1.4. SUMMARY

In this section, it has been demonstrated that the morphology of zinc coatings significantly changes with deposition parameters. Morphological observations are made at various current densities, pH of electrolyte and coating thickness.

1. As the current density increases, the morphology of zinc coatings evolves from the hexagonal platelets and ridges to the pyramidal grains. The hexagonal ridges are well-aligned towards the rolling direction of steel substrate, while the pyramidal grains are randomly oriented.
2. As the pH of electrolyte increases, the coating surface changes from the combined morphology of flat area and well-aligned hexagonal ridges to the hexagonal ridge-only morphology.
3. As the coating thickness increases, the morphology evolves from the sub-micron sized particles to the thin hexagonal ridges, to the packets of thicker hexagonal platelets, to the “cauliflower-like” structure and finally to the hexagonal columnar crystals.

## 4.2. EVOLUTION OF TEXTURE AT DIFFERENT DEPOSITION PARAMETERS

Texture is one of the important factors which affects the coating's properties. It has been known that strong preferred crystallographic orientations can be produced in electrodeposited zinc coatings. It is necessary, therefore, to investigate systematically how the coating texture evolves at various deposition parameters. This section demonstrates the characteristics of texture at different current density, pH of electrolyte and coating thickness for zinc electrodeposits. The influence of substrate orientation is also demonstrated. The correlation between texture and morphology of zinc coatings is discussed.

## 4.2.1. INFLUENCE OF CURRENT DENSITY

The influence of current density on the texture of zinc coatings was examined. Texture was measured for the coatings deposited at various current densities ranging from 30 to 500 mA/cm<sup>2</sup>. Texture of the coatings changes as the current density increases. The coating deposited at 30 mA/cm<sup>2</sup> has two texture components; the basal {0001} texture and the pyramidal {10 $\bar{1}$ 3} texture (Fig. 4.7a). In the {0001} pole figure, the poles at the center represent the basal {0001} texture component. This basal texture is a strong sharp fiber component with the intensity maxima 43 times higher than random orientation. The poles aligned towards the rolling direction with a tilted angle of 35 degrees from the center represent the {10 $\bar{1}$ 3} pyramidal non-fiber texture.

As the current density increases to 300 mA/cm<sup>2</sup>, both of the {0001} and the {10 $\bar{1}$ 3} texture components still coexist. It should be noted that in the case of the {10 $\bar{1}$ 3} texture, the {10 $\bar{1}$ 3} poles are more widely dispersed within the range of 30 degrees from the center of the {10 $\bar{1}$ 3} pole figure rather than concentrated around the center (Fig. 4.7b). Further increases in current density to 400 and 500 mA/cm<sup>2</sup>

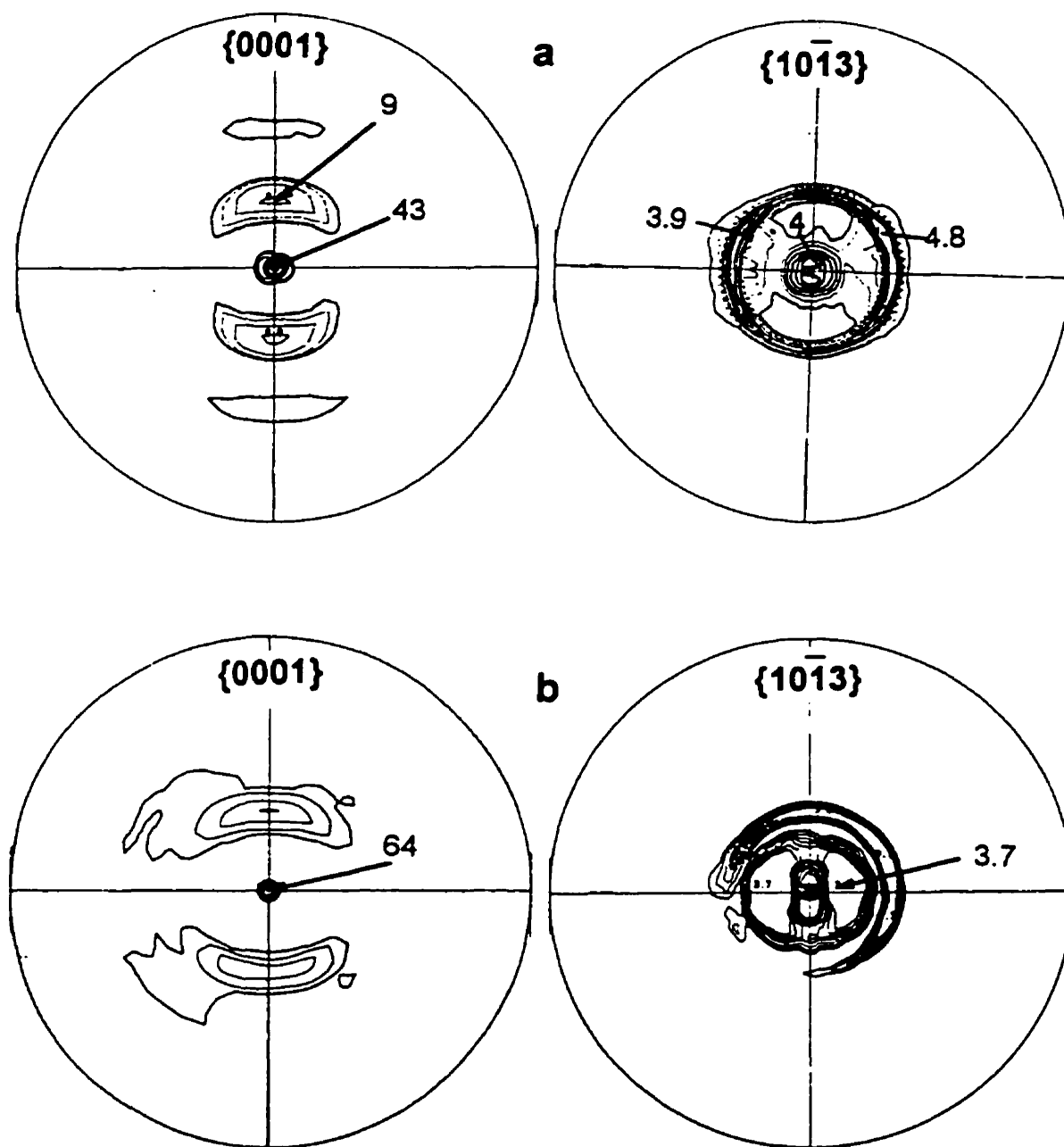


Figure 4.7. The pole figures of zinc electrodeposited coatings deposited at different current density: (a) 30, (b) 300, (c) 400, (d) 500 mA/cm<sup>2</sup>; The basal component completely disappears while the non-fiber pyramidal component evolves to fiber at high current density.

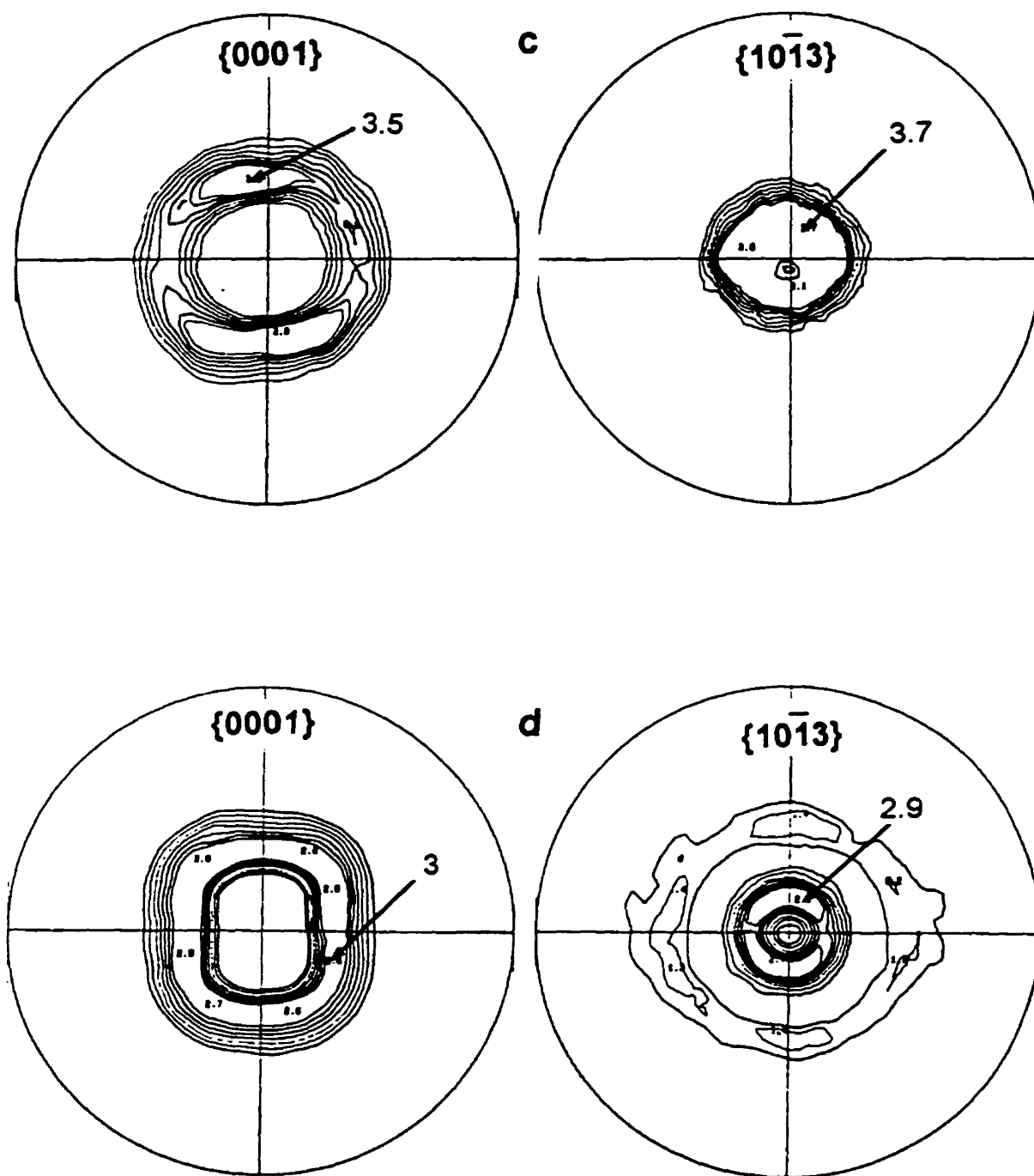


Figure 4.7. Continued.

leads to significant changes in the coating texture. An important observation is that the  $\{0001\}$  basal texture component disappears completely, while the non-fiber pyramidal component transforms to the fiber  $\{10\bar{1}X\}$  pyramidal texture (Fig. 4.7c. d). It should be noted that the coatings deposited at this current density range have only fiber pyramidal texture, which contrasts to the coatings of both the basal fiber and non-fiber pyramidal components at the lower range of current densities.

In order to demonstrate the influence of substrate orientation on coating texture, the texture of substrate was measured and compared to the texture of coatings. Fig. 4.8 shows pole figures and ODF (Orientation Distribution Function) of an annealed steel sheet used as a substrate during the electrodeposition. It is clear from the pole figures and the ODF that the substrate has the typical annealing texture of the steel sheet. It should be noted that the poles of  $\{110\}$  plane are aligned towards the rolling direction, and tilted about 35 degrees from the center of  $\{110\}$  pole figure. The coatings at low current density have the  $\{0001\}$  poles aligned towards the rolling direction with the tilted angle of 35 degrees from the center of  $\{0001\}$  pole figure (Fig. 4.7a). Therefore, comparing the  $\{0001\}$  pole figure of zinc coatings to the  $\{110\}$  pole figure of steel substrate indicates a strong influence of substrate orientation upon coating texture, because zinc coatings have a specific crystallographic orientation relationship with the steel substrate:  $\{0001\}_{Zn} // \{110\}_{Fe}$  and  $\langle 1\bar{2}10 \rangle_{Zn} // \langle 1\bar{1}1 \rangle_{Fe}$  (refer to section 2.8).

It was observed that the coatings at low current densities have textures of the  $\{0001\}$  basal fiber component and the  $\{10\bar{1}3\}$  pyramidal non-fiber component (Fig. 4.7a). The above discussion suggested that the formation of the pyramidal component is attributed to the influence of the substrate. The basal fiber component, on the other hand, implies that the evolution of coating texture is also governed by the deposit growth mode which is closely related to the current density. The basal texture, which represents the basal plane parallel to the



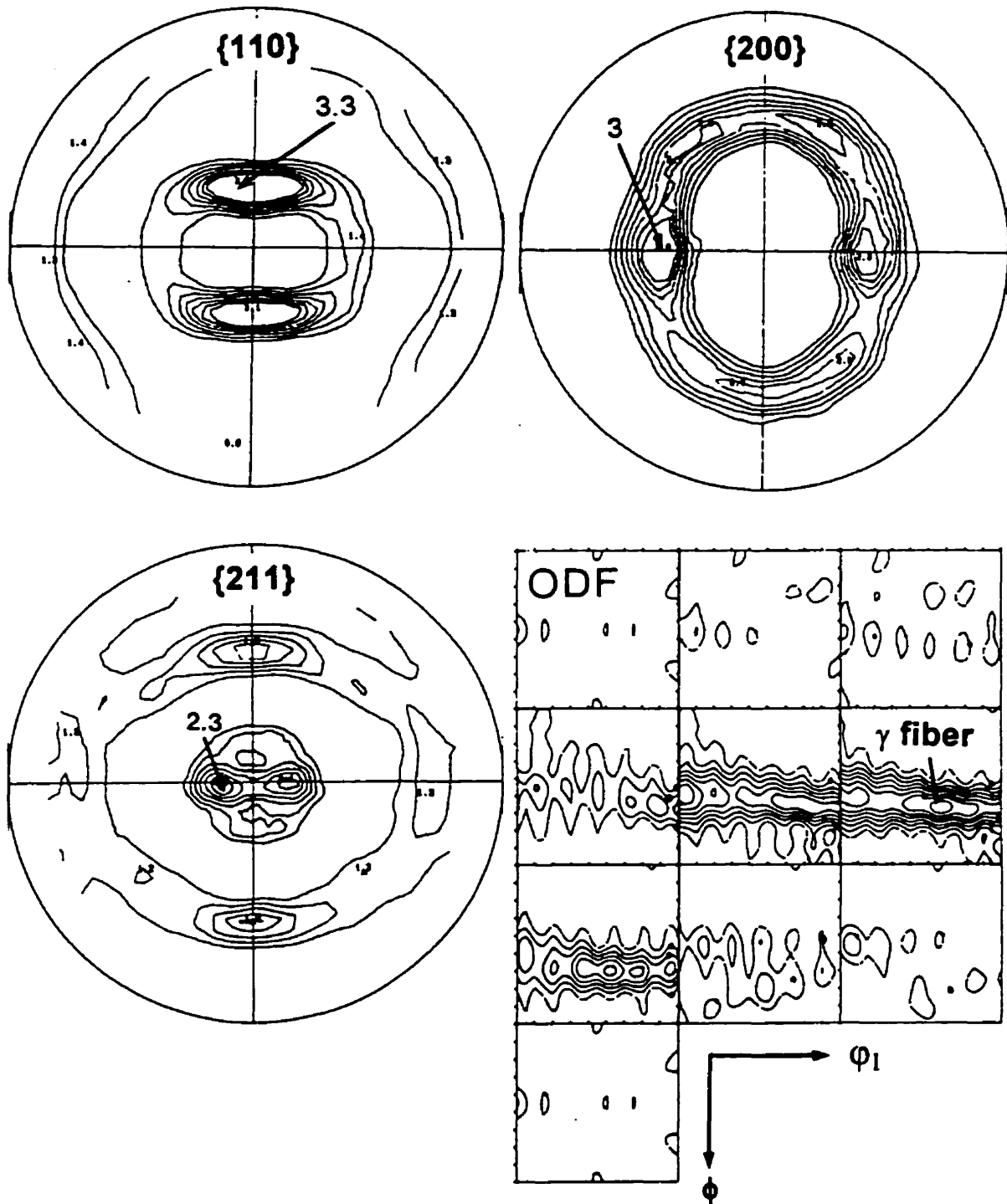


**Figure 4.8.** The pole figures and ODF of steel substrate exhibit typical annealing texture of steel sheet; The poles of  $\{110\}$  plane are tilted about 35 degrees from the center of  $\{110\}$  pole figure.

substrate surface is formed due to the lateral growth mode which is the predominant growth mechanism at low current densities. The formation of basal texture also can be explained by the difference of surface free energy between different crystallographic planes. The  $\{0001\}$  plane of zinc is the close-packed plane, and thus has the lowest surface energy among the other planes. From this point of view, it appears that the  $\{0001\}$  texture can be predominantly formed at low current densities, since zinc ad-atoms have more of a chance to move to the site to decrease the surface energy at low current densities.

The strong basal fiber texture is also found in other zinc coatings, e.g. hot-dip coatings and electrodeposited coatings on amorphous steel substrate [Takechi et. al. 1981]. The formation of the basal texture on various substrate orientations indicates that basal texture is the component which evolves regardless of the substrate orientations and tends to develop preferably at low current densities. At high current densities, on the other hand, the basal components disappear while the pyramidal fiber texture forms (Fig. 4.7c, d). The absence of basal texture implies that coating growth is no longer governed by the lateral growth mode. With increasing current density, the nucleation rate increases and the orientation of grains becomes randomized.

In the  $\{10\bar{1}3\}$  pole figures of coatings deposited at 300 to 500 mA/cm<sup>2</sup>, the poles are widely dispersed (Fig. 4.7b,c,d). Thus, the coatings have the pyramidal component of the  $\{10\bar{1}X\}$  texture with higher indices, i.e.  $X \geq 3$ . This finding is in contrast to the sharp  $\{10\bar{1}3\}$  texture found in the coating deposited at 30 mA/cm<sup>2</sup> (Fig. 4.7a). The formation of  $\{10\bar{1}X\}$  texture is an indication of the weaker substrate influence as well as the higher rate of random nucleation with increasing current densities.

Comparing the observations of texture to the morphology of coatings described in section 4.1 indicates that a correlation is found between the texture and the morphology of coatings. The coatings deposited at low current density have the morphology of hexagonal ridges and platelets (Fig. 4.1a). The ridges are tilted 35 degrees from the substrate surface and aligned towards the rolling direction of the substrate. The texture measurement on the same coatings shows that the basal poles are tilted 35 degrees from the normal direction and aligned towards the rolling direction (Fig. 4.7a). This fact indicates that the morphology of hexagonal ridges represent the  $\{10\bar{1}3\}$  pyramidal texture. It can be suggested that the morphology of hexagonal platelets represent the  $\{0001\}$  basal texture. The coatings deposited at high current density have the morphology of randomly oriented pyramidal grains (Fig. 4.1d) as well as the pyramidal fiber texture (Fig. 4.7c). Thus, the morphology of pyramids represents the pyramidal fiber texture.

#### 4.2.2. INFLUENCE OF PH

The effects of pH on the coating texture were examined. Fig. 4.9 shows the pole figures of zinc coatings electrodeposited at different pH values (1 to 5). Both the  $\{0001\}$  basal texture and the  $\{10\bar{1}X\}$  pyramidal texture are observed in all the coatings. The intensity of texture varies significantly as the pH value changes. The coating deposited at a pH 1 has a strong and sharp  $\{0001\}$  basal fiber texture (Fig. 4.9a). The intensity maxima of the basal pole is 433 times stronger than the random orientation. As the pH value increases through 2 to 3.8, the intensity of basal texture decreases through 357 to 64. No significant change is found in the pyramidal texture component. Further increase in the pH value (pH 5) leads to completely different textural characteristics from those of the lower pH (Fig. 4.9d). In Fig. 4.9d, the  $\{0001\}$  pole figure shows that the intensity of the basal texture drops to 2.4, thereby, the pyramidal  $\{10\bar{1}X\}$  texture becomes a major component. This  $\{10\bar{1}X\}$  texture represents the  $\{10\bar{1}3\}$  poles which have the intensity maxima at 10 degrees from the normal of  $\{10\bar{1}3\}$  pole figure along the transverse direction.

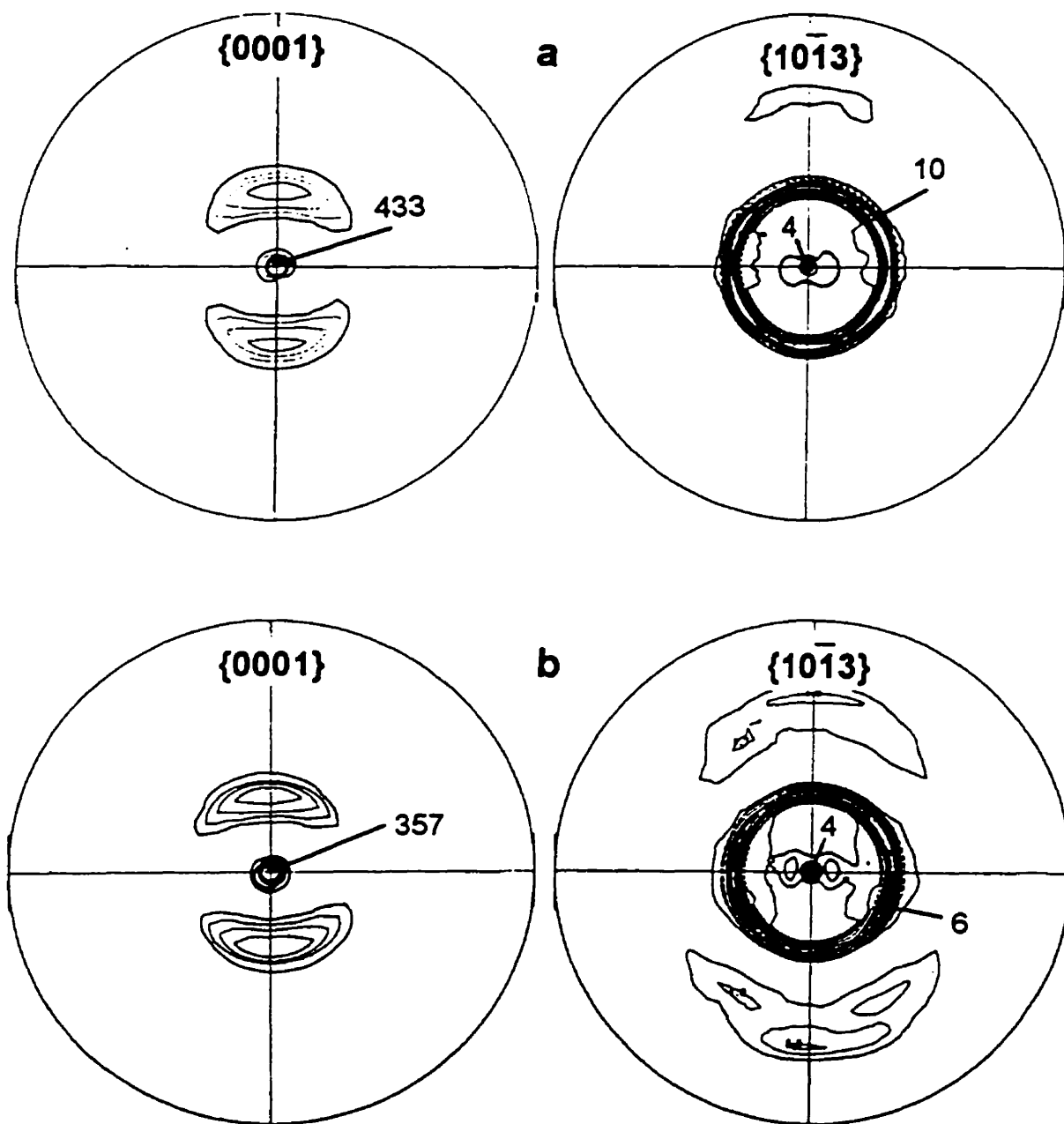


**Figure 4.9.** The pole figures of zinc electrodeposited coatings deposited at different pH value of electrolyte: (a) pH 1, (b) pH 2, (c) pH 3.8, (d) pH 5; The extremely strong basal texture becomes weak, while the pyramidal component becomes predominant as the pH value increases.

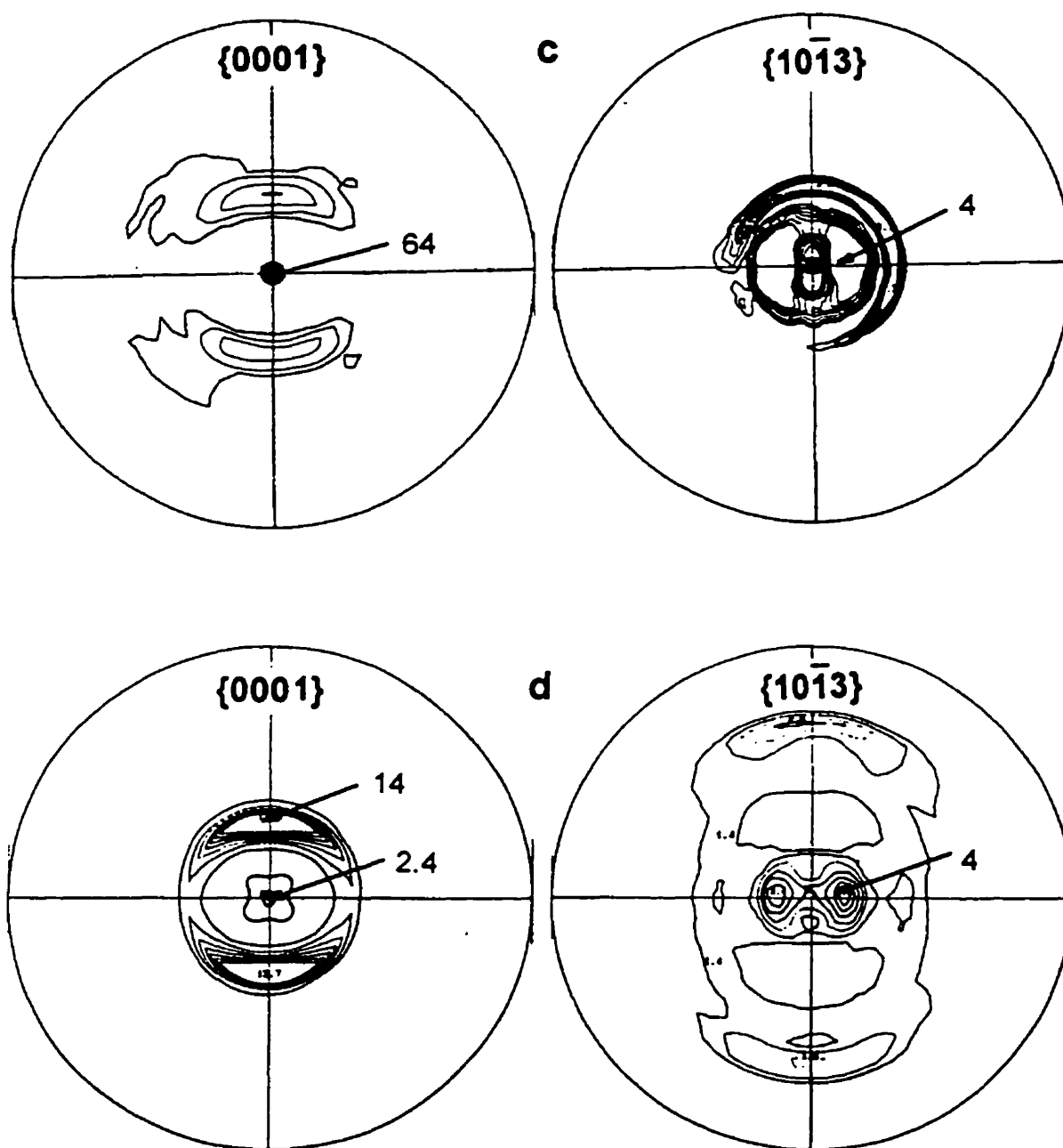
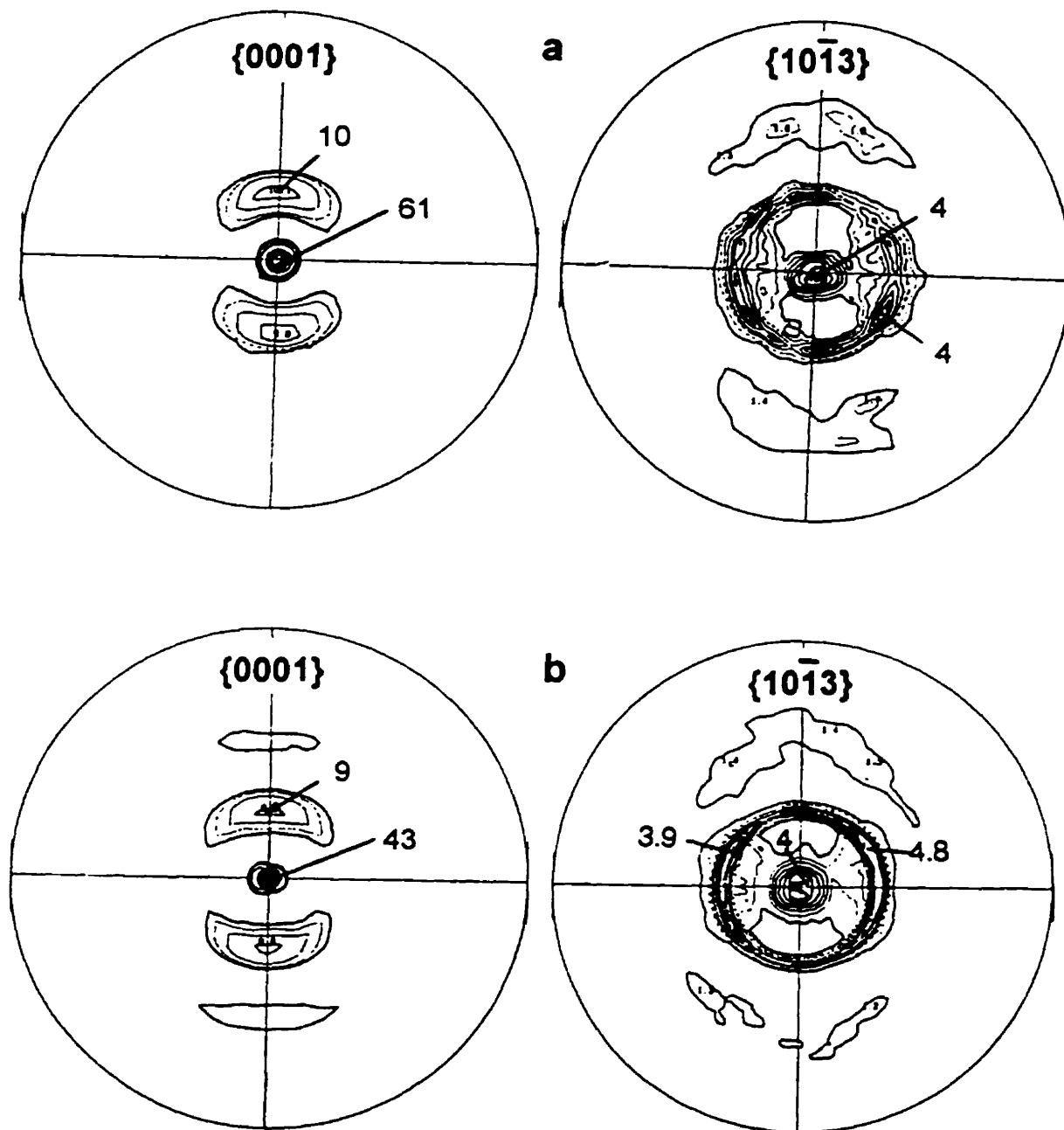


Figure 4.9. Continued.

From the previous observations, it is concluded that the coating texture is sensitive to the pH of the bath. The fact that a strong basal component exists at low pH indicates that the hydrogen absorption capability is different for each of the crystallographic planes. It can be therefore argued that the coatings having a strong basal texture, i.e. the higher density of grains with their basal planes parallel to the substrate surface, have a higher capability of absorbing hydrogen atoms than the pyramidal texture. On the basis of the experimental results, it can be concluded that the basal texture is predominant at low pH value, whereas the pyramidal texture is the main component at higher pH values.

#### 4.2.3. INFLUENCE OF COATING THICKNESS

The influence of coating thickness upon the texture of coatings was examined. The {0001} pole figures in Fig. 4.10 illustrate the characteristics of coating textures at various coating thicknesses. This figure shows that the intensity of texture decreases as the coating thickness increases. Overall, thin coatings have strong, sharp pyramidal non-fiber and basal fiber texture. As the coating thickness increases, the pyramidal texture gradually disappears, while the basal texture becomes widely dispersed. In the case of the thinnest coating of 600 nm in thickness, both textures exhibit the strongest intensity compared to the thicker coatings. The intensity of basal poles, which represents the basal texture, is 61 and that which represents the pyramidal texture is 10 (Fig. 4.10a). As the coating thickness increases to 6  $\mu\text{m}$ , the intensity of both textures slightly decreases; the intensity of the basal component is 43 and that of the pyramidal component is 9 (Fig. 4.10b). The intensity of both textures significantly decreases as the coating thickness increases to 30  $\mu\text{m}$ ; the intensity of the basal component is 3.5 and that of the pyramidal component is 1.8 (Fig. 4.10c). Once the coating thickness grows to 100  $\mu\text{m}$ , the pyramidal component completely disappears. The basal poles are



**Figure 4.10.** The pole figures of zinc electrodeposited coatings deposited at different coating thicknesses: (a) 600 nm, (b) 6  $\mu\text{m}$ , (c) 30  $\mu\text{m}$ , (d) 100  $\mu\text{m}$ ; Both of the texture components become weak and dispersed as the coating thickness increases.

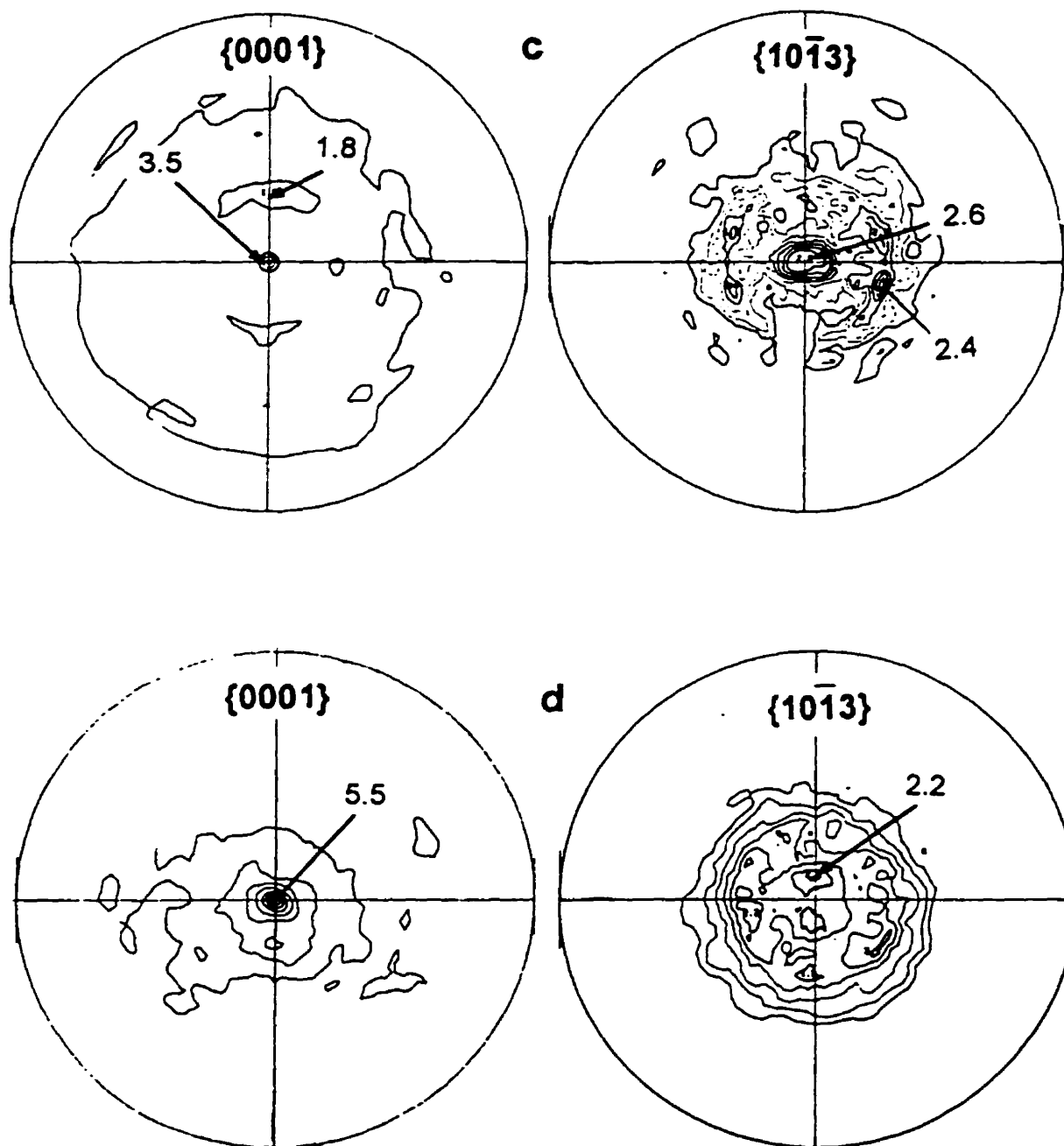


Figure 4.10. Continued.



widely dispersed from the normal direction of  $\{0001\}$  pole figure and the intensity maxima is slightly increased to 5.5 (Fig. 4.10d).

From the above results, it is found that the pyramidal texture disappears as the coating thickness increases. In the previous section of 4.2.1, it was discussed and suggested that the formation of pyramidal non-fiber texture is due to the influence of substrate. Based upon this suggestion, it can be inferred that the strong pyramidal texture for the thin coatings are induced by the influence of substrate. A decrease in pyramidal texture intensity with thickness increase indicates the weaker effect of the substrate.

Unlike the pyramidal texture, the basal component does not disappear in the coating with thicknesses of 100  $\mu\text{m}$  (Fig. 4.10d). This fact indicates that the formation of basal textures is not related to the substrate influence. It appears that the formation of basal textures is attributed to the influence of current densities. This seems true because the coatings were deposited at a low current density (30  $\text{mA}/\text{cm}^2$ ). As was discussed in section 4.1.1, a low current density favors the lateral growth of deposits in which the coatings grow with the basal planes parallel to the substrate surface.

#### 4.2.4. SUMMARY

In this section, it has been demonstrated that the texture of zinc coatings evolves at different current densities, pH and coating thicknesses. A correlation is found between the texture and the morphology of zinc coatings.

1. As the current density increases, the texture evolves from the texture of the basal  $\{0001\}$  fiber component and the pyramidal  $\{10\bar{1}3\}$  non-fiber component to the pyramidal  $\{10\bar{1}X\}$  fiber texture only.

2. As the pH of the electrolyte increases, the texture changes from the strong and sharp basal fiber and the pyramidal non-fiber component to the major pyramidal  $\{10\bar{1}X\}$  texture.
3. As the coating thickness increases, the intensity of both textures decrease. The pyramidal component eventually disappears, while the basal component remains.
4. Correlation is found between the morphology and texture of zinc coatings. The morphology of hexagonal ridges represents the  $\{10\bar{1}3\}$  pyramidal non-fiber texture, while the morphology of hexagonal platelets represents the  $\{0001\}$  basal fiber texture. The morphology of pyramidal grains represents the  $\{10\bar{1}X\}$  pyramidal fiber texture.

## CHAPTER FIVE

### CHARACTERISTICS OF ZINC ALLOY COATINGS

#### 5.1. SURFACE MORPHOLOGY AT THE EARLY STAGE OF DEPOSITION

This section demonstrates the evolution of coating morphology at the early stage of deposition. Under normal deposition conditions, it is difficult to observe the initial stage of coating growth because the applied current density and deposition time are too high and long to observe the thin layer of initial deposit. In the present work, zinc-iron electrodeposition was conducted at very low current density and short deposition time.

Detailed observations of the evolution of surface morphology were performed by AFM. This analysis was concentrated on the very early stages of deposition at low current density. Examples of the surface morphology of coatings obtained at  $7 \text{ mA/cm}^2$  are shown in Fig. 5.1. After 30 sec of deposition, the coating surface has evolved to the morphology of “fish scale-like” platelets (Fig. 5.1a). The AFM section analysis shows that the platelets are slightly tilted about 1 to 3 degrees from the substrate surface (Fig. 5.1b). The size of the platelet is 50 to 70 nm in width and 10 nm in height.

The coating obtained from the deposition time of 90 seconds exhibits the morphology of sub-micron sized grains (Fig. 5.1c). Detailed coating morphology is shown in Fig. 5.1d. The average size of the subgrain is about 350 nm in width and about 100 nm in height. As the coating grows further with a deposition time of 300 sec, the coating evolves to the morphology of pyramidal grains (Fig. 5.1e). An additional increase in deposition time to 1800 sec leads to the morphology of well-

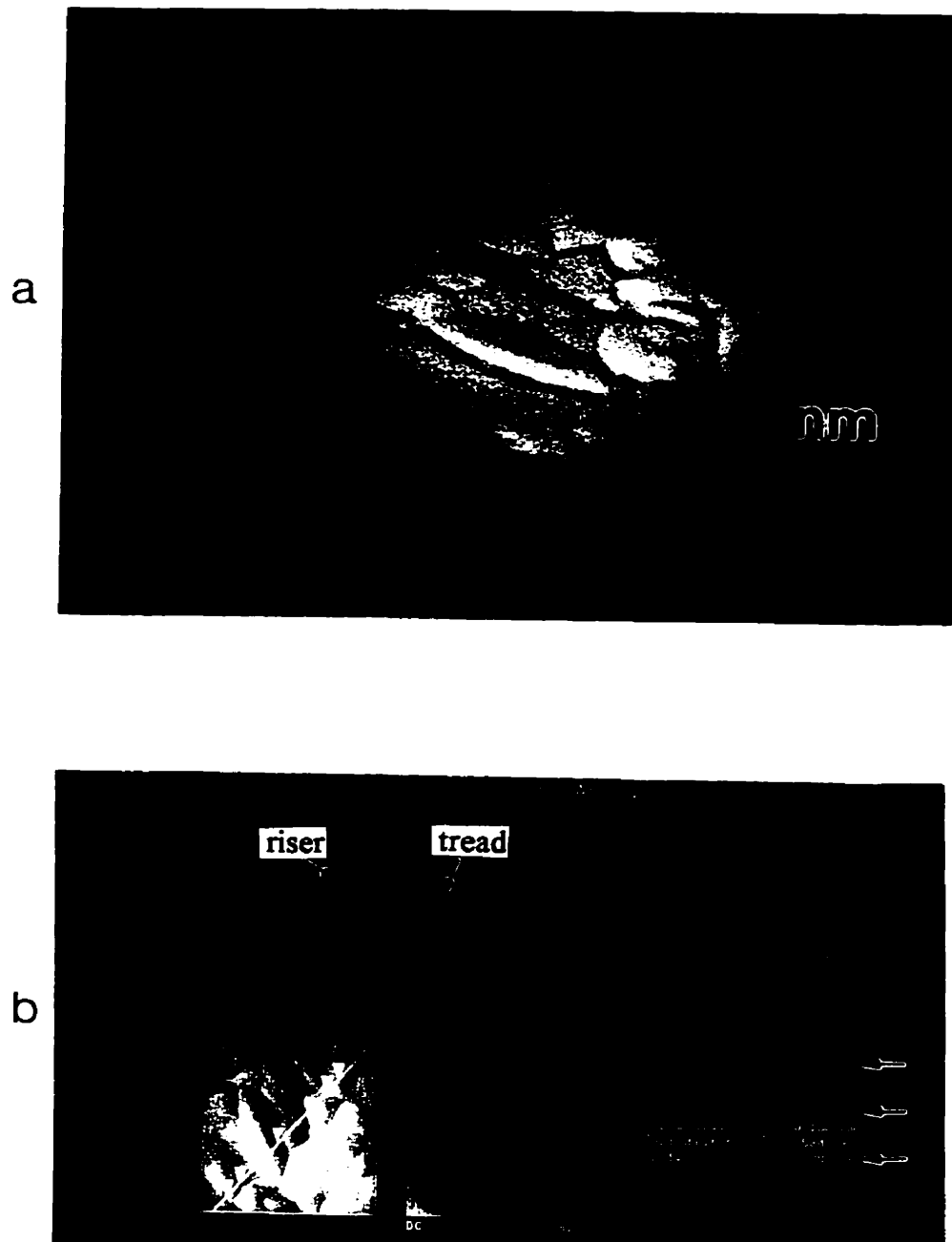
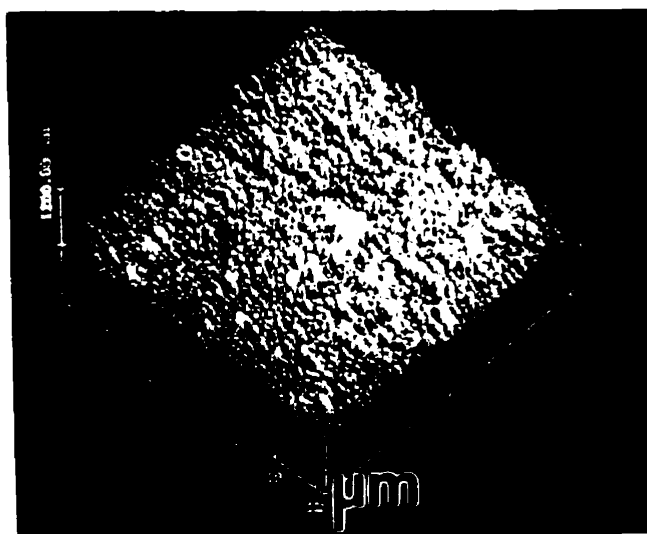
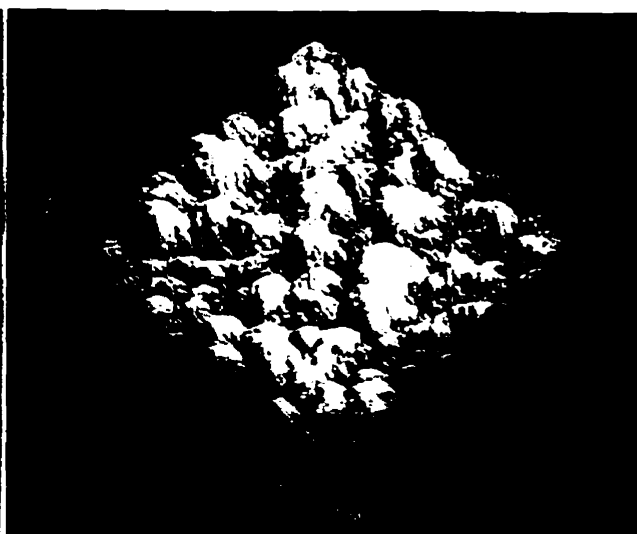


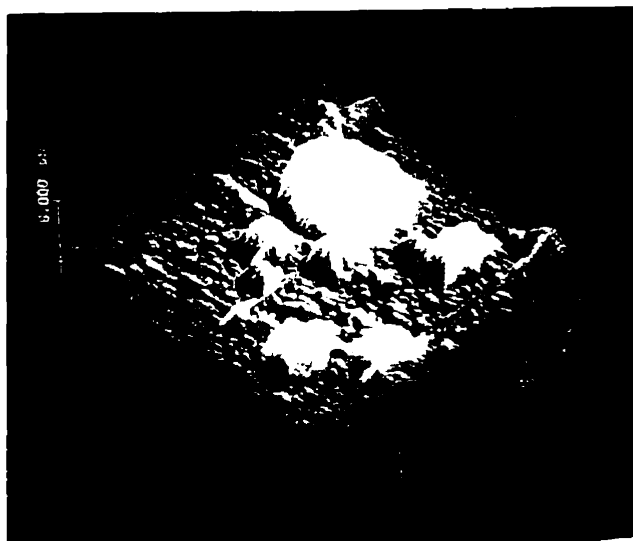
**Figure 5.1.** The AFM morphology and section profile analysis show the evolution of deposit with coating time: (a) the initial morphology of deposits in the form of “fish scale-like” platelets slightly tilted from substrate surface (coating time-30 sec), (b) the section analysis exhibits that the platelets are tilted about 1~3 degrees (arrow marked) from substrate surface, (c) the growing surface is covered by a number of particles (c.t.-90 sec), (d) detailed morphology of particles in (c), (e) formation of pyramidal grains (c.t.-300 sec), and (f) well developed morphology of pyramidal grains (c.t.-1800 sec).



c



d



e



f

Figure 5.1. Continued

developed pyramidal grains. The average size of the pyramidal grain is about 1 to 3  $\mu\text{m}$  (Fig. 5.1f).

Although the AFM image can provide more detail of the three-dimensional surface morphology, there are some artifacts which can be misinterpreted as a real image. The image of pyramids, for instance, sometimes may be produced not from the real morphology but from the artifact of the tip shape of the cantilever. To ensure that the AFM images represent the real coating morphology, the same specimens were examined using SEM. The AFM images are compared to the SEM images as is shown in Fig. 5.2. The morphology of the subgrains and the pyramidal grains in SEM is consistent with that of the AFM. The size and the shape of morphological features are in good agreement with each other.

From the above observation, the initial stage of deposition is characterized by the morphological evolution of “fish scale-like” platelets. This suggests that the morphology of the “fish scale-like” platelets represents the  $\eta$  phase of zinc with their basal plane parallel to the platelet surface. This is because the planar view shows that the platelet has a hexagonal shape (Fig. 5.1b). There is another indication that the platelets represent the basal plane parallel to the platelet surface. These platelets are formed on the same substrate grain orientation. The steel substrate has a large grain of about 5 to 10  $\mu\text{m}$ . which have often the  $\{110\}$  plane parallel to the substrate. Since the  $\{0001\}$  planes of  $\eta$  phase grow epitaxially on the  $\{110\}$  plane of steel substrate, it is suggested that the “fish scale-like” platelets which represent basal plane are epitaxially formed on the  $\{110\}$  steel substrate .

It is a characteristic that the “fish scale-like” platelets in Fig. 5.1a show the morphology of terraced-growth. The AFM section profile indicates that the

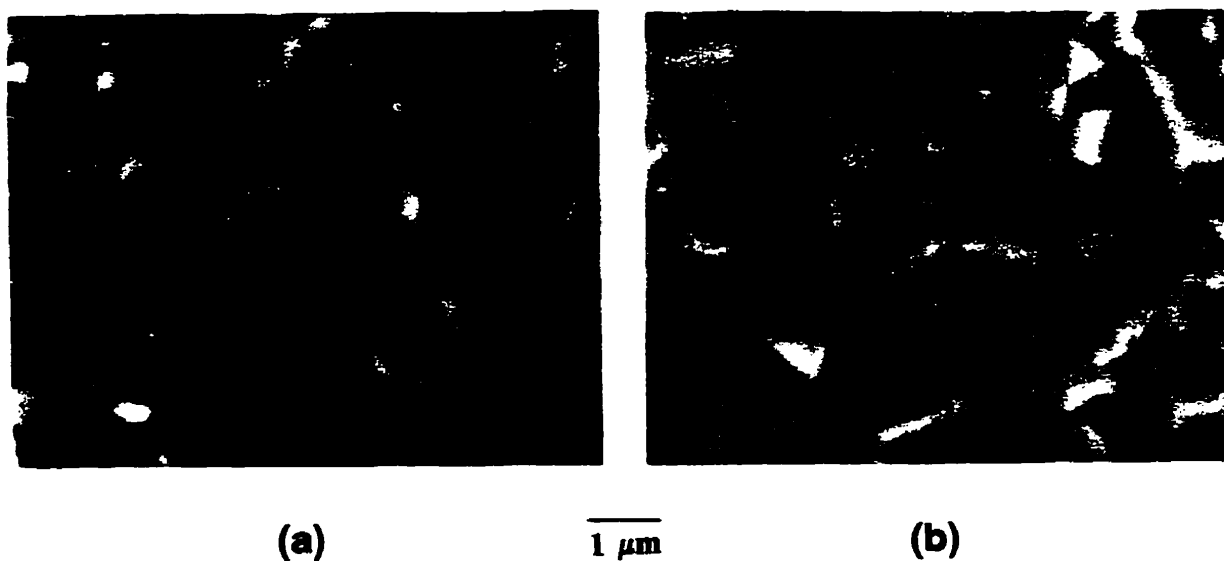


Figure 5.2. The SEM images show (a) the particle formation, (b) the pyramidal grains in the evolution of coating morphology.

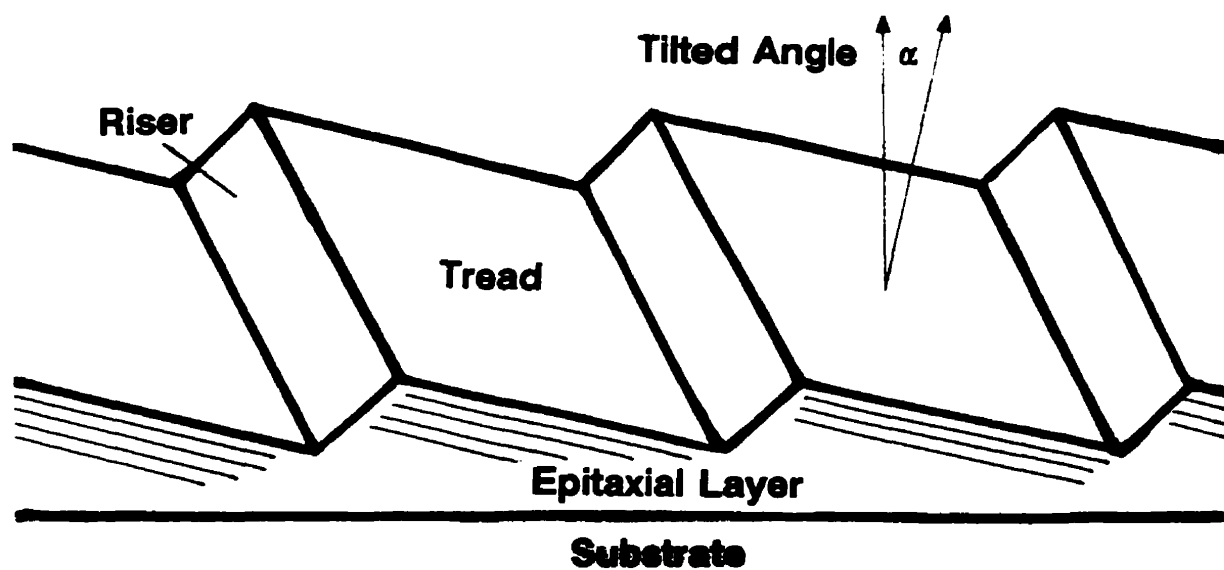


Figure 5.3. Schematic illustration of the terraced growth; The platelets of the terraces are slightly tilted with respect to the substrate surface by angle  $\alpha$ . The morphology is characterized by periodic tread and riser surfaces.

platelets are formed with a slight misoriented angle from the substrate surface (Fig. 5.1b). The morphology is characterized by the treads (flat area facets) and the risers which are marked in Fig. 5.1a. Schematic illustration of the terraced-growth at the early stage of deposition is shown in Fig. 5.3, where the treads are slightly tilted from substrate surface by an angle of  $\alpha$ . It should be noted that the morphology of "fish scale-like platelets is similar to the terraced-growth morphology of AlGaAs epitaxial layers grown by chemical vapor deposition [Johnson and Legg 1988]. In terraced-growth morphology, the deposit grows by the development of clustered multiples of monatomic ledges. The terraced-growth morphology is not known to the commercial electrodeposited zinc based coatings, but is commonly observed in the epitaxial layer of CVD coatings. The observation of the terraced-growth morphology in electrodeposit suggests that the epitaxial growth is predominant at the early stage of deposition as it is the case in CVD coatings.

#### SUMMARY

The evolution of surface morphology during the early stages of electrodeposition was observed in detail by AFM. Initially, the substrate surface shows the morphology of "fish scale-like" platelets. As the growth continues, the growing morphology evolves to the well-developed triangular-based pyramidal grains.

#### 5.2. SURFACE MORPHOLOGY OF ZINC ALLOY COATINGS

Zinc alloy coatings have various morphological characteristics which are strongly dependent upon alloy content of the deposits. The alloy content of the coatings is controlled by the electrolyte composition. Other deposition parameters can also influence the alloy composition of the coatings. Current density, for instance, is directly responsible for the anomalous codeposition behavior which



results in different alloy content in the deposit. It is important, therefore, to characterize the coating morphology of zinc alloy coatings at various deposition conditions. This section describes the morphological evolution of zinc-iron and zinc-nickel coating mainly at different current densities. The influence of current density upon coating morphology and alloy composition is discussed.

#### 5.2.1. INFLUENCE OF CURRENT DENSITY (ZINC-IRON COATINGS)

The zinc-iron coatings were electrodeposited at different current densities ranging from 50 to 500 mA/cm<sup>2</sup>. The pH of the electrolyte was kept around 3.8 and the bath temperature was kept at 50 °C. The electrodeposition time was adjusted to produce coatings with a thickness of 5 μm. The morphology of coatings significantly changes with the change of applied current density as is shown in Fig. 5.4. The coating deposited at a current density of 50 mA/cm<sup>2</sup> exhibits the morphology of hexagonal platelets and ridges (Fig. 5.4a). The hexagonal platelets are randomly distributed, while the ridges are aligned parallel to the rolling direction of the steel substrate (arrow marked in Fig. 5.4a). The average size of the hexagonal platelets is 3 to 6 μm. This morphology of hexagonal platelets and ridges is similar to the morphology of zinc coatings deposited at a low current density range previously described in Fig. 4.1a, b. As the applied current density increases, the hexagonal platelets and ridges gradually disappear while the pyramidal morphology becomes predominant. Fig. 5.4b shows that the coating deposited at 100 mA/cm<sup>2</sup> exhibits a mixed morphology of hexagonal ridges and pyramidal grains. These pyramidal grains are about 1 μm in size, and evolve from the boundaries between the ridges as indicated by the arrows in Fig. 5.4b. As the applied current density increases to 200 mA/cm<sup>2</sup>, the coating surface is completely covered with fine pyramidal grains and no hexagonal platelets or ridges are found (Fig. 5.4c). The pyramidal grains continue to grow as the current density increases to 300 mA/cm<sup>2</sup> (Fig. 5.4d). Fig. 5.4d shows well-developed triangular-based pyramids about the size of 1 to 3 μm. The pyramidal grains are randomly

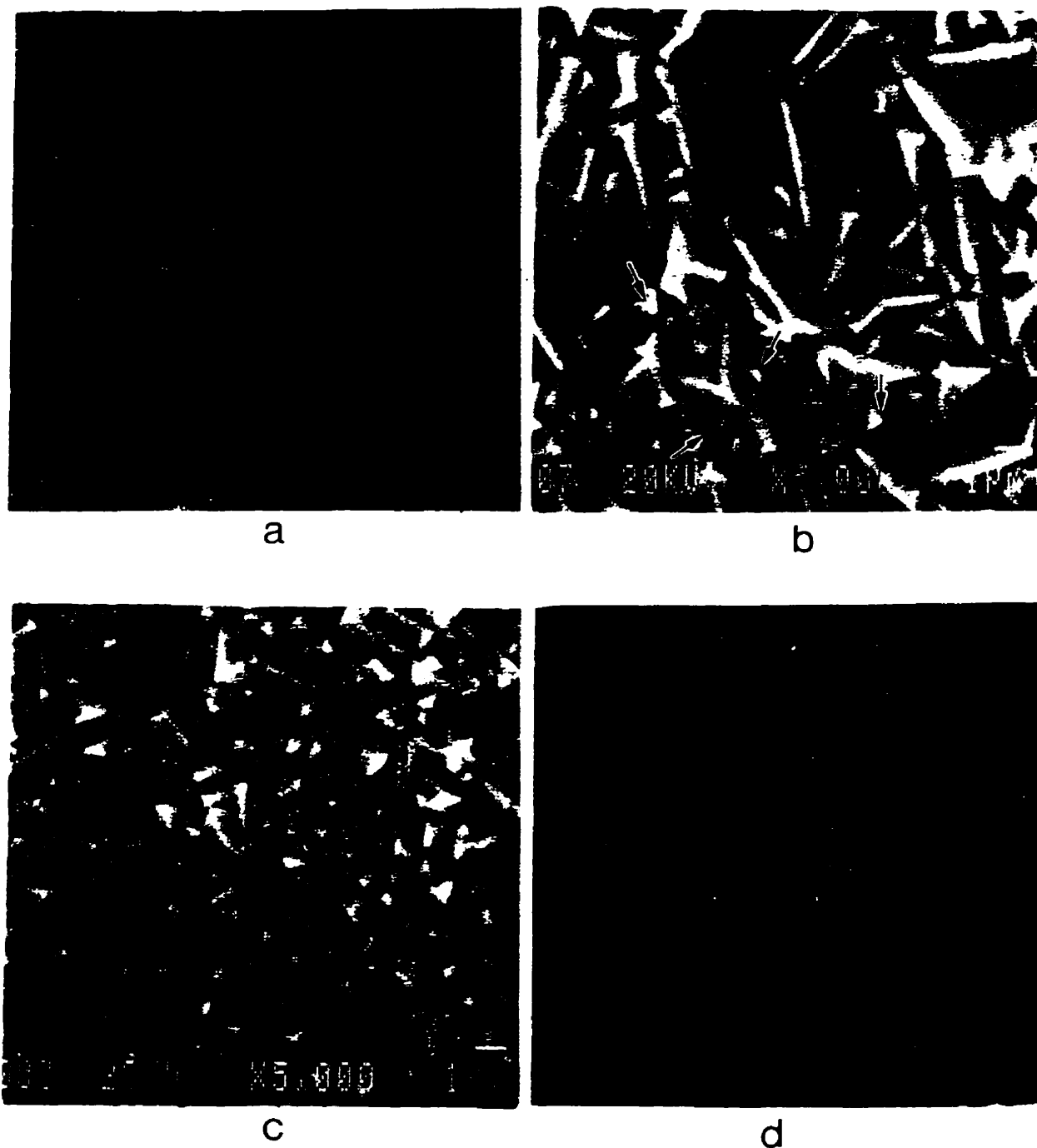


**Figure 5.4.** The SEM images exhibit morphological evolution of zinc-iron electrodeposited coatings at different current density: (a) 50, (b) 100, (c) 200, (d) 300 mA/cm<sup>2</sup>; The morphology of coatings continuously changes from hexagonal platelets and ridges to triangular pyramids with current density increase.

distributed over the surface. Further increase in current density up to  $500 \text{ mA/cm}^2$  does not change the morphology of the triangular-based pyramids.

Detailed observations of surface morphology were carried out by AFM. An example of the triangular-based pyramid morphology obtained at  $500 \text{ mA/cm}^2$  is shown in Fig. 5.5. The AFM images show that each of the triangular-based pyramidal grains represent part of the hexagonal columnar crystal which is tilted from the substrate surface. A good agreement is found with the results of the AFM section profile analysis. The section analysis was conducted along the two  $\{10\bar{1}0\}$  prismatic planes. The profile analysis shows that the angle between each  $\{10\bar{1}0\}$  plane is about 120 degrees which corresponds to the hexagonal geometry. Therefore, it is evident that the morphology of triangular-based pyramids represents a part of the hexagonal columnar crystal which consists of one  $\{0001\}$  plane and two  $\{10\bar{1}0\}$  planes.

The EPMA (Electron Probe Micro Analysis) was conducted on the zinc-iron coatings deposited at various current densities. It is found from the EPMA results that the iron content in the deposit changes as the applied current density changes (Fig. 5.6). As the current density increases from 50 to  $300 \text{ mA/cm}^2$ , the percentage of iron in the zinc-iron coatings increases from 1.8 to 9.8. A further increase in the current density up to  $500 \text{ mA/cm}^2$  causes a slight increase in the percentage of iron to 10.5.

From the above result, it is found that the coating morphology changes from hexagonal platelets and ridges to triangular-based pyramidal grains, while the iron content in the deposit increases with increasing current density. Therefore, the comparison of coating morphology and alloy composition indicates that changing the current density is responsible not only for the evolution of coating morphology but also for the change of alloy composition in the deposit.

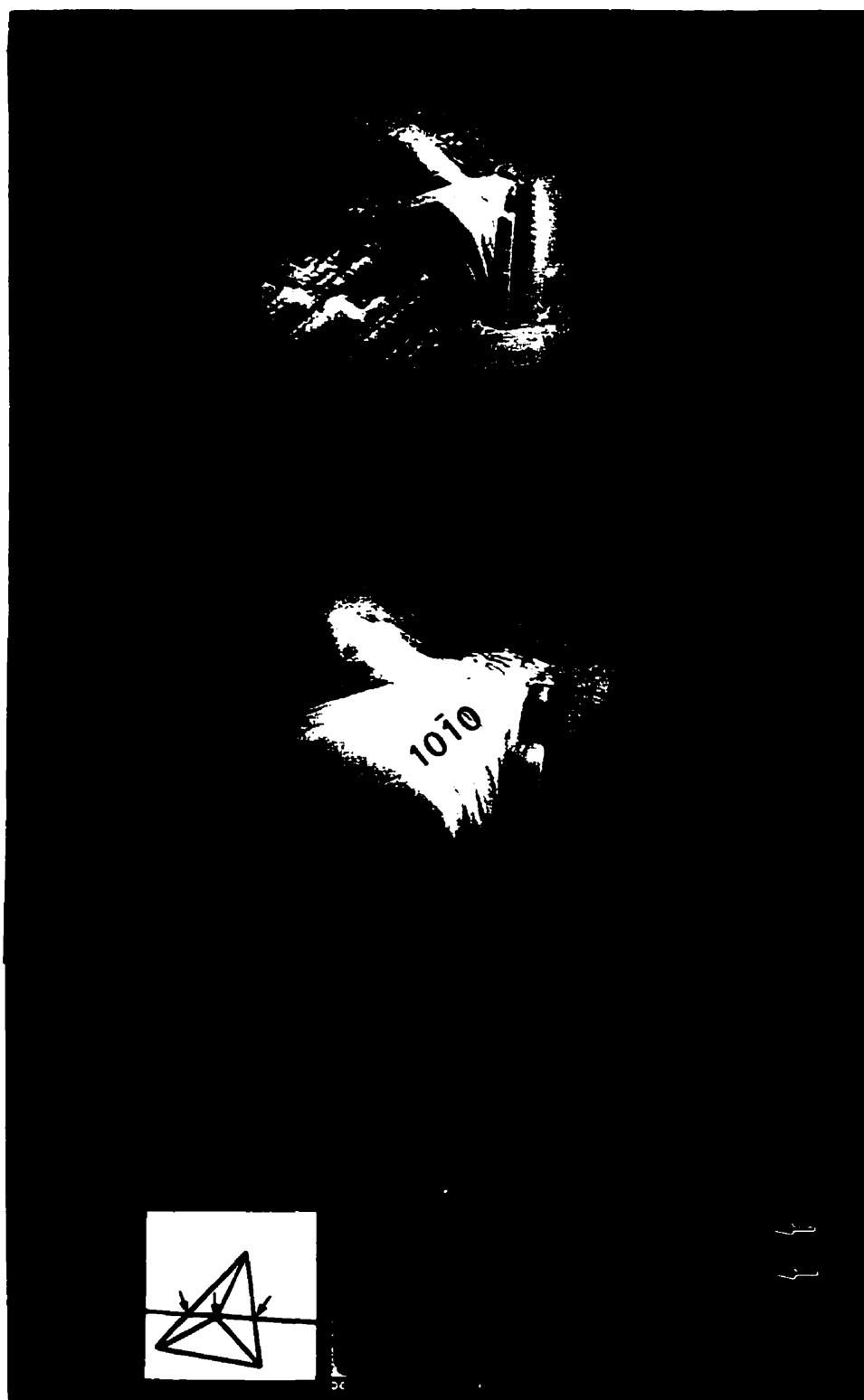


**Figure 5.5.** The AFM morphology and section profile analysis of triangular pyramidal morphology of zinc-iron electrodeposited coatings; The pyramid represents part of a hexagonal columnar crystal tilted from the substrate surface. Thus, one wall represents  $\{0001\}$  plane while the other two walls represent  $\{10\bar{1}0\}$  planes. The section analysis exhibits the angle between each  $\{10\bar{1}0\}$  plane is about 120 deg. which corresponds to the hexagonal geometry.

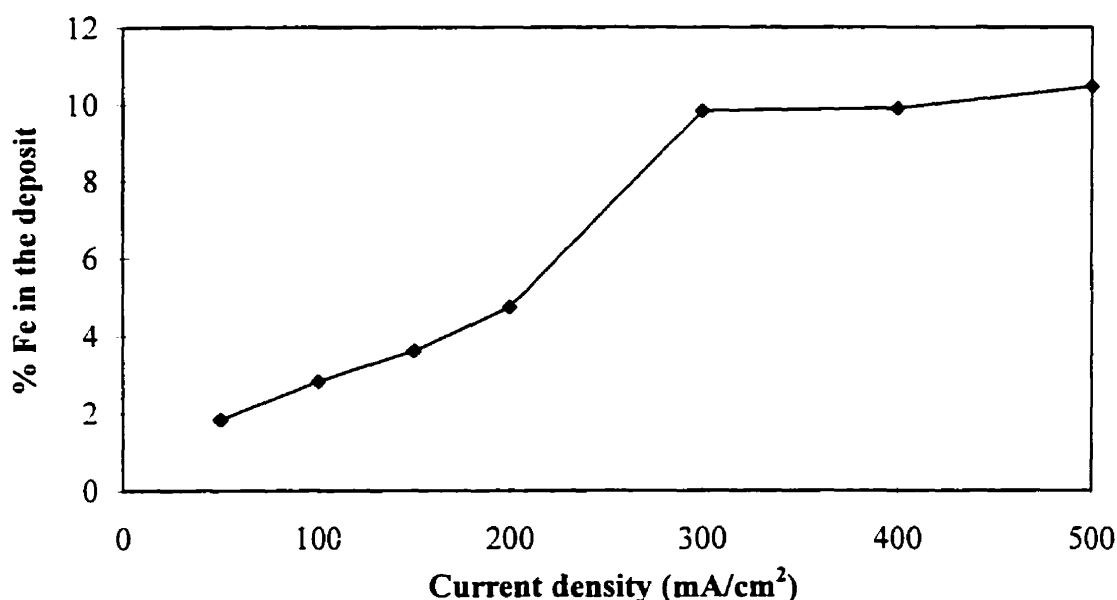


**Figure 5.6. The change of iron content in the zinc-iron electrodeposited coatings at various current densities.**

At a low current density range, the effect of increasing current density on the electrodeposition of alloys causes a decrease in the content of the more noble metal in the deposit as is reviewed previously in section 2.5. This type of codeposition behavior, however, does not correspond to the experimental results. The present results show that the percentage of more noble metal (iron) in the deposit increases as the current density increases from 50 to 500 mA/cm<sup>2</sup>. It should be noted that the operating current density range of the experiment is higher than the current density range (less than 50 mA/cm<sup>2</sup>) which shows a decrease in more noble metal with current density increase. Thus, the anomalous codeposition behavior of zinc-iron coatings can be attributed to the high depletion of zinc ion concentration in the cathode diffusion layer at high current density range. At high applied current density, the zinc ion will be deposited preferentially at the initial state and subsequently, the electrolyte near the cathode surface is depleted of zinc ions. Since the metal deposition occurs only at the interface between the cathode and the electrolyte, where the migration of zinc ion is under diffusion control, the zinc

content in the deposit should decrease as a consequence. Moreover, high current densities promote an increase of hydrogen evolution which results in a lack of agitation which subsequently develops the zinc depletion layer.

It is concluded from the observations that the iron content in the zinc-iron coatings increases with the applied current density increase due to their anomalous codeposition behavior. Other studies which are in good agreement with the present work of anomalous codeposition are reviewed in section 2.5.

#### 5.2.2. INFLUENCE OF COATING THICKNESS (ZINC-IRON COATINGS)

The zinc-iron coatings were electrodeposited with different deposition times to produce coating thicknesses of 1, 5, 10, 30, and 100  $\mu\text{m}$ . The current density was kept constant at 300  $\text{mA}/\text{cm}^2$ . Fig. 5.7 exhibits the morphology of coatings at different coating thicknesses. At a thickness of 5  $\mu\text{m}$ , the coating shows typical triangular pyramidal grains which have already been described in the previous section of 5.2.1. As the coating thickness increases to 10  $\mu\text{m}$ , the surface morphology is dominated by large pyramidal grains with a size of 3 to 4  $\mu\text{m}$ . Further increase in coating thickness to 30  $\mu\text{m}$  causes morphological transformation to the randomly oriented hexagonal ridges (Fig. 5.7c). Eventually, hexagonal columnar crystals evolve when the coating thickness reaches 100  $\mu\text{m}$  as is shown in Fig. 5.7d. The coating deposited at the higher current density of 500  $\text{mA}/\text{cm}^2$  has a completely different morphology. Fig. 5.8 shows an example of the morphology of large hexagonal ridges in the coatings of thickness 100  $\mu\text{m}$ . The current density is usually associated with the change in alloy composition. The EPMA analysis indicates that the alloy composition of coatings changes as the coating thickness changes (Fig. 5.9). In the case of the coatings deposited at 300  $\text{mA}/\text{cm}^2$ , as the coating thickness increases from 1 to 100  $\mu\text{m}$ , the percentage of iron in the zinc-iron coating significantly decreases from 10.2 to 0.6. Thus, it is concluded

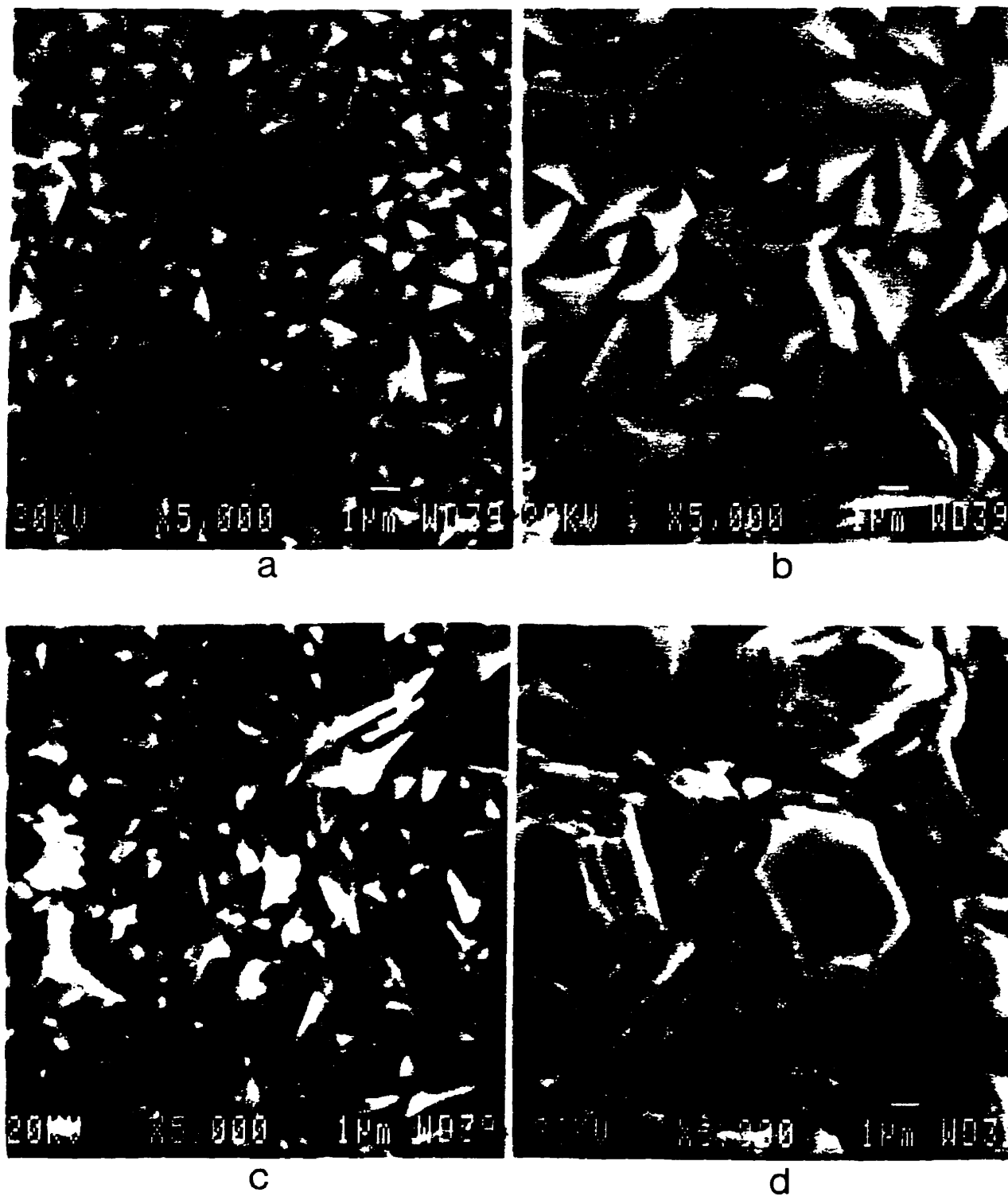


**Figure 5.7.** The SEM images exhibit morphological evolution of zinc-iron electrodeposited coatings at different coating thickness (current density at  $300\text{mA}/\text{cm}^2$ ): (a)  $5\mu\text{m}$ , (b)  $10\mu\text{m}$ , (c)  $30\mu\text{m}$ , (d)  $100\mu\text{m}$ .



Figure 5.8. The SEM image of zinc-iron electrodeposited coating with a coating thickness of 100  $\mu\text{m}$ , deposited at 500mA/cm<sup>2</sup>.

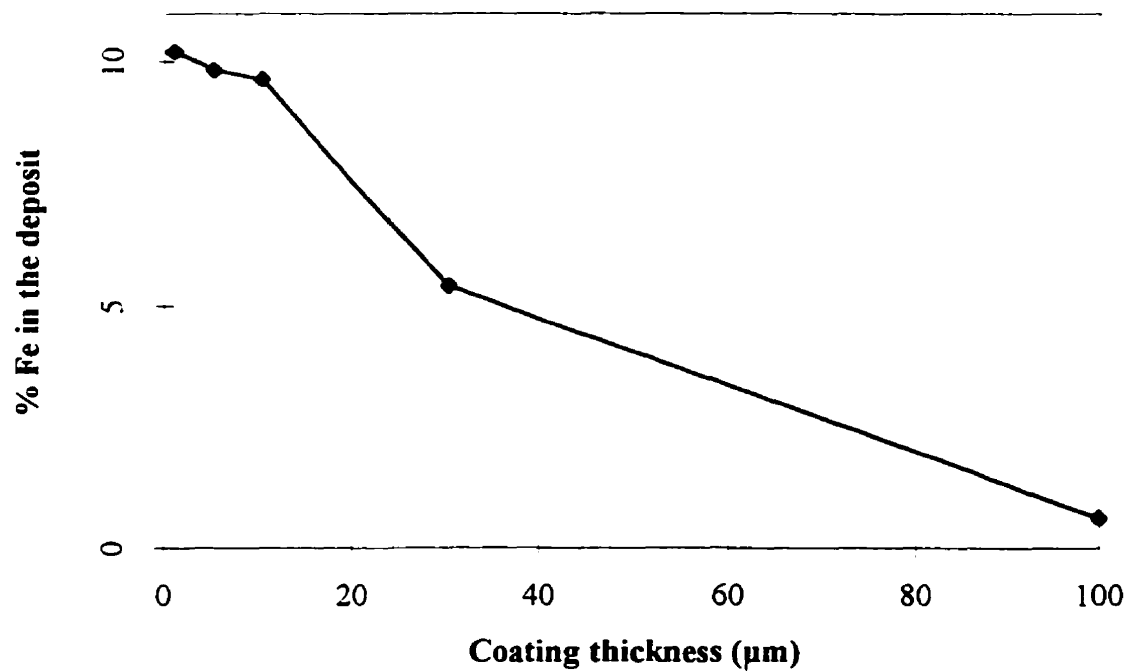


Figure 5.9. Correlation between coating thickness and percent of iron in the zinc-iron electrodeposited coatings.



that the observed changes in morphology are related to changes in the deposit thickness and the alloy composition.

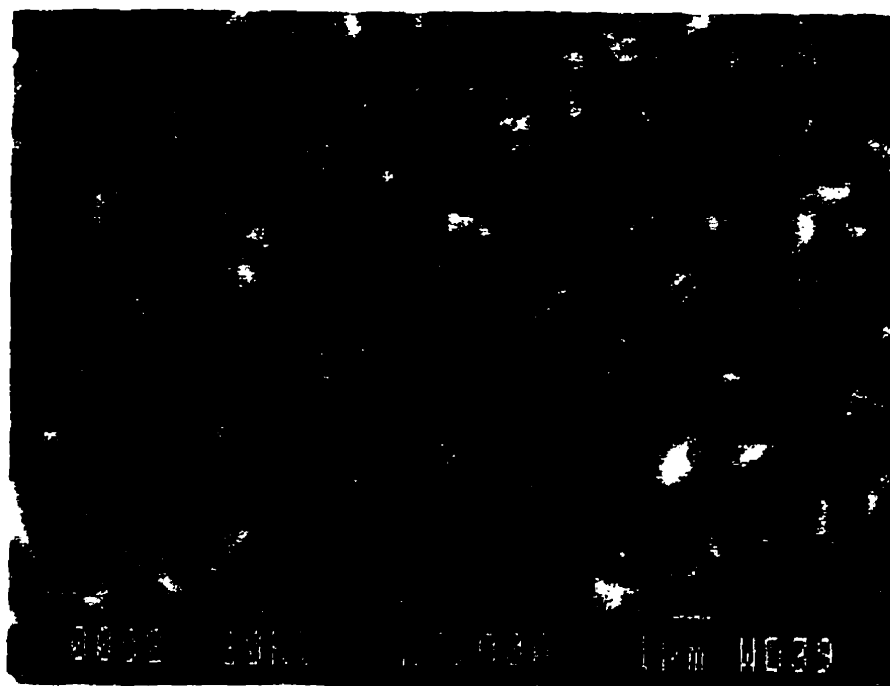
### 5.2.3. INFLUENCE OF CURRENT DENSITY (ZINC-NICKEL COATINGS)

This section describes the influence of current density upon coating morphology of zinc-nickel coatings. The zinc-nickel coatings were electrodeposited under different current densities ranging from 50 to 1200 mA/cm<sup>2</sup>. The pH of the electrolyte was kept at about 2.3. The electrodeposition time was adjusted to produce a coating with a thickness of 15 µm. Fig. 5.10 shows different coating morphologies produced at different current densities. The coating deposited at 50 mA/cm<sup>2</sup> shows the morphology of pyramids in Fig. 5.10a. As the deposition current density increases to 200 mA/cm<sup>2</sup>, the coating morphology transforms to the nodular pyramidal grains (Fig. 5.10b). The size of the grains is about 1 to 2 µm. Additional increases of current density up to 500 mA/cm<sup>2</sup> does not cause any significant morphological change (Fig. 5.10c). Eventually, further increase in current density to 1200 mA/cm<sup>2</sup> results in a completely different coating morphology. The coating surface is covered by a number of submicron sized grains conglomerated together to form the “cauliflower-like” structure (Fig. 5.10d).

The AFM observation for detailed surface morphology is demonstrated in Fig. 5.11. A good agreement is found between the morphological observations of AFM and SEM. Fig. 5.11a exhibits the coating morphology of nodular pyramidal grains obtained at 200 mA/cm<sup>2</sup>. The morphology of pyramidal grains represents the η phase of zinc-nickel coatings. The coating obtained at 50 mA/cm<sup>2</sup> has the morphology of pyramids combined with sub-grains (Fig. 5.11b). It is a characteristic that the pyramids are surrounded by the sub-micron sized grains which are too small to be identified by SEM observation.



a



b

**Figure 5.10. The SEM images exhibit morphological evolution of zinc-nickel electrodeposited coatings at different current density: (a) 50, (b) 200, (c) 500, (d) 1200 mA/cm<sup>2</sup>.**

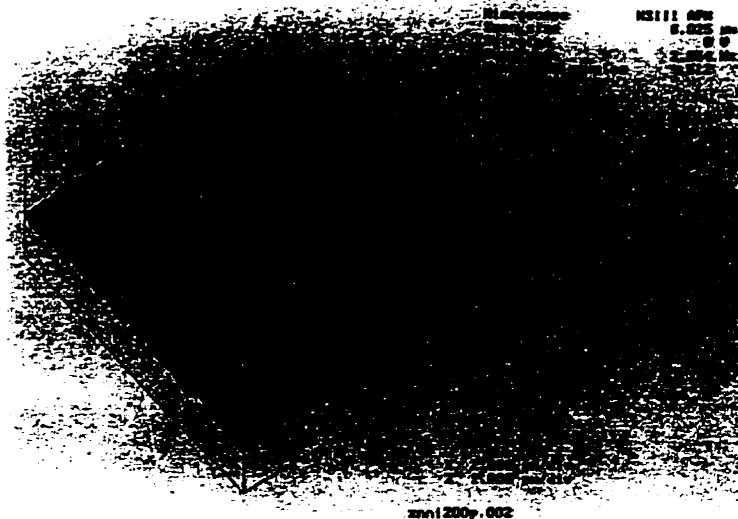


c



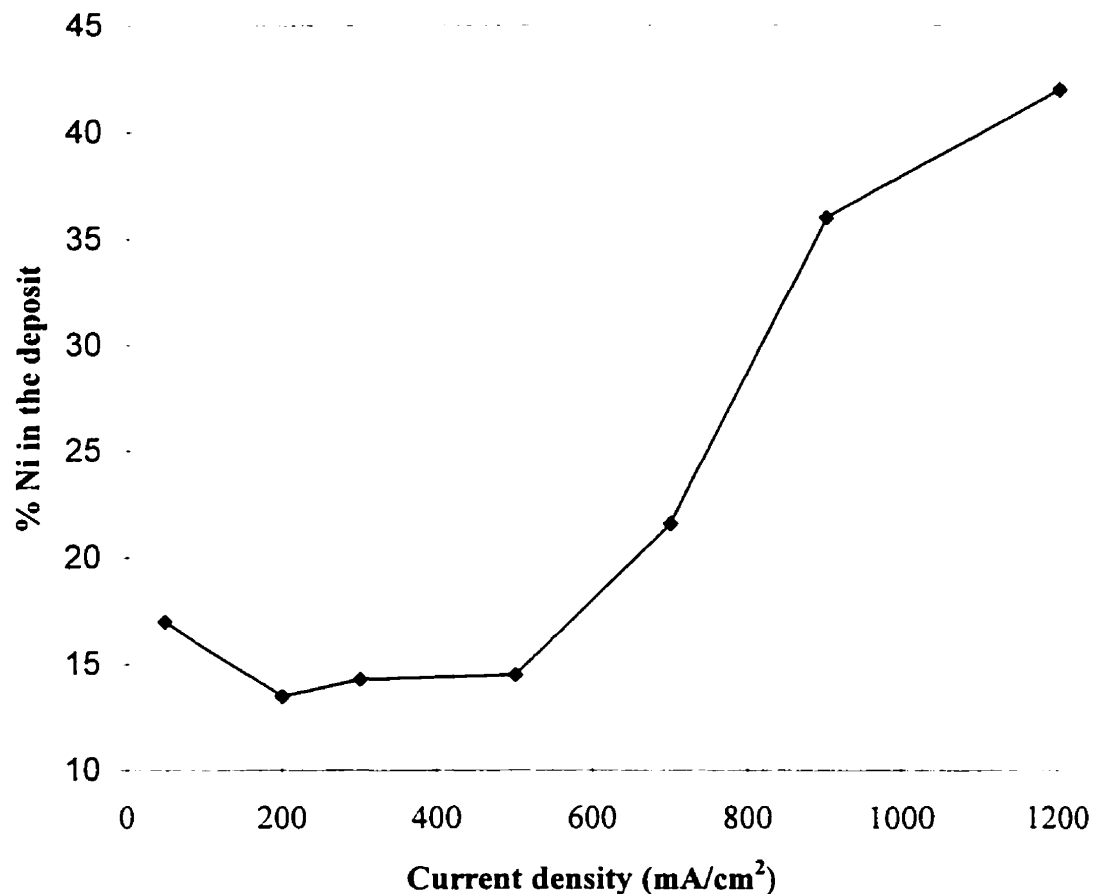
d

Figure 5.10. Continued.

**a****b**

**Figure 5.11.** The AFM morphology of zinc-nickel electrodeposited coatings at different deposition current density: (a) pyramidal grains at 200 mA/cm<sup>2</sup>, (b) mixed morphology of triangular pyramids and tiny particles at 50 mA/cm<sup>2</sup>.

Nickel percent was measured in the zinc-nickel coatings deposited at various current densities. As is the case in zinc-iron coatings, the nickel content of zinc-nickel coatings significantly changes as the deposition current density changes (Fig. 5.12). The EPMA analysis indicates that the coatings deposited at the current density of  $50 \text{ mA/cm}^2$  have about 17 % of Ni in the deposit. As the current density increases to the range of 200 to  $500 \text{ mA/cm}^2$ , the nickel content in the deposit drops to 13 to 15 %. Further increase of the current density up to  $1200 \text{ mA/cm}^2$  results in a dramatic increase of nickel content up to 42 %.



**Figure 5.12. Correlation between current density and percent of nickel in the zinc-nickel electrodeposited coatings.**

## 5.2.4. SUMMARY

The morphological evolution of zinc-iron and zinc-nickel coatings is described. A correlation is found between the coating morphology and the deposition current density.

1. The morphology and alloy composition of the zinc-iron coatings varies with current density. As the current density increases, the coating morphology changes from the hexagonal platelets and ridges to the triangular pyramidal grains, while the iron content in the deposit increases.
2. The morphology of triangular pyramids represents a hexagonal columnar crystal tilted from the substrate surface. Thus, one wall of the pyramid represents the  $\{0001\}$  basal plane while the other two walls represent the  $\{10\bar{1}0\}$  prismatic planes.
3. The morphology and alloy composition of the zinc-iron coatings vary with coating thickness. As the coating thickness increases, the coating morphology changes from the triangular pyramidal grains, to the randomly oriented hexagonal ridges and then to the hexagonal columnar crystals, while the iron content in the deposit decreases.
4. The morphology of zinc-nickel coatings changes from the pyramidal grains and tiny particles, to the pyramidal grains, then to the conglomerated subgrains of the “cauliflower-like” structure, whereas the nickel content in the deposit initially drops from 17 % to 13 %, and then increases up to 42 % with increasing current density from 50 to 1200 mA/cm<sup>2</sup>.

### 5.3. INTERPLANAR SPACINGS AND MICROSTRESS OF COATINGS

In section 5.2, it was shown that the current density influences the characteristics of coating morphology and alloy composition in the deposit. The changes in alloy composition were attributed to the anomalous codeposition behavior caused by the current density. The alloy composition in the deposit determines the phase composition of the coatings, which is one of the important factors in characterizing the coating properties. Even without the major phase transformation, the crystallographic structure of coatings can be influenced by changing the alloy composition in the deposit. Several works reported the change of alloy composition of zinc based coatings using different bath composition, as is reviewed in chapter 2. However, there is a lack of knowledge on crystallographic structure at different current densities. This section describes the change of parameters characterizing the crystallographic structure, showing for instance, interplanar spacings,  $c/a$  ratio, and also phase composition of the zinc alloy coatings produced at different current densities. In addition, the change of microstress in coatings at different current densities is also demonstrated in this section.

#### 5.3.1. CHANGE OF INTERPLANAR SPACINGS OF ZINC-IRON COATINGS WITH CURRENT DENSITY

The zinc-iron coatings deposited at different current densities were analyzed using an X-ray diffractometer. Fig. 5.13 shows various X-ray diffraction patterns of the zinc-iron coatings deposited at different current densities ranging from 50 to 500 mA/cm<sup>2</sup>. All the coatings have peaks which represent the  $\eta$  phase. It is noticeable that each of the peaks which represents a specific crystallographic plane gradually shifts either to higher or lower  $2\theta$  angles as the current density changes. The  $\{0002\}$  peak, for instance, is located at the lowest  $2\theta$  position for the coating

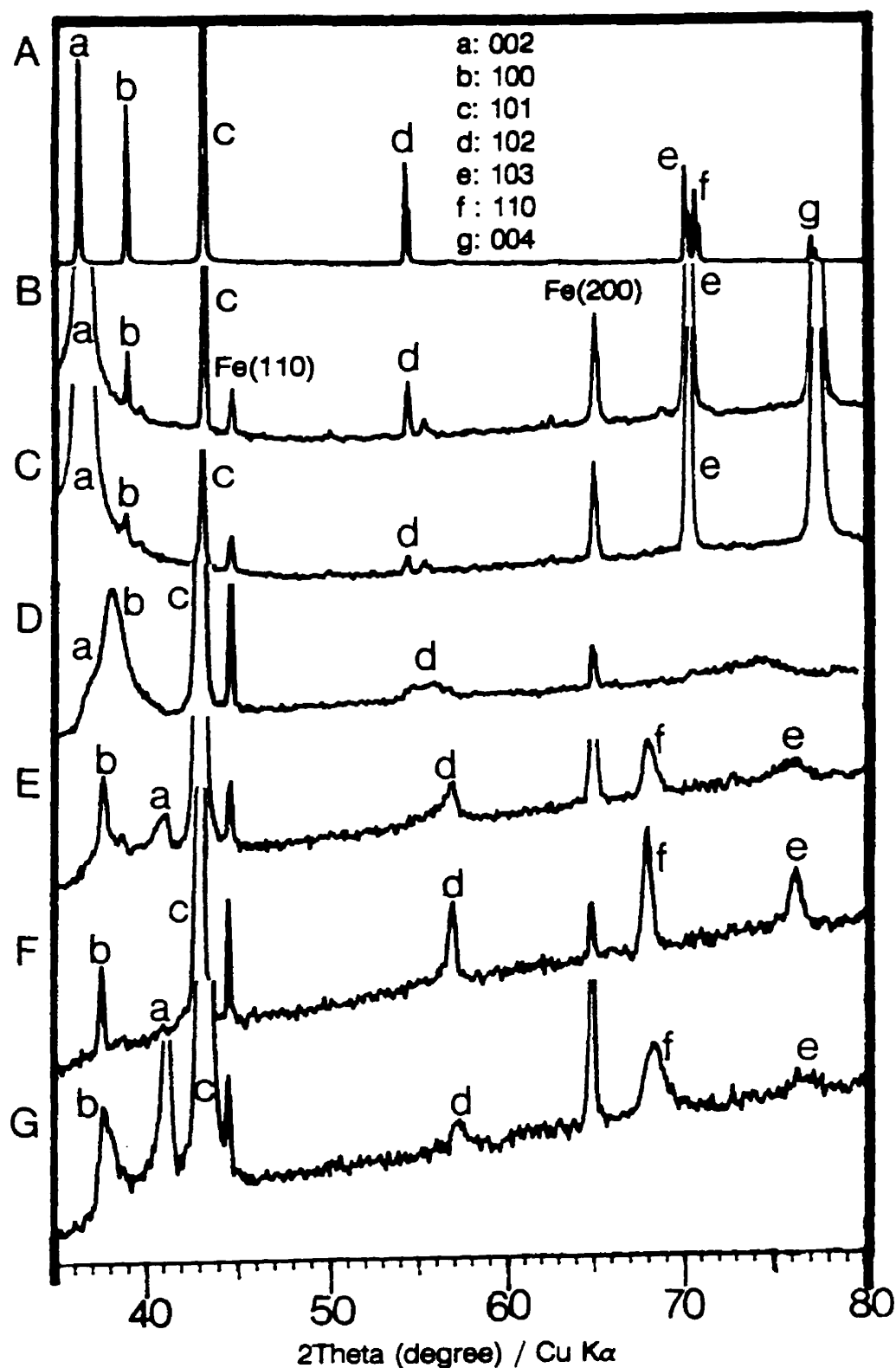


Figure 5.13. X-ray diffractometry of zinc-iron electrodeposited coatings at various current density: (A) zinc random powder (B) 50 , (C) 100, (D) 200, (E) 300, (F) 400, (G) 500  $\text{mA}/\text{cm}^2$ ; Each of the peaks shift either to higher or lower  $2\theta$  angles as the current density changes.



deposited at 50 mA/cm<sup>2</sup> (Fig. 5.13b). As the current density increases, the {0002} peak gradually shifts to a higher angle. Eventually, the {0002} peak shifts to a higher 2θ position than the {10 $\bar{1}$ 0} peak, as the current density increases up to 500 mA/cm<sup>2</sup> (Fig. 5.13g). By contrast, the {10 $\bar{1}$ 0} peak shifts to a lower 2θ value as the current density increases. Meanwhile, the {10 $\bar{1}$ 1} peak does not shift significantly with the current density increase. It is also observed that the {10 $\bar{1}$ 2} and {10 $\bar{1}$ 3} peaks shift to higher 2θ values, whereas the {11 $\bar{2}$ 0} plane shifts to a lower 2θ value as the current density increases.

Fig. 5.14 illustrates the change of interplanar spacings of η phase as a function of current density. As the current density increases, the interplanar spacing of {0002}, {10 $\bar{1}$ 2} and {10 $\bar{1}$ 3} planes decrease, whereas the interplanar spacing of {10 $\bar{1}$ 0} and {11 $\bar{2}$ 0} increase. It should be noted that the change of interplanar spacing is most significant at a current density range between 200 to 300 mA/cm<sup>2</sup>. The c/a ratio was calculated from this X-ray diffraction data, and plotted against the current density change (Fig. 5.15). The coating deposited at 50 mA/cm<sup>2</sup> has the c/a ratio of 1.86. The c/a ratio gradually decreases as the current density increases. The coatings deposited at 100 and 200 mA/cm<sup>2</sup> have the c/a ratio of 1.83 and 1.78, respectively. A sudden drop of c/a to 1.6 is found at the current density range between 200 to 300 mA/cm<sup>2</sup>. Further increase in current density from 300 to 500 mA/cm<sup>2</sup> does not influence the c/a ratio. As previously described in section 5.2.1, the percentage of iron in the zinc-iron coating increases as current density increases. Therefore, the c/a ratio and the percentage of iron in the coatings are correlated. The c/a ratio decreases as the percentage of iron increases. This result is in agreement with other experimental works [Shima et. al. 1986, Lin 1992, Kondo 1994]. The previous observation indicates that by changing the current density, the c/a ratio of the zinc-iron coating can be controlled.

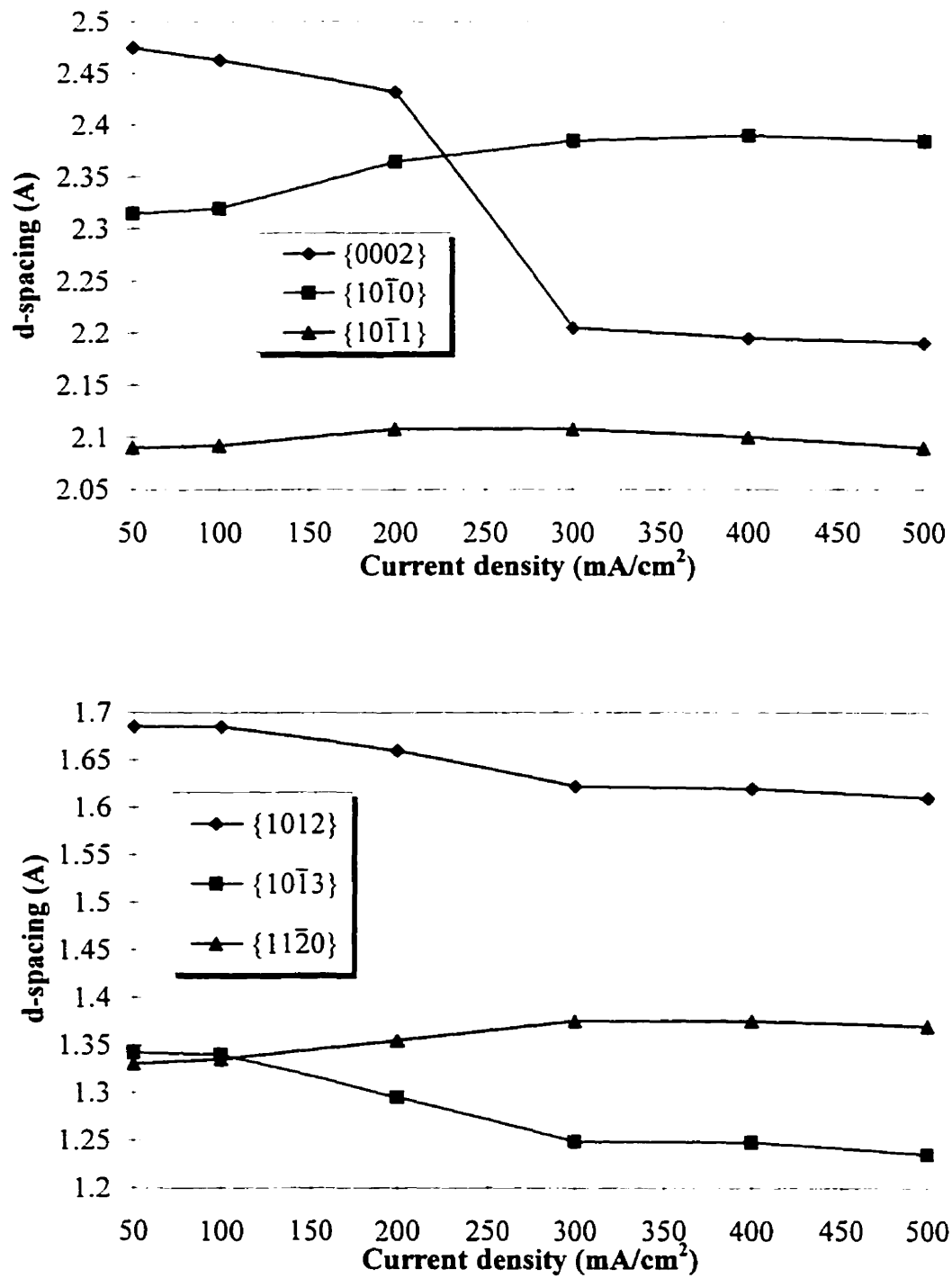
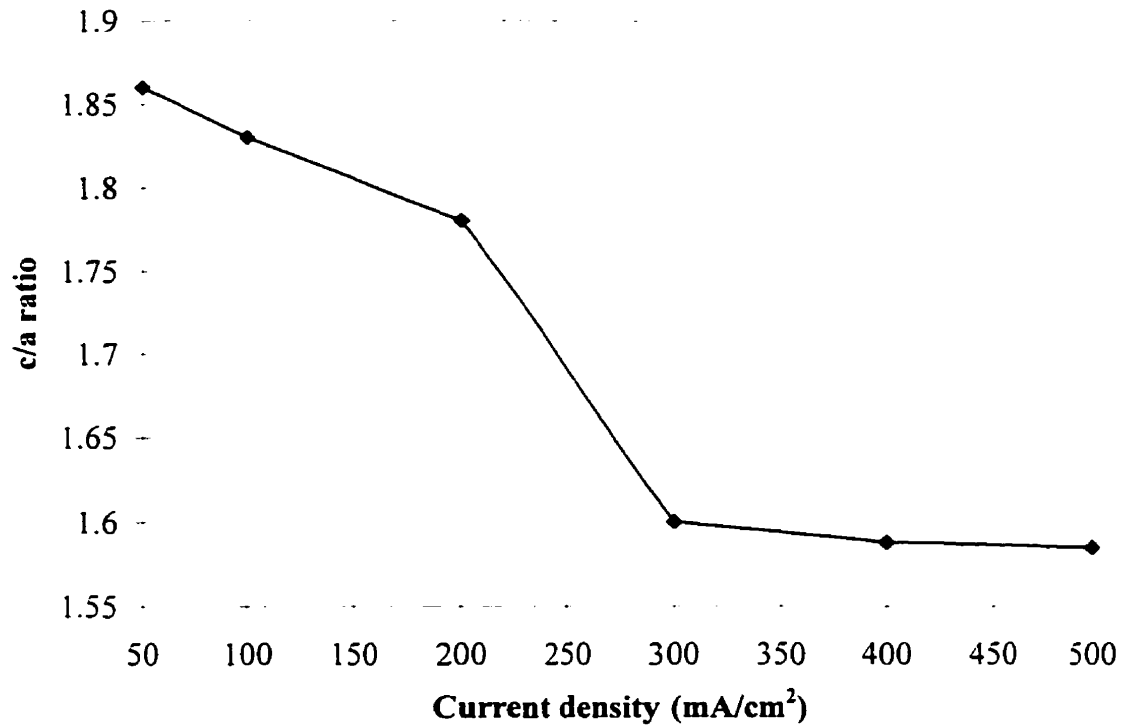


Figure 5.14. Correlation between deposition current density and interplanar spacings of zinc-iron electrodeposited coatings.



**Figure 5.15. Correlation between deposition current density and c/a ratio of zinc-iron electrodeposited coatings.**

### 5.3.2. CHANGE OF PHASE COMPOSITION OF ZINC-NICKEL COATINGS WITH CURRENT DENSITY

To determine the phase composition of zinc-nickel coatings, X-ray diffraction patterns were measured at various current densities. Unlike the zinc-iron coatings which have a single  $\eta$  phase in the previous section, the zinc-nickel coatings have peaks which represent the secondary  $\gamma$  phase at a high current density. Fig. 5.16 shows the X-ray diffraction peaks of electrodeposited zinc-nickel coatings at the current density range of 50 to 1200 mA/cm<sup>2</sup>. Overall, the coatings have either the  $\eta$  peak which represents the  $\{10\bar{1}1\}$  or the  $\gamma$  peaks which represent the  $\{411/330\}$  or  $\{442/600\}$ . There are no other peaks found which represent other planes of the  $\eta$  or the  $\gamma$  phases. The X-ray diffraction data shows

that the coating deposited at 50 mA/cm<sup>2</sup> has two major peaks which represent the  $\eta$  {10 $\bar{1}$ 1} as well as the  $\gamma$  {442/600} (Fig. 5.16a). The intensity of the  $\eta$  peak is stronger than the  $\gamma$  peak. At the current density of 100 mA/cm<sup>2</sup>, the coating also has the  $\eta$  {10 $\bar{1}$ 1} peak and the  $\gamma$  {442/600} peak. However, the intensity of  $\gamma$  peak becomes weaker than  $\eta$  peak (Fig. 5.16b). The coatings deposited at the current density range from 200 to 500 mA/cm<sup>2</sup> have the  $\eta$  {10 $\bar{1}$ 1} peak, while the intensity of  $\gamma$  peak is small (Fig. 5.16c,d,e). When the current density reaches 900 to 1200 mA/cm<sup>2</sup>, the  $\eta$  peak completely disappears, while the coatings have the peaks which represent the  $\gamma$  {411/330} as well as the  $\gamma$  {442/600} peaks (Fig. 5.16f,g). The intensity of the  $\gamma$  {411/330} peak is stronger than the  $\gamma$  {442/600} peak. The present observation of X-ray diffraction patterns indicates that the zinc-nickel coatings have the  $\eta + \gamma$  dual phase at the current density range of 50 to 100 mA/cm<sup>2</sup>, and the coatings have the  $\eta$  single phase at the range of 200 to 500 mA/cm<sup>2</sup>. This also indicates that the coatings have the  $\gamma$  single phase at the current density range of 900 to 1200 mA/cm<sup>2</sup>. Therefore, the result indicates that the phase of zinc-nickel coatings transforms with changes in current density.

It was previously observed in section 5.2.3 that the nickel content changes with current density changes. Obviously, the amount of nickel in the deposit determines the phase composition of the zinc-nickel alloy coatings. The phase diagram in section 2.3 shows that the phase transforms from  $\eta$ , through  $\gamma$ , to  $\alpha$  with the increase of nickel content. It is reasonable, therefore, to compare the above result of phase transformation with the previous observation of change of nickel content. A good agreement is found between the phase composition and the nickel content in the deposit. The coatings of  $\eta$  single phase have the lowest nickel content ranging from 13 to 15 % at the current density range of 200 to 500 mA/cm<sup>2</sup>. The coatings of  $\eta + \gamma$  dual phase show an increase in nickel content to 17 % at 50 mA/cm<sup>2</sup>. The coatings of  $\gamma$  single phase have the highest nickel content of up to 42 % at the current density of 1200 mA/cm<sup>2</sup>.

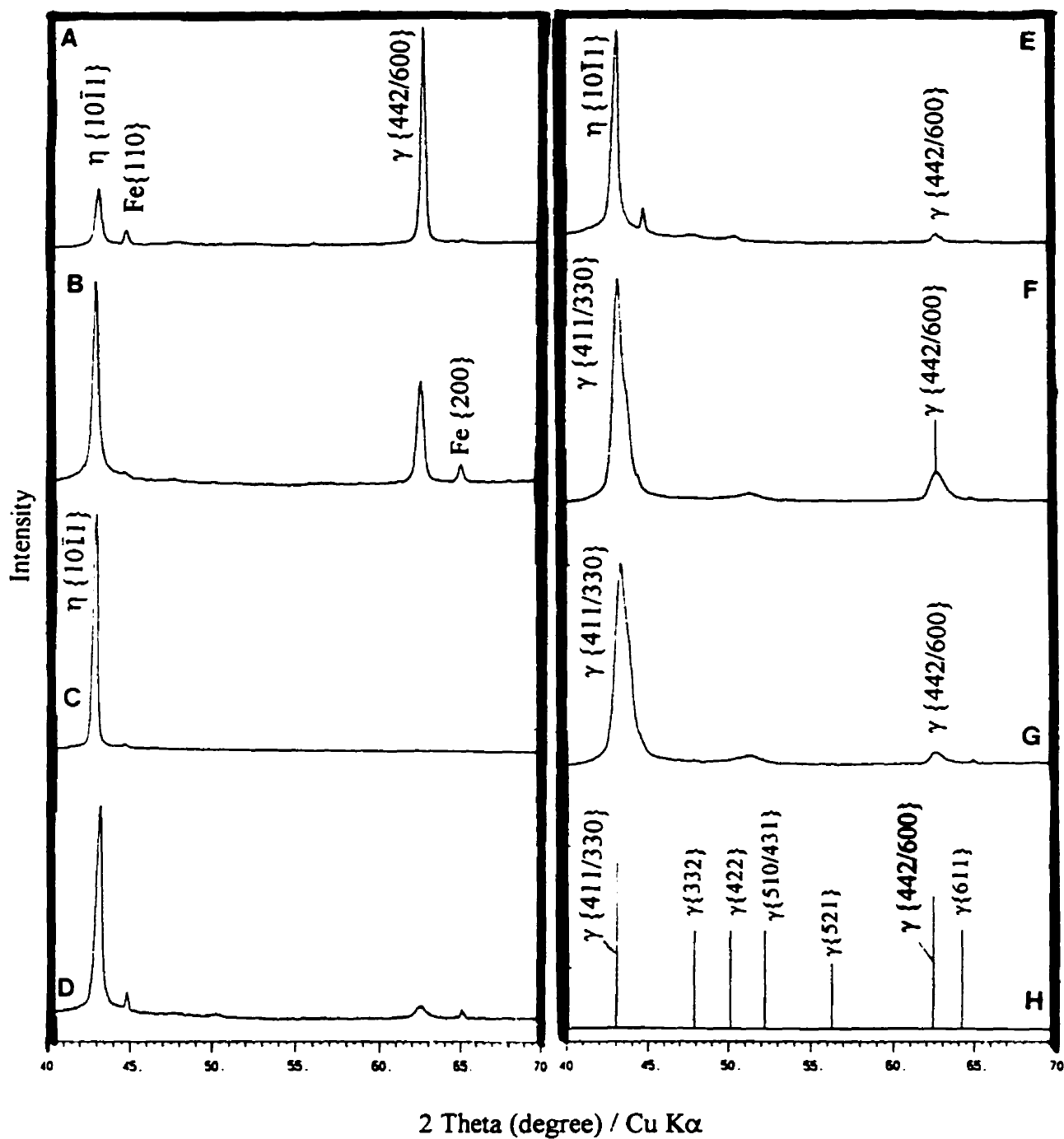


Figure 5.16. X-ray diffractometry of zinc-nickel electrodeposited coatings at various current density: (a) 50, (b) 100, (c) 200, (d) 300, (e) 500, (f) 900, (g) 1200 mA/cm<sup>2</sup>, and (h) standard peak position of  $\gamma$  phase of zinc-nickel.

## 5.3.3 MICROSTRESS OF ZINC-IRON COATINGS

This section describes the changes of diffraction peak broadening on zinc-iron coatings with different current densities. The internal microstress on coatings are analyzed by measuring the Full Width Half Maxima (FWHM) of the X-ray peak. Fig. 5.17 illustrates the change of the FWHM of the  $\{20\bar{2}3\}$  peak with current density. The FWHM continuously increases with increasing current density. This peak broadening indicates that the internal stress continuously increases as the deposition current density increases.

The FWHM of the  $\{11\bar{2}2\}$  peak is plotted as a function of the coating thickness in Fig. 5.18. The thinnest coating is the most highly stressed. However, the stress drops significantly as the coating thickness increases to 10  $\mu\text{m}$ . Further increase in the coating thickness of up to 100  $\mu\text{m}$  does not affect the stress significantly.

The results implies that the internal stress increases with an increase of the current density and also that the stress is high for thin coatings. The increase of stress with the current density can be attributed to the influence of current density upon the coating microstructure. High current densities induce high nucleation rate. A high nucleation rate causes the deposit to have high dislocation density and lattice distortion because ad-atoms on the cathode surface do not have enough time to move to the step or kink sites. This subsequently leads the deposit to a state of high internal stress. The high microstress in the thin coatings is attributed to the strong influence of substrate.

It is found in the previous section that the zinc-iron coatings exhibit significant compositional change with current density and coating thickness. Since the peak broadening analysis was conducted on the zinc-iron coatings, it is reasonable to extend the discussion to the influence of alloy composition upon the

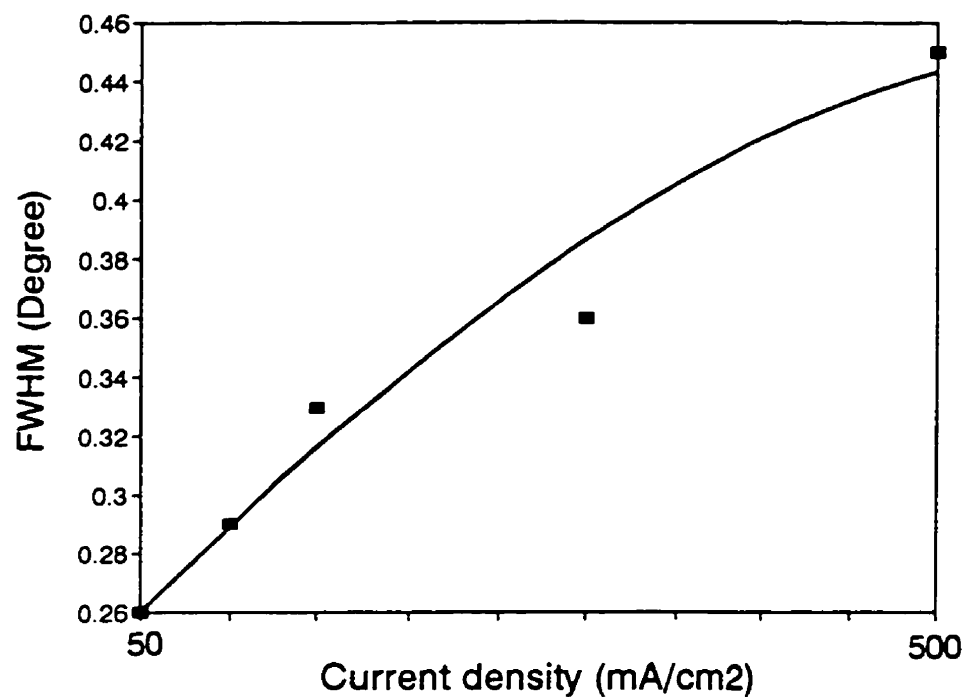


Figure 5.17. Change of FWHM of zinc-iron electrodeposited coatings with current density.

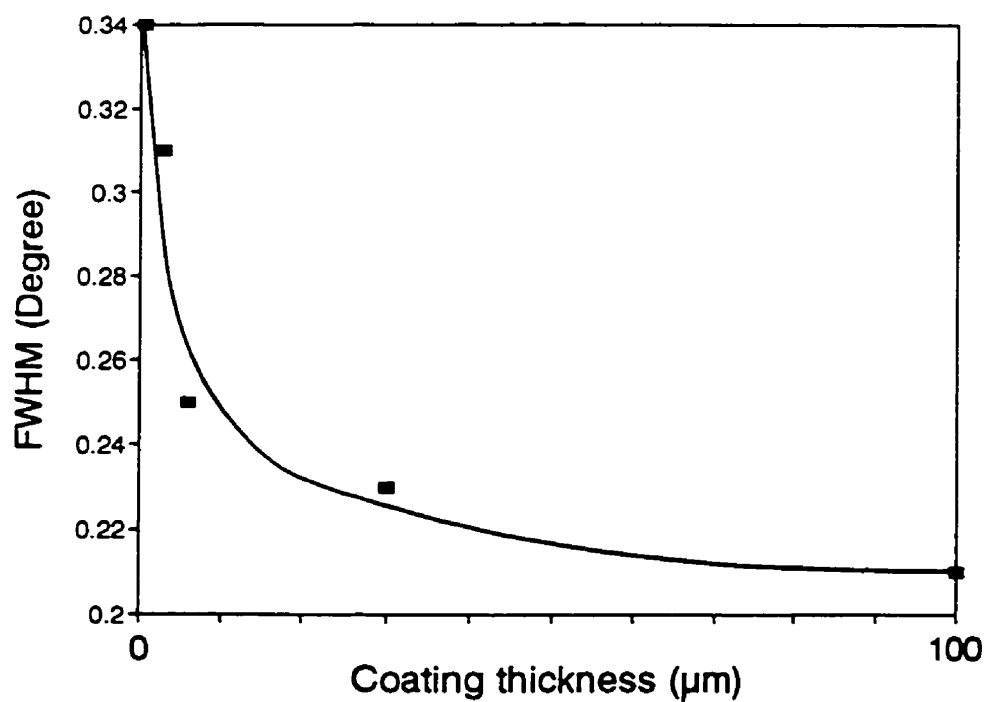
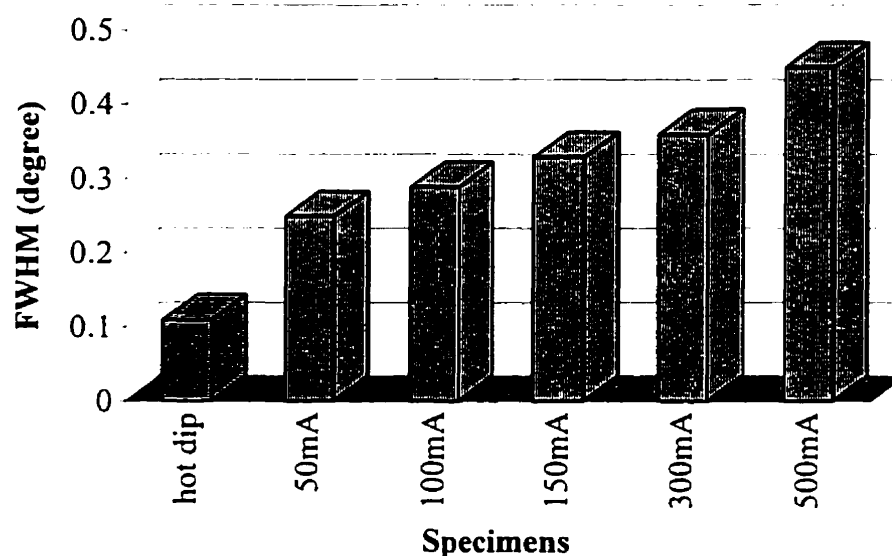


Figure 5.18. Change of FWHM of zinc-iron electrodeposited coatings with coating thickness.

microstress of the coatings. The coatings with high iron content have a high level of microstress. It appears that the incorporation of iron atoms and zinc atoms into the deposition site induces lattice distortion because of the difference in atom size, and therefore causes internal stress. The observation is in good agreement with another experimental finding which described an increase of the microstress with an increase of alloy content in the deposit [Armyanov et. al. 1993].

For the purpose of comparison, the FWHM of a commercially produced hot dip galvanized coating is plotted along with those of electrodeposited coatings at various current densities in Fig. 5.19. The FWHM of hot-dip galvanized coatings is smaller than all of the electrodeposited coatings. More specifically, the FWHM of hot dip galvanized coating is less than half of the smallest FWHM of the electrodeposited coatings. This indicates that the stored internal energy is released during the annealing process, thereby relieving the existing internal stress.



**Figure 5.19. Difference of FWHM between hot-dip zinc-iron galvanized coating and electrodeposited zinc-iron coatings obtained at various current densities.**



#### 5.3.4. SUMMARY

The alloy composition, c/a ratio, phase composition and microstress of zinc alloy electrodeposited coatings are investigated at various current densities and coating thicknesses.

1. Correlation is found between the c/a ratio and iron content in the zinc-iron coatings. The c/a ratio decreases as the iron content in the deposit increases with increasing current density.
2. The nickel content in the zinc-nickel coatings initially drops from 17 % to 13 % and increases up to 42 % with increasing current density from 50 to 1200 mA/cm<sup>2</sup>. The phase composition of coatings also changes from the  $\gamma + \eta$  dual phase to the  $\eta$  single phase, and finally to the  $\gamma$  single phase with increasing current density.
3. The internal microstress in the zinc-iron coatings increases with an increase of current density and is higher for thinner coatings. The coatings with high iron content show high microstress.

#### 5.4. EVOLUTION OF TEXTURE WITH CHANGING CURRENT DENSITY

This section describes the characteristics of texture during the electrodeposition of zinc-iron and zinc-nickel coatings deposited at different current densities.

##### 5.4.1. TEXTURE OF ZINC-IRON COATINGS

Fig. 5.20 shows the pole figures for the coatings deposited at different current densities. The coating deposited at 50 mA/cm<sup>2</sup> has two major texture components: the {0001} basal and the {10 $\bar{1}$ 3} pyramidal texture. The intensity of the basal pole texture is 33 times higher than the intensity from the random component. While the {0001} component shows a very sharp and strong fiber

texture, the  $\{10\bar{1}3\}$  component is affected by the steel substrate. The basal and the pyramidal texture components coexist until the deposition current density increases to  $100 \text{ mA/cm}^2$ .

As the applied current density increases to  $200 \text{ mA/cm}^2$ , the characteristics of zinc-iron coating textures change significantly. The basal texture component completely disappears, whereas the pyramidal texture component remains. It should be noted that this pyramidal component gradually transforms to the fiber texture component as the current density increases further. At the current density of  $300 \text{ mA/cm}^2$  (Fig. 5.20d), the coating texture transforms to a very weak fiber pyramidal texture component. This texture is widely dispersed, and is an incomplete fiber component with an intensity of 2.2 to the rolling direction, and an intensity of 1.2 to the transverse direction. Further increase in current density up to  $500 \text{ mA/cm}^2$  leads to the  $\{10\bar{1}3\}$  fiber texture (Fig. 5.20e,f). The pole figure of the coating deposited at  $500 \text{ mA/cm}^2$  shows a widely dispersed fiber component with an intensity of 2.1 times higher than random.

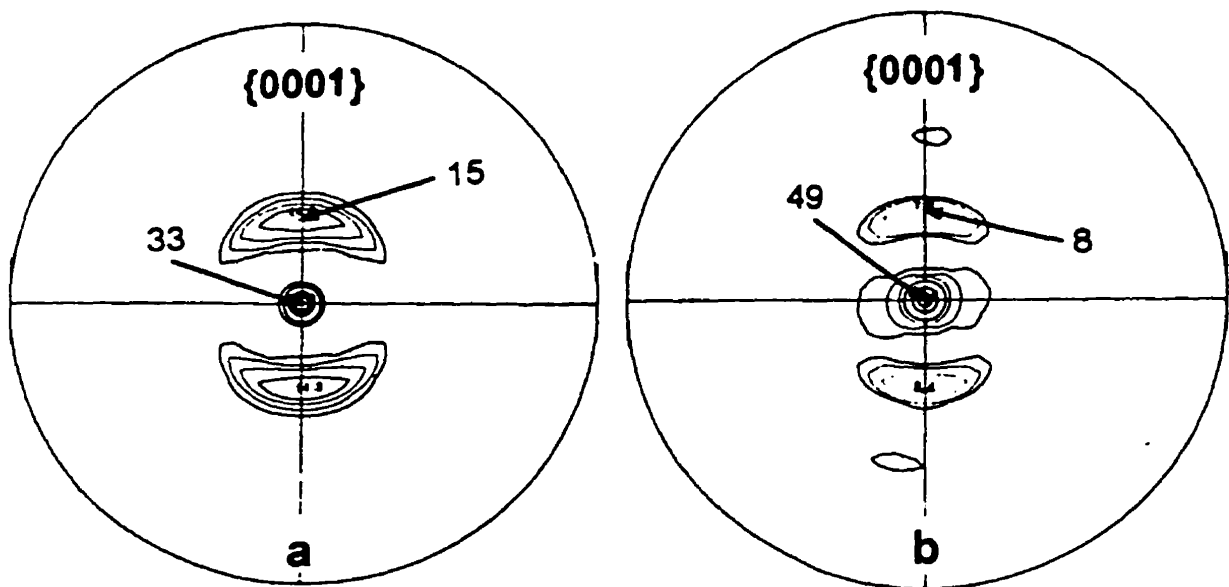


Figure 5.20. Continued.

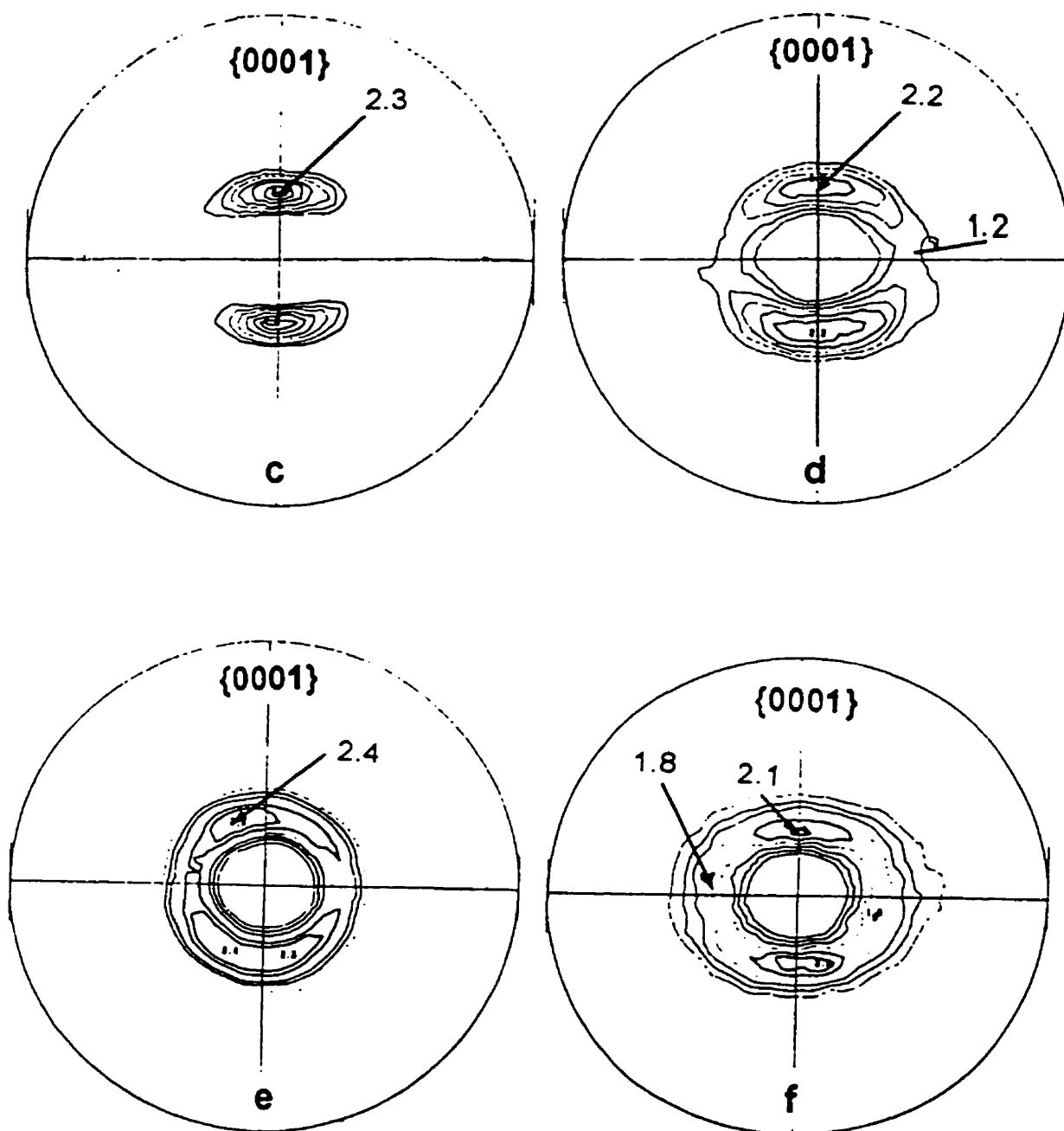


Figure 5.20. The pole figures of zinc-iron electrodeposited coatings deposited at different current density: (a) 50, (b) 100, (c) 200, (d) 300, (e) 400, (f) 500 mA/cm<sup>2</sup>; The basal component completely disappears at 200 mA/cm<sup>2</sup> while the non-fiber pyramidal component gradually evolves to fiber at higher current density.

From the above observation, it is found that the texture of zinc-iron coating evolves from the  $\{0001\}$  basal fiber and the  $\{10\bar{1}3\}$  pyramidal non-fiber component to the pyramidal fiber texture with a current density increase. This result is similar to the texture evolution of zinc coatings. The texture of zinc-iron coatings at low current densities in the range between 50 to 100 mA/cm<sup>2</sup> is quite similar to that obtained in the zinc coatings deposited at the current density range of 30 to 300 mA/cm<sup>2</sup>. The basal fiber and the pyramidal non-fiber texture components are also observed there. This is attributed to the fact that at low current density, the iron content in the deposit is less than 3 %, and thus the texture characteristics of zinc-iron coating is close to that of zinc coatings.

The mechanism of texture evolution developed by different current densities was previously discussed in section 4.2.1. The correlation of texture and morphology of coatings was also demonstrated at different deposition parameters. When the deposition parameters change, the iron content of zinc-iron coatings also changes. This compositional change is directly responsible for the characteristics of coating morphology which, in turn, lead to the texture evolution. Therefore, it is necessary to discuss whether the iron content in the zinc-iron coatings is related to the texture. The previous result of EPMA analysis (Fig. 5.6) showed that the iron content abruptly jumped from less than 2 % to 10 % as the current density increased from 50 to 300 mA/cm<sup>2</sup>, while the present observation found a major transformation of texture at the same current density range. This fact indicates that there is correlation between the alloy content and the coating texture. With an increase of iron content in the deposit, the coating texture is transformed from the  $\{0001\}$  fiber and the  $\{10\bar{1}3\}$  non-fiber component to the  $\{10\bar{1}3\}$  fiber texture.

## 5.4.2 TEXTURE OF ZINC-NICKEL COATINGS

This section describes the evolution of texture during the electrodeposition of zinc-nickel coatings at different current densities. Fig. 5.21 shows the pole figures of electrodeposited zinc-nickel coatings obtained in the current density range of 50 to 1200 mA/cm<sup>2</sup>. It should be noted that the coatings with  $\gamma$  phase have two X-ray diffraction peak maxima at which two sets of  $\{hkl\}$  planes overlap; One is the peak at which  $\{330\}$  and  $\{411\}$  maxima overlap. The other is the peak maxima which consists of  $\{600\}$  and  $\{442\}$  reflections. In order to describe the texture, it is necessary to identify from which of the two planes the X-rays are diffracted. There is no direct method to separate the maxima from two different planes, because those planes have the same diffraction angle which satisfies Bragg's law. Therefore, texture can only be identified by comparing the  $\{hkl\}$  interplanar angles with the pole locations in the pole figures. Two pole figures were measured from the  $2\theta$  positions of two peak maxima. For example, the pole figures of the coating deposited at 50 mA/cm<sup>2</sup> are shown in Fig. 5.21a. The pole figure obtained from the  $\{330/411\}$  diffraction maxima shows two rings located at 20 deg and 45 deg. The other pole figure obtained from  $\{600/442\}$  peak shows the intensity maxima at the center of the pole figure. To identify whether the coating has  $\{100\}$  or  $\{221\}$  fiber texture, the interplanar angle between those planes are calculated, and subsequently compared with the maxima that are observed in the pole figure. The ring at 20 deg corresponds to the interplanar angle between  $\{100\}$  and  $\{411\}$ , while the ring at 45 deg corresponds to the interplanar angle between  $\{100\}$  and  $\{110\}$ . In the case of the  $\{221\}$ , however, the interplanar angles do not correspond to the ring positions. Therefore, it can be suggested that the coating has  $\{100\}$  fiber texture.

At a current density of 200 mA/cm<sup>2</sup>, the  $\{100\}$  fiber texture completely disappears, whereas the  $\{10\bar{1}1\}$  fiber texture which characterizes the  $\eta$  phase becomes a main texture component (Fig. 5.21b). No significant change in texture

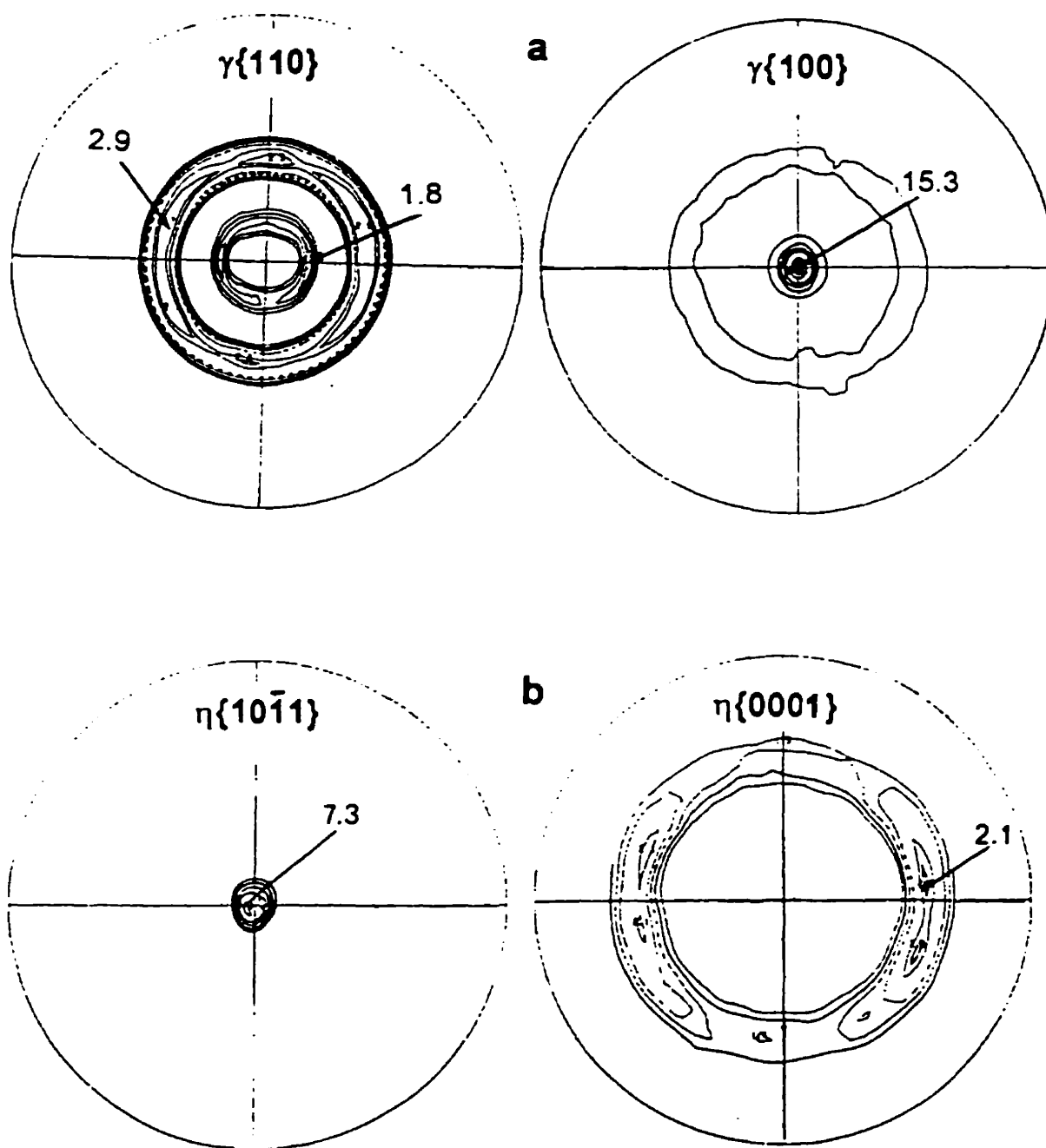


Figure 5.21. The pole figures of zinc-nickel electrodeposited coatings deposited at different current density: (a) 50, (b) 200, (c) 700, (d) 900, (e) 1200 mA/cm<sup>2</sup>.

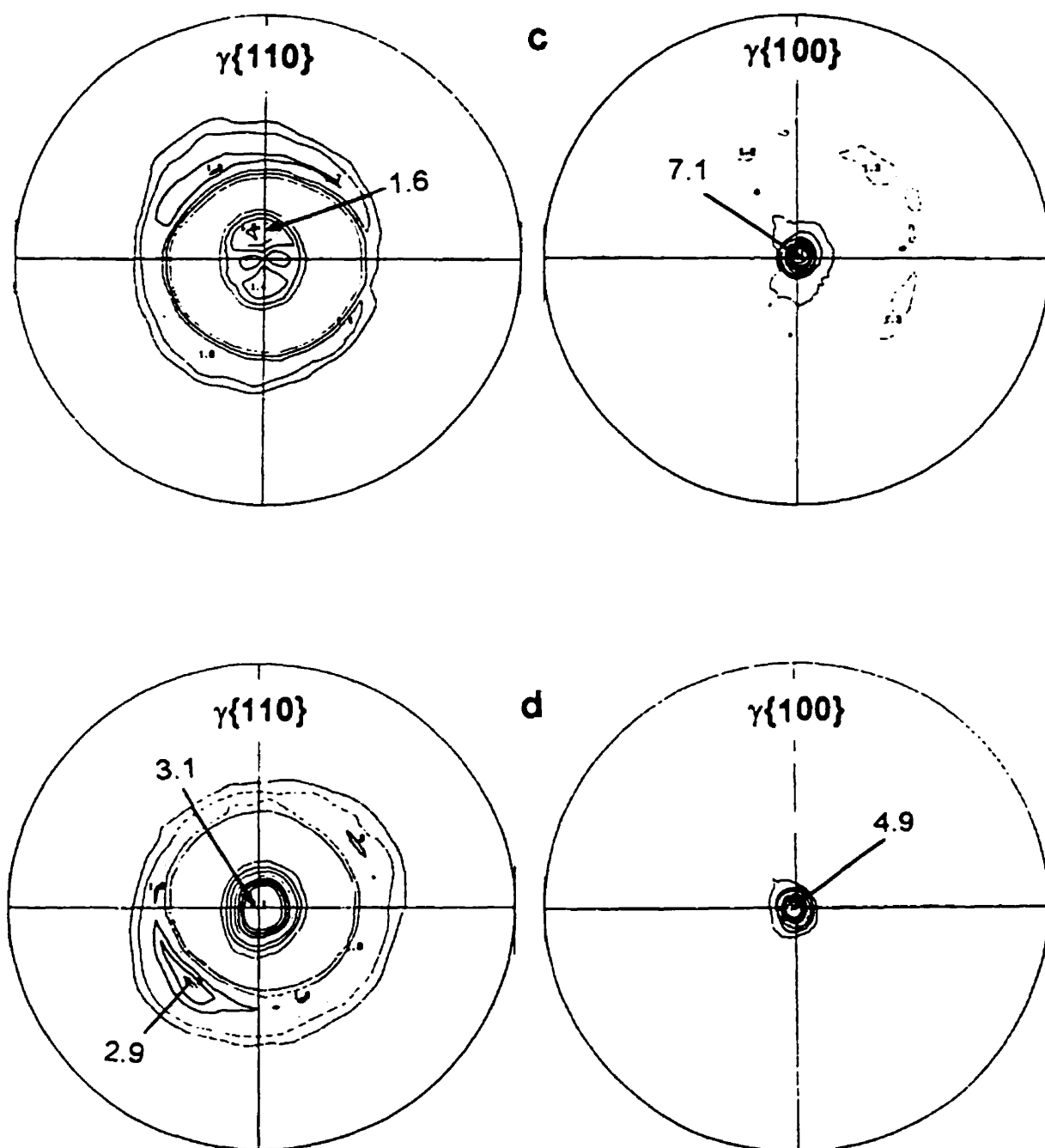


Figure 5.21. Continued.

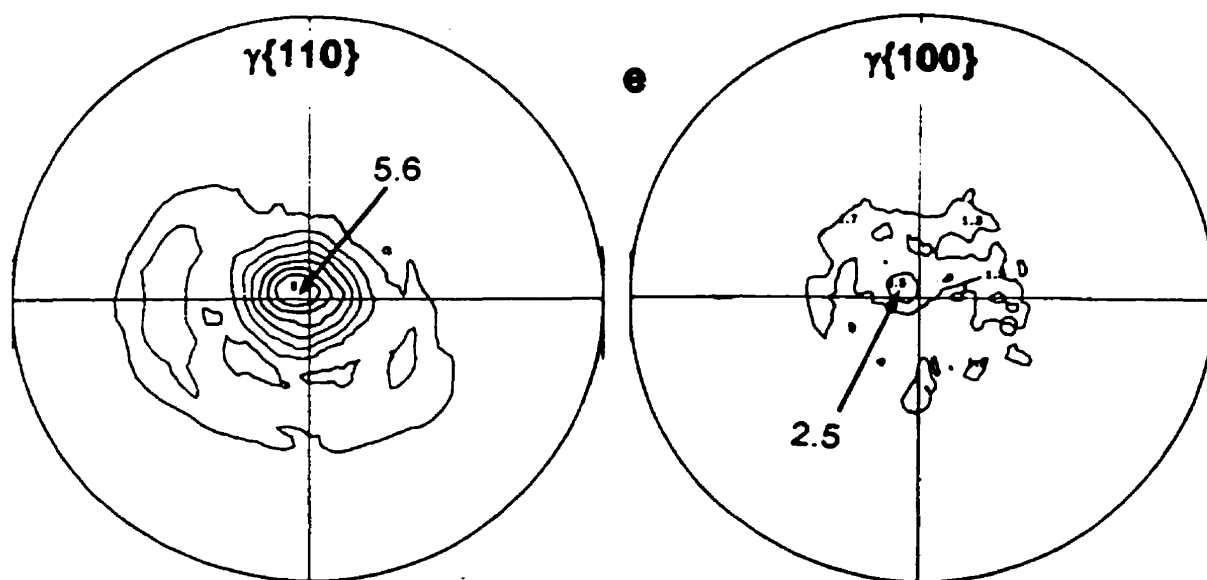


Figure 5.21. Continued.

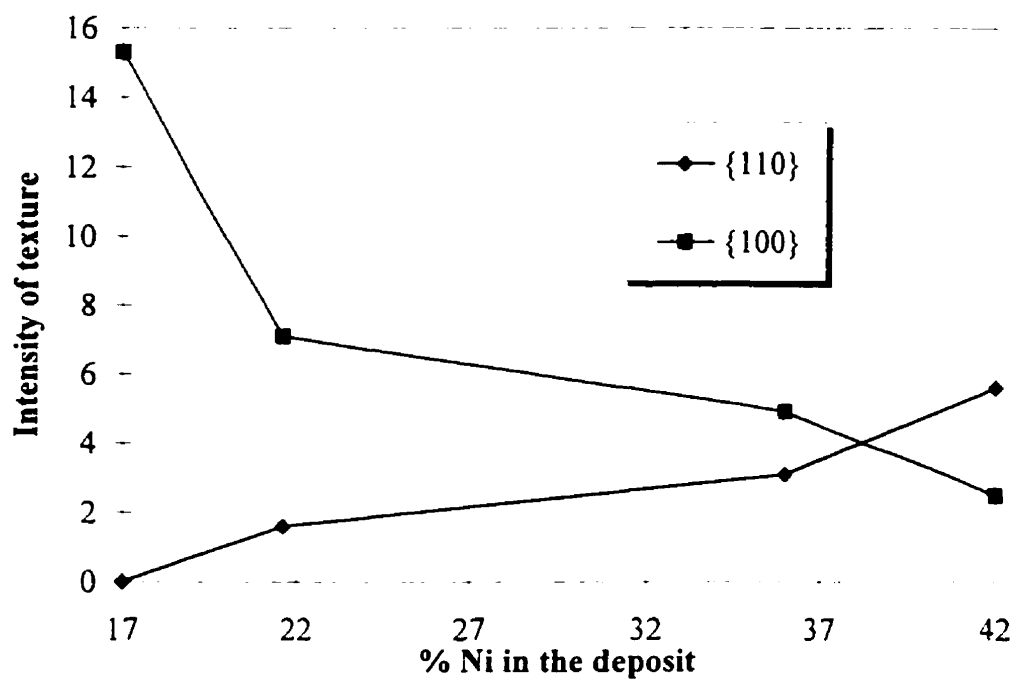


Figure 5.22. Correlation between the intensity of texture and nickel percentage in the zinc-nickel coatings.



is found when the current density increases up to  $500 \text{ mA/cm}^2$ . As the deposition current density increases further to  $700 \text{ mA/cm}^2$ , the  $\gamma$  phase dominates, and the  $\{110\}$  and the  $\{100\}$  textures are observed (Fig. 5.21c). The intensity maxima characterizing both textures are 1.6 and 7.1, respectively. The  $\{110\}$  texture is weak and plane orientations are widely dispersed within the range of 20 degrees, while the  $\{100\}$  texture is strong and the maxima is well defined. Further increase in the current density range of 900 to  $1200 \text{ mA/cm}^2$  causes continuous changes in the texture intensity (Fig. 5.21d, e). The intensity of  $\{110\}$  texture, for instance, increases to 3.1 and then to 5.6, while the intensity of  $\{100\}$  component decreases to 4.9 and then to 2.5.

The observation indicates that the texture of zinc-nickel coatings transforms at different current densities. It is known as well that the current density is directly responsible for changing the nickel content of the deposit, the texture changes can then be linked to the change of nickel content. Since the coatings have low nickel content of 13 to 15 % in the current density range of 200 to  $500 \text{ mA/cm}^2$ , the  $\eta$  phase is formed and corresponding texture has only a pyramidal component. It is interesting to compare this result to the exclusive formation of the pyramidal texture in zinc-iron coatings at similar alloy composition. This observed similarity suggests that in both cases, the pyramidal component dominates when the alloying element content increases in this range. The coatings have high nickel content of more than 21 % in the current density range 700 to  $1200 \text{ mA/cm}^2$ . In this range, the  $\gamma$  phase is formed and corresponding texture intensity varies with the nickel content as is shown in Fig. 5.22. The intensity of  $\{110\}$  texture continuously increases with increasing nickel content while the intensity of  $\{100\}$  texture decreases.

## 5.4.3. SUMMARY

The characteristics of texture are demonstrated at various current densities during deposition of zinc-iron and zinc-nickel coatings. It is observed that the zinc alloy coatings exhibit a significant variation in texture with changing current density. The present work suggests that the evolution of texture during the alloy codeposition is closely related to morphological characteristics of the surface and the change of alloy and phase composition.

1. A correlation is found between current density, alloy content, the texture and the coating morphology. As the current density increases, the texture of zinc-iron coatings changes from the combined texture of basal fiber and non-fiber pyramidal component to the pyramidal fiber texture only. This results from anomalous codeposition which induces a high content of iron in the deposit and thereby facilitates the transformation from the morphology of hexagonal ridges and platelets to the triangular pyramidal morphology as the current density increases.
2. In the  $\gamma$  phase zinc-nickel coatings, the intensity of  $\{110\}$  texture increases with increasing nickel content, while the intensity of  $\{100\}$  texture decreases.

## **CHAPTER SIX**

# **CORROSION PROPERTIES OF ZINC AND ZINC ALLOY COATINGS**

### **6.1. CORROSION BEHAVIOR OF ZINC COATINGS**

This section demonstrates the change of corrosion properties of zinc coatings with coating texture and morphology. As previously reviewed in section 2.9, several attempts have been made to observe the correlation between texture and corrosion resistance of coatings. Researchers reported that the  $\{0001\}$  texture of hot dip zinc coatings showed better corrosion resistance than the  $\{11\bar{2}2\}$  texture. However, it is so far not clear why the coating with the  $\{0001\}$  texture is more resistant against corrosion attack. Moreover, there is no attempt to correlate the coating morphology and texture to the corrosion resistance.

In the present work, the electrochemical corrosion tests were carried out on the coatings of different texture and morphology. This work not only demonstrates what is a desirable texture and morphology, but also suggests the optimum electrodeposition conditions required to obtain the best corrosion resistance.

#### **6.1.1 INFLUENCE OF TEXTURE AND MORPHOLOGY UPON CORROSION RESISTANCE**

Fig. 6.1 illustrates the correlation between the intensity of  $\{0001\}$  basal texture and the corrosion current of zinc electrodeposited coatings. The intensity maxima of the basal pole is defined as the basal texture intensity. The coatings with a different texture were obtained by varying the current density in the range of 30 to 500 mA/cm<sup>2</sup>. The error bars were obtained from an analysis of differences in

corrosion currents of five samples, each produced at the same deposition conditions. It is clear from Fig. 6.1 that the texture of coatings are directly responsible for the corrosion resistance of coatings. The coatings which have no basal texture (zero intensity) exhibit the highest corrosion current (average of  $363 \mu\text{A}/\text{cm}^2$ ). As the intensity of basal texture increases, the corresponding corrosion current significantly decreases, and thereby the corrosion resistance of coatings improves. This observation is in good agreement with the previous works where the corrosion behavior in textured zinc coatings was studied [Takechi et. al. 1981, Ohbu et. al. 1973, and Ashton et. al. 1968]. From these results, it is confirmed that the zinc coatings with a strong intensity of basal texture exhibit better corrosion resistance than the coatings with weak basal texture or pyramidal texture.

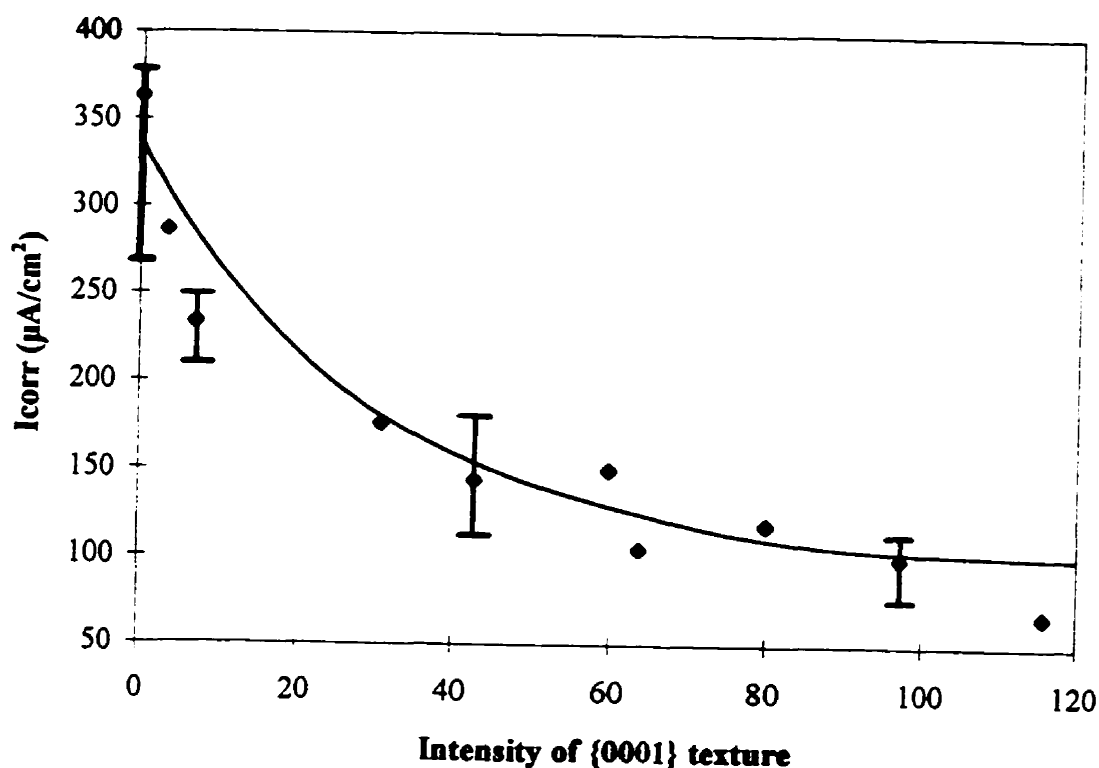


Figure 6.1. Correlation between intensity of {0001} texture and corrosion current of zinc electrodeposited coatings.

The results also demonstrate that the surface morphology is linked to the corrosion properties of coatings. As previously demonstrated in section 4.2.1, the coatings with a high intensity of basal texture have the morphology of hexagonal platelets and ridges. The coatings with no basal component but pyramidal texture have the pyramidal grain morphology. Therefore, the morphology of hexagonal platelets and ridges is associated with a better corrosion resistance, whereas the pyramidal morphology is associated with a poor corrosion resistance.

To understand the influence of texture and morphology upon the corrosion resistance of coatings, a schematic description of different coating surfaces is proposed. Three types of surface morphology are illustrated in Fig. 6.2; (a) the morphology of hexagonal platelets which represents the basal texture, (b) the morphology of well aligned hexagonal ridges which represents the pyramidal non-fiber texture, and (c) the morphology of triangular pyramids which is associated with the pyramidal fiber texture.

The present study found that the coatings show better corrosion resistance in the case of the combined morphology described in Fig. 6.2a and 6.2b: the  $\{0001\}$  planes parallel to the substrate surface as well as the tilted basal planes. The coatings also show poor corrosion resistance in the case of the pyramidal morphology described in Fig. 6.2c: The triangular pyramids are composed of two prismatic  $\{10\bar{1}0\}$  planes and one basal plane. It should be noted that in Fig. 6.2a,b, the coating surface is covered mainly by  $\{0001\}$  planes. In Fig. 6.2c, on the other hand, the surface is covered mainly by  $\{10\bar{1}0\}$  planes. As previously reviewed in section 2.9 [Bockris and Khan 1993, Scully 1990], the  $\{0001\}$  plane has better resistance against corrosion attack than other planes, because the close packed plane has the lowest surface free energy. Therefore, the coating surface which is covered by a higher fraction of a basal plane has a better corrosion resistance.

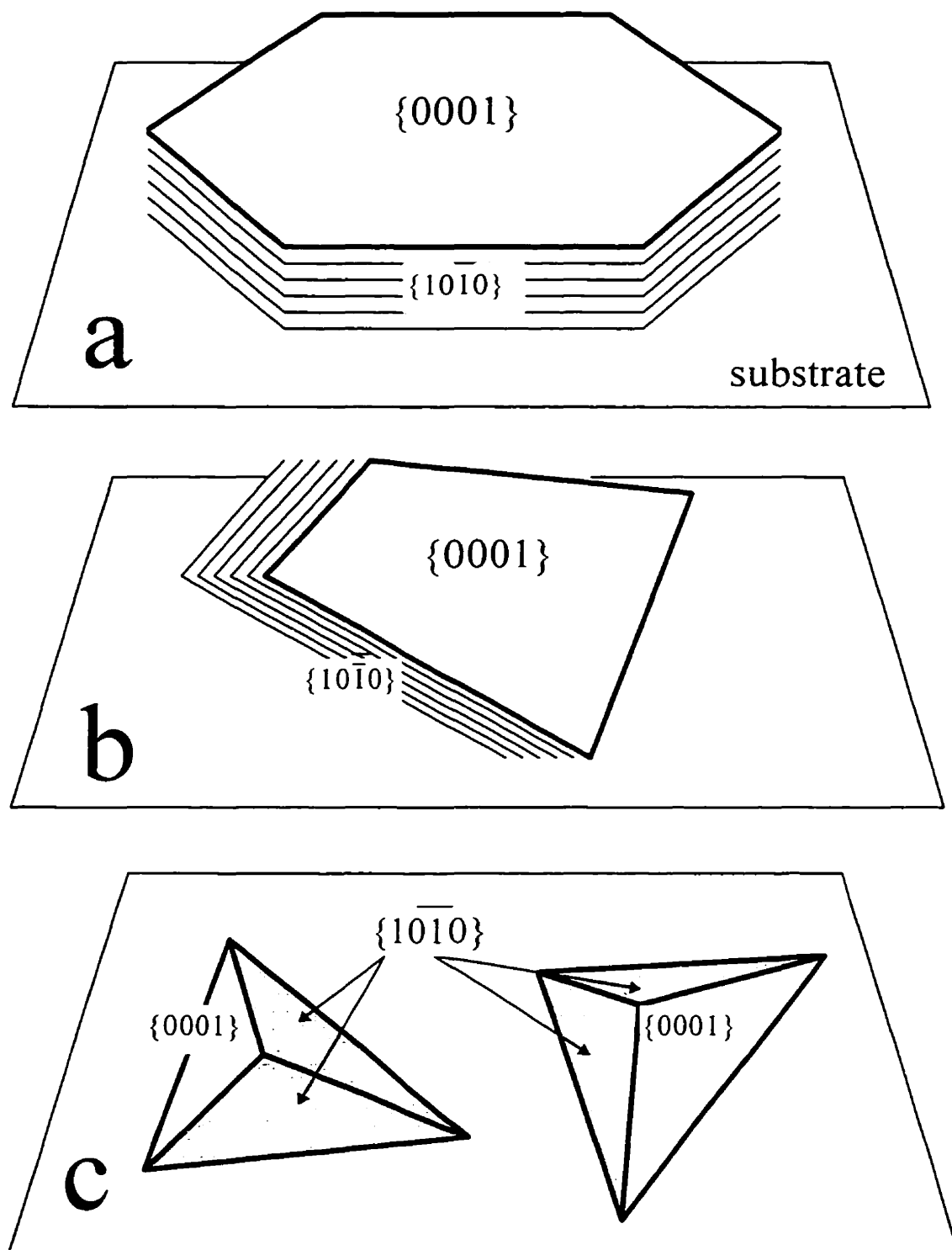


Fig. 6.2. Schematic illustration of three different types of coating surface: (a) basal, (b) pyramidal non-fiber, (c) pyramidal fiber textured coating morphology.

## 6.1.2. OPTIMUM CURRENT DENSITY FOR THE BEST CORROSION RESISTANCE

This section proposes the optimum deposition condition for the best corrosion resistance based upon the results obtained for various zinc electrodeposits. It should be noted that the zinc coatings were deposited at a wide range of current densities, while other deposition parameters were kept constant. The pH value of the electrolyte was about 3.8 and the bath temperature was held at 50°C. The deposition time was adjusted to produce a coating thickness of 6  $\mu\text{m}$ . Therefore, the optimization of the deposition condition is focused on the current density which is one of the most important factors influencing corrosion resistance. Fig. 6.3 shows the corrosion current and the intensity of {0001} texture as a function of the deposition current density.

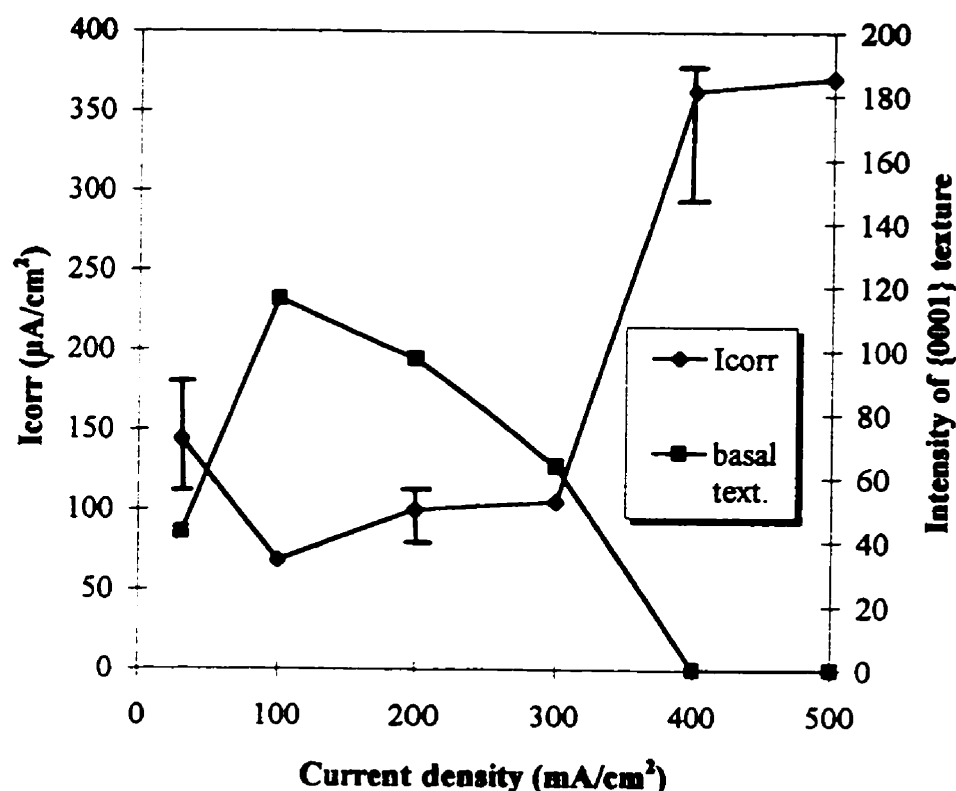


Figure 6.3. Correlation between deposition current density and corrosion current as well as intensity of {0001} texture of the zinc electrodeposited coatings.

High corrosion current, which corresponds to a high corrosion rate, is observed for the coatings deposited at 400 and 500 mA/cm<sup>2</sup>. The average values of the corrosion current of these coatings are 363 and 371  $\mu$ A/cm<sup>2</sup>, respectively. The coatings deposited at this range of current density show the lowest intensity (zero) of basal texture. On the contrary, the coatings deposited at a lower current density range, i.e. 100 to 300 mA/cm<sup>2</sup> exhibit strong basal plane texture as well as low corrosion current values. It is recommended, therefore, that the zinc coating should be electrodeposited at a current density range of 100 to 300 mA/cm<sup>2</sup>.

### 6.1.3. SUMMARY

Corrosion tests were performed on the zinc coatings which have different texture and morphologies. Correlation was found between texture, surface morphology and the corrosion resistance of zinc coatings. The optimum deposition conditions are proposed for better corrosion performance.

1. The zinc coatings having a strong basal plane texture show a better corrosion resistance. The pyramidal fiber texture is linked to poor corrosion resistance.
2. The morphology of the hexagonal platelets and ridges usually associated with a low current density has a better corrosion resistance, whereas the morphology of triangular pyramids which is obtained at high current density shows poor corrosion resistance.
3. For the best corrosion resistance of zinc electrodeposited coatings, the optimum current density is proposed in the range of 100 to 300 mA/cm<sup>2</sup>, while other deposition parameters are kept constant (pH: 3.8 and coating thickness: 6  $\mu$ m).



## 6.2. CORROSION PROPERTIES OF ZINC ALLOY COATINGS

This section demonstrates different corrosion behavior of the zinc-iron and zinc-nickel coatings deposited at various current densities. In the previous chapter 5, the zinc alloy coatings showed a significant change in alloy composition. This change in alloy composition is linked to the evolution of texture and morphology; changes in the texture and morphology are closely related to the corrosion behavior of the coatings. Compositional change is also associated with phase transformation which, in turn, also influences the corrosion behavior of the coatings. It has been reported that corrosion resistance is dependent upon the alloy content of zinc based coatings [Mottate 1989, Vlad 1990, Alfantazi 1994]. Mottate observed that the zinc-iron coatings containing 10 to 20 % Fe provide the optimum result for corrosion performance, paintability and formability. Vlad [1990] reported that the best corrosion protection is achieved with the zinc-nickel coatings containing 10 to 16 % Ni content. Another investigation of zinc-nickel coatings by Alfantazi [1994] suggested that the optimum percent of nickel in the pulse-plated zinc-nickel coatings should be around 20 % for the best corrosion resistance.

As far as the alloy coating is concerned, there has always been an emphasis on the direct influence of alloy content and phase composition on corrosion resistance, while only a few researchers studied the influence of texture and morphology upon corrosion resistance. It is necessary, therefore, to demonstrate the correlation between texture, morphology and the corrosion behavior of coatings. This section describes the correlation of texture and morphology with the corrosion resistance of zinc alloy coatings. In addition, the influence of alloy content and phase composition on corrosion behavior is discussed.

### 6.2.1 CORROSION BEHAVIOR OF ZINC-IRON COATINGS

This section describes various corrosion behaviors of the zinc-iron coatings produced at different deposition conditions. An example of typical polarization curves of zinc-iron electrodeposited coatings is shown in Fig. 6.4. The polarization curves indicate the difference in corrosion behavior of the coatings deposited at low and high deposition current density. The corrosion current and the corrosion potential were measured on the polarization curves by using the Tafel extrapolation method. The coating (A) deposited at  $50 \text{ mA/cm}^2$  shows a corrosion current of  $16 \text{ } \mu\text{A/cm}^2$  and a corrosion potential of  $-1100 \text{ mV}$ , while the coating (B) deposited at  $500 \text{ mA/cm}^2$  shows a corrosion current of  $146 \text{ } \mu\text{A/cm}^2$  and a corrosion potential of  $-1020 \text{ mV}$ . Obviously, this is good evidence that zinc-iron coatings exhibit different corrosion behavior when the coatings were deposited at different applied current density.

In Fig. 6.5, the intensity of basal texture is plotted as a function of the corrosion current. The coatings having zero intensity of basal texture show the highest corrosion current; the average value of corrosion current is  $151 \text{ } \mu\text{A/cm}^2$ . On the other hand, the coatings having high intensity of basal texture show low corrosion current. This fact indicates that the texture is correlated to the corrosion behavior of coatings.

The corrosion behavior of zinc-iron coatings can be linked also to the alloy composition in the deposits in addition to texture. As previously discussed in section 5.2.1, the change of electroplating current density affects alloy composition through the anomalous codeposition process. Therefore, the values of corrosion current can be directly plotted against the content of Fe in the coatings as is shown in Fig. 6.6. Fig. 6.6 shows that the corrosion current increases as the % Fe in the coating increases. At this point, it should be pointed out why the corrosion current

suddenly increases at the range of 3 to 4 % Fe. Since there is only one  $\eta$  phase in the deposit, the observed increase in corrosion current must be related to transformation of texture in the coatings. At this range of iron percentage, the texture completely transforms from the basal and pyramidal component texture to the pyramidal fiber texture as is discussed in chapter 5. Therefore, the disappearance of the basal type texture component is responsible for the deterioration of corrosion resistance.

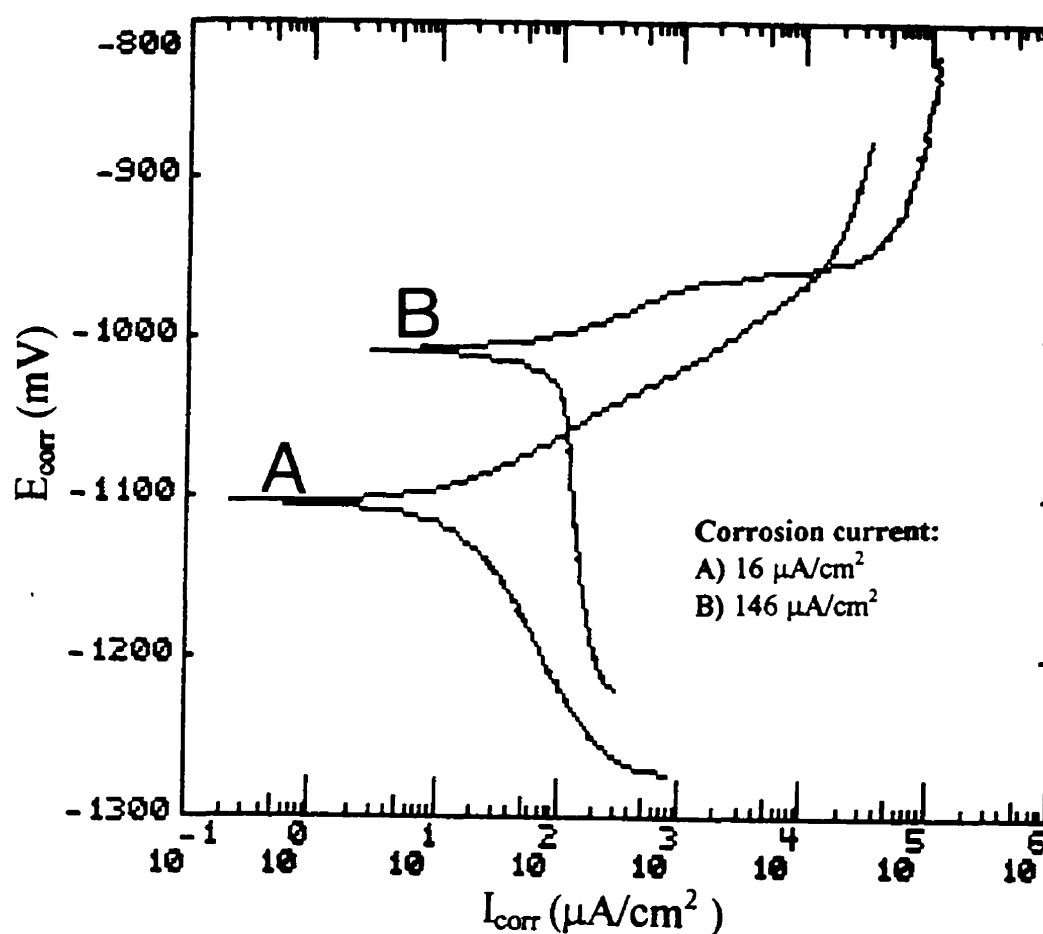


Figure 6.4. Polarization curves of zinc-iron electrodeposited coatings exhibit different corrosion behavior of the coatings deposited at low (A) and high (B) current density.

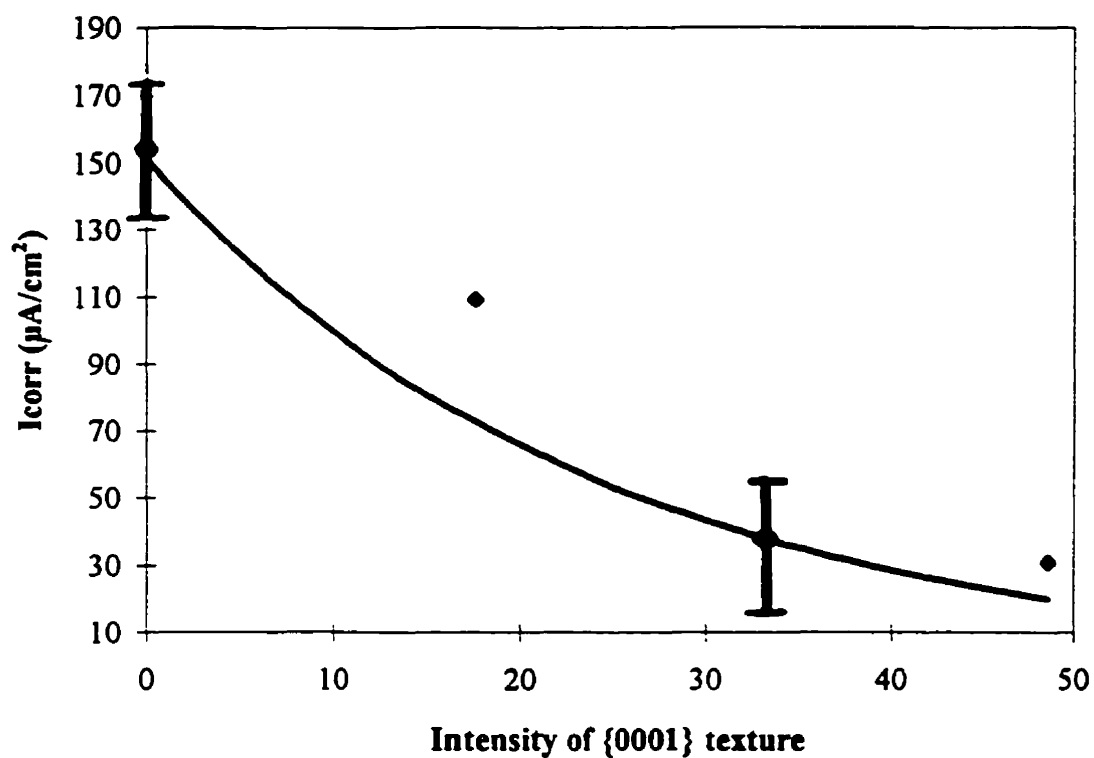


Figure 6.5. Correlation between intensity of {0001} texture and corrosion current of zinc-iron electrodeposited coatings.

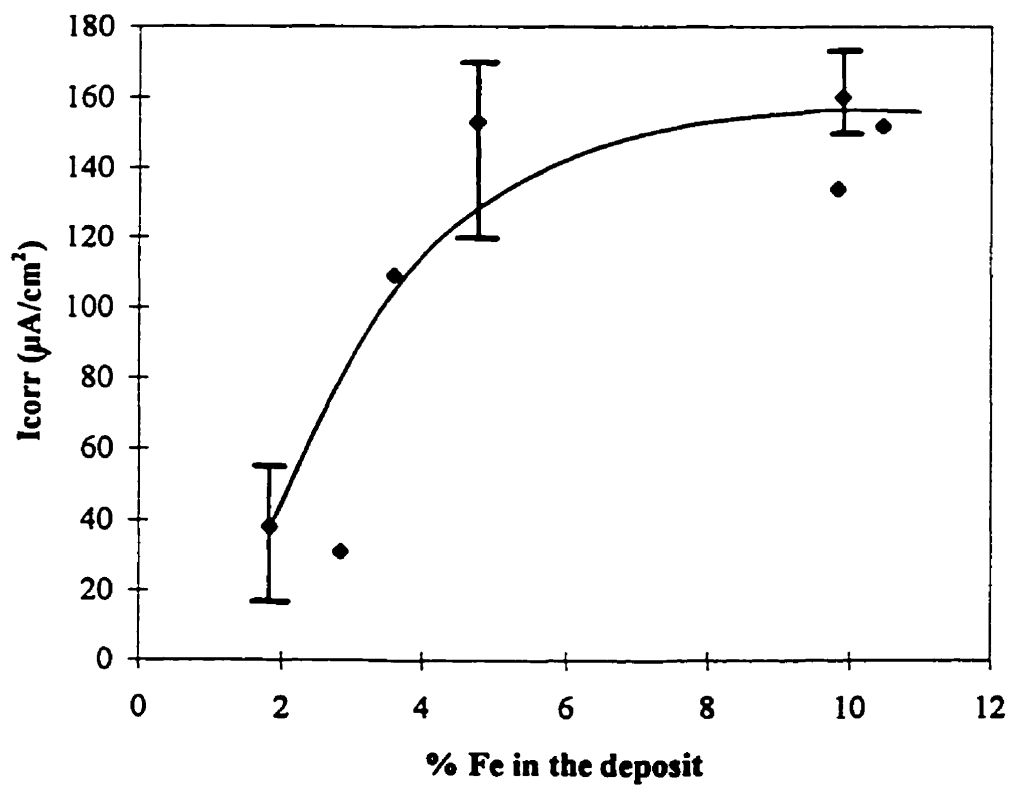


Figure 6.6. Correlation between iron content in the deposit and corrosion current of zinc-iron electrodeposited coatings.

The comparison of the microstructural characteristics and the corrosion behavior of coatings strongly indicates that texture is one of the most important microstructural parameters responsible for corrosion resistance. Of course, the influence of other parameters, e.g. the surface morphology and alloy content cannot be excluded, because these parameters also change and are closely correlated with texture changes. The present study demonstrates that corrosion resistance is quite sensitive to the coating texture because a sudden increase of corrosion current for the coating deposited at  $200 \text{ mA/cm}^2$  definitely coincides with the transformation of texture from the basal to the pyramidal fiber components. The result obtained is consistent with the observation made on zinc coatings which had a better corrosion resistance for higher intensity of basal texture. From the discussion, it is concluded that the zinc-iron coatings exhibit the best corrosion resistance at a high intensity of the basal type texture as well as when the iron content in the deposit is small.

The corrosion potential of zinc-iron coatings is also a function of the iron content. Fig. 6.7 illustrates the change of corrosion potential as a function of percentage of iron in the deposit. It is evident that the corrosion potential of the investigated coatings continuously increases as the % Fe in the coating increases. The coating with an iron content of 1.9 %, for instance, has a corrosion potential value of -1100 mV. As the iron content increases up to 10.5 %, the corrosion potential also increases up to -1020 mV.

The phenomena of corrosion potential changing with the deposition current density should be attributed to compositional changes in the deposit. Since iron is more noble than zinc, the increase of iron content in the deposit causes the increase of corrosion potential. The corrosion potential for all the zinc-iron coatings tested remained negative with respect to the steel substrate. Therefore, all of the investigated zinc-iron coatings can provide a sacrificial protection to the substrate.

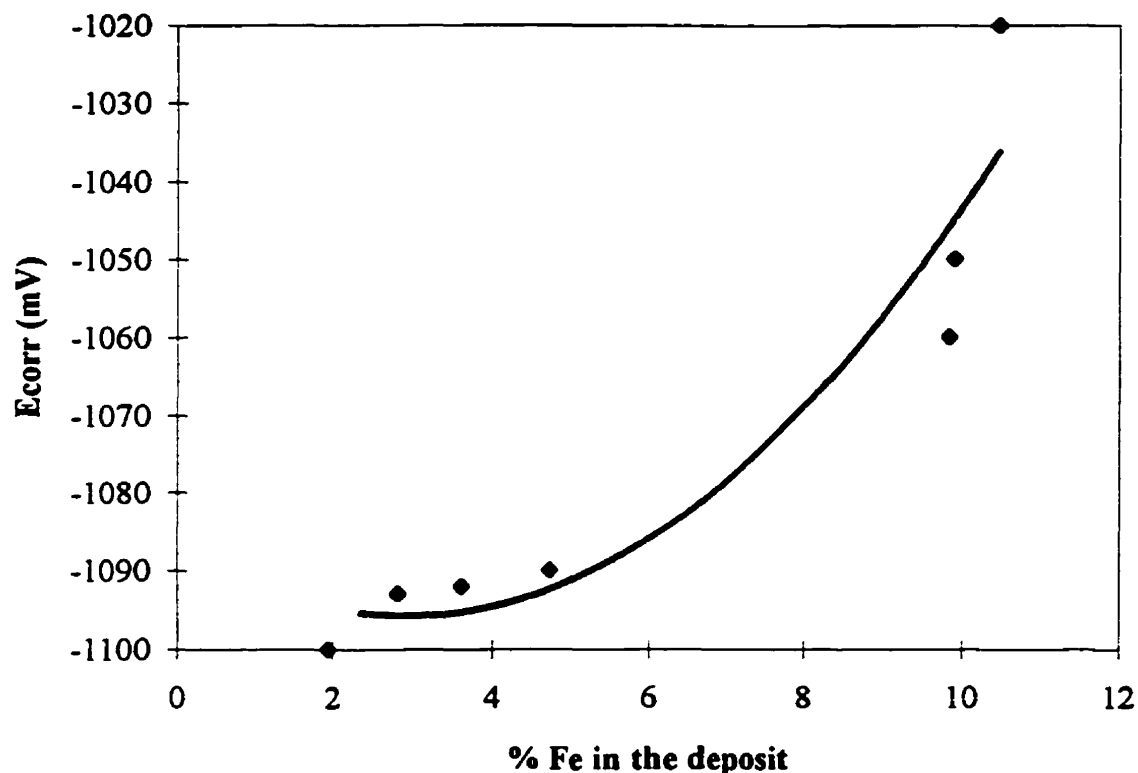


Figure 6.7. Correlation between iron content in the deposit and corrosion potential of zinc-iron electrodeposited coatings.

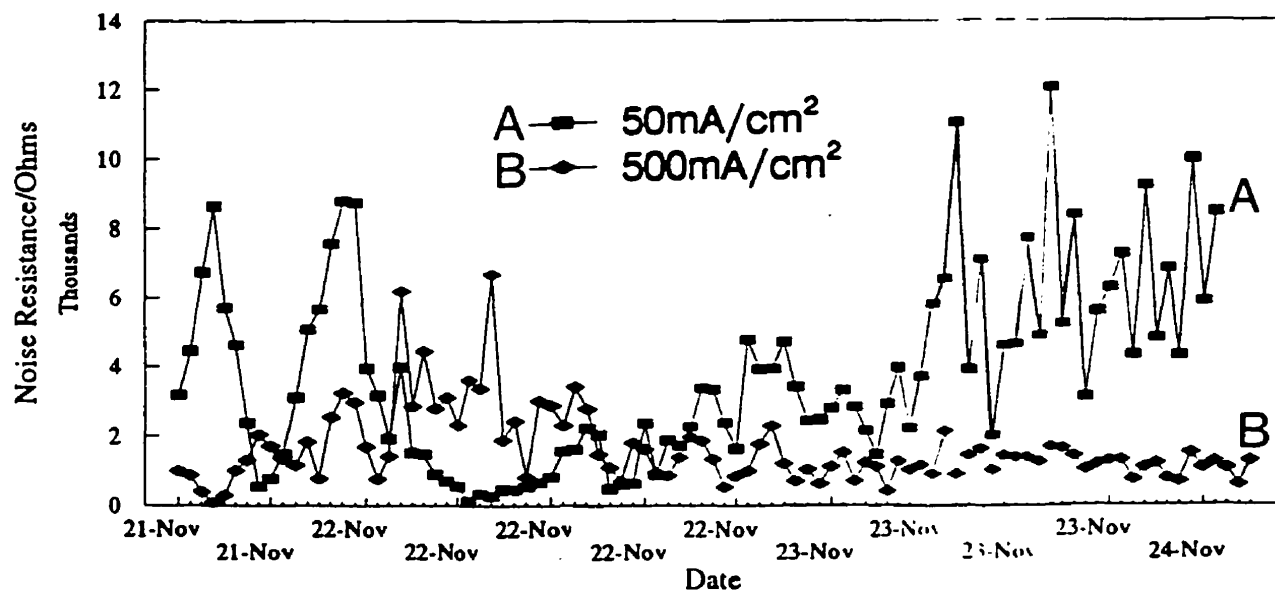


Figure 6.8. Electrochemical noise resistance measurement exhibits different corrosion behavior of zinc-iron electrodeposited coatings deposited at different current density; The coating of 50 mA/cm<sup>2</sup> shows large fluctuation of noise resistance possibly induced by the repeated reaction of passivation and localized corrosion attack, while the other coating of 500 mA/cm<sup>2</sup> shows a relatively small variation interpretable as an overall corrosion attack.

The electrochemical noise analysis was carried out to investigate the characteristics of corrosion behavior by measuring the electrochemical noise resistance of the coatings. This method characterizes the kinetics of the corrosion process by measuring the spontaneous fluctuation of the potential or the current of a corroding specimen. It also interprets the data as characteristics of corrosion behavior during the overall corrosion process. Fig. 6.8 shows an example of the different corrosion behavior of the coatings by illustrating the different corrosion noise resistance of the zinc-iron electrodeposited coatings. The coating deposited at the current density of  $50 \text{ mA/cm}^2$ , which has a strong basal texture intensity, exhibits higher noise resistance, indicating a better corrosion resistance compared to the coating that was deposited at  $500 \text{ mA/cm}^2$  which has a pyramidal texture. It is found that the coating with basal texture shows a fluctuation of noise resistance which is an indication of the repeated reaction of passivation and localized corrosion, while the coating with the pyramidal texture exhibits a relatively small variation which is an indication of overall homogeneous corrosion attack.

#### 6.2.2 CORROSION BEHAVIOR OF ZINC-NICKEL COATINGS

This section demonstrates the various corrosion behaviors of the zinc-nickel coatings produced at different deposition conditions. Fig. 6.9 illustrates the change of corrosion current as a function of nickel content in the deposit. The coatings that have a low ( $\sim 13\%$ ) nickel content show the lowest corrosion current, whereas coatings with nickel content higher than  $15\%$  show a high corrosion current. At this point, the contribution of phase transformation to the corrosion behavior should also be considered, since the  $\gamma$  phase starts to form at a nickel content above  $15\%$ . In the zinc-nickel coatings, the  $\eta$  phase dominates when the nickel content is around  $13\%$ , whereas the coatings have the  $\eta + \gamma$  dual phase at about  $15\%$  of nickel, as is demonstrated in chapter 5. This fact indicates that the formation of the dual phase is responsible for the sudden increase of corrosion current at this nickel percent range. Meanwhile, the coatings with higher nickel content (above  $20\%$ )

show poor corrosion resistance even though the coatings have a single  $\gamma$  phase. This observation implies that a further increase of nickel content above 20 % appears to have a detrimental effect on the corrosion resistance. Overall, it is concluded that the zinc-nickel coatings consisting of the  $\eta$  single phase at the lower nickel content of 13 to 15 % have better corrosion resistance than the coatings consisting of  $\gamma$  secondary phase produced at higher than 15 % of nickel content in the deposit.

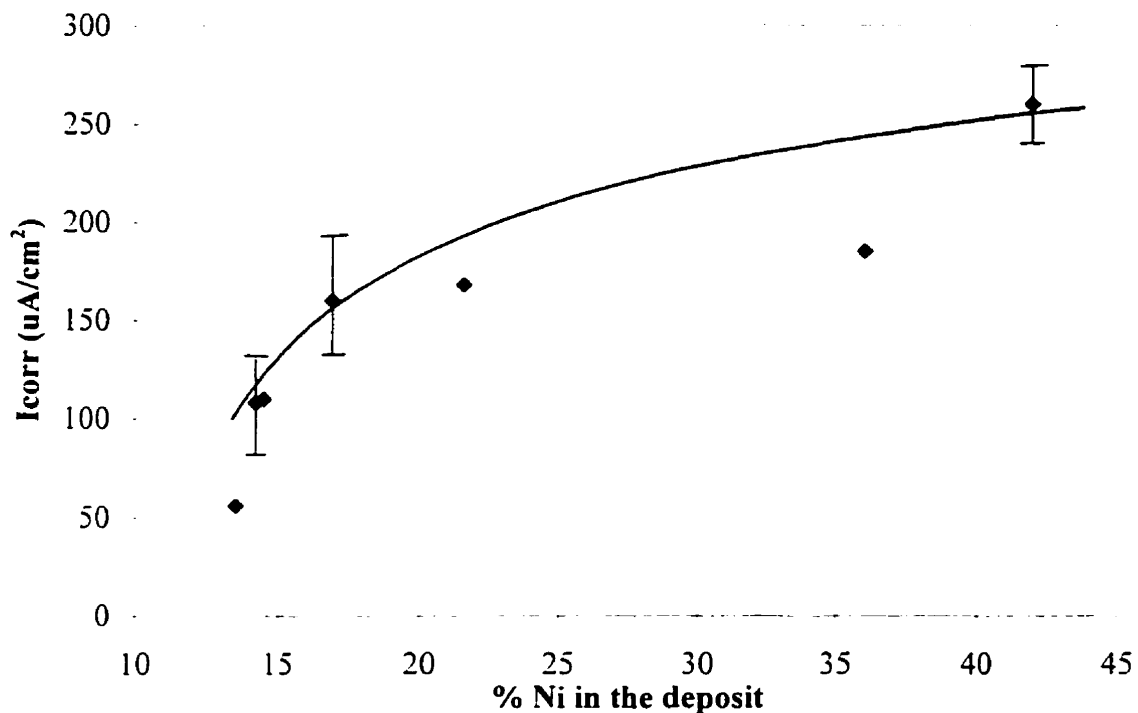


**Figure 6.9. Correlation between nickel content in the deposit and corrosion current of zinc-nickel electrodeposited coatings.**

From the above experimental results, one can learn the optimum alloy and phase compositions. The observation is in good agreement with the results of other researchers. Vlad [1990] reported the best corrosion resistance at Zn-13%Ni coatings. Alfantazi [1994] observed that the zinc-nickel coatings that consist of a single  $\gamma$  phase lower the corrosion resistance once the nickel content exceeds 20 %. Alfantazi also proposed that in the pulse-plated zinc-nickel coatings, the best



corrosion resistance is observed in the coatings having a nickel content of 14 to 20 % which consists of the  $\gamma$  single phase. At a similar range of nickel content, the DC plated zinc-nickel coatings consist of the  $\eta + \gamma$  dual phase. It can be argued that in the case of pulse plating, the absence of the  $\eta$  phase is attributed to the selective dissolution of the  $\eta$  phase during pulse-off time caused by the local electrochemical cell between the  $\gamma$  phase and the  $\eta$  phase [Kondo 1994, Alfantazi 1994]. Since the  $\gamma$  phase is electrochemically more noble than the  $\eta$  phase, the local cell between the two phases promotes the formation of a single  $\gamma$  phase.

The influence of texture upon the corrosion behavior of zinc-nickel coatings is described in Fig. 6.10. Fig. 6.10 illustrates the changes of the corrosion resistance of coatings as functions of the texture intensity. It is found that the corrosion resistance is improved when the intensity of  $\{100\}$  texture increases or the intensity of  $\{110\}$  texture decreases.

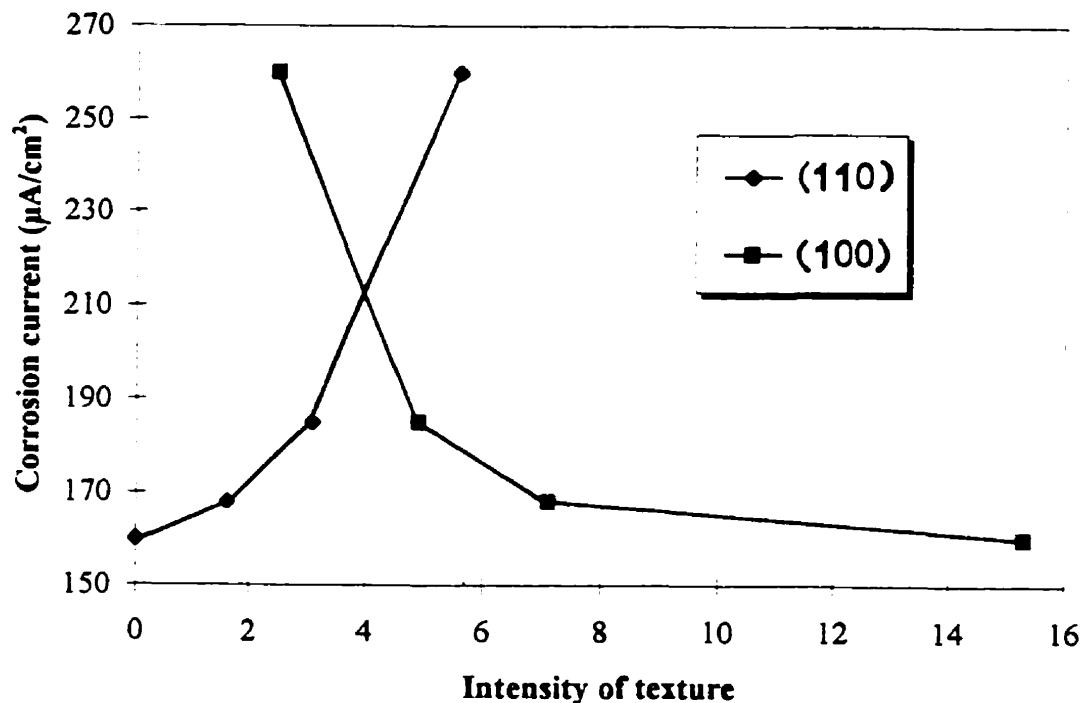
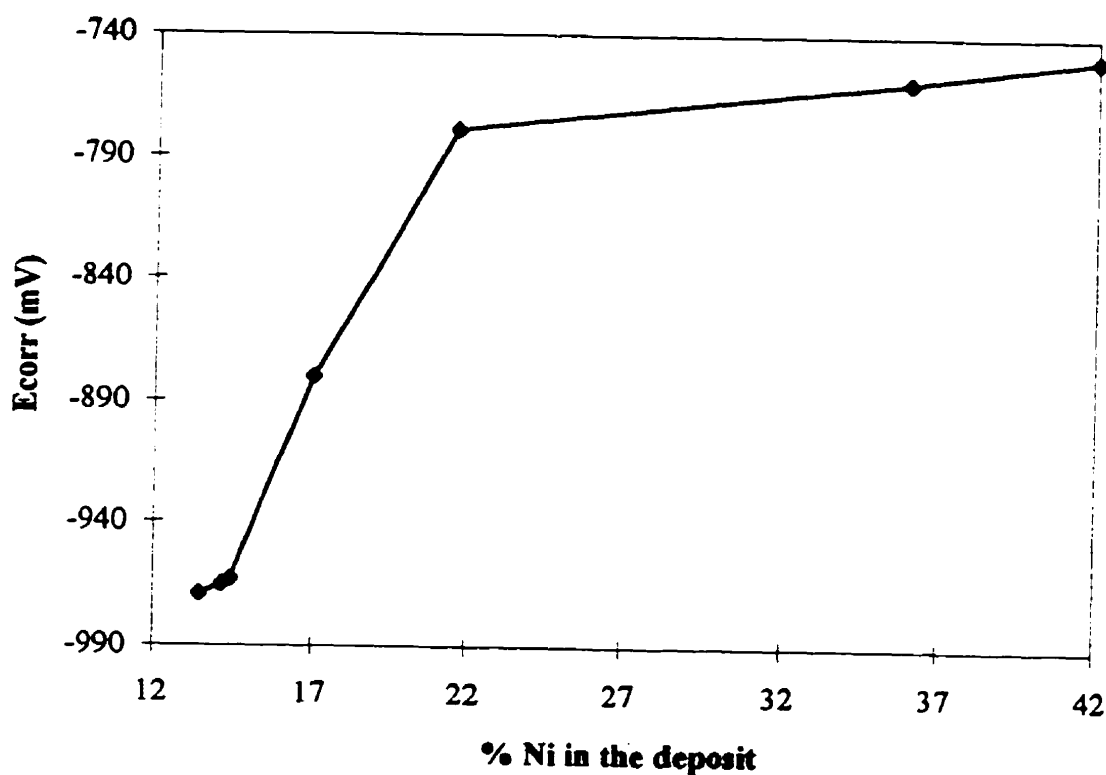


Figure 6.10. Correlation between intensity of texture and corrosion current of zinc-nickel electrodeposited coatings.

The effect of alloy composition on the corrosion potential is demonstrated. Fig.6.11 illustrates the change of corrosion potential as a function of nickel content in the deposit. The corrosion potential increases as the nickel content in the deposits increases. The coating that consists of 13.5 % Ni, for instance, has a corrosion potential of -969 mV. As the nickel content increases up to 42 %, the corrosion potential also increases up to -749 mV. The corrosion potential of zinc-nickel coatings increases with nickel content in the deposit because nickel is more noble than zinc. Similar observations were made for zinc-iron coatings (see 6.2.1).



**Figure 6.11. Correlation between nickel content in the deposit and corrosion potential of zinc-nickel electrodeposited coatings.**

The observation is in good agreement with other works [Alfantazi 1994]. Alfantazi reported that the corrosion potential of zinc-nickel coatings initially increased sharply from -1000 mV to -650 mV, as the nickel content in the deposit increased from 11 to 22 % and then, increases more slowly from -650 mV to -600 mV as the nickel content increased from 22 to 63 %. Alfantazi also concluded that the corrosion potential for all the coatings remained negative with respect to the steel substrate, and thereby the coatings play a role of galvanic protection for the substrate. Zinc-nickel coatings are also anodic with respect to the steel substrate in all compositional ranges and thus represent a sacrificial protective layer for the substrate.

From the present results and discussion, the influence of alloy composition, phase composition, and texture upon the corrosion behavior of zinc-nickel coatings was demonstrated. On the other hand, the effect of surface morphology on corrosion resistance, can also be assessed. In order to investigate how the surface morphology influences corrosion behavior, two zinc-nickel coatings were electrodeposited at identical deposition conditions. Thus, the texture, the alloy composition as well as the phase composition of deposits, are the same in both coatings. One of the coatings was then polished with 1  $\mu\text{m}$  diamond paste after the electrodeposition while the other coating was left unpolished. The polishing process allows us to reduce the roughness and to reveal the coating surface with the  $\{100\}$  plane parallel to the substrate. The coating has a sharp  $\{100\}$  fiber texture as was previously demonstrated in section 5.4.2. The specimens after such preparations have different surface morphologies, but the texture, alloy composition and phase composition of the deposit is the same. Fig. 6.12 demonstrates that the polarization curves obtained from both coatings are different. It is clear that the change of surface condition is directly responsible for different corrosion behavior. In order to characterize the influence of the initial surface morphology on corrosion behavior, corrosion tests were repeated on the same specimens several times. Fig. 6.13 shows the change of corrosion current as a function of time. Overall, the polished coatings exhibit lower corrosion currents

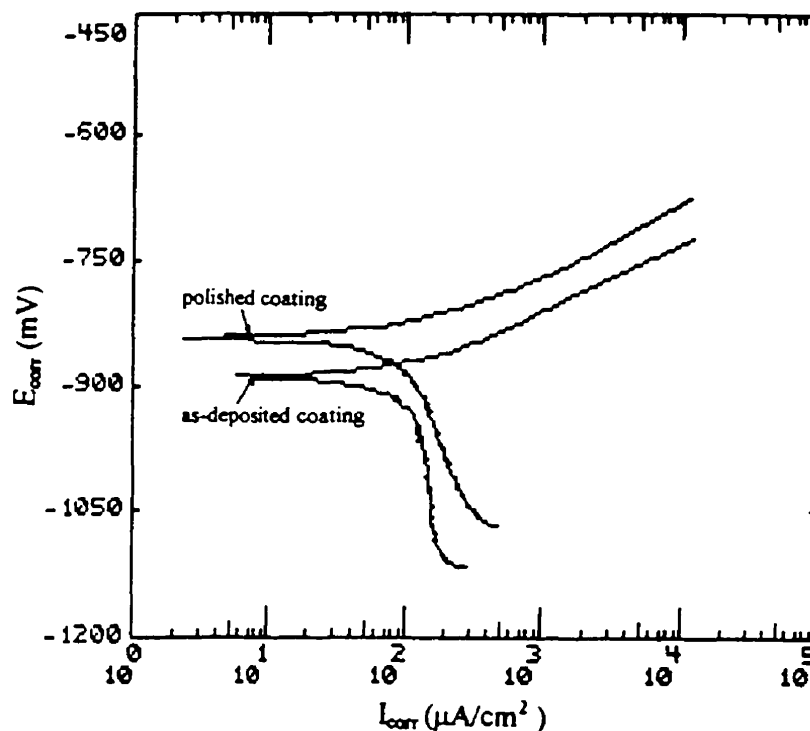


Figure 6.12. Polarization curves of zinc-nickel electrodeposited coatings exhibit different corrosion behavior from the coatings of polished surface and as-deposited.

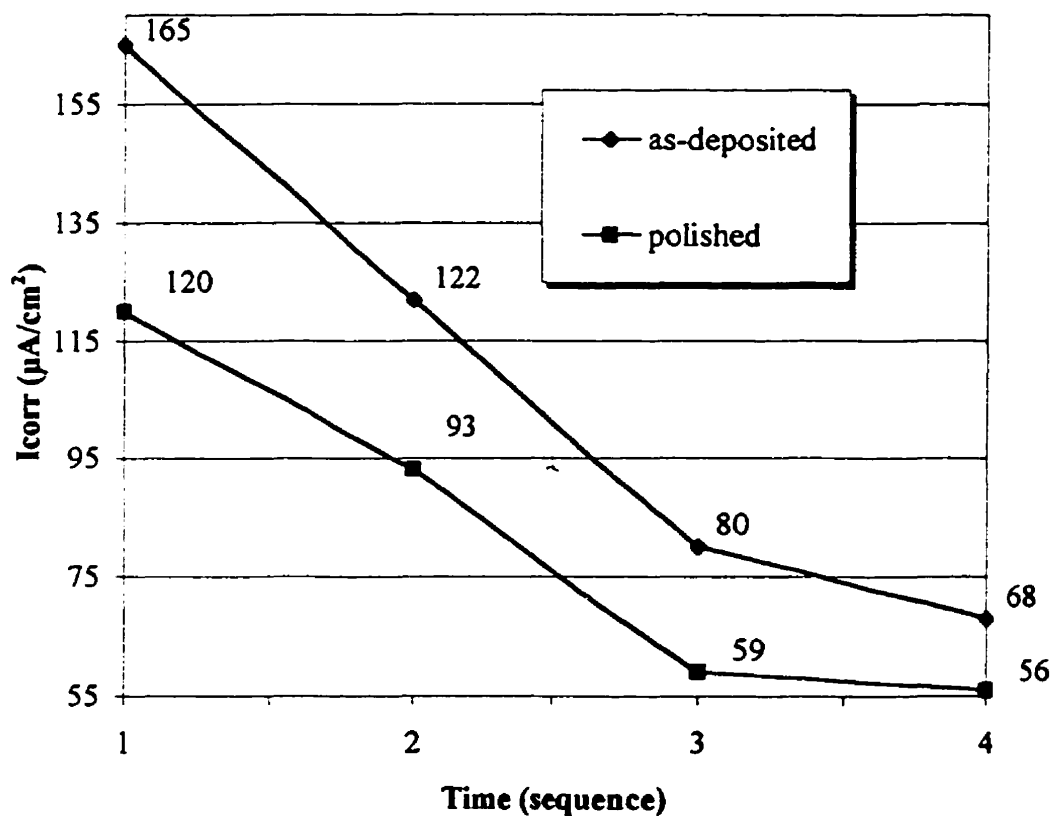


Figure 6.13. Change of corrosion current as a function of time for the zinc-nickel electrodeposited coatings of different surface morphology.

compared to those obtained from the as-deposited coating. Both coatings show a gradual decrease in corrosion current as the corrosion test is repeated. It is characteristic that the difference in corrosion current value between the two coatings gradually decreases as the corrosion test is repeated. This observation suggests that the initial surface morphology of coatings plays an important role in improving the corrosion resistance of coatings. It can be concluded that the coating with the polished surface has a better corrosion resistance than the coating with the surface as-deposited.

Since changes of surface conditions are responsible for different corrosion resistance, the following two factors should be taken into account: (1) the surface area of the coating, (2) a proportion of crystallographic planes which are exposed to the corrosion attack. In the case of the polished coating, the deposit has a lower roughness than the as-deposited coating, thereby having a smaller surface area which means that the corrosion reaction is slower. Moreover, the polished coating has the {100} plane parallel to the coating surface, whereas the surface of the as-deposited coating is covered with crystallographic planes other than the {100} planes. Since the {100} texture is found to be beneficial to the corrosion resistance, the {100} plane can protect the coating surface better than other crystallographic planes from corrosion attack.

It should be noted that, as the corrosion test is repeated, both the corrosion current values and the difference between corrosion current of the two coatings diminishes. This indicates that the surface conditions of the two coatings eventually become similar after repeated corrosion tests. A decrease of corrosion current as seen after repeating the corrosion tests can be attributed to the barrier protection mechanism suggested by several researchers [Lambert et. al 1986, Alfantazi 1994]. They proposed the barrier protection mechanism to explain the superior corrosion resistance observed for the zinc-nickel coatings. According to

them, during the corrosion process, zinc dissolves preferentially leaving a top layer enriched with nickel and this layer would act as a barrier against further corrosion attack.

Fig. 6.14 demonstrates changes of corrosion potential as a function of time. The corrosion potential changes in a similar way as the corrosion current changes. The difference of corrosion potential between two coatings is highest at the early stage of the corrosion test. The corrosion potential of the polished coating is -815 mV, while that of the as-deposited coating is -898 mV. With time, the corrosion potential of the polished coating decreases to -858 mV, while that of the as-deposited coating increases to -860 mV.

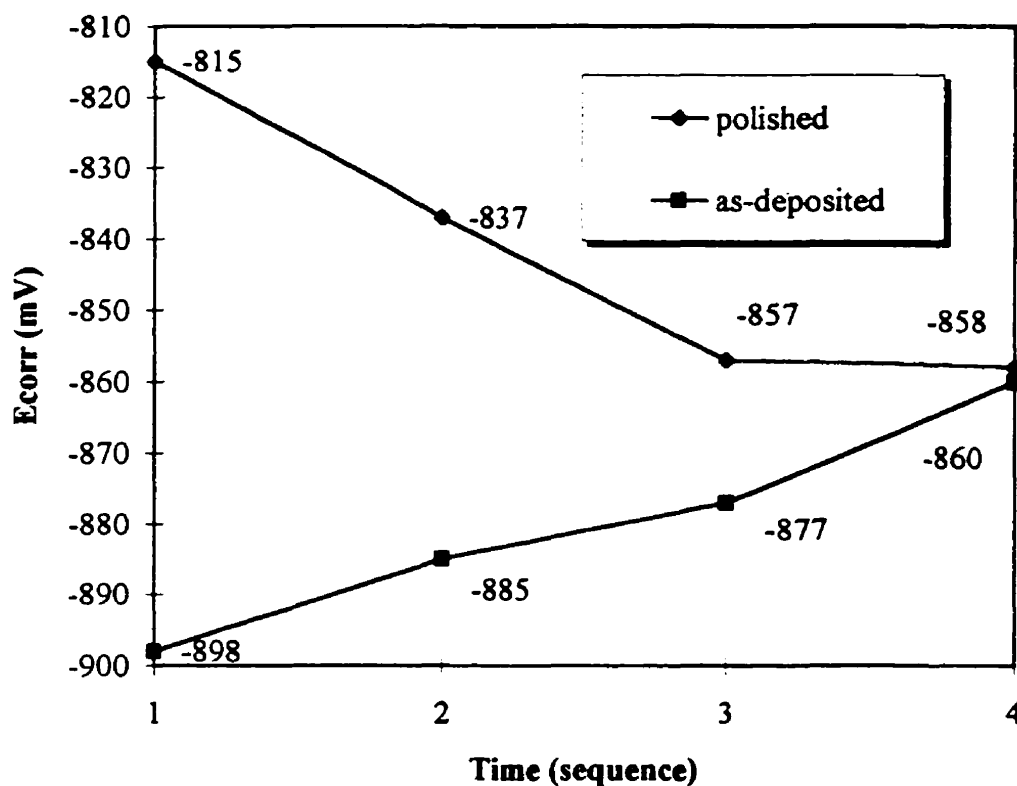


Figure 6.14. Change of corrosion potential as a function of time for the zinc-nickel electrodeposited coatings of different surface morphology.

After the corrosion test, X-ray diffraction patterns are measured for both coatings to investigate differences in the peak intensity of coatings and the substrate. As is shown in Fig. 6.15, both coatings have diffraction peaks for the zinc-nickel coating and the steel substrate. The peaks for the coatings represent the  $\eta$  {1011} and the  $\gamma$  {100} planes, while the three peaks of the substrate are the {110}, {200} and {211} of Fe. The relative peak intensity of the steel substrate to the coating is higher in as-deposited coating than for the polished coating. This is an indication that a larger amount of deposit is removed from the steel substrate during the corrosion reaction of the as-deposited coating than the polished coating. The X-ray diffraction data is, therefore, in agreement with the result of the electrochemical corrosion testing which showed that the corrosion resistance of the polished coating is better.

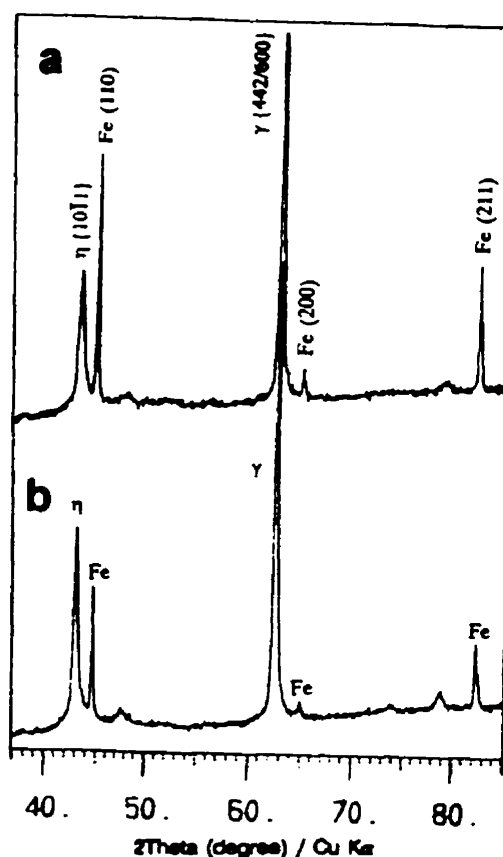


Figure 6.15. X-ray diffractometry exhibits that after the corrosion test, the polished coating has weaker Fe substrate peaks compared to those of the as-deposited coating: (a) as-deposited coating and (b) polished coating.

### 6.2.3. OPTIMUM DEPOSITION CONDITIONS FOR THE BEST CORROSION RESISTANCE OF ZINC ALLOY COATINGS

In this section, the optimum deposition conditions for the best corrosion resistance of zinc alloy coatings are discussed. Fig. 6.16 shows the changes of the corrosion current as a function of the deposition current density which varies from 50 to 500 mA/cm<sup>2</sup> during the deposition. It is clear that the corrosion current increases as the deposition current density increases. The coatings deposited at 50 mA/cm<sup>2</sup> exhibit values of corrosion current around 38 μA/cm<sup>2</sup>. In the case of coatings deposited at the higher applied current densities of 200 mA/cm<sup>2</sup>, the corrosion behavior changes dramatically and the corrosion current significantly increases to an average value of 153 μA/cm<sup>2</sup>. Further increase in the current density from 200 to 500 mA/cm<sup>2</sup> does not change the corrosion current significantly. The best corrosion resistance is achieved in the coating deposited at low current density which is in favor of a strong basal texture, morphology of hexagonal platelets and ridges, a low iron content and a single η phase in the deposit. It is recommended, therefore, that the zinc-iron coatings should be electrodeposited at a low current density range of less than 100 mA/cm<sup>2</sup>. In this case, other deposition parameters were kept constant. The pH value of the electrolyte was about 3.8 and the bath temperature was kept at 50°C. The bath composition is described in section 3.2. The deposition time was adjusted to produce a coating thickness of 5 μm.

The zinc-nickel coatings show a different corrosion behavior as the deposition current density changes. The change in corrosion current is plotted as a function of the deposition current density in Fig. 6.17. The coatings deposited at the current density of 50 mA/cm<sup>2</sup> show an average corrosion current of 160 μA/cm<sup>2</sup>. As the current density increases to 100 mA/cm<sup>2</sup>, the corrosion current drops to 56 μA/cm<sup>2</sup>. Further increase in the deposition current density up to 1200 mA/cm<sup>2</sup> results in a dramatic increase of corrosion current up to 260 μA/cm<sup>2</sup>. It is



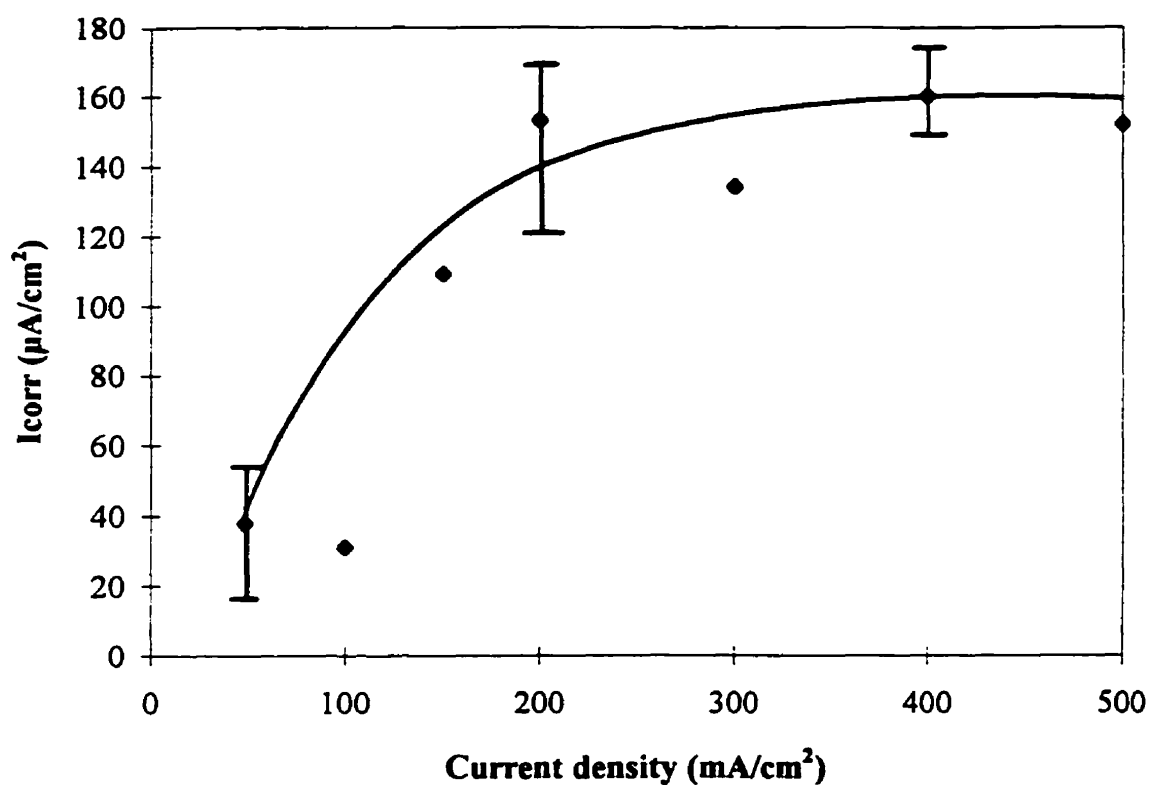


Figure 6.16. Correlation between deposition current density and corrosion current of zinc-iron electrodeposited coatings.

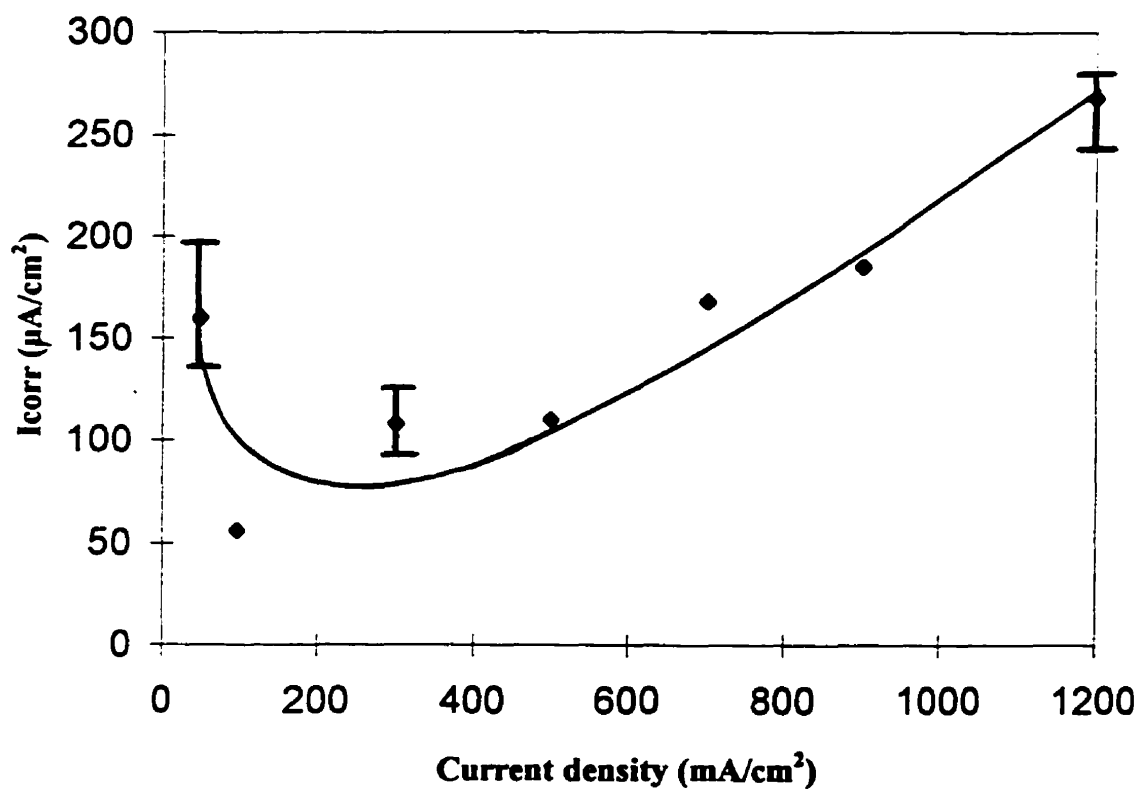


Figure 6.17. Correlation between deposition current density and corrosion current of zinc-nickel electrodeposited coatings.

surprising to find a similarity between Fig. 6.17 and Fig. 5.12 of section 5.2.3, in which the change of the percentage of nickel is plotted as a function of current density. Obviously, this suggests that there is a correlation between the applied current density, nickel content in the deposit as well as the corrosion behavior of zinc-nickel coatings. Therefore, for the best corrosion resistance, it is recommended that the coatings should be deposited in the current density range of 100 to 500 mA/cm<sup>2</sup> to produce the deposit with the nickel content of 13 to 15 %. It should be noted that the zinc-nickel coatings at this range of composition consist of the  $\eta$  single phase only.

#### 6.2.4. SUMMARY

This section demonstrates that corrosion behavior of the zinc-iron and the zinc-nickel coatings which have different texture, morphology, and alloy content in the deposit is different. Optimum deposition conditions are proposed for acquiring the best corrosion resistance for coatings.

1. In the zinc-iron coatings, the deposits consisting of a strong basal texture have better corrosion resistance.
2. The kinetics of the corrosion process is investigated using the electrochemical noise resistance test. The coating consisting of a basal texture shows large fluctuation of noise resistance which is an indication of repeated reaction of passivation and localized corrosion, while the coating with pyramidal texture exhibits a relatively small variation which is an indication of overall corrosion attack.
3. In zinc-nickel coatings, a correlation is found between the nickel content in the deposit, the phase composition and the corrosion resistance. The

coatings that consist of the  $\eta$  single phase with a nickel content of 13 to 15 % exhibit a better corrosion resistance than the coatings composed of the  $\eta$  +  $\gamma$  dual phase with a high nickel content in the deposit.

4. For optimizing the corrosion resistance of zinc-iron electrodeposited coatings, it is recommended that the coatings should be deposited at a current density range of 50 to 100 mA/cm<sup>2</sup>. Other deposition parameters were kept constant (pH: 3.8 and coating thickness: 5  $\mu$ m).
5. For the best corrosion resistance of zinc-nickel electrodeposited coatings, it is recommended that the coatings should be deposited at a current density range of 200 to 500 mA/cm<sup>2</sup> to produce a deposit with a nickel content of around 13%. Other deposition parameters were kept constant (pH: 2.3 and coating thickness: 15  $\mu$ m).

## ***CHAPTER SEVEN***

# **MICROSTRUCTURAL CHARACTERIZATION OF ZINC ALLOY COATINGS**

In chapters 4 and 5, it was demonstrated that a variety of microstructures of zinc based coatings can be obtained at different deposition conditions. The evolution of microstructure - texture, morphology, alloy composition, interplanar spacings, and phase composition as functions of current density, pH, and coating thickness were also discussed. The research has been focused on obtaining experimental results. In this chapter, discussion, comparison and analysis of the observations with the experimental works by other researcher's is done. Since the texture and morphology of zinc based coatings were discussed in chapter 4 and 5, this chapter mainly focuses on the characteristics of alloy composition and phase of zinc alloy coatings.

### **7.1. CHANGE OF MORPHOLOGY AND ALLOY COMPOSITION WITH COATING THICKNESS**

The observation in section 5.2.2 demonstrated that the morphology and alloy content of zinc-iron coatings changes when the coating thickness changes. It was found that the morphology of zinc-iron coatings evolves from triangular pyramids to hexagonal columnar crystals with increasing coating thickness, while the iron content in the deposit decreases from 10.2 to 0.6 %. The changes in alloy composition of coatings can be explained by two phenomena proposed by Brenner [1962]; (1) the nature of the initial cathode surface, and (2) the diffusion phenomenon. Brenner noted that cathode overpotential or current efficiency can influence the composition of electrodeposited alloys. Since the cathode surface of

the substrate metal is immediately covered with a layer of the deposit, the next layer is less affected by the substrate, and therefore different morphologies can be formed in thicker deposits. This discussion, however, is confined to a very thin layer, and thus is insufficient to explain the observation of the continuous decrease of iron content up to 100  $\mu\text{m}$ , since the effects of the substrate would diminish as soon as the coating became a few layers thick and consecutive layers would contact another layer of coating and not the substrate.

The diffusion phenomenon in the vicinity of the cathode surface will also affect the composition of the deposit. At the initial state of deposition, the concentration of more noble metal ions (iron) in the electrolyte adjacent to the cathode starts to decrease and, eventually reaches a steady state in which the concentrations become constant. Since more noble metals preferentially deposit at the initial stage of the deposition, a thin deposit exhibits a higher concentration of noble metal than a thick deposit. The experimental results indicate that the concentration of the more noble metal (iron) is higher in the layers close to the substrate and gradually decreases as the coating thickness increases. There is other supportive evidence for changes of the alloy composition with thickness. In zinc-copper codeposition, Brenner [1963] reported that the initial deposit contains a higher percentage of noble metal (copper), and this percentage gradually decreases as thickness increases.

The morphological observation also suggests that the change of cathode surface area can influence the alloy composition in the deposits. It was observed that the surface morphology of the coatings consists of pyramidal grains when the coating thickness is under 10  $\mu\text{m}$ . Further increase in thickness, however, is associated with a rough surface morphology and, subsequently increases the total cathode surface area. This fact causes the redistribution of current density on the cathode surface. During the electrodeposition, the applied current is kept constant.

Thus, the real value of current density would decrease because of the surface area increase, as the coating thickness increases.

It should be noted that in these observations the alloy composition changes significantly in the range of thick coatings (10 to 100  $\mu\text{m}$ ), whereas only small change was observed in thin coatings ( $< 10 \mu\text{m}$ ). This fact indicates that the thin coatings are more homogeneous and less rough than thick coatings. In commercial application, the zinc-iron coatings have a thickness of about 5 to 8  $\mu\text{m}$ , and no significant change of alloy composition is found at this thickness range.

It was also found that the coating obtained at high applied current density has a higher iron content than the coating deposited at low current density. The coating deposited at 500  $\text{mA}/\text{cm}^2$  with a thickness of 100  $\mu\text{m}$  has the pyramidal morphology and about 8 percent of iron. The coating deposited at 300  $\text{mA}/\text{cm}^2$  contains 0.6 percent iron in the deposit. This fact indicates that high applied current compensates for the current density drop caused by an increase of surface area in thick deposits.

## 7.2. THE OVERSATURATED $\eta$ PHASE OF ZINC-IRON COATINGS

In the present work, it is observed that zinc-iron coatings have the iron oversaturated single  $\eta$  phase at an iron content higher than 10 percent. Since the solid solubility of iron in zinc is quite minimal in the equilibrium state (less than 0.02 %) [Hamsen and Anderko 1958, Fujieda 1992, Porter 1991, Mackowiak 1979], the iron oversaturated  $\eta$  phase is a metastable phase formed under non-equilibrium conditions during the electrodeposition process.

The coatings are composed of the single  $\eta$  phase with a large variation (about 2 to 11 %) in the iron content. The existence of the  $\eta$  phase at such a wide

range of iron content indicates that there is a continuous microstructural change without any major phase transformations. This is confirmed by X-ray diffraction experiments that show large variations in interplanar spacings with a change in the percentage of iron in the deposit. The change of interplanar spacings subsequently influences the  $c/a$  ratio of  $\eta$  phase. It was found that the  $c/a$  ratio decreases with increasing iron percentage in the coatings.

In section 5.3.1, it is demonstrated that the  $c/a$  ratio of  $\eta$  phase zinc-iron coatings decreases when the iron content in the deposit increases. The change of the  $c/a$  ratio with iron content might be related to the atomic lattice geometry. The  $\eta$  phase has an hcp structure, and the iron atoms should locate themselves in substitutional sites and form an oversaturated solid solution of the  $\eta$  phase with zinc atoms. It should be noted that these substitutional atoms (iron) are smaller in size than zinc atoms: The diameter of an iron atom is 2.482 Angstrom, and that of a zinc atom is 2.665 Angstrom, thus the volume of an iron atom is about 80% of a zinc atom. The substitution of atoms which have a different size will induce a change of lattice geometry. Suppose that the iron atoms are added randomly to the zinc hexagonal structure, the equilibrium lattice parameters of the pure zinc structure should gradually change in such a manner that the free energy of the atomic lattice is minimized. Since the linear density along the  $c$ -axis is lower than the  $a$ -axis, the addition of iron atoms results in a significant shrinkage of the  $c$ -axis. Of course, there is also a decrease in linear density along the  $a$ -axis, but this does not cause shrinkage of the  $a$ -axis because the  $\{0001\}$  basal plane is a close packed plane and therefore, a small portion of substitutional iron atoms ( $\sim 10\%$ ) in zinc does not cause a decrease of the  $a$ -axis.

The observation of the change of  $c/a$  ratio with iron content is in good agreement with results obtained by other researchers [Shima et. al. 1986, Lin 1992, Kondo 1994]. Kondo and Lin observed that the interplanar spacings for the  $\eta$  phase varies as the alloy content of zinc-iron coatings change. They reported that the  $c/a$  ratio of the  $\eta$  phase decreases as the percent of iron in the coatings increases.

### 7.3. ANOMALOUS CODEPOSITION OF ZINC ALLOY COATINGS

The observation made on zinc-iron coatings demonstrates that the content of more noble metal (iron) in the deposit increases when the current density increases. The change of iron content was attributed to the anomalous codeposition behavior during electrodeposition, as was discussed in section 5.2.1. In the case of zinc-nickel coatings, the deposition behavior is completely different from that of zinc-iron. It was discovered that the content of the more noble metal (nickel) decreases at low current densities and increases at high current densities. The decrease of nickel content at the range of low current densities can be attributed to the anomalous codeposition behavior that is, the content of the more noble metal (nickel) decreases with increasing current density. Further increase in current density, eventually results in the opposite reaction in which the nickel content in the deposit increases significantly due to the high depletion in zinc ions at the cathode film.

### 7.4. PHASE COMPOSITION AND MORPHOLOGY OF ZINC-NICKEL COATINGS

In section 5.3.2, it is demonstrated that the phase of zinc-nickel coatings transforms from the single  $\eta$  phase, through the dual  $\gamma + \eta$  phase, to the  $\gamma$  phase, as the nickel percentage in the deposit increases. This dual phase has also been reported on by other studies on zinc-nickel coatings produced by pulse plating [Alfantazi 1994]. In the pulse plating cases, however, the dual phase exists at a low nickel content (8 to 12 %). This differs from the present result obtained from DC plated coatings because the single  $\eta$  phase exists at low nickel contents, while the dual phase is formed only at a high nickel contents ( $\sim 17$  %). Different plating methods may be responsible for the existing difference. At low nickel contents, the  $\eta$  phase is the major phase. The evolution of a secondary  $\gamma$  phase, therefore, should



be followed by diminishing of the  $\eta$  phase. The evolution of the  $\gamma$  phase can be attributed to the effect of a local galvanic cell between two phases, which was argued by Kondo [1994]. Kondo proposed that the formation of a local galvanic cell between the  $\eta$  and the  $\gamma$  phase during pulse current-off time might dissolve the  $\eta$  phase selectively and promote the formation of a secondary  $\gamma$  phase and consequently produce the  $\gamma + \eta$  dual phase even at low nickel contents. Other experimental results are in agreement with the present observations [Fountoulakis et. al. 1984]. They reported that the dual  $\gamma + \eta$  phase formed at low nickel contents ( $\sim 8\%$ ) for the case of pulse plating, whereas only the single  $\eta$  phase was obtained in DC plated coatings.

It was demonstrated in section 5.2.3 that the morphology of the zinc-nickel coatings evolves with a nickel content increase from the pyramidal grains, through the mixed morphology of pyramids and tiny particles and finally to the “cauliflower-like” structure. Similar findings are reported by Alfantazi and Erb [1994] and Kondo [1994]. Alfantazi and Erb observed that the morphology of zinc-nickel coatings change from hexagonal platelets to nodular and eventually to “cauliflower-like” structures when the nickel content increases. Kondo found that the morphological characteristics of  $\eta + \gamma$  dual phase is the tiny submicron size granules, which represents the  $\gamma$  phase dispersed among the pyramidal grains of the  $\eta$  phase. Those observations are in agreement with the present study.

## **CHAPTER EIGHT**

### **SUMMARY AND CONCLUSIONS**

#### **8.1. SUMMARY AND CONCLUSIONS**

In this work, the microstructure and corrosion behavior of the electrodeposited zinc, zinc-iron, and zinc-nickel coatings are analyzed. The evolution of texture, surface morphology, crystallographic lattice, alloy composition and phase of coatings are investigated at various deposition conditions. It is demonstrated that the corrosion behavior of coatings can be correlated with the microstructure and texture of coatings. Consequently, it is proposed how to optimize the deposition process to obtain the desirable texture, morphology and alloy content of the deposit for better corrosion resistance.

#### **Morphology and Texture of Zinc Coatings**

1. It is demonstrated that the morphology and the texture of zinc coatings significantly changes with deposition parameters. As the current density increases from 30 to 500 mA/cm<sup>2</sup>, the coating surface evolves from the morphology of hexagonal platelets and ridges to the pyramidal morphology, while the texture changes from the texture of the basal {0001} fiber and the pyramidal {10 $\bar{1}$ 3} non-fiber component to the pyramidal {10 $\bar{1}$ X} fiber texture. Other deposition parameters are kept constant (pH: 3.8 and coating thickness: 6  $\mu$ m).
2. As the pH of the electrolyte increases from 1 to 5, coating morphology changes from the hexagonal platelets and ridges type to the hexagonal ridge-

only morphology, while the texture changes from the texture of an extremely strong and sharp basal fiber and some pyramidal non-fiber components to the major pyramidal  $\{10\bar{1}X\}$  texture. Other parameters are kept constant (current density:  $300 \text{ mA/cm}^2$  and coating thickness:  $6 \text{ }\mu\text{m}$ ).

3. As the coating thickness increases from  $0.6$  to  $100 \text{ }\mu\text{m}$ , the morphology evolves from the sub-micron sized particles to the thin hexagonal ridges, to the packets of thicker hexagonal platelets, then to the randomly oriented ridges and finally to the hexagonal columnar crystals. At the same time, the pyramidal texture gradually disappears, while the basal texture becomes widely dispersed. Other parameters are kept constant (current density:  $30 \text{ mA/cm}^2$  and pH: 3.8). This observation indicates that the influence of the substrate gradually diminishes with increasing coating thickness.

#### Microstructural Characteristics of Zinc-Iron and Zinc-Nickel Coatings

1. Investigation of zinc-iron coatings demonstrates that the texture evolves from the basal fiber and non-fiber pyramidal components to the pyramidal fiber texture when the current density increases from  $50$  to  $500 \text{ mA/cm}^2$ . Other parameters are kept constant (pH: 3.8 and coating thickness:  $5 \text{ }\mu\text{m}$ ).
2. The iron content in the zinc-iron coatings increases with the current density increase, whereas the c/a ratio decreases.
3. The morphology of zinc-iron and zinc coatings is strongly correlated with texture. The morphology of hexagonal ridges represents the  $\{10\bar{1}3\}$  non-fiber texture. The morphology of flat hexagonal platelets represents the  $\{0001\}$  fiber texture. The  $\{10\bar{1}X\}$  fiber texture corresponds to the morphology of triangular pyramids which represents a hexagonal columnar

crystal tilted from the substrate surface; one wall of the pyramid represents the  $\{0001\}$  basal plane, while the other two walls represent the  $\{10\bar{1}0\}$  prismatic planes.

4. The morphology of the zinc-nickel coatings changes with the current density range of 50 to 1200 mA/cm<sup>2</sup>. Other deposition parameters are kept constant (pH: 2.3 and coating thickness: 15  $\mu$ m). The morphology of pyramidal grains and tiny particles transforms to the pyramidal grains, and finally to the “cauliflower-like” structure. This morphological transformation is associated with compositional changes from 13 to 42 % Ni, and changes in phase composition. The phase composition of coating changes from the  $\eta$  single phase, to  $\gamma + \eta$  dual phase and is then transformed to the  $\gamma$  single phase.
5. A special low current density deposition was conducted to illustrate the early stage of the deposition process. Initially, the substrate surface shows the morphology of “fish scale-like” platelets. As the growth continues, the morphology evolves to the triangular pyramidal grains.

### Corrosion Properties of Zinc and Zinc alloy Coatings

1. It is demonstrated that the texture of zinc and zinc-iron coatings strongly influences the corrosion resistance. The coatings with a strong basal texture exhibit a better corrosion resistance than the coatings with a weak basal texture or texture with a pyramidal fiber component.
2. In zinc-nickel coatings, a correlation is found between the nickel content in the deposit, the phase composition and the corrosion resistance. The coatings that consist of the single  $\eta$  phase at a nickel content of 13 to 15 % exhibit a

better corrosion resistance than the coatings composed of the  $\eta + \gamma$  dual phase observed at high nickel contents in the deposit.

3. For better corrosion resistance, optimum deposition conditions are suggested. This study focuses on proposing the most desirable range of deposition current densities, while other parameters are kept constant (see page 149 ~ 151). In the case of zinc coatings, the optimum current density is between 100 to 300 mA/cm<sup>2</sup>. Zinc-iron coatings are recommended to be deposited at 50 to 100 mA/cm<sup>2</sup>. Zinc-nickel coatings should be deposited in the current density range of 200 to 500 mA/cm<sup>2</sup>.

## 8.2. THE CONTRIBUTION TO ORIGINAL KNOWLEDGE

### **Demonstrating the correlation of texture and morphology of coatings at various deposition parameters**

Various researchers investigated the texture of electrodeposited coatings. Until now, however, there was no systematic experimental study on the evolution of texture and morphology under various deposition conditions. The author demonstrated that a correlation exists between texture, morphology and phase composition of zinc-based coatings at various deposition parameters, e.g. current density, pH of the electrolyte and coating thickness. This data may be used to control the microstructure of coatings for various engineering applications.

### **Proposing the optimum deposition conditions for the best corrosion resistance**

It was demonstrated that by changing texture, morphology and microstructure, one can significantly influence the corrosion properties of zinc-based coatings. Following this study, the author suggests the optimum deposition

conditions to obtain the desirable microstructure of coatings. As a main objective of this study, this work proposed how to control texture, morphology and the microstructure of the deposit by optimizing the deposition parameters for the best corrosion resistance.

### **Illustrating the morphology of zinc-based coatings by Atomic Force Microscopy**

Using conventional microscopy, surface morphology observation is limited to two-dimensional image analysis. However, the recent invention of AFM enabled a more precise three-dimensional topographic analysis of surface structure. The author used AFM for a better understanding of the evolution of the surface morphology of coatings. To the best of the author's knowledge, this is the first AFM study on the morphological evolution of zinc-based electrodeposited coatings at various deposition conditions, although there have been a large number of morphological studies on zinc-based coatings using SEM and TEM. The AFM section profile analysis enabled us to demonstrate the correlation between the morphology and texture of deposits by providing an exact value of the tilted angle between hexagonal ridges and the substrate surface and by obtaining a profile of triangular pyramidal grains.

### **Description of the early stage of electrodeposition at very low deposition current density**

The early stage of deposition behavior was described and analyzed by AFM for a better understanding of the growth mechanism of zinc-based electrodeposited coatings. In the initial stage, deposits have the morphology of "fish scale-like" hexagonal platelets. This was not known in the field of electrodeposited coatings. Therefore, the results obtained strongly supports that the facet and terrace growth

mode which is common for the CVD coatings are also valid for electrodeposited zinc-based coatings.

### **Demonstrating anomalous codeposition at high current densities**

Although the anomalous codeposition behavior is relatively well investigated in the range of low current densities, the studies of codeposition behaviors in the high current density range are very few. Electrodeposited zinc-based coatings have been produced at a high current density range for various industrial applications, and thus it is important to provide precise information about the coating microstructure at this range. The present work demonstrated the anomalous codeposition behavior of zinc-iron and zinc-nickel coatings in a wide range of current densities. Consequently, it was found that the anomalous codeposition led to a significant change in alloy content and c/a ratio in addition to changes in texture and morphology.

### **8.3. SUGGESTIONS FOR FURTHER WORK**

The experimental work performed in this thesis describes the characteristics of the microstructure of electrodeposited zinc-based coatings, which have attracted a lot of interest because of their application in the automotive industry. Further study can be suggested for a better understanding of coating behaviors.

1. The present study demonstrated that texture is closely related to the corrosion resistance of zinc-based coatings. The deposit's performance, however, is not only dependent on the corrosion resistance but is also dependent on other factors; for instance, paintability and formability are important mechanical properties essential to the coating performance. Therefore, further investigation

should be carried out on the influence of texture and microstructure on the mechanical properties of coatings to ensure the best coating performance.

2. It has been shown that the microstructure of coatings changes with deposition parameters. In order to verify the coating behavior more extensively, the electrodeposition should be conducted at various bath compositions and temperatures in addition to current densities and pH of the bath.
3. The present research was focused on zinc-iron coatings which have the oversaturated  $\eta$  single phase. Further work can be conducted on coatings with various phase composition in order to demonstrate the evolution of texture and morphology at the wide range of alloy content.



## REFERENCES

- Adaniya T., Hara T., Sagiya M., Honma T. and Watanabe T., *Plating and Surface Finishing*, August, 52 (1985).
- Adaniya T., Hara T., Sagiya M., Watanabe T. and Honma T., *ASM Metals / Materials Tech. Series*, No. 8512-022, 1 (1985).
- Ahmed M. and Pushpanaden F., *J. Crystal Growth*, **22**, 47 (1974).
- Ahmed M. and Pushpanaden F., *J. Crystal Growth*, **41**, 77 (1977).
- Akiyama T. and Fukushima H., *ISIJ International*, **32**, 787 (1992).
- Alfantazi A.M., El-Sherik A.M. and Erb U., *Scripta Metallurgica et Materialia*, **30**, 1245 (1994).
- Alfantazi A.M., *A study on the Synthesis, Characterization and Properties of Pulse-plated Ultrafine-grained Zn-Ni Alloy Coatings*, Ph.D. thesis, Queen's University, Kingston, Ontario (1994).
- Amblard J., Epelboin I., Froment M. and Maurin G., *J. Appl. Electrochem.*, **9**, 233 (1979).
- Amblard J., Froment M., Maurin G., Spyrellis N. and Trevisan-Souteyrand E., *Electrochim. Acta.*, **28**, 909 (1983).
- Armyanov S. and Sotirova-Chakarova G., *Metal Finishing*, Nov., 61 (1992).
- Armyanov S. and Sotirova-Chakarova G., *Metal Finishing*, Mar., 42 (1993).
- Ashton R.F. and Hepworth M.J., *Corrosion*, NACE, **24**, 50 (1968).
- ASTM standard 3-89, *Metals Test Methods and Analytical Procedures*, Annual book of ASTM standards (v.03.02, Wear and erosion; metal corrosion), ASTM (1994).
- Baraboshkin A.N., Martemyanova Z.S., Plaksin S.V. and Esina N.O., *Elektrokhimiya*, **14**, 9 (1978).
- Baraboshkin A.N., Martemyanova Z.S., Plaksin S.V. and Esina N.O., *Elektrokhimiya*, **13**, 1807 (1977).

- Barrett C. and Massalski T.B., *Structure of Metals*, 3rd ed., Pergamon Press, Elmsford, New York (1980).
- Bastin G. and Van Loo F.J.J. and Rieck G.D., *Z. Metallkde.*, **65**, 656 (1974).
- Bastin G. and Van Loo F.J.J., *Z. Metallkde.*, **67**, 694 (1976).
- Bastin G. and Van Loo F.J.J., *Z. Metallkde.*, **69**, 540 (1978).
- Bockris J.O'M. and Khan S.U.M., *Surface Electrochemistry - A Molecular Level Approach*, Plenum Press, New York (1993).
- Bockris J.O'M. and Razumney G.A., *Fundamental Aspects of Electrocrystallization*, Plenum Press, New York, (1967).
- Brenner A., *Electrodeposition of alloys*, Volume I and II, Academic Press, New York (1963).
- Budman E., *Metal Finishing*, February, 60 (1995).
- Bungue H.J., *Texture Analysis in Materials Science*, Butterworths, London (1982).
- Bush G.W., *JOM*, August, 34 (1989).
- Chang S., *Proc. TMS symposium on Zinc-based Steel Coating Systems* (Krauss G. and Matlock D.K. eds.), Detroit, Michigan, Oct. 7-11, 319 (1990).
- Chen Y.L. and Snyder D.D., *Proc. TMS Symposium on Zinc-based Steel Coating Systems* (Krauss G. and Matlock D.K. eds.), Detroit, Michigan, Oct. 7-11, 95 (1990).
- Chen Z.W., Gregory J.T. and Sharp R.M., *Metallurgical Transaction A*, **23A**, 2393 (1992).
- Crow D.R., *Principles and Applications of Electrochemistry*, Chapman & Hall, London, (1974).
- Cullity B.D., *Elements of X-ray Diffraction*, 2nd ed., Addison-Wesley Publ. Co. (1978).
- Damjanovic, Raicev R. and Bockris J.O'M., *J. Chem. Phys.* **47**, 2198 (1967).
- Dawson J.L. and Hladky K., *Corros. Sci.*, **22**, 231 (1982).
- Despic A., Raicev R. and Bockris J.O'M., *J. Chem. Phys.* **49**, 926 (1968).

EG&G, *Application Note: corr-1*, EG&G Princeton Applied Research (1982).

EG&G, *Application Note: corr-4*, EG&G Princeton Applied Research (1986).

Farr J.P.G. and Keen J.M., *J. Electrochem. Soc.*, **109**, 668 (1962).

Finch G.I. and Sun C.H., *Trans. Faraday Soc.*, **32**, 852 (1936).

Fontana M.G. and Greene N.D., *Corrosion Engineering*, 2nd ed., McGraw-Hill, New York (1978).

Forshee A.G., *Metal Finishing*, September, 50 (1993).

Fountoulakis S.G., Steinbicker R.N. and Fisher T.W., *Proc. AES 4th Continuous Strip Plating Symposium*, Chicago, Illinois, May 1-3 (1984).

Fujieda T., Naganawa A., Toyota M., Higuchi S. and Takahashi S., *ISIJ Int'l.*, **32**, 1044 (1992).

Fukushima H., Akiyama T., and Higashi K., *Metallwissenschaft und Technik*, **44**, 754, (1990).

Fukushima H., Akiyama T., Yano M., Ishigawa T. and Kammel R., *ISIJ*, **33**, 1009 (1993).

Gabe D.R., Wilcox G.D. and Pearson B.R., *Metal Finishing*, August, 34 (1993).

Gawne D.T. and Gudyanga T.F.P., in *Coatings and Surface Treatment for Corrosion and Wear Resistance*, Strafford K.N. et. al. eds., Ellis Horwood Ltd. Chichester, 28 (1984).

Geduld H., *Zinc Plating*, ASM Int'l Finishing Publication Ltd. (1988).

Girin O.B. and Panasenko A., *Zashchita Metallov*, **25**, 480 (1989).

Glocker R. and Kaupp E., *Z. Physik.*, **24**, 121 (1924).

Goodwin F.E., *Proc. TMS Symposium on Zinc-based Steel Coating Systems* (Krauss G. and Matlock D.K. eds.), Detroit, Michigan, Oct. 7-11, 183 (1990).

- Gu M., Notis M.R. and Marder A.R., *Proc. Int'l. Conf. on Zinc and Zinc Alloy Coated Steel Sheet (GALVATECH)*, ISIJ, Tokyo, Japan, 470 (1989).

Gu M., Notis M.R. and Marder A.R., *Proc. Int'l. Conf. on Zinc and Zinc Alloy Coated Steel Sheet (GALVATECH)*, ISIJ, Tokyo, Japan, 462 (1989).

- Gu M., Notis M.R. and Marder A.R., *Metallurgical Transactions A*, **22A**, 1737 (1991).
- Hada T., *Proc. Int'l. Conf. on Zinc and Zinc Alloy Coated Steel Sheet (GALVATECH)*, ISIJ, Tokyo, Japan, 111 (1989).
- Hansen M. and Anderko K., *Constitution of Binary Alloys*, 2nd ed., McGraw-Hill, New York, 738 (1958).
- Handreg I., Klimanek P. and Weidner H., *Mater. Sci. Forum*, **133-136**, 885 (1993).
- Hara T., Sagiya M. and Adaniya T., *Japanese Metal Society Bulletin*, **27**, 258 (1988).
- Hosny A.Y., El-Rafei M.E., Ramadan T.A. and El-Gafari B.A., *Metal Finishing*, November 55 (1995).
- Inagaki J., Morita M. and Sagiya M., *Proc. 5th Int'l. Conf. on Surface Modification Tech., The Inst. of Metals*, Birmingham, Sept. 2-4, 331 (1991).
- Irie T., *Proc. TMS Symposium on Zinc-based Steel Coating Systems* (Krauss G. and Matlock D.K. eds.), Detroit, Michigan, Oct. 7-11, 143 (1990).
- Itoh S., Okada G. and Seiyama T., *Denki Kagaku*, **42**, 242 (1974).
- Jesson D.E., Chen K.M. and Pennycook S.J., *MRS Bulletin*, April, 31 (1996).
- Jiricny V., *J. Appl. Electrochem.*, **17**, 91 (1987).
- Johnson E.S. and Legg G.E., *J. of Crystal Growth*, **88**, 53 (1988).
- Jones D.A. and Nair R., *NACE*, **41**, 357 (1985).
- Jordan D.L., *Proc. TMS Symposium on Zinc-based Steel Coating Systems* (Krauss G. and Matlock D.K. eds.), Detroit, Michigan, Oct. 7-11, 195 (1990).
- Kamei K. and Ohmori Y., *J. of Appl. Electrochem.*, **17**, 821 (1987).
- Kandeil A.Y. and Mourad M.Y., *Surface and Coating Technology*, **37**, 237 (1989).
- Kim H.M. and Szpunar J.A., *Material Science Forum*, **157-162**, 1997 (1994).
- Kimoto M., Yakawa A., Tsuda T. and Kammel T., *Metallwissenschaft und Technik*, **44**, 1148 (1990).

- Kondo K., Hinotani S. and Ohmori Y., *J. Appl. Electrochem.*, **18**, 154 (1988).
- Kondo K., *Morphology and Microstructure of Electrodeposited Zinc-Iron and Zinc-Nickel Binary Alloys; A Basic Study on Surface Treatment of Steel Sheets Used for Automobile Body*, Ph.D. Thesis, Kyoto University, Kyoto, Japan (1994).
- Kondo K., Yokoyama M. and Shinohara K., *J. Electrochem. Soc.* **142**, 2256 (1995).
- Kubaschewski O., *Binary Alloy Phase Diagram*, 2nd edition, Editor-in chief: Massalski T.B., ASM, 1795 (1991).
- Lambert M.R. and Hart R.G., *SAE technical report* No. 860266, (1986).
- Lawless, K.R., *Physics of Thin Films* (Hass G. and Thun R.E. eds.), Academic Press, (1967).
- Li D.Y. and Szpunar J.A., *Materials Science Forum*, **157-162**, 547 (1994).
- Li D.Y., *Texture Formation in Iron Electrodeposits*, Ph.D. Thesis, McGill University, Montreal, Canada (1995).
- Li D.Y. and Szpunar J.A., *Electrochimica Acta*, **42**, 37 (1997).
- Li D.Y. and Szpunar J.A., *Electrochimica Acta*, **42**, 47 (1997).
- Lin K-L, Yang C-F. and Lee J-T., *Corrosion*, **47**, 9 (1991).
- Lin Y., *Microstructure of Zinc-based Coatings on Steel Sheets*, Ph.D. Thesis, Northwestern University, Evanston, Illinois, (1992).
- Lin Y., Pak S.-W. and Meshii M., *Proc. TMS Symposium on Zinc-based Steel Coating Systems* (Krauss G. and Matlock D.K. eds.), Detroit, Michigan, Oct. 7-11, 109 (1990).
- Lin Y., Chiou W.-A. and Meshii M., *International Conference on Zinc and Zinc Alloy Coated Steel Sheet (GALVATECH)*, Amsterdam, 429 (1992).
- Lin Yu-Po and Selman R., *J. Electrochem. Soc.*, **140**, 1304 (1993).
- Lindsay J.H., Paluchi R.F., Nine H.D., Miller V.R. and O'keefe T.J., *Plating and Surface Finishing*, **76**, 62 (1989).
- Lowenheim F.A., *Electroplating*, McGraw-Hill Book Co., New York (1978).
- Mackowiak J. and Short N.R., *Int'l. Metals Reviews*, **1**, 1 (1979).

- Marder A., *Proc. TMS Symposium on Zinc-based Steel Coating Systems* (Krauss G. and Matlock D.K. eds.), Detroit, Michigan, Oct. 7-11, 55 (1990).
- Martyak N.M., McCaskie J.E. and Harrison L., *Metal Finishing*, February, 65 (1996).
- Martyak N.M., McCaskie J.E. and Nichols R.J., *Metal Finishing*, January, 20 (1996).
- Metals Handbook, *Properties and Selection: Irons, Steels and High Performance Alloys*, 10th edition, Volume 1, ASM International (1990).
- Mottate T., *Proc. of the International Conference of Zinc and Zinc Alloy Coated Steel Sheet (GALVATECH)*, The Iron and Steel Institute of Japan, Tokyo, 625 (1989).
- Ohbu M. and Asakawa K., *J. Metal. Finish. Soc. Japan*, **24**, 13 (1973).
- Ohmori Y., Nakai K., Ohtsubo H., Yagi T. and Matsumoto T., *ISIJ International*, **33**, 1196 (1993).
- Ohtsubo H., Matsumoto, Nakai K. and Ohmori Y., *ISIJ International*, **34**, 1002 (1994).
- Okamoto G., Horiuti J. and Hirota K., *Sci. Papers Inst. Phys. Chem. Res. Tokyo*, **29**, 223 (1936).
- Pak S.W., *Study on The Deformation Behavior of Electrogalvanized Coatings*, Ph.D. Thesis, Northwestern University, Evanston, Illinois (1991).
- Pak Suk-Wan and Meshii M., *Proc. TMS Symposium on Zinc-based Steel Coating Systems* (Krauss G. and Matlock D.K. eds.), Detroit, Michigan, Oct. 7-11, 341 (1990).
- Pak Suk-Wan and Meshii M., *Proc. TMS Symposium on Zinc-based Steel Coating Systems* (Krauss G. and Matlock D.K. eds.), Detroit, Michigan, Oct. 7-11, 357 (1990).
- Pangalov N.A., *J. of Electroanal. Chem.*, **9**, 70 (1965).
- Pangarov N.A. and Vitkova S.D., *Electrochimia Acta*, **11**, 1719 (1966).
- Park H. and Szpunar J.A., *submitted to Electrochimia Acta* (1997)
- Park H. and Szpunar J.A., *submitted to J. Appl. Electrochemistry* (1997).

- Park H. and Szpunar J.A., *submitted to Corrosion Science* (1997).
- Park H., Czerwinski F. and Szpunar J.A., *Material Science Forum*, **204-206**, part 2 703 (1995).
- Park H., Czerwinski F. and Szpunar J.A., *The Electrochemical Society Proceedings The Electrochem. Soc.*, Pennington, NJ, Volume **94-31** 146 (1994).
- Park H., Brennenstuhl A. and Szpunar J.A., *Proc. the 11th Int'l. Conf. on Texture of Materials (ICOTOM)*, Xi'an, China, Volume **2**, 1177 (1996).
- Parthasaradhy N.V., *Practical Electroplating Handbook*, Prentice-Hall Inc., Englewood Cliffs, New Jersey (1989).
- Petch N.J., *Phil. Mag.*, **1**, 331 (1956).
- Philippe M.J., *Material Science Forum*, **157-162**, 1337 (1994).
- Porter F., *Zinc Handbook*, Macel Dekker Inc (1991).
- Raichevski and Vitkova, *Zashchita Metallov*, **11**, 418 (1973).
- Rangarajan V., Giallourakis N.M., Matlock D.K. and Krauss G., *J. Mater. Shaping Technol.* **6**, 217 (1989).
- Rangarajan V., Matlock D.K. and Krauss G., *Proc. TMS Symposium on Zinc-based Steel Coating Systems* (Krauss G. and Matlock D.K. eds.), Detroit, Michigan, Oct. 7-11, 263 (1990).
- Raub E. and Muller K., *Fundamentals of Metal Deposition*, Elsevier Publishing Co., Amsterdam, (1967).
- Reddy A.K.N., *J. Electroanal. Chem.*, **6**, 141 (1963).
- Sangwal K., *Surface Morphology of Crystalline Materials*, Trans Tech Publ. Ltd. (1991).
- Scully J.C., *The Fundamentals of Corrosion*, Pergamon Press (1990).
- Shaffer S.J., Morris Jr. J.W. and Wenk H.R., *Proc. TMS Symposium on Zinc-based Steel Coating Systems* (Krauss G. and Matlock D.K. eds.), Detroit, Michigan, Oct. 7-11, 129 (1990).
- Shaffer S.J., Nojima W.E., Skarpelos P.N. and Morris Jr. J.W., *Proc. TMS Symposium on Zinc-based Steel Coating Systems* (Krauss G. and Matlock D.K. eds.), Detroit, Michigan, Oct. 7-11, 251 (1990).

- Sheshadry B.S. and Setty T.H.V., *J. Crystal Growth*, **21**, 110 (1974).
- Shima Y., Terasaka M., Nakaoka K., Hara T. and Honma T., *Tetsu-to-Hagan*, **8**, 954 (1986).
- Sun T., Wan C.C. and Shy Y.M., *Metal Finishing*, May, 33 (1979).
- Suzuki T., *J. Crystal Growth*, **20**, 202 (1973).
- Takechi H., Matsuo M., Kawasaki K. and Tamura T., *Proc. 6th Int'l. Conf. on Textures of Materials*, ISIJ, Tokyo, Japan, **2**, 210 (1981).
- Tang P.T., Watanabe T., Andersen J.E.T. and Bech-Nielsen G., *J. Appl. Electrochem.*, **25** 347 (1995).
- Teremura T., Kobayashi M. and Okutani M., *Japanese J. Appl. Phys.*, **25** 1439 (1986).
- Tomov I., *Materials Science Forum*, **157**, 1495 (1994).
- Venkataraman R., Giallourakis N.M., Matlock D.K. and Krauss G., *J. Mat. Shaping Tech.*, **6**, 217 (1989).
- Vlad C.M., *Proc. TMS Symposium on Zinc-based Steel Coating Systems* (Krauss G. and Matlock D.K. eds.), Detroit, Michigan, Oct. 7-11, 129 (1990).
- Walsh F. and Herron M., *J. Phys. D: Appl. Phys.*, **24**, 217 (1991).
- West J.M., *Electrodeposition and Corrosion Process*, 2nd ed., Van Nostrand Reinhold Co., London (1970).
- Winand R., *Fundamentals and Practice of Aqueous Electrometallurgy* (short course, coordinator: Demopoulos G.P.), sponsored by The Metallurgical Society of CIM, chapter 2, (1990).
- Wranglen G., *Corrosion and Protection of Metals*, Chapman & Hall, London, (1985).
- Wright D.A., Gage N. and Bushell P.G., *Metal Finishing*, April, 40 (1995).
- Wright J.E., *Epitaxial Growth: part A* (Matthews J.W. ed.), Academic Press, (1975).
- Ye G.C. and Lee D.N., *Proc. TMS-AIME*, Chicago, Illinois, Feb. 23-25, 493 (1981).



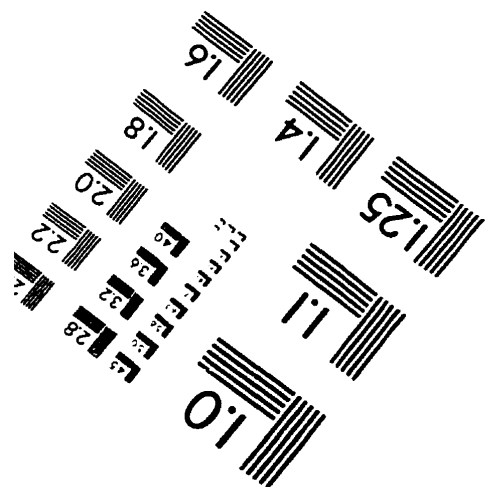
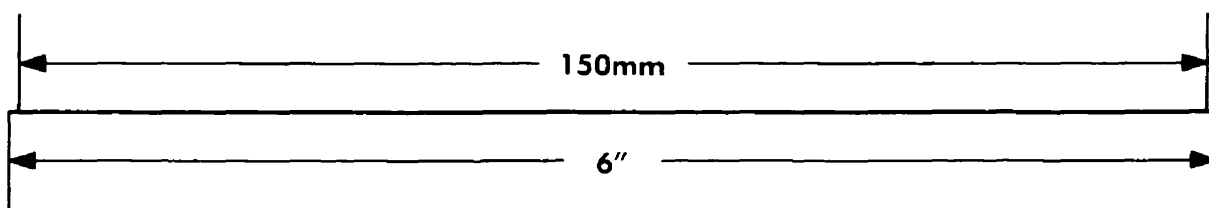
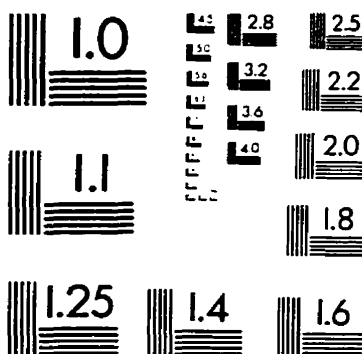
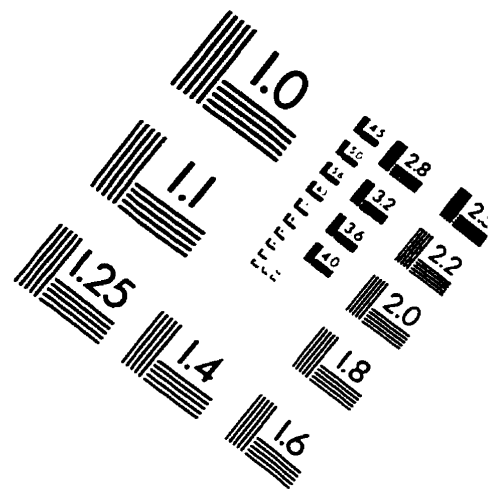
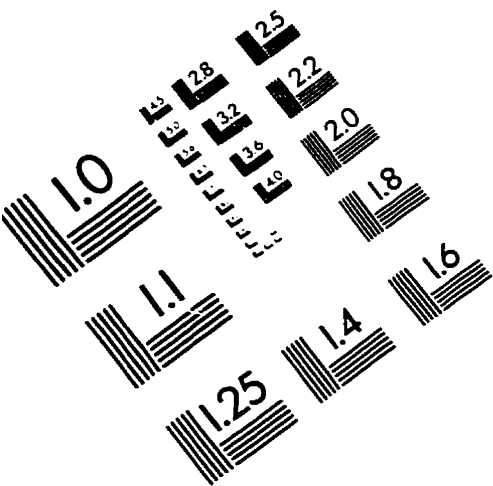
Ye G.C. and Lee D.N., *Plating and Surface Finishing*, **A**, 60 (1981).

Ye X., Celis J.P., DeBonte M. and Roos J. R., *J. Electrochem. Soc.*, **141**, 2698 (1994).

Yim Y.B., Hwang W.S. and Hwang S.K., *J. Electrochem. Soc.*, **142**, 2604 (1995).

Younan M.M., Ichino R. and Oki T., *Metal Finishing*, April, 40 (1996).

# IMAGE EVALUATION TEST TARGET (QA-3)



APPLIED IMAGE, Inc.  
1653 East Main Street  
Rochester, NY 14609 USA  
Phone: 716/482-0300  
Fax: 716/288-5989

© 1993, Applied Image, Inc., All Rights Reserved

